UNIVERSITY OF CALIFORNIA, SAN DIEGO

Lithospheric Bending at Subduction Zones
and
Geophysical Investigations of the Pukapuka Volcanic Ridge System, Altimeter Gravity Lineations and South Pacific Superswell Depth Anomaly

A Dissertation submitted in partial satisfaction of the requirements
for the degree Doctor of Philosophy in Earth Sciences

by

Daniel A. Levitt

Committee in charge

Professor David T. Sandwell, Chair
Professor Steve C. Cande
Professor Douglas MacDougall
Professor Martin J. Rudwick
Professor Edward L. Winterer

1996

The dissertation of Daniel A. Levitt is approved, and it is acceptable in quality and form for publication on microfilm:

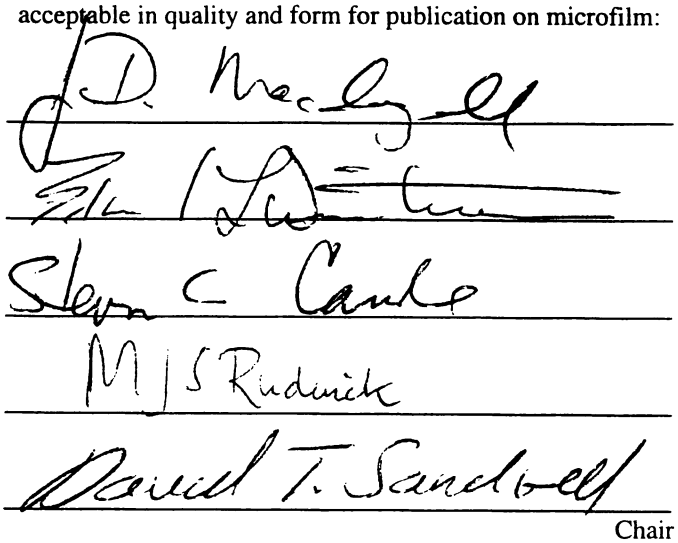

Chair

University of California, San Diego

1996

To my parents and the late Zehava Shnitzer

It was morning, and the new sun sparkled gold across the ripples of a gentle sea . . .

Jonathan Livingston Seagull

Table of Contents

List of Figures and Tables

Chapter 2

Chapter 3

ACKNOWLEDGMENTS

Six years ago I walked into David Sandwell's office where I was entranced by colorful computer images, satellite orbiters, differential equations and cutting-edge geophysical research. In my subsequent graduate career at Scripps Institution of Oceanography I grew to rely on him in practically every respect. While I was free to explore my scientific interests, he was always available for a good theoretical chat, always had the correct reference. Completion of this dissertation is a tribute to his continued support, for which I am very grateful.

The text of Chapters Two and Three, in full, are reprints of material as they appear in the Journal of Geophysical Research and Earth and Planetary Science Letters, respectively. The dissertation author was the primary researcher and author. The co-author listed in these publications, David Sandwell, directed and supervised the research which forms the basis of these chapters.

The Scripps experience is considerably undervalued by those (such as myself) who have grown overly accustom to it. Students are blessed with a comprehensive accessible library, state of the art equipment and facilities, and most importantly, an interdisciplinary faculty whose broad experience and knowledge are nearly inexhaustible. The members of my dissertation committee are due a special thanks for focusing the content and for thoughtful discussions. In particular, Steve Cande introduced me to the black art of seafloor magnetic anomaly picking, Jerry Winterer provided a fundament for marine geomorphologic interpretation and Doug MacDougall bridged the geochemical gap. Peter Lonsdale, Jason Phipps Morgan, Walter Smith, Miriam Kastner, Andrew Goodwillie, Catherine Johnson, Mara Yale and Marie Doin provided illumination in many thoughtful discussions.

I am thankful for core geology curriculum and seminar series professors, which forcibly provided a basis of current earth science research, especially in fields outside my own. Over the summer of 1995 Brad Werner conducted a private, open seminar in his home. Extended, free discussions plumbed the nature of the scientific process and firmly emplaced in my mind the principal role which science plays in rigorously testing reality.

I'd like to thank the R/V Melville, a wonderful ship, and her crew for faultless operation. Stu Smith and the folks at the geological data center are exemplary professional members of the Scripps community who do their utmost to supply the scientific contingent with everything they need.

Many wonderful people have touched my life. I must thank Catherine Johnson and Chris Small, the older generation in the lab, for keeping my head from getting overly inflated and for good career advice. The crazy ultimate-playing beach folk and the sentimental/exhibitionist crowd at Pier Review Toastmasters were always there for a good mental cleansing. Steve Mojzsis grew from an office-buddy to

a close friend whom I admire very much. I thank the young stallions in Brad Werner's complex systems lab for tolerating my antics; I accept responsibility for whatever errors there might be in their work.

Perhaps the greatest lesson I learned is the value of friendship. The support and love bestowed upon me by Scott, Amir, Stacey and Clair are immeasurable. Most importantly, it is difficult to express the debt owed to my family, especially my parents, who have given me life and continue to give all a man could ask.

VITA

September 19th, 1968	Born, New York, United States
1990	Bachelor of Science in Marine Science and Geology, University of Miami, United States
1990 - 1991	Regents Fellow, Scripps Institution of Oceanography, University of California, San Diego
1991 - 1994	National Science Foundation Fellow
1994 - 1996	Graduate Student Researcher, Scripps Institution of Oceanography, University of California, San Diego
1996	PhD. Earth Sciences, Universtiy of California, San Diego

PUBLICATIONS

Levitt, D. A., and D. T. Sandwell, Lithospheric bending at subduction zones based on depth soundings and satellite gravity, *Jour. Geophys. Res.*, 100, 1, 379-400, 1995.

Levitt, D. A. and D. T. Sandwell, Modal depth anomalies from multibeam bathymetry; is there a south Pacific Superswell?, *Earth. Planet. Sci. Lett.*, 139, 1-2, 1-16, 1996.

Sandwell, D. T., Winterer, E. L., Mammerickx, J., Duncan, R. A., Lynch. M. A., Levitt, D. A., and C. L. Johnson, Evidence for diffuse extension of the Pacific plate from Pukapuka ridges and cross-grain gravity lineations, *Jour. Geophys. Res.*, 100, B8, 15087-15099, 1995.

ABSTRACTS

Levitt, D. A., and D. T. Sandwell, Lithospheric bending at subduction zones based on depth soundings and satellite gravity, *EOS Trans. Amer. Geophys. Union*, 74, 43, 549, 1993.

Levitt, D. A., and D. T. Sandwell, Modal estimation of depth anomalies on the western flank of the EPR; implications for the South Pacific Superswell, *EOS Trans. Amer. Geophys. Union*, 75, 44, 647, 1994.

Sandwell, D. T., Johnson, C., Levitt, D., Lynch, M. A., Mammerickx, J., Small, C., Winterer, E. L., and M. Simons, Survey of Pukapuka volcanic ridge in the trough of a gravity roll, *EOS Trans. Amer. Geophys. Union*, 74, 16, 285, 1993.

Sandwell, D. T., Winterer, E. L., Mammerickx, J., Duncan, R. A., Lynch, M. A., Levitt, D. A., and C. Johnson, Evidence from the Pukapuka ridges for diffuse extension of the Pacific Plate; no mini hotspots, no convection, *EOS Trans. Amer. Geophys. Union*, 75, 44, 581, 1994.

Winterer, E. L., Johnson, C., Levitt, D., Lynch, M. A., Mammerickx, J., Sandwell, D., Small, C. and M. Simons, Morphology of Pukapuka volcanic ridge system, Southeast Pacific, *EOS Trans. Amer. Geophys. Union*, 74, 16, 285, 1993.

ABSTRACT OF THE DISSERTATION

Lithospheric Bending at Subduction Zones

and

Geophysical Investigations of the Pukapuka Volcanic Ridge System,

Altimeter Gravity Lineations and South Pacific Superswell Depth Anomaly

by

Daniel A. Levitt

Doctor of Philosophy in Earth Sciences

University of California, San Diego, 1996

Professor David T. Sandwell, Chair

The dissertation consists of two unrelated parts. Chapter 2 investigates the flexural response of subducting oceanic lithosphere worldwide. Chapters 3-5 use satllite altimeter gravity and multibeam acoustic soundings to investigate anomalous subsidence in the southcentral Pacific, the distribution of volcanic features on young Pacific seafloor and the devlopment of elongate Pukapuka ridges.

In chapter 2, a global study of trench flexure was performed by simultaneously modeling 117 bathymetric and satellite-derived gravity profiles. A tilt parameter is not required after age correction. Though bending moment increases by a factor of ten with lithospheric age, systematic mechanical thickness-age relations are obscured by inelastic bending and accumulated thermoelastic stress. The PSM and half-space cooling models provide better fit than GDH1 to calculated bending moments and zero-crossing depths.

In chapter 3, modal depth estimates from a multibeam bathymetry survey of the Pukapuka volcanic system and an original age model are used to re-examine the magnitude and regional of extent of

depth anomalies attributed to the South Pacific Superswell. Modal techniques accurately estimate normal seafloor depth in highly perturbed terrain. ETOPO-5 values in the region are shallower than survey data suggesting that lithosphere is normal. Low subsidence for seafloor younger than 24 Ma cannot be explained by a local hotspot or small scale convective rolls, and requires implausible crustal thickness variation.

In chapter 4, multibeam bathymetry from the Pukapuka volcanic system is tightly fit to a small circle model which is incompatible with established fixed hotspot model poles. Multibeam bathymetry and corresponding altimeter gravity at the Pukapuka ridges are closely correlated. Altimeter bumps attributed to volcanoes in this tectonically complex region are concentrated in gravity lineations troughs. Many small melting anomalies may interact with lithospheric zones of weakness attributed to tension and boudinage.

In chapter 5, multibeam bathymetry and imagery are used to seek evidence of normal faulting and to examine the gradation of Pukapuka volcanic features. Elongate summit vents, flank rift zones and a crestal ridge develop with increasing height. Gradient and form linearity increase with size but azimuths are persistently near-east-west. Morphologic resemblance to Hawaiian rift zones suggests that internal structure and eruptive and mass-wasting modes are similar. A tectonic tensional stress is likely to control azimuthal elongation within the edifice and during melt ascent.

CHAPTER 1

INTRODUCTION AND ORGANIZATION OF THESIS

The exploration of geological and geophysical processes occuring beneath the world ocean has expanded enormously with the initiation of ship-board acoustic surveying and the development of a global satellite altimeter gravity map. In particular, multi-narrow-beam sonar developed in the 1970's has revealed both the location and morphologic shape and structure of tectonic and volcanic features such as fracture zones, spreading centers and volcanic chains. Together with a suite of geophysical probing techniques including marine gravity, magnetics and seismics as well as heat flow and dredge-sample geochemical analysis, geologists operating in the marine environment have rivaled the geological sophistication of their continental counterparts. Because sea-going research is expensive, the global coverage availed by satellite altimeter gravity anomaly maps has critically supplemented existing bathymetric information in regions where surveying is poor, in the southern oceans and for small features. In concert, these sources of data continue to elucidate the surficial distribution of volcanic and tectonic features and their inter-relation.

At the same time, marine geophysical research has been directed upward from a fundamental basis of only a few cooperative overarching theoretical systems or paradigms (also born in the 1960's and 1970's) — the plate tectonics hypothesis, that the surface of the earth is composed of lithospheric plates which respond to stress rigidly and are driven by the negative bouyancy of subducted slabs, the hotspot

hypothesis, that deep mantle plumes produce volcanic chains recording plate motion directions, and the half-space cooling model, that lithosphere cools and thickens and seafloor deepens with age. In the last 25 years a number of theories have extended predictions of the mechanical and geodynamic behavior of oceanic lithosphere. For example, studies of load compensation due to seamounts, subduction zone bending and at fracture zones has shown that the mechanical thickness of oceanic lithosphere increases with age, roughly following the cooling model. Also, though the mantle convects on various length scales, the mantle-plume reference frame has grown to constitute a fixed absolute frame of reference such that the rotation pole prescribed based on one volcanic chain can be used to predict the age progression and orientation of other chains on the same plate for the same period of time. Conversely, second order questions have arrisen where the overarching principles have failed and where additional detail has been discovered not predicted by these paradigms. For example, careful investigation of radiometric ages from sequencial volcanic chain edifices has been commonly inconsistent with the monotonic age prediction of the hotspot hypothesis. Also, many unusual observations in the southcentral Pacific including anomalous low regional subsidence rates and altimeter gravity lineations has prompted the small-scale convection hypothesis in order to supply additional heat to the lithosphere. Recently a great deal of emphasis has been focused, using submersible equipment, on determining the fine scale volcanic processes occurring on the ocean floor, including factors controling volcano emplacement (at spreading centers and for well surveyed volcanoes), melt genesis and ascent.

The research presented in this dissertation is essentially a sequence of tests of major paradigms listed above. The chapter order is chronological. While projects are nearly independent the latter three (chapter 3-5) share data and scope. From December of 1992 through February of 1993 I participated in two consecutive legs of the Gloria expedition aboard the R/V Mellvile in the southcentral Pacific. This survey of the Pukapuka volcanic system comprises the primary source of data for chapters 3-5. Research undertaken prior to this expedition is presented in chapter 2.

Since the mid 1970's mounting evidence has suggested that the elastic thickness of oceanic lithosphere, the thickness to a particular isotherm, monotonically increases with the square root of age.

Confidence in the regularity of this relation has extended to prediction, so that overly thin results are considered anomalous. Chapter 2 simultaneously models a global set of satellite gravity and ship-sounding profiles to explore the flexural response to loading at subduction zones, in order to test the relation between age and elastic thickness as well as proposed perturbations due to inelastic bending and thermal pre-stressing. A recent re-evaluation of seafloor depths and heat flow has suggested that normal lithospheric cooling with age (the half-space model), interrupted by a large supply of heat to the base of the lithosphere (plate model), is better approximated by a shorter distance to the basal isotherm. The bending moments supported at subduction zone locations are used to test the maximum bending moments predicted for proposed plate and half-space models.

While the depth-age relation of seafloor is remarkably regular, distinct regions of seafloor exhibit depth anomalies which are departures from this relation. Shallowing associated with volcanic chains has been attributed to dynamic uplift and/or thermal rejuvination by a convective heat source in the mantle, such as a hot plume. The superswell hypothesis was advanced to explain a number of observations, most importantly, a regional depth anomaly in a bathymetry grid which increases broadly with age even where there are no hotspots. In chapter 3, a suite of multibeam surveys from a portion of the proposed Superswell region away from known hotspot tracks are tested for a long-wavlength depth anomaly. Since the surveys are focused about volcanically perturbed terrain, "normal" seafloor depths are estimated with a mode.

Volcanoes on the young portion of the Pacific Plate, south of the Marquesas Fracture Zone have been variably attributed to small hotspots, parallel asthenospheric convective rolls and magma escape through extensional faults. Chapter 4 presents tests of primary predictions of these models for the Pukapuka volcanic system and other volcanoes on young Pacific seafloor south of the Marquesas Fracture Zone. First, the close alignment of Pukapuka volcanic features is compared with the orientation predicted by the 0-18 Ma fixed hotspot absolute rotation pole. Next, the topographic and satellite altimeter signals of Pukapuka volcanoes are compared in order to test the reliability of satellite altimeter gravity as a proxy for topography. Finally, I test whether small altimetric bumps attributed to volcanic features are

preferrably located in peaks or troughs of gravity lineations, respectively predicted by convective and stretching models.

Finally, in chapter 5 I consider potential factors which influence the remarkably consistent azimuth and elongation of prism-shaped Pukapuka volcanoes in an area which is expected to have been subject to anisotropic tension. Normal faults predicted by the extension model are sought in multibeam bathymetry and sidescan image datasets. Morphologic and structural characteristics and gradational morphometric systematics with form are used to investigate the potential role of deviatoric stress, lithospheric thickness and magmatic flux. The resemblance of features to a well studied analog, Hawaiian flank rift zones, is considered as well as processes occuring within growing edifices and during melt ascent.

CHAPTER 2

LITHOSPHERIC BENDING AT SUBDUCTION ZONES

BASED ON DEPTH SOUNDINGS AND SATELLITE GRAVITY

JOURNAL OF GEOPHYSICAL RESEARCH, VOL. 100, NO. B1, PAGES 379–400, JANUARY 10, 1995

Lithospheric bending at subduction zones based on depth soundings and satellite gravity

Daniel A. Levitt and David T. Sandwell
Scripps Institution of Oceanography, La Jolla, California

Abstract. A global study of trench flexure was performed by simultaneously modeling 117 bathymetric profiles (original depth soundings) and satellite-derived gravity profiles. A thin, elastic plate flexure model was fit to each bathymetry/gravity profile by minimization of the L_1 norm. The six model parameters were regional depth, regional gravity, trench axis location, flexural wavelength, flexural amplitude, and lithospheric density. A regional tilt parameter was not required after correcting for age-related trend using a new high-resolution age map. Estimates of the density parameter confirm that most outer rises are uncompensated. We find that flexural wavelength is not an accurate estimate of plate thickness because of the high curvatures observed at a majority of trenches. As in previous studies, we find that the gravity data favor a longer-wavelength flexure than the bathymetry data. A joint topography-gravity modeling scheme and fit criteria are used to limit acceptable parameter values to models for which topography and gravity yield consistent results. Even after the elastic thicknesses are converted to mechanical thicknesses using the yield strength envelope model, residual scatter obscures the systematic increase of mechanical thickness with age; perhaps this reflects the combination of uncertainties inherent in estimating flexural wavelength, such as extreme inelastic bending and accumulated thermoelastic stress. The bending moment needed to support the trench and outer rise topography increases by a factor of 10 as lithospheric age increases from 20 to 150 Ma; this reflects the increase in saturation bending moment that the lithosphere can maintain. Using a stiff, dry-olivine rheology, we find that the lithosphere of the GDH1 thermal model (Stein and Stein, 1992) is too hot and thin to maintain the observed bending moments. Moreover, the regional depth seaward of the oldest trenches (~150 Ma) exceeds the GDH1 model depths by about 400 m.

Introduction

Analysis of the flexural response of the lithosphere to loading at seamounts, trenches and fracture zones has provided estimates of the mechanical thickness (h_m) of oceanic lithosphere as a function of age, generally confirming an age-thickening relationship [*Watts*, 1978; *Caldwell and Turcotte*, 1979] in accordance with lithospheric cooling models [*Turcotte and Oxburgh*, 1967; *McKenzie*, 1967; *Parsons and Sclater*, 1977]. The base of the mechanical lithosphere, defined as the depth to which deviatoric stress can be maintained over geological timescales, is believed to correspond to a specific isotherm. Estimates of mechanical thickness have been obtained by modeling flexural behavior as elastic [*Turcotte*, 1979], as elastic-plastic with constant yield strength [*McAdoo et al.*, 1978], as elastic-plastic with variable yield strength [*Goetze and Evans*, 1979] and as viscous [*DeBremaecker*, 1977]. Presently, models employing elastic and elastic-plastic theory are preferred, though horizontal stress components are often deemed necessary in order to optimally reduce data misfit [*Parsons and Molnar*, 1976; *McQueen and Lambeck*, 1989]. In order to keep the data analysis simple, the classic approach estimates the thickness of a thin elastic plate (h_e) that approximates the flexural behavior of the real lithosphere [*Gunn*, 1943; *Watts*, 1978]. These elastic model parameters can then be used to establish the mechanical thickness (h_m) of an elastic-plastic lithosphere by assuming a given rheology [*McNutt and Menard*, 1982; *McNutt*, 1984] or lithospheric viscosity [*DeBremaecker*, 1977].

At many trenches the large curvatures of the flexed lithosphere cause brittle fracture of the upper lithosphere and ductile flow of the lower lithosphere so that the estimated elastic thickness is much less than the true mechanical thickness; at seamounts, smaller curvatures result in less fracture and flow so that h_e is a good approximation of h_m. Following the method of *McNutt and Menard* [1982], true mechanical thickness values can be estimated based on the elastic thickness and curvature. Nevertheless, the current database of thickness estimates displays a distinct bimodality between h_m values deduced at seamounts and trenches [*Wessel*, 1992]. One possible explanation of this is that thermal bending stress due to cooling of the lithosphere with age can prestress the flat-lying plate so that when it is bent concave downward (trench) it appears stronger than when it is bent concave upward (seamount) [*Wessel*, 1992].

Present published results concerning trench flexure have been obtained from a composite of mixed data sources (topography, geoid, and gravity) as well as a variety of analytical techniques. Having limited computer power, *Caldwell et al.* [1976], *Caldwell and Turcotte* [1979], *Jones et al.* [1978], and *Turcotte et al.* [1978] determined elastic thickness for topographic profiles by measuring the distance

Paper number 94JB02468.
0148-0227/95/94JB-02468$05.00

between the first zero crossing and the outer rise peak x_b after arbitrarily assigning a baseline local depth. *McNutt* [1984] utilized a similar technique on topographic profiles generated from contour maps. *Bodine and Watts* [1979] did not estimate elastic thickness but assumed the base of the elastic layer was defined by the 500°C isotherm; they then varied the amplitude of the flexure w_b to best match eight topographic profiles. *McAdoo et al.* [1978] fitted topographic and gravity profiles to model-generated flexural deflection curves. *McAdoo and Martin* [1984] and *McAdoo et al.* [1985] generated estimates of flexural wavelength α and w_b from an ensemble of Seasat geoid observations. *Carey and Dubois* [1981] used a finite element method with specific point determination on topographic and seismic data. *Judge and McNutt* [1991] utilized a composite topography-geoid-gravity database to estimate the elastic thickness and plate curvatures at the Peru and Chile Trenches. A potential problem with their analysis is the use of highly interpolated topographic profiles where the interpolation algorithm uses thin, elastic plate flexure theory to fill the gaps [*Smith*, 1993]. *McQueen and Lambeck* [1989] fitted thin, elastic plate flexure models to 14 topographic profiles across the major western Pacific trenches where they specifically included model parameters for regional depth, regional slope, and first zero crossing location. By simultaneously minimizing these parameters along with the standard flexural parameters, they found a very wide range of acceptable models and suggested that estimates of elastic thickness from all previous studies are very uncertain.

The purpose of this study is to perform a uniform, unbiased analysis of global trench flexure by using original bathymetric soundings combined with a newly constructed global gravity grid derived from ERS 1, Geosat, and Seasat altimetry data [*Sandwell and Smith*, 1992]. Trench outer rise profiles are obtained from a global database of original geophysical data [*Smith*, 1993]. Many (117) profiles are selected in an effort to sample a range of relevant parameters such as lithospheric age, geographic location, subduction rate, slab dip, and slab depth (Figure 1). In order to maximize data quality and consistency, profiles are located in close proximity to long, approximately trench-normal bathymetric tracks. Free air gravity anomalies are extracted from a global grid of satellite altimetry data [*Sandwell and Smith*, 1992] along the topographic profiles. We simultaneously model trench outer rise topography and gravity using a thin elastic plate flexure model, but in contrast to previous studies, we also specifically include regional depth and first zero crossing position as model parameters. By using an improved seafloor age model [*Roest et al.*, 1992] we are able to correct the topographic profiles for regional slope so that this parameter is not required. Later we interpret these results in terms of yield strength envelope models.

Stein and Stein [1992] have recently developed a model of a thinner, hotter lithosphere (GDH1) than the plate (PSM) and half-space (HS) models of *Parsons and Sclater* [1977] in an effort to explain depth/age and heat flow/age observations for old oceanic lithosphere. More than 50 of our flexure profiles cross old lithosphere (100-140 Ma), where the differences in the predictions of these models is greatest, thus allowing for discrimination between lithospheric thermal models on the basis of their respective predicted mechanical properties. We use the regional depth, the bending moment needed to support the outer rise, and the mechanical thickness obtained at these sites to place constraints on the asymptotic lithospheric thickness.

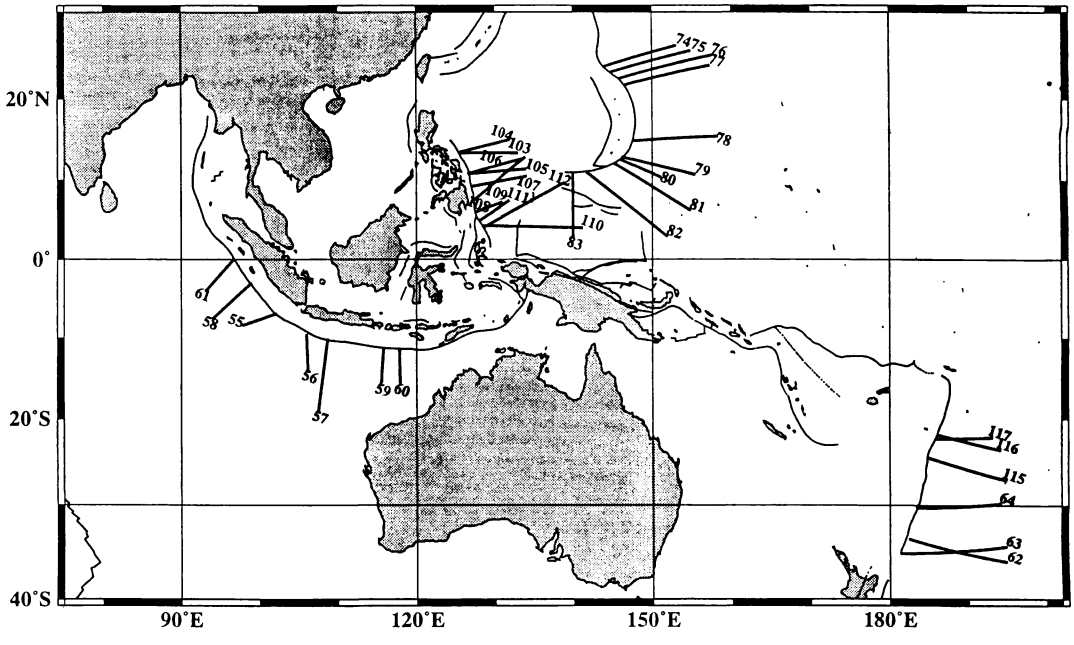

Figure 1a. Global great circle profile location map of Java, Kermadec, Marianas, Philippines, and Tonga Trenches. End points are presented in Table 1.

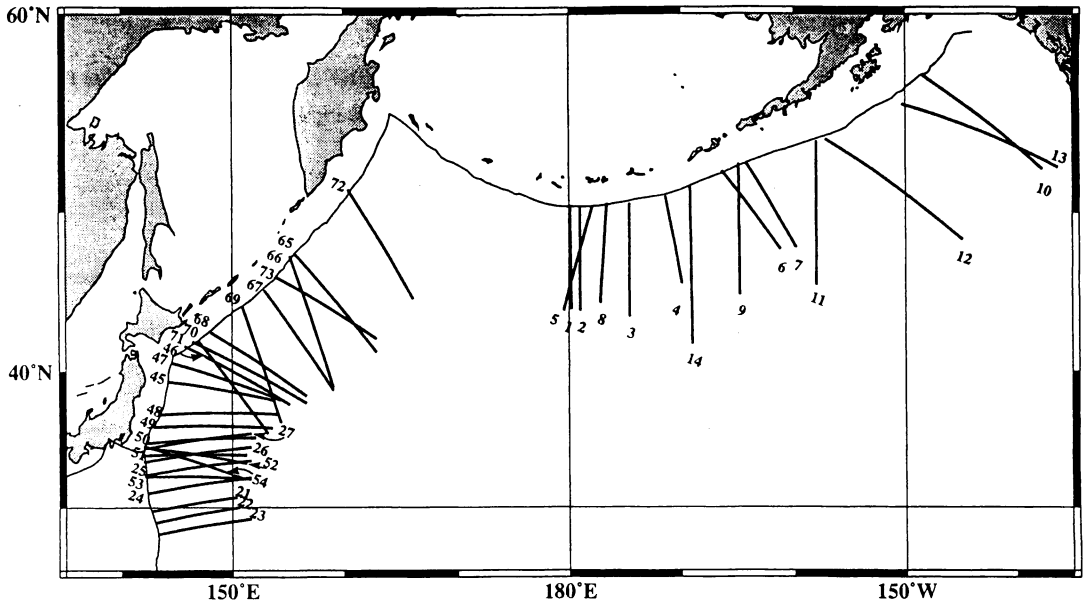

Figure 1b. Global great circle profile location map of Aleutians, Bonin, Japan, and Kuril Trenches. End points are presented in Table 1.

Flexure Model

In the elastic flexure model [*Gunn*, 1943; *Watts*, 1978], the thin plate is acted upon by a restoring force $g(\rho_m - \rho_w)w$, where w is the plate deflection, g is average gravity, and ρ_m and ρ_w are mantle and water density, respectively. If the applied load comprises a horizontal force P and a bending moment M the equilibrium equation is [*Turcotte and Schubert*, 1982]

$$\frac{d^2M}{dx^2} + P\frac{d^2w}{dx^2} - g(\rho_m - \rho_w)w = 0\,, \qquad (1)$$

where the bending moment M is related to the negative curvature of the plate by the flexural rigidity D:

$$M = -D\frac{d^2w}{dx^2}\,. \qquad (2)$$

Parsons and Molnar [1976] demonstrate that the end load is only an important factor in modeling flexure profiles when it is a substantial fraction of the load required to buckle the lithosphere. Tectonic regimes landward of subduction zones do not show evidence for large compressive stress (~500 MPa) [*Molnar and Atwater*, 1978] and in many cases are sites of extension and spreading. Furthermore, S. Mueller and R. J. Phillips (unpublished manuscript, 1992) found, from synthetic profile analysis, that inplane stress regime cannot be reliably constrained by attempting to recover parameters from best fitting elastic profiles, even with respect to distinguishing between compression and tension. Therefore we do not include the end load as a parameter in our flexural modeling. Under these simplifications and assumptions, a model for the deflection of the plate in response to an applied bending moment M_o is

$$w(x) = w_o \exp\left[\frac{-(x - x_o)}{\alpha}\right] \sin\left[\frac{(x - x_o)}{\alpha}\right] + s\,(x - x_o) + d_o\,, \qquad (3)$$

where w_o is the flexural amplitude parameter, x_o is the location of the load, s is the tilt parameter, d_o is the undeflected depth , and α is the flexural parameter (Figure 2). The flexural parameter is related to the elastic thickness h_e by

$$\alpha = \left[\frac{E\,h_e^3}{3\,(\rho_m - \rho_w)\,g\,(1 - \nu^2)}\right]^{\frac{1}{4}}, \qquad (4)$$

where E is Young's modulus and ν is Poisson's ratio. Later we will show that the tilt parameter is not needed if the regional depth versus age relation is accounted for using an accurate age model.

In order to discriminate between uncompensated topographic variation due to flexure and unrelated topographic deflection, we utilize gravity profiles corresponding to the topographic profiles. Following *McAdoo et al.* [1978], a modified Bouguer approximation is used to determine gravity, and we include the approximate reduction in gravity amplitude due to upward continuation of a constant wavelength signal ($2\pi\alpha$) from the crust/water interface at a mean ocean depth of d_a as well as the mantle/crust interface at an additional crustal thickness depth h_C. The attenuated gravity anomaly amplitude is thus obtained by

$$\Delta g(x) = 2\pi G\rho_o w_o \exp\left[\frac{-(x - x_o)}{\alpha}\right] \sin\left[\frac{(x - x_o)}{\alpha}\right]$$

$$\cdot\left\{\left(\frac{\rho_c - \rho_w}{\rho_m - \rho_w}\right)\exp\left[\frac{-d_a}{\alpha}\right] + \left(\frac{\rho_m - \rho_c}{\rho_m - \rho_w}\right)\exp\left[\frac{-(d_a + h_c)}{\alpha}\right]\right\} + \Delta g_o \qquad (5)$$

where G is the gravitational constant, Δg_o is the mean regional gravity anomaly, and ρ_o is a density parameter which measures the density of the mantle relative to sea water density (Figure 2).

The overall objective of the modeling is to establish a set of parameters which sensitively characterize the flexural

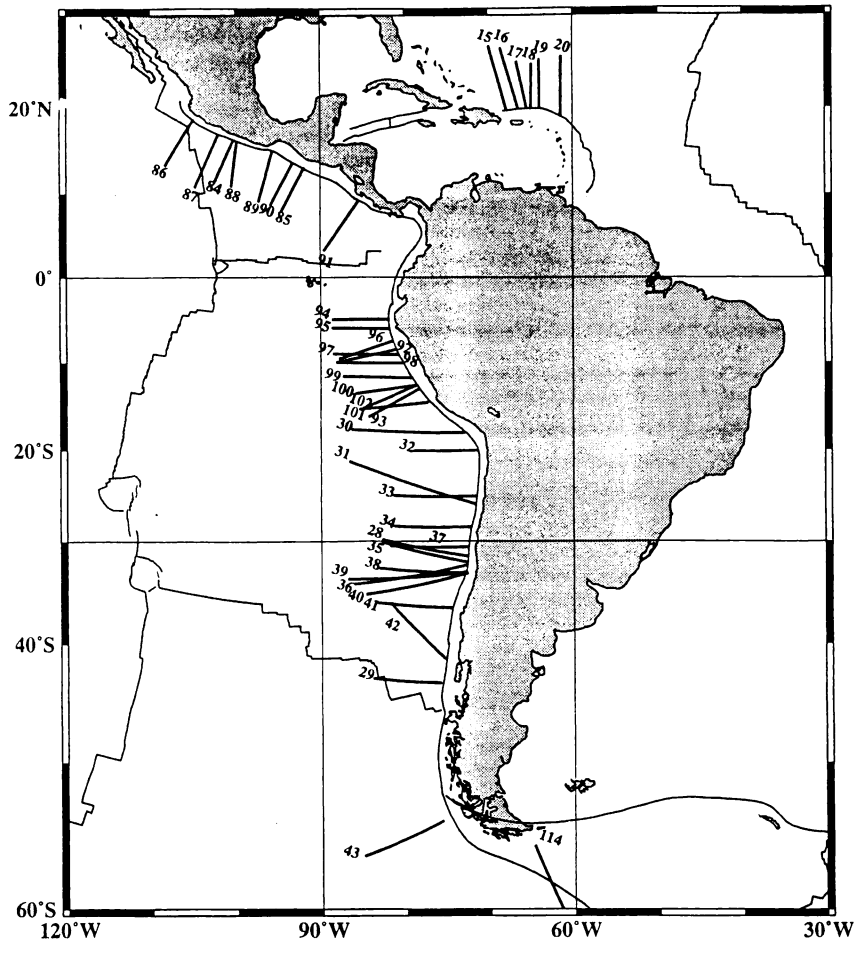

Figure 1c. Global great circle profile location map of Antilles, Chile, Middle America, Peru, and Shetland Trenches. Sandwich profile (113) is not shown for display purposes. End points are presented in Table 1.

behavior of plates experiencing bending at subduction zones. Therefore we wish to find the smallest number of parameters which will simultaneously minimize the misfit between the models (3) and (5) and the topography and gravity data. The most important issue, however, is not the modeling method but the selection, quality and treatment of the data.

Data

Bathymetry

A total of 117 projected great circle bathymetric profiles were obtained for 16 trench-outer rise complexes (Figure 1 and Table 1). Data were acquired from the Lamont-Doherty Earth Observatory on-line geophysical database [*Smith*, 1993] using GMT software [*Wessel and Smith*, 1991]. No effort was made to exclude profiles that had poor trench-outer rise signatures unless some obvious feature obscured the trench signature (e.g., aseismic ridges, complete sediment fill, or indeterminate trench axis location). Later on we use objective criteria to quantitatively eliminate poorly fit profiles. Within a particular complex, projected profile endpoint pairs (trench axis and basin) were selected so that the connecting great circles were in close proximity to long, continuous, straight, nearly trench-normal bathymetric ship tracks. All track data points which fell within a 100-km band of the great circle were retained and projected onto the great circle line. Typical bathymetric profiles are continuous and over 800 km in length, thus constraining mean ocean depth and regional tilt, and are usually less than 20° from normality to trench trend, minimizing cross trend topographic effects. In order to correct data for nonnormality, distance values were multiplied by $\cos\theta$, the angle between the profile and trench-perpendicular azimuths.

Before modeling, gross errors must be corrected in order to reduce deflection perturbation and density bias. Travel time errors occasionally arise due to an ambiguity in analog precision depth recorder (PDR) records [*Smith*, 1993]. For a

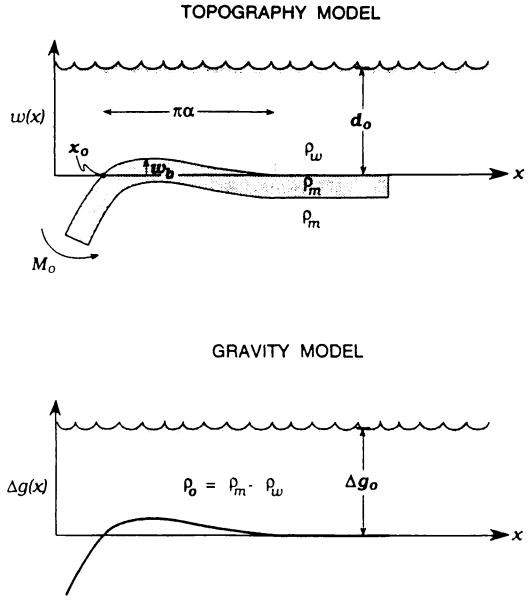

Figure 2. Schematic representation of topography (w_o, x_o, α, and d_o) and gravity (w_o, x_o, α, and g_o) model parameters, where $w_o \sim 3.10\ w_b$. See equations (3) and (5) for details of the model. Combined model (topograv) contains all of the above parameters and ρ_o. After application of a depth versus age correction, a regional slope parameter was not required. Topograv parameters are bold.

given trench profile, this error may result in a DC shift of bathymetric depths, appearing as a parallel set of depths above or below the general trend of values. Since these values are clearly erroneous, they were eliminated from each profile before any other processing was performed.

Indiscriminate data acquisition usually results in a nonuniform density of data throughout the profile length (Figure 3, points): crossing tracks result in dense sampling, while course changes and jumps result in data gaps. In order to reduce the biasing effects of erratic densities upon the modeling, a filter was applied to the raw data set. The median value within a 2-km moving window was retained at a 1-km spacing, and importantly, gaps were not filled with dummy values [*Wessel and Smith*, 1991]. A robust median filter was employed instead of a mean filter so as to minimize the weighting effects of outliers. The filter generally reduced the quantity of data by an order of magnitude while retaining the short-wavelength topographic variations (Figure 3).

The two-way travel time from which depths are determined is a function of the velocity structure of the water column, which is in turn a function of salinity, temperature, and pressure. *Smith* [1993] reports that these variations in the velocity are ignored and a nominal velocity is arbitrarily assigned to all bathymetric data, resulting in 5% inaccuracies. These nominal depths can be corrected to a first approximation by utilizing tabulated regional depth-related correction factors, or *Carter* [1980] tables. The filtered profile data were Carter-corrected, having minimal effect for shallow and middepth data, and significant effect with respect to deep-water values.

Thick layers of sediment on the basement topography adversely influence estimates of model parameters in (3). A uniform thickness layer of sediments will reduce the estimate of d_o, while extreme (>400 m) variations in sediment thickness will affect the α estimate, particularly where near the outer trench slope and outer rise. We have not accounted for sediment thickness mainly because sediment thickness data are not available along most of the profiles. Moreover, later we show that where sediment thickness is highly nonuniform, the gravity and bathymetry data will yield inconsistent models that are eliminated from further analysis.

It is known that ocean bottom depth increases with age [*Parsons and Sclater*, 1977]. Lithospheric ages may vary by tens of millions of years along trench profiles, resulting in age-related depth variation of hundreds of meters, particularly for "young" profiles. In order to minimize this effect, an age-related depth correction was applied to the Carter-corrected profiles. Ages were assigned to every point on a given profile based on a two-dimensional interpolation of an age grid [*Roest et al.*, 1992]. Then each point was corrected for age effects by subtracting the appropriate age formula [*Parsons and Sclater*, 1977]. For points younger than 20 Ma, we deduct a predicted depth d_{age}:

$$d_{age} = 2500 + 350\sqrt{t} \qquad (6)$$

where t is age in Ma. For points older than 20 Ma the correction formula is

$$d_{age} = 6400 - 3200 \exp\left(\frac{-t}{62.8}\right). \qquad (7)$$

While this depth-age relationship is known to be variable throughout the ocean basins [*Cochran*, 1986; *Hayes*, 1988; *Marty and Cazenave*, 1989], it is only the first-order depth variations that influence the flexural modeling, since interregional anomalous subsidence will not result in significant differential depth correction within a particular profile. An example of the age correction is shown in Figure 3, top curve; the age correction brings the entire profile to near zero depth.

Local perturbations along profiles due to the presence of seamounts and aseismic ridges were reduced by clipping the topographic highs above a uniform depth. Though such correction often improves the apparent quality of a profile, results obtained from profiles in which topographic noise is substantial must be considered poor.

Gravity

Gravity anomalies were extracted from a global gravity grid [*Sandwell and Smith*, 1992] which is derived from a combination of ERS 1, Geosat, and Seasat altimeter profiles using the method of *Sandwell* [1984, 1992]. For areas south of 30°S, where the density of Geosat profiles is relatively high, the satellite-derived gravity anomalies have a precision of 5.5-7 mGal [*Sandwell*, 1992; *Neumann et al.*, 1993]. In midlatitude areas, where the track density is worse, the anomalies are less accurate, especially at short wavelengths. However, since gravity amplitudes at trenches usually exceed 100 mGal and generally have wavelengths greater than the satellite track spacing (< 60 km), we believe that they are sufficiently accurate.

Table 1. Profile End Points, Model Ages, and Parameters

	Trench	Start		End		Age*,	Misfit,	w_o,	d_o,	α,	Range+,	ρ_o,	K_o,	M_o,	h_e,	h_m,
		Latitude	Longitude	Latitude	Longitude	Ma	m	m	m	km	km	kg m^{-3}	10^{-7}m^{-1}	10^{16} N	km	km
1	aleutian1	50.4	180.1	44.1	180.2	58.0	0.312	1712.7	-328.8	63.2	21.0	2048	8.58	7.38	24.6	36.6
2	aleutian2	50.3	181.0	44.0	181.0	58.0	0.312	1767.8	-291.0	67.1	24.0	2200	7.85	8.6	26.7	38.5
3	aleutian4	50.5	185.4	43.6	185.4	57.6	0.462	1496.8	-383.8	82.2	67.0	2200	-	-	-	-
4	aleutian5	50.9	188.6	45.7	190.1	58.3	0.405	613.4	-11.3	47.2	55.0	2300	-	-	-	-
5	aleutian6	50.3	182.1	44.0	179.5	57.9	0.309	2082.2	-315.1	62.6	19.0	2200	10.6	8.81	24.3	38.2
6	aleutian7	52.3	193.6	47.8	198.8	59.4	0.224	540.5	280.6	62.6	58.0	2383	-	-	-	-
7	aleutian8	52.7	195.8	47.9	200.2	58.1	0.298	880.8	228.4	83.9	54.0	2096	2.50	6.69	35.9	41.2
8	aleutian9	50.5	183.4	44.5	182.8	58.0	0.337	1779.0	-264.5	68.3	28.0	2206	7.63	8.95	27.3	39.8
9	aleutian10	52.7	195.1	45.0	195.2	58.6	0.252	794.8	175.4	84.2	35.0	2199	2.24	6.08	36.1	40
10	aleutian11	57.2	211.6	52.4	222.3	43.8	0.432	932.7	577.4	110.6	70.0	2200	1.52	12.3	51.9	61
11	aleutian12	53.9	202.0	45.6	202.0	56.4	0.476	662.7	259.6	89.5	125.0	2199	-	-	-	-
12	aleutian13	54.0	202.8	48.4	215.1	55.4	0.301	1490.3	140.4	102.9	35.0	1598	-	-	-	-
13	aleutian15	55.8	209.7	52.5	223.7	42.8	0.526	62.0	520.2	31.7	53.0	1882	-	-	-	-
14	aleutian17	51.4	190.8	41.8	191.0	60.0	0.624	638.8	-120.9	49.6	82.0	2819	-	-	-	-
15	antilles1	19.7	292.2	26.8	290.1	109.3	0.736	386.0	458.3	21.4	64.0	700	-	-	-	-
16	antilles2	19.8	293.6	26.6	291.5	111.0	0.327	1424.7	144.4	73.9	43.0	2200	5.21	8.41	30.3	40.5
17	antilles3	19.9	294.6	25.1	293.4	103.3	0.209	1315.2	-9.1	68.7	18.0	2200	5.58	6.69	27.5	36.4
18	antilles4	19.8	295.1	24.9	295.2	101.2	0.161	1819.5	-100.2	69.3	11.0	2076	7.57	9.44	27.8	40.3
19	antilles5	19.9	296.1	25.4	296.1	97.5	0.305	1851.8	-133.6	77.7	16.0	2050	6.14	12.1	32.4	45.2
20	antilles6	18.9	298.6	25.7	298.7	87.3	0.424	1587.6	-290.2	74.5	44.0	2200	5.72	9.51	30.6	41.3
21	bonin2	29.7	142.7	30.8	150.4	141.8	0.265	1836.8	-104.3	65.8	23.0	1797	8.48	8.59	26	38.8
22	bonin3	28.8	143.0	30.0	150.6	142.2	0.290	1534.0	-129.1	85.2	51.0	1795	4.23	12	36.6	47
23	bonin4	27.9	143.3	29.1	151.7	143.2	0.339	954.2	38.9	84.3	73.0	1467	-	-	-	-
24	bonin6	31.1	142.3	32.3	151.7	141.7	0.414	336.9	108.5	35.0	75.0	2074	-	-	-	-
25	bonin7	32.5	142.1	33.6	151.7	140.7	0.363	1791.6	79.6	114.2	77.0	2245	2.75	25.2	54.1	75
26	bonin8	33.5	142.0	34.6	151.7	140.9	0.361	1706.1	161.0	80.9	46.0	1860	5.21	12.1	34.2	46.7
27	bonin9	34.5	142.0	35.6	151.7	139.9	0.340	601.0	231.1	46.2	66.0	2366	-	-	-	-
28	chile2	-31.6	287.4	-29.8	277.1	40.0	0.476	1079.3	423.5	57.6	37.0	2322	6.5	3.86	21.7	28.4
29	chile3	-43.5	284.1	-43.1	276.0	13.6	0.564	1239.9	-100.4	82.1	44.0	269	-	-	-	-
30	chile4	-18.1	287.1	-17.7	273.6	41.9	0.530	1239.2	59.0	71.2	70.0	2101	-	-	-	-
31	chile5	-26.1	288.5	-21.3	273.3	43.9	0.599	2442.7	305.8	150.6	187.0	1189	-	-	-	-
32	chile6	-20.1	288.7	-20.1	280.9	49.3	0.460	2971.1	-113.9	74.6	37.0	1027	-	-	-	-
33	chile8	-25.2	288.5	-25.1	278.5	44.2	0.610	1220.9	510.6	148.0	222.0	2200	-	-	-	-
34	chile9	-28.5	287.9	-28.4	278.6	41.8	0.365	537.2	516.3	62.1	63.0	1740	-	-	-	-
35	chile10	-32.2	287.3	-30.1	277.1	39.5	0.448	528.3	550.1	35.9	46.0	2604	-	-	-	-
36	chile11	-32.5	287.2	-34.4	273.8	38.9	0.318	2178.1	359.1	64.6	17.0	1471	-	-	-	-
37	chile12	-30.6	287.5	-30.5	278.0	40.4	0.455	632.8	396.6	56.2	44.0	2254	-	-	-	-
38	chile13	-33.3	287.2	-32.8	276.8	36.7	0.429	1483.8	421.8	58.2	29.0	2442	8.75	5.43	22.1	32.4
39	chile14	-33.2	287.3	-33.9	273.1	36.7	0.493	1466.8	423.3	60.6	35.0	2237	7.99	5.81	23.3	33.5
40	chile15	-33.3	287.4	-35.4	275.2	36.4	0.481	718.5	462.8	78.0	51.0	3516	-	-	-	-
41	chile16	-36.7	285.4	-36.2	276.6	32.2	0.434	327.7	351.5	66.6	53.0	3099	-	-	-	-
42	chile17	-41.4	284.6	-36.2	278.1	21.0	0.913	-22.1	288.5	48.3	161.0	2199	-	-	-	-
43	chile18	-54.3	284.3	-56.7	274.9	20.2	0.624	1021.7	-149.2	123.4	72.0	1615	-	-	-	-
44	hjort1	-58.1	157.6	-58.0	149.6	15.6	0.327	591.9	458.5	39.3	36.0	2087	-	-	-	-

Table 1. (continued)

	Trench	Start		End		Age*,	Misfit,	w_o,	d_O,	α,	Range+,	ρ_o,	K_o,	M_o,	h_e,	h_m,
		Latitude	Longitude	Latitude	Longitude	Ma	m	m	m	km	km	kg m^{-3}	10^{-7}m^{-1}	10^{16} N	km	km
45	japan1	39.3	144.3	38.0	153.7	132.0	0.312	1625.2	266.4	117.1	48.0	2028	2.37	24.1	56	72
46	japan2	41.7	145.7	37.7	155.2	127.0	0.416	602.3	510.0	86.8	65.0	3675	-	-	-	-
47	japan3	40.6	144.5	38.0	154.4	130.0	0.376	1475.2	387.5	125.9	55.0	2241	1.86	25.2	61.7	70
48	japan4	37.0	143.4	37.0	154.2	135.1	0.321	994.1	189.2	119.3	66.0	2381	1.4	15.3	57.4	63
49	japan5	36.1	142.9	36.0	153.6	135.9	0.553	237.8	263.0	46.7	122.0	2607	-	-	-	-
50	japan6	34.9	142.1	35.3	152.1	139.3	0.388	897.5	176.8	60.2	51.0	2240	-	-	-	-
51	japan7	34.0	141.9	34.0	151.3	140.6	0.325	1562.3	172.3	53.3	40.0	1750	-	-	-	-
52	japan8	34.6	142.0	33.4	151.3	140.0	0.416	1986.6	101.8	94.9	71.0	2200	-	-	-	-
53	japan9	32.4	142.1	32.2	151.7	140.8	0.317	1100.5	142.4	71.7	57.0	2199	-	-	-	-
54	japan10	34.7	142.0	32.3	150.8	140.1	0.438	929.0	237.0	56.1	70.0	2199	-	-	-	-
55	java3	-6.9	102.2	-8.4	97.8	71.8	0.520	591.9	-111.7	43.3	29.0	1673	-	-	-	-
56	java4	-9.5	106.0	-14.1	106.2	82.1	0.388	2639.2	-101.6	57.1	20.0	1679	-	-	-	-
57	java5	-10.1	108.7	-19.1	107.5	85.8	0.768	209.1	300.0	21.7	215.0	2016	-	-	-	-
58	java6	-3.0	99.0	-7.6	94.0	58.9	0.467	2089.1	-76.1	112.4	65.0	1227	-	-	-	-
59	java7	-11.3	115.8	-15.6	115.5	92.3	0.365	1381.3	-59.4	84.1	40.0	2199	3.9	10.5	36	45
60	java11	-11.3	117.8	-15.7	117.9	93.9	0.252	836.2	-55.0	61.8	16.0	2196	4.38	3.44	23.9	29.2
61	java13	0.1	96.8	-4.1	93.1	47.9	0.626	511.6	136.7	74.3	106.0	2070	-	-	-	-
62	kermadec1	-33.6	182.4	-36.1	195.0	95.5	0.651	258.7	34.6	49.4	230.0	1800	-	-	-	-
63	kermadec2	-35.2	181.3	-34.4	195.0	94.8	0.335	262.9	52.5	60.9	72.0	2200	-	-	-	-
64	kermadec4	-30.3	183.3	-29.8	194.2	96.9	0.582	354.1	176.8	26.9	161.0	2355	-	-	-	-
65	kuril2	47.5	155.7	41.3	162.9	114.8	0.473	2006.3	554.5	106.7	80.0	2199	-	-	-	-
66	kuril3	47.4	155.2	38.9	159.1	116.1	0.365	1963.6	467.8	109.4	37.0	2200	3.28	25.4	51.2	71
67	kuril4	45.3	152.9	38.7	159.1	120.3	0.265	1325.1	451.7	66.2	22.0	2359	6.05	6.27	26.2	35
68	kuril5	42.6	148.1	38.3	156.7	120.0	0.363	1729.9	359.2	120.2	66.0	2200	2.39	27	58	75
69	kuril6	44.3	150.9	36.4	154.4	122.6	0.229	2589.5	316.8	103.9	26.0	1748	4.8	30.2	47.7	70
70	kuril7	42.1	146.9	35.6	153.2	120.0	0.446	1023.3	428.9	70.5	94.0	2491	-	-	-	-
71	kuril8	42.0	146.4	37.8	156.7	120.0	0.372	1175.3	366.6	110.1	89.0	2586	-	-	-	-
72	kuril9	51.3	160.4	44.8	166.1	100.2	0.523	1267.4	-10.7	128.1	110.0	1848	-	-	-	-
73	kuril10	46.1	154.0	42.2	162.9	118.1	0.286	2056.8	495.2	94.8	31.0	2029	4.57	20	42.3	57.8
74	mariana1	23.8	143.8	26.3	153.1	145.4	0.592	1887.2	289.6	72.4	46.0	2200	-	-	-	-
75	mariana2	23.2	144.8	25.7	154.9	146.1	0.575	173.9	272.4	47.8	76.0	2733	-	-	-	-
76	mariana3	22.4	145.7	25.2	157.6	148.1	0.600	463.5	376.2	78.4	126.0	2200	-	-	-	-
77	mariana4	21.7	146.6	24.0	157.3	148.7	0.588	171.0	454.1	29.2	89.0	2520	-	-	-	-
78	mariana7	14.9	147.6	15.5	158.3	152.5	0.857	636.0	168.3	132.7	236.0	2199	-	-	-	-
79	mariana8	12.9	146.1	10.7	155.4	144.0	0.307	2523.0	183.9	88.6	28.0	1947	6.43	21.4	38.6	57
80	mariana9	12.6	145.9	10.4	151.1	142.7	0.308	1339.7	237.0	67.8	32.0	1928	5.83	6.65	27	36.4
81	mariana10	12.1	145.2	6.2	154.8	140.6	0.588	650.4	950.2	58.2	79.0	1307	-	-	-	-
82	mariana11	11.0	141.7	2.9	151.9	133.3	0.684	7350.3	150.0	618.0	409.0	894	-	-	-	-
83	mariana12	10.9	140.0	2.7	140.0	130.3	0.847	5194.7	1692.8	242.1	22.0	436	-	-	-	-
84	middle1	16.3	259.8	11.3	257.5	11.1	0.510	638.5	-10.9	44.9	52.0	1797	-	-	-	-
85	middle2	13.1	268.1	7.9	265.4	27.3	0.327	1241.1	179.1	71.8	33.0	1881	4.82	6.90	29.1	37.5
86	middle3	18.7	255.1	13.3	251.7	1.7	0.666	461.6	-357.7	48.8	122.0	1377	-	-	-	-
87	middle4	16.9	258.0	10.7	255.2	7.5	0.587	505.6	-204.8	51.2	54.0	2178	-	-	-	-
88	middle5	16.1	260.2	10.8	259.5	12.6	0.345	415.4	156.0	43.5	30.0	2231	4.39	0.848	15	17.2
89	middle7	15.1	264.4	9.0	262.7	22.6	0.710	626.5	-58.3	43.6	92.0	2200	-	-	-	-
90	middle8	13.7	266.8	8.6	264.1	24.8	0.569	833.4	-13.4	64.4	66.0	2483	-	-	-	-
91	middle9	9.2	274.5	3.2	270.4	27.3	0.741	2331.2	723.9	75.4	76.0	587	-	-	-	-

Table 1. (continued)

	Trench	Start		End		Age*,	Misfit,	w_o,	d_o,	α,	Range+,	ρ_o,	K_o,	M_o,	h_e,	h_m,
		Latitude	Longitude	Latitude	Longitude	Ma	m	m	m	km	km	kg m^{-3}	10^{-7}m^{-1}	10^{16} N	km	km
92	peru1	-8.5	278.9	-10.0	271.8	29.5	0.352	213.6	-73.8	59.2	84.0	2018	-	-	-	-
93	peru2	-13.0	281.7	-16.3	275.6	38.9	0.552	314.8	-88.6	90.6	152.0	4741	-	-	-	-
94	peru3	-5.0	278.1	-5.0	271.3	29.7	0.520	443.2	470.2	75.5	79.0	1986	-	-	-	-
95	peru4	-6.1	278.2	-6.0	271.3	29.4	0.409	379.5	285.0	58.8	64.0	1931	-	-	-	-
96	peru5	-7.5	278.6	-9.6	272.1	29.5	0.342	598.1	-75.9	90.4	55.0	2199	1.46	5.28	39.7	46
97	peru6	-9.1	279.2	-9.0	271.4	29.5	0.354	205.4	-93.8	60.8	88.0	2200	-	-	-	-
98	peru7	-10.1	279.7	-10.0	271.9	29.5	0.383	228.0	-199.4	81.0	78.0	2159	-	-	-	-
99	peru8	-11.8	280.7	-11.6	272.6	36.2	0.454	488.2	-163.6	69.9	44.0	1837	2	2.58	28.2	30.2
100	peru9	-12.6	281.4	-13.6	274.0	38.7	0.602	160.1	-89.4	48.8	190.0	2741	-	-	-	-
101	peru10	-12.6	281.4	-15.3	275.0	38.8	0.323	1060.1	-233.5	108.1	52.0	2061	1.81	13.4	50.4	58
102	peru11	-14.6	282.7	-15.4	274.5	39.4	0.359	2154.1	-222.8	126.6	45.0	902	-	-	-	-
103	philippine3	13.4	125.6	13.4	133.0	117.6	0.536	2835.7	23.2	118.7	69.0	484	-	-	-	-
104	philippine4	13.5	125.5	15.0	131.7	117.9	0.477	1029.7	387.7	117.1	64.0	1701	1.5	15.2	56	62
105	philippine5	10.8	126.6	11.4	134.0	116.2	0.467	314.2	198.4	45.1	135.0	2200	-	-	-	-
106	philippine6	10.8	126.5	12.7	133.6	116.4	0.470	555.8	124.8	24.6	150.0	1713	-	-	-	-
107	philippine7	9.2	126.9	10.5	134.1	115.3	0.668	331.6	61.9	42.1	141.0	2200	-	-	-	-
108	philippine8	7.4	127.2	12.9	133.9	113.9	0.737	2856.4	9.6	52.8	108.0	1254	-	-	-	-
109	philippine9	6.0	127.5	7.3	131.0	112.5	0.396	1067.1	323.6	53.3	71.0	2118	-	-	-	-
110	philippine10	4.3	128.3	4.0	141.2	111.3	0.641	3536.2	571.5	355.6	387.0	836	-	-	-	-
111	philippine11	4.9	128.0	7.5	131.9	111.7	0.306	1616.8	315.2	47.7	22.0	1503	-	-	-	-
112	philippine12	4.1	128.6	9.7	138.9	111.3	0.722	806.1	638.0	95.0	200.0	2207	-	-	-	-
113	sandwich1	-55.8	334.8	-51.6	351.0	72.8	0.449	3239.7	523.4	89.2	52.0	962	-	-	-	-
114	shetland1	-61.3	299.8	-56.0	295.2	16.3	0.869	528.9	1731.6	251.4	16.0	2200	-	-	-	-
115	tonga1	-24.6	184.8	-27.2	195.0	100.1	0.477	996.3	101.6	69.3	110.0	1869	-	-	-	-
116	tonga2	-21.9	186.1	-23.7	194.2	101.4	0.366	319.2	-19.2	81.1	70.0	2836	-	-	-	-
117	tonga3	-22.4	186.0	-22.2	193.2	101.3	0.374	254.2	-3.3	71.8	61.0	2326	-	-	-	-

Fractional misfit, flexural amplitude, regional depth, flexural parameter, 10% flexural parameter range, and lithospheric density obtained using the topograv modeling scheme. Curvature, bending moment, and effective elastic thickness are determined by the thin elastic plate model, with mechanical thickness values determined using the h_e to h_m conversion method proposed by *McNutt and Menard* [1982], for "successfully" fit topograv ($\lambda = 0.4$). Data for grav ($\lambda = \infty$) and topo ($\lambda = 0$) are available on microfiche.

* Age [*Roest et al.*, 1992] is measured at first zero crossing seaward of trench axis.

+ Range is the difference between the maximum and minimum α. Note that the range is not always centered at α.

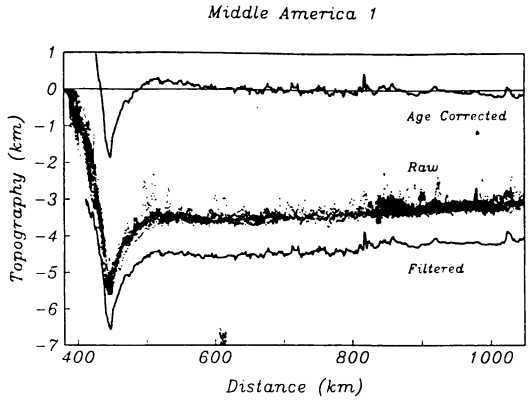

Figure 3. Raw, filtered, and age-corrected plots of the Middle America 1 profile data (84). One-kilometer window, median filter data are shifted 1 km downward from raw data for presentation. Age-corrected data are displayed with reference to zero depth.

Flexural Modeling

Age-corrected topographic profile data and gravity were modeled by fitting them to the topographic model (3) and gravity model (5), respectively. We develop a misfit formula which minimizes the difference between observed data and predicted values in order to obtain a best fitting parameter set for six model parameters: w_o, ρ_o, α, x_o, d_o, and Δg_o. (Below we discuss the rationale for not using a slope parameter in the topographic model.) Note that this is a nonlinear parameter estimation problem in both x_o and α so a standard linear least squares approach cannot be used and there may be local minima that do not correspond to the global minimum. The minimization algorithm we use is the downhill simplex method [*Nelder and Mead*, 1965], implemented in Matlab [*Mathworks*, 1993]. This is a multidimensional minimization that requires only function evaluations without derivatives. The downhill simplex method is started with an initial multidimensional point, defining the initial simplex. The method then takes a series of steps (reflections, expansions and contractions within parameter space) until a tolerance limit is reached in the change of the function value or the change in the magnitude of the parameter vector. The algorithm locates the first local minimum which satisfies the tolerance criteria. Therefore it is critical to determine the sensitivity of minimum misfit estimates to the initial parameter set. If the minimum obtained by the simplex minimization scheme varies substantially for reasonable starting guesses, then the method may be considered inappropriate, as the method and not the data is constraining the best fit model parameters.

The downhill simplex method can accommodate almost any reasonable type of minimization so we have devised a function to simultaneously optimize topography and gravity fits. First, in order to reduce sensitivity to seamounts and other large topographic features, the sum of the absolute residuals (data - model), rather than rms misfit is calculated. Second, since we wish to model outer rise profiles with distant, seaward portions of profiles serving only to constrain the undeflected profile depth, the data were assigned a weight that decreases linearly with distance from the trench axis. Third, the residuals are normalized by the absolute deviation of the data from the mean (the "linear" variance). The total misfit is

$$\psi = \frac{1}{(1+\lambda)}\left[\sum_{i=1}^{N}\left|\frac{w_i - w(x_i)}{\sigma_w}\right| + \lambda\sum_{i=1}^{N}\left|\frac{\Delta g_i - \Delta g(x_i)}{\sigma_{\Delta g}}\right|\right], \qquad (8)$$

where the linear variances of the deflection σ_w and gravity $\sigma_{\Delta g}$ are given by

$$\sigma_w = \sum_{i=1}^{N}\left|w_i - d_o\right| \qquad \sigma_{\Delta g} = \sum_{i=1}^{N}\left|\Delta g_i - \Delta g_o\right|. \qquad (9)$$

N is the number of data points, $w(x_i)$ and $\Delta g(x_i)$ are the model topography and gravity, w_i and Δg_i are the observed topography and gravity, and λ is a parameter that scales the weight of the topography relative to the weight of the gravity data; later we will set λ to 0 (topo), 0.4 (topograv), and ∞ (grav). The L_1 norm misfit parameter ψ is a measure of the improvement of the six-parameter model over a two-parameter model, d_o and Δg_o.

Prior to the complete analysis, we tested whether or not a regional topographic slope is needed to obtain reliable fits to the topographic profiles. *McQueen and Lambeck* [1989] have suggested that regional topographic tilt, due to poor depth/age correction, thermal swell, or dynamic uplift, has a significant effect on elastic fit models, which, if left unaccounted for, results in poor and biased estimates of model parameters. We used a least squares minimization on the topography data so that established statistical tests could be utilized (e.g., F test). In the majority of cases, the models displayed good visual fits to the data, regardless of presence or absence of free tilt. We believe the lack of significant tilt in most of our profiles is due to the improved age model provided by *Roest et al.* [1992]. In most cases where both models converge on similar outer rise dimensions, the fractional misfit yielded by the free-tilt model is marginally lower than that obtained by a fixed-tilt model. However, sensitivity to the relevant parameters is sacrificed. Figure 4a shows a typical profile obtained at the Aleutian Trench, containing a medium-sized outer rise, nearly no regional tilt, and relatively noise-free topography. The fixed- and free-tilt models appear to fit the topography equally well (Figure 4a) and result in similar flexural parameters (no tilt, 59.5 km; tilt, 62.2 km) and similar flexural amplitudes (no tilt, 1.53 km; tilt, 1.72 km). The modest positive tilt accommodates a gentle slope seaward of the trench and outer rise. Plots of fractional rms misfit as a function of α for the best fit model (Figure 4b) demonstrate that there is a slight decrease in misfit for the free tilt model (< 1%). However, the increase in the width about the minimum of the misfit curve (dashed) confirms the loss in sensitivity of the free-tilt model to the flexural wavelength [*McQueen and Lambeck*, 1989]. Furthermore, the mutual dependence of the model parameters implies that the tilt term is altering the wavelength value.

In contrast to this Aleutian Trench profile which has low tilt, we also selected a profile at the Middle America Trench which displays moderate tilt (Figure 4c). In this case, the free-tilt model provides an improved fit to the data (Figure 4d) and results in a shorter flexural parameter (no tilt, 56 km; tilt, 30 km) and a lower flexural amplitude (no tilt, 0.85 km; tilt, 0.26 km). Because the tilt is large relative to the amplitude of the flexure, the fixed-tilt model probably provides a poor estimate of the flexural parameter. Conversely, while the free-tilt model provides a better fit to the data (improved misfit by >10%) it

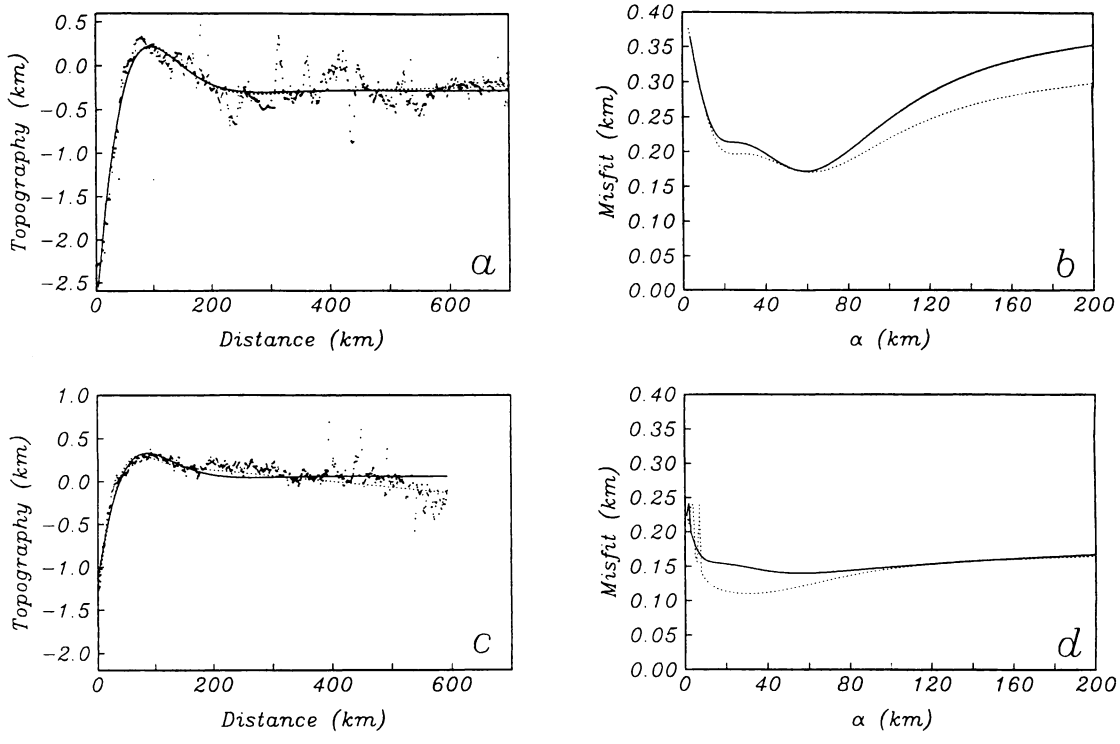

Figure 4. (a) Best fit RMS models for the Aleutian 1 profile (1). Solid line corresponds to a zero, fixed-slope model. Dashed line corresponds to a free-slope model. (b) Best fit RMS misfit values for a range of flexural parameter values (α) for the Aleutian 1 profile (1). Solid line corresponds to a zero, fixed slope model. Dashed line corresponds to a free slope model. (c) Same as Figure 4a for the Middle America 5 profile (88). (d) Same as Figure 4b for the Middle America 5 profile (88).

probably estimates slopes well and the flexural parameters poorly.

In general, a tangible improvement in model misfit is necessary in order to justify the substantial decrease in sensitivity to the parameters of interest. An F test comparing the variances of both models fails to justify the use of the additional tilt parameter at the 90% confidence level even for the most tilted profiles. Considering the loss in sensitivity to the parameters of interest and minimal improvement in misfit we chose not to include the tilt parameter. In addition, the gravity anomaly profiles provide the additional information needed to reduce the error caused by our fixed-tilt assumption.

Results

The bathymetry and gravity data were fit to formula (8) with λ values of 0, ∞, and 0.4, which correspond to fitting topography (topo), gravity (grav), and combined topography-gravity (topograv) with a respective topography-gravity weight ratio of 2.5 / 1, which reflects our emphasis on original depth soundings over gridded altimeter gravity. The bathymetry data set is characterized by higher precision and superior short-wavelength resolution to the gridded and interpolated gravity even south of 30°S, where unclassified altimetry allows for increased resolution. The topographic modeling is limited to the parameters, w_o, x_o, d_o, and α, the gravity modeling is limited to the parameters w_o, x_o, Δg_o, and α, and the combined modeling contains the parameters w_o, x_o, d_o, Δg_o, α, and ρ_o. Table 1 lists the best fit modeling parameters (w_o, d_o, α, and ρ_o only) and misfit values for topograv with misfits and 10% alpha ranges (for alpha range discussion, see below; complete data for the three fitting schemes are available on microfiche[1]). The simplex minimization algorithm generally required several hundred iterations for reasonable starting values. Restarts with varied, though similar, initial values yielded consistent results with a nominal precision, set by the tolerance limits, of the parameter value. One hundred and nine of the original profiles were successfully fit to some extent by at least one of the procedures. Figure 5 shows the model fitting to the topography and gravity of all of the profiles used in the study.

Though the models provide fits to all of the profiles, the utilization of the parameterization for flexural analysis requires a mechanism by which bad or suspect data can be eliminated. Visual inspection only provides a qualitative,

[1]Supplementary data are available with entire article on microfiche. Order from American Geophysical Union, 2000 Florida Avenue, N.W., Washington, DC 20009. Document B94-004; $2.50. Payment must accompany order.

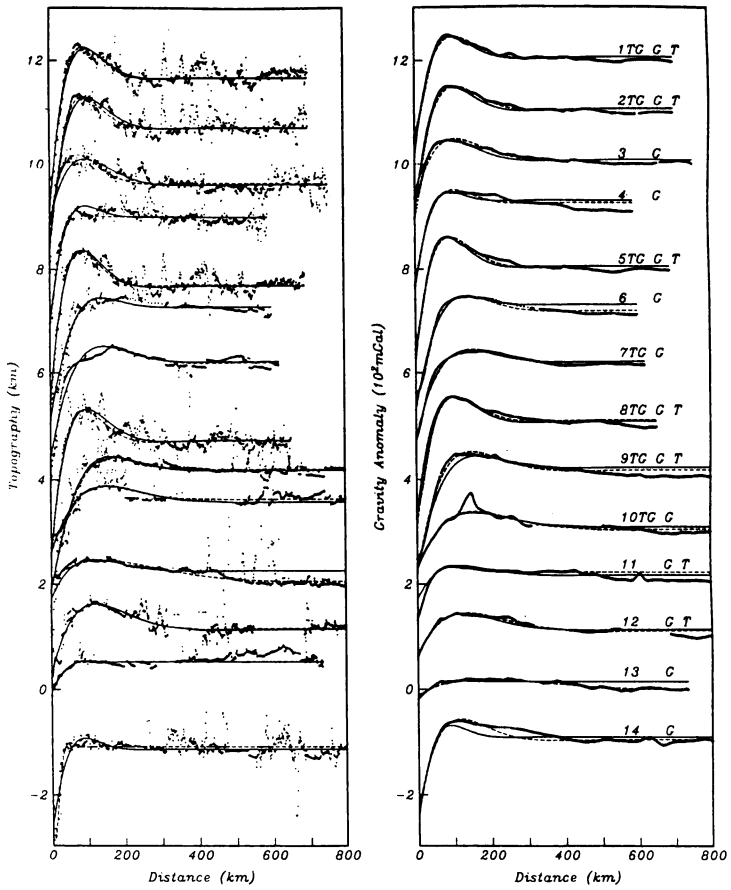

Figure 5. Topography and gravity data for 117 profiles modeled in the study. Profiles are arbitrarily shifted vertically for presentation. For topography (shown at left), solid lines correspond to the best fit model for topograv (λ = 0.4) and dashed lines correspond to the best fit model for topo (λ = 0). For gravity (shown at right), solid lines correspond to the best fit model for topograv (λ = 0.4) and dashed lines correspond to the best fit model for grav ($\lambda = \infty$). Profiles are numbered according to the numbering scheme of Table 1. TG, G, and T mark profiles that were "successfully" modeled by topograv, grav, and topo, respectively.

approximate discrimination regarding adequacy of fit and precision of parameter estimation. In an effort to quantitatively evaluate fit, three semiobjective criteria were established that, in general, coincided with our intuitive expectations:

1. Acceptable profiles must have a misfit of less than 0.5, which means that the addition of the flexure parameters reduces the variance by 50% with respect to the model with just a mean depth (and/or gravity) as a parameter.

2. In an effort to determine the sensitivity of the model to the flexural parameter (α), the fitting procedure was performed for each profile by varying a fixed alpha value until a 10% increase in misfit had resulted, establishing conservative "error bars" for flexural wavelength. The 10% alpha range must not exceed 0.7 of the alpha value.

3. For topograv fits only, profiles were kept when the modeled density contrast ρ_o was within the range 1700-2600 kg m^{-3}. When both gravity and topography were modeled, the density contrast parameter was usually about 2200 kg m^{-3} corresponding to an uncompensated outer rise with a mantle density of 3200 kg m^{-3}. Lower densities indicate that the outer rise consists of partially compensated topography (i.e., profile 102, Figure 5, ρ_o = 902 kg m^{-3}), while higher densities may reflect areas of thick sediment cover that reduces the topographic signal but preserves most of the gravity signal. A primary asset of the topograv approach is the ability, unlike in previous studies, to discriminate between fits to flexural and nonflexural topography.

In this manner, 37 topograv, 47 topo, and 108 grav profiles were considered acceptable for further analysis of flexural behavior (Figure 5). The validity of the flexural modeling technique for the inversion of systematic variations of elastic thickness, flexural rigidity, applied moment, and other bending parameters is greatly limited by the presence of short- and long-wavelength bathymetric noise. By averaging nearby profiles, we have greatly diminished the weight of

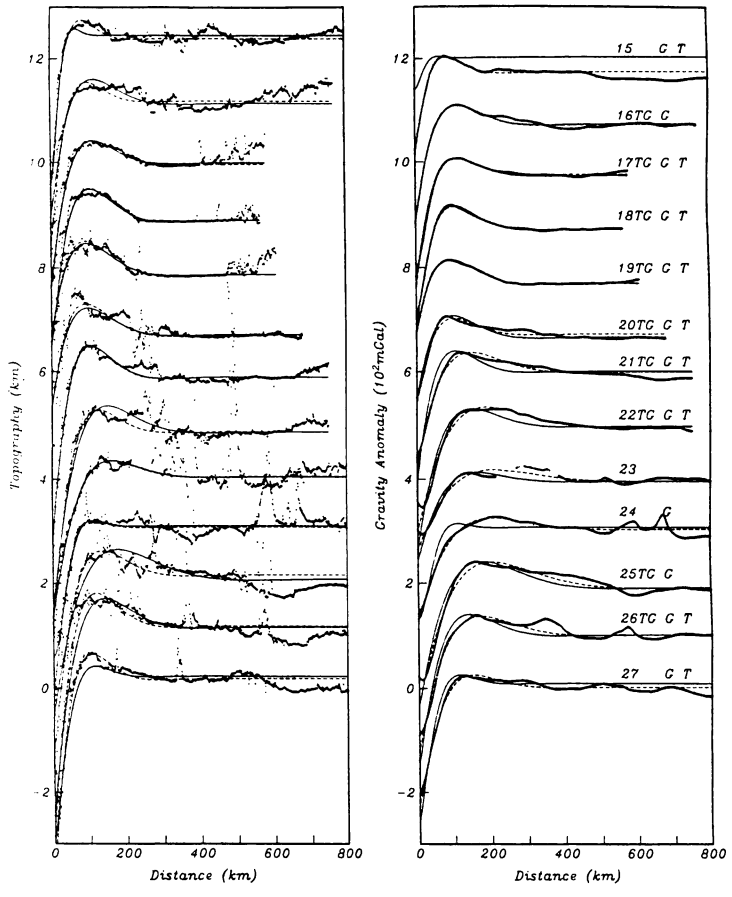

Figure 5. (continued)

uncorrelated, short-wavelength features. Nevertheless, the bathymetry retains a sensitivity to nonflexural long-wavelength, bathymetric features (non-age-related regional tilt and swell, irregular sediment deposition, outer rise shaped nonflexural topography), which limit the accuracy of parameters inferred based on fitting topography alone. Satellite altimeter gravity modeling reflects the effect of deeper structures [*McQueen and Lambeck*, 1989] and is less dependent on surface deformational effects.

Figure 6 shows the flexural parameter values obtained from the topograv modeling procedure against the grid-derived age at the first zero crossing, along with the 10% alpha ranges for each of the topograv data points. To a limited extent, the fact that the three flexural parameter estimates coincide, falling consistently within the topograv 10% range, confirms a correlation between the two data sets and establishes the 10% range as conservative with respect to the true wavelength value. The flexural parameter α displays a positive age correlation (Figure 6), particularly with respect to the gravity parameter set. However, the α obtained by the gravity modeling usually exceeds the α obtained from the topographic modeling. This behavior has been noted by *McAdoo and Martin* [1984] and by *Judge and McNutt* [1991] and has been attributed to attenuation of short-wavelength noise (i.e., seamounts) by the gravity representation.

The topograv modeling approach allows for the rejection of profiles for which the topography and gravity modeling schemes yield divergent parameter values. Eighteen profiles that were adequately fit by the topography and gravity modeling separately were not fit by the combined model. Where topo and grav flexural parameter values were substantially different (see profiles 11, 50, and 111), the fit to the combined data set was moderately poor and the 10% alpha range was large, reflecting a compromised fit over a wide range of flexural parameter values. The wavelength sensitivity criterion effectively removed the vast majority of profiles for which the flexural parameter values differed by more than 15 km (mean α grav /α topo = 0.88, s.d. = 0.19, for quality topograv fits). In our modeling scheme, the estimated α is usually closer to either the topo or grav estimates rather than lying between the two. Moreover, the model generally favors a fit to the topographic wavelength because the topography data are more heavily weighted (mean α topograv / α topo = 1.07, s.d. = 0.13, for quality topograv fits). Even where separate topographic and gravity modeling yielded similar flexural parameter values, profiles were rejected where the

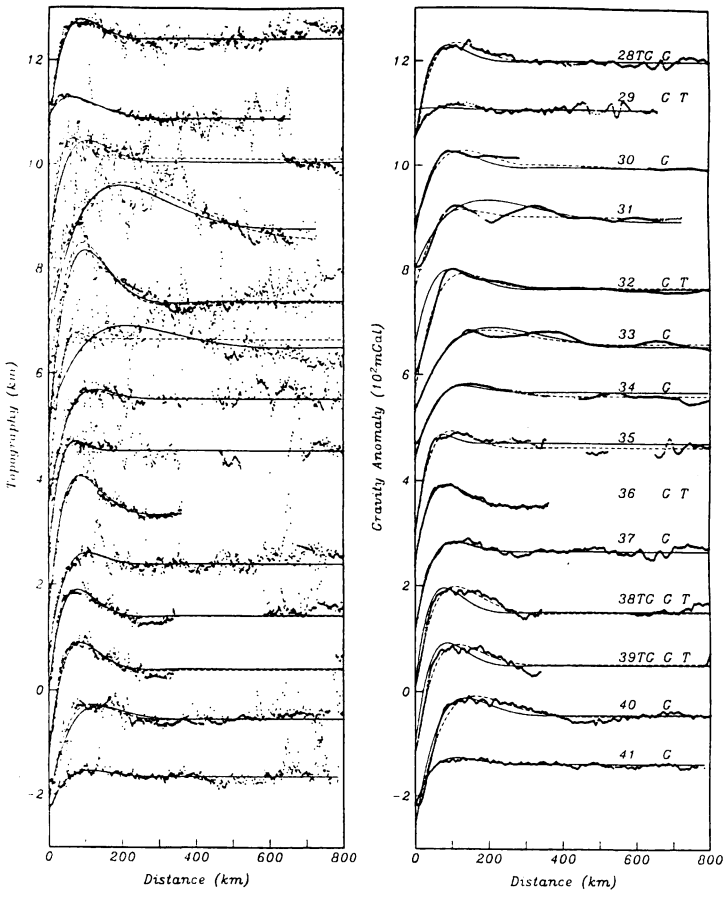

Figure 5. (continued)

mantle-water density contrast parameter was outside the acceptable range (usually below 1700 kg m^{-3}; for example, profiles 36 and 58). In these cases, the flexural amplitude parameter (and the bending moment value, below) is highly suspect because the model may be fitting nonflexural topography.

Profiles which could not be adequately fit by modeling topography alone were successfully fit in the combined modeling scheme. Where the topo misfit value was marginally unacceptable, a well-fit gravity model with a similar α value to the topo model and a reasonable ρ_o value, could diminish the total misfit in the combined topograv model (see profiles 99 and 104). Where a small outer rise and/or a substantial bathymetric noise component allowed for an inadmissible wide-ranging flexural parameter value, a well-fit gravity model with similar α value to the topo model and a reasonable ρ_o value could reduce the 10% α range to within acceptable limits in the combined topograv model (see profiles 10 and 96). A primary asset of a joint topography-gravity minimization scheme with misfit, wavelength sensitivity, and density contrast quality criteria is that it limits acceptable model fits to those for which the flexural parameter and amplitude are consistent for both the topography and gravity data sets. The parameter sets obtained by simultaneous modeling are therefore more suitable for depth, moment and mechanical thickness analysis than those obtained by modeling topography and gravity alone.

Discussion

Depth Versus Age

The value of d_o, the depth at the first zero crossing, should be approximately zero, assuming a perfect age correction. The mean value of d_o is approximately +112 m with a standard deviation of about 268 m for the topo and topograv modeling schemes. Furthermore, there is no apparent age relation for the depth parameter (correlation coefficient of 0.17). Thus the *Parsons and Sclater* [1977] age correction has adequately and unbiasedly corrected the depth at least with respect to the DC offset. The low degree of slope evident in the vast majority of profiles further affirms that age related tilt has, for the most part, been adequately corrected. These depth versus age results are shown in Figure 7 (after adding the previously subtracted PSM depth) where we have plotted the modeled ocean depth at each trench-outer rise versus the age of the seafloor at the first

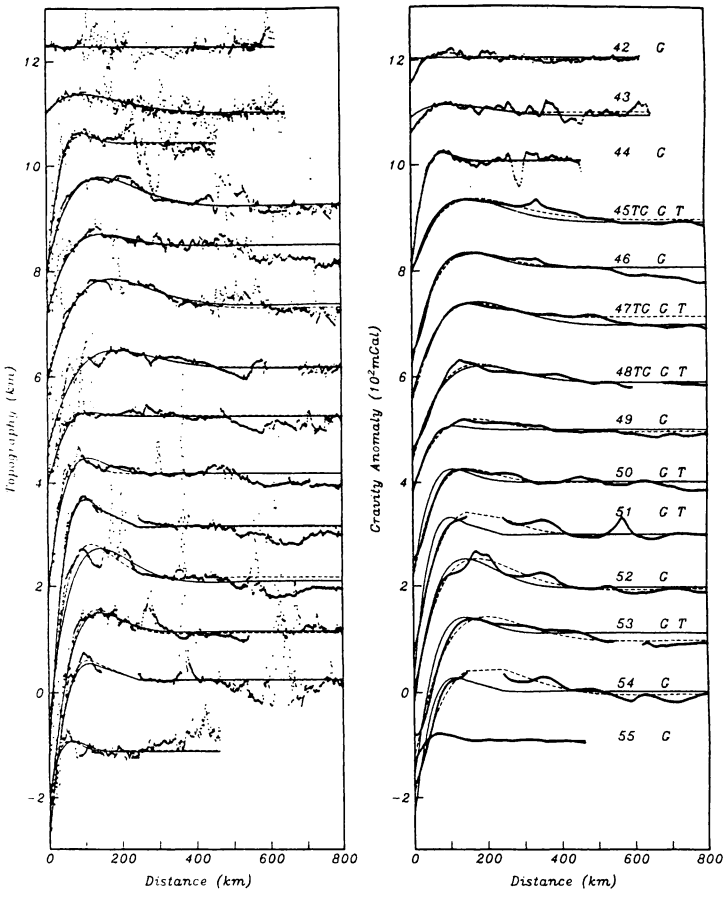

Figure 5. (continued)

zero crossing seaward of the trench axis. Also shown are depth versus age relations predicted by the *Parsons and Sclater* [1977] plate cooling model (PSM, solid curve), the half-space cooling model (HS, dashed curve) and the GDH1 model (dotted curve) of *Stein and Stein* [1992] (i.e., a plate-cooling model having a hot and thin lithosphere). For ages less than 70 Ma the data are equally scattered about all of the models. In many cases the estimated depth is less than all model depths; this bias is to be expected since we have not accounted for sediment loading. Between 80 and 100 Ma the PSM model fits best, while between 110 and 130 Ma the GDH1 model fits best. One advantage of our analysis over previous depth versus age studies is that since we model the trench/outer rise signature, we are able to estimate seafloor depth on very old seafloor near the trench axis. Several of our estimates are for 130 Ma seafloor where we find that the PSM model fits better than the GDH1 model; a sediment correction would increase the depth estimates and improve the fit to the PSM curve. Next, we show that the lithosphere of the GDH1 model is too hot and thin to maintain the bending moment needed to support the observed outer rise topography at older subduction zones (> 100 Ma).

Bending Moment Versus Age

The flexural amplitude (w_o) values for the three modeling schemes range from several hundred to several thousand meters. For comparisons with previous studies [*Caldwell et al.*, 1976; *Caldwell and Turcotte*, 1979; *Jones et al.*, 1978; *Turcotte et al.*, 1978], the theoretical elastic plate relation between the amplitude parameter w_o and the nominal height of the outer bulge w_b is

$$w_o = \sqrt{2}\,\exp\left(\frac{\pi}{4}\right) w_b \cong 3.10\, w_b \quad . \tag{10}$$

Usually, the model amplitude values w_o and the values obtained by visual inspection of the profiles w_b roughly correspond after scaling. Also, our values generally conform to those obtained by the previous studies at the same trenches. However, it should be noted that visual estimates of w_b are very sensitive to the value of reference depth d_o used. In many previous studies [*Caldwell et al.*, 1976; *Caldwell and Turcotte*, 1979; *Jones et al.*, 1978; *Turcotte et al.*, 1978; *Judge and McNutt*, 1991], d_o was chosen visually prior to flexural

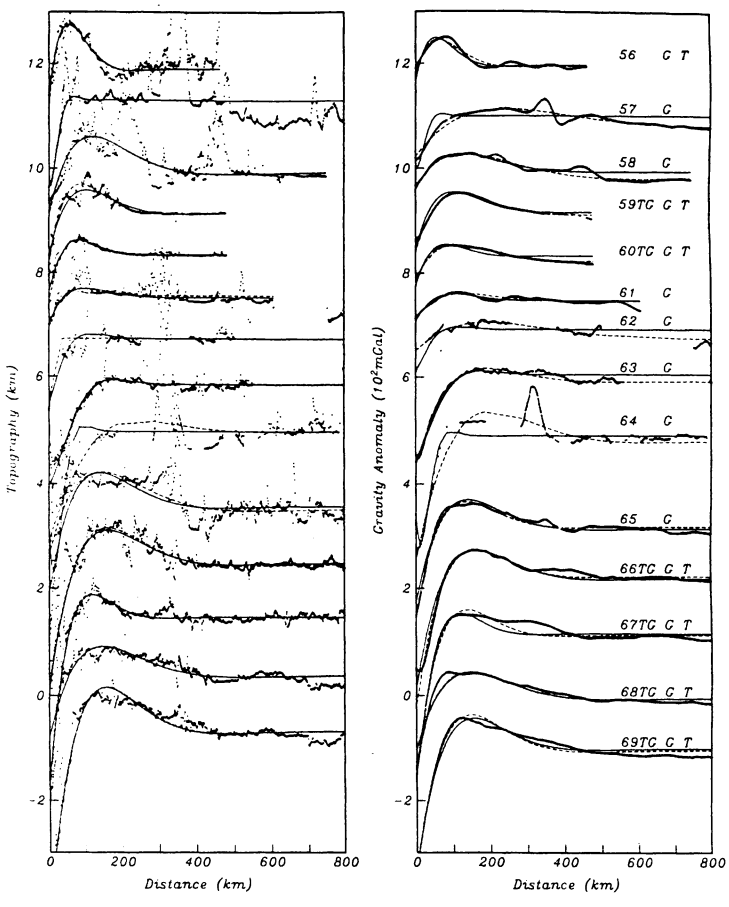

Figure 5. (continued)

modeling. We believe our misfit method is better because w_o and d_o are estimated simultaneously.

As noted by *Goetze and Evans* [1979], the bending moment needed to support the outer rise can be estimated by simply integrating the excess topography times the mantle/water density contrast ρ_o times the moment arm:

$$M(x_o) = \int_{x_o}^{\infty} w(x)\, \rho_o\, (x - x_o)\, dx \quad , \tag{11}$$

where $w(x)$ is the excess topography and x_o is the location of the moment. Although, in theory, a model fit is not needed to estimate this moment, topographic noise causes this integral to be unstable. The thin elastic plate flexure model provides a smooth fit to the observations that can easily be integrated to estimate the moment at x_o:

$$M_o = \frac{\rho_o\, g}{2}\, \alpha^2\, w_o \, , \tag{12}$$

where ρ_o is set to 2200 kg m^{-3}.

A plot of this moment (for topograv) for the 37 trench profiles that pass all three editing criteria versus age is shown in Figure 8. Bending moment values are presented in Table 1 together with their associated curvature (K_o) values (see (2)). For ages less than 60 Ma, in the Middle America, Peru, Chile, and Aleutian Trenches, the bending moments are, in most cases, less than 10^{17} N and at greater ages, bending moments have a wide range up to a maximum of 3×10^{17} N. This maximum bending moment provides an upper limit on the overall strength of the oceanic lithosphere in response to bending [*Turcotte et al.*, 1978; *Goetze and Evans*, 1979]. Our results are in general agreement with previous studies which show a rapid increase in maximum bending moment with increasing age [*McNutt and Menard*, 1982; *McAdoo et al.*, 1985]. However, our study uses a much larger data set and spans a much wider range than previously reported. These bending moment data can be used to constrain models of the thermal and mechanical properties of the oceanic lithosphere.

At high curvatures, the large fiber stresses cause brittle failure and ductile flow in the upper and lower lithosphere, respectively. The lithosphere is said to be moment saturated when the plate continues to bend without an increase in applied moment; it is nearly moment saturated when the curvature of the plate exceeds about 5×10^{-7} m^{-1}. The vast majority of our model profiles exhibit curvatures which exceed

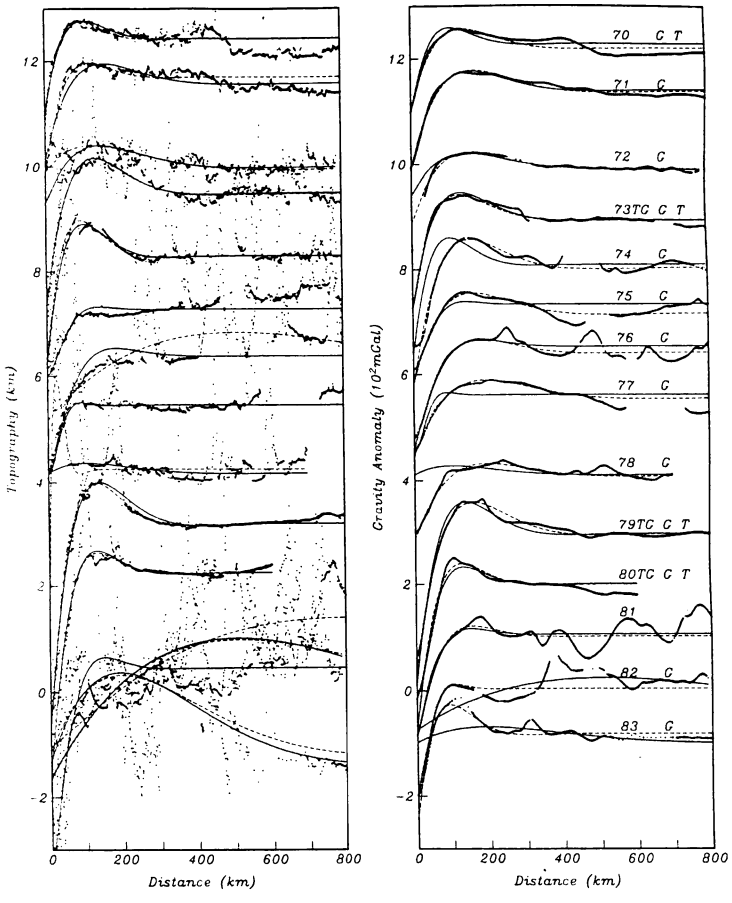

Figure 5. (continued)

10^{-7} m^{-1}, and many are moment saturated (Table 1). Thus these near-maximum moments can be compared with theoretical maximum moments calculated from models of lithospheric strength versus depth. To estimate these saturation moments, we used the yield strength envelope formulation of *Brace and Kohlstedt* [1980] with zero pore pressure and a dry olivine rheology from *Kirby* [1983]. This combination provides a maximum strength lithosphere for a given thermal profile. At a given lithospheric age the temperature versus depth profile was calculated for three models, the *Parsons and Sclater* [1977] cooling plate (PSM) and half-space (HS) model and the GDH1 model of *Stein and Stein* [1992]. We calculated the yield strength versus depth for both tension and compression and then imposed a stress versus depth profile corresponding to a large curvature with zero horizontal, inplane end load. After limiting the imposed stress to be less than the yield stress envelope, the depth of the nodal stress was adjusted iteratively so the end load was zero. The final saturation bending moment is

$$M = \int_0^h \Delta\sigma(z - z_n)\, dz\,, \qquad (13)$$

where $\Delta\sigma$ is the deviatoric stress, z is depth, z_n is the nodal stress depth, and h is the plate thickness. Saturation bending moments versus age for each of the three thermal models are plotted in Figure 8 along with the moments estimated from the profiles. The observed bending moments should not exceed the saturation bending moment. Except for three estimates between 24 and 45 Ma both the HS and the PSM models provide an upper bound on the observations. In contrast, about one half of the observed moments in the 120-150 Ma age range exceed the GDH1 model. We conclude that the lithosphere of the GDH1 model is too hot and thin to maintain the observed outer rises seaward of many subduction zones, especially outer rises on older lithosphere (> 100 Ma).

Mechanical Thickness Versus Age

The flexural parameter α displays a positive age correlation (Figure 6), particularly with respect to the gravity parameter set. Best estimates of α are used to calculate the corresponding effective elastic thickness (Table 1) using (4). Unlike most previous studies [*Caldwell et al.*, 1976; *Caldwell and Turcotte*, 1979; *Carey and Dubois*, 1981; *Jones et al.*, 1978; *McAdoo et al.*, 1978], our individual estimates of h_e have considerable scatter and do not constrain a particular isotherm increasing as

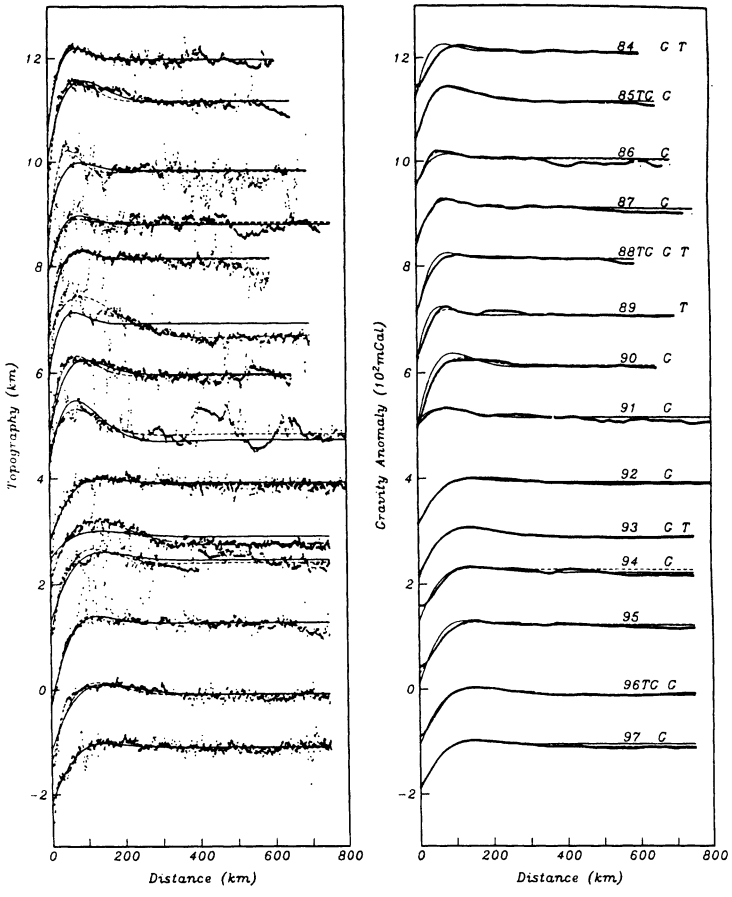

Figure 5. (continued)

the square root of age. The scatter is not likely to be caused by the utilization of a combined modeling scheme since there is substantial scatter within the topo and grav best fit α values. Nevertheless, these values agree, in general, with the compiled list presented in Table 1c of *Wessel* [1992], particularly for the topo modeling scheme ($\lambda = 0$), with noteworthy exceptions of the Aleutian Trench, for which our values are lower, and the Kuril Trench, for which our values are higher. We believe the scatter in our results and the poor agreement with the simple square root of age increase reflects uncertainties inherent in estimating flexure parameters, such as bathymetric noise and non flexural topography [*McQueen and Lambeck*, 1989] as well as inelastic bending and accumulated thermoelastic stress [*Wessel*, 1992].

As discussed in the previous section, the moderate-high curvatures observed for a majority of profiles indicate that a significant proportion of the plate is behaving inelastically. For these trenches, the true mechanical thickness (i.e., the depth to the nominal isotherm where materials are no longer capable of sustaining stress over geologic periods) is greater than the elastic thickness estimate. Following *McNutt and Menard* [1982], mechanical thickness estimates are obtained from the elastic thickness and curvature. According to S. Mueller and R. J. Phillips (unpublished manuscript, 1992), using this conversion method with curvatures obtained at the first zero crossing of the best fitting elastic profile results in an underestimation of the mechanical thickness by 10% for 50 Ma lithosphere and by 8% for lithosphere older than 90 Ma. This error does not exceed 10% even at near-full saturation.

The variation of mechanical thickness estimates (Table 1), for topograv, with age is shown in Figure 9 along with mechanical thickness-age curves (750° isotherm) obtained by the half-space (HS), plate (PSM), and GDH1 models. Mechanical thickness increases rapidly over the age range of 10 to 60 Ma and then flattens over the range 80 to 150 Ma. While mechanical thickness estimates appear to confirm that lithospheric cooling results in thickening of the mechanical lithosphere with age, the wide scatter of the data do not allow for discrimination between the three thermal models, or even the determination of the isotherm which may define the base of the lithosphere.

Limitations of the Modeling

The high scatter exhibited by the flexural parameter, effective elastic thickness and mechanical thickness values

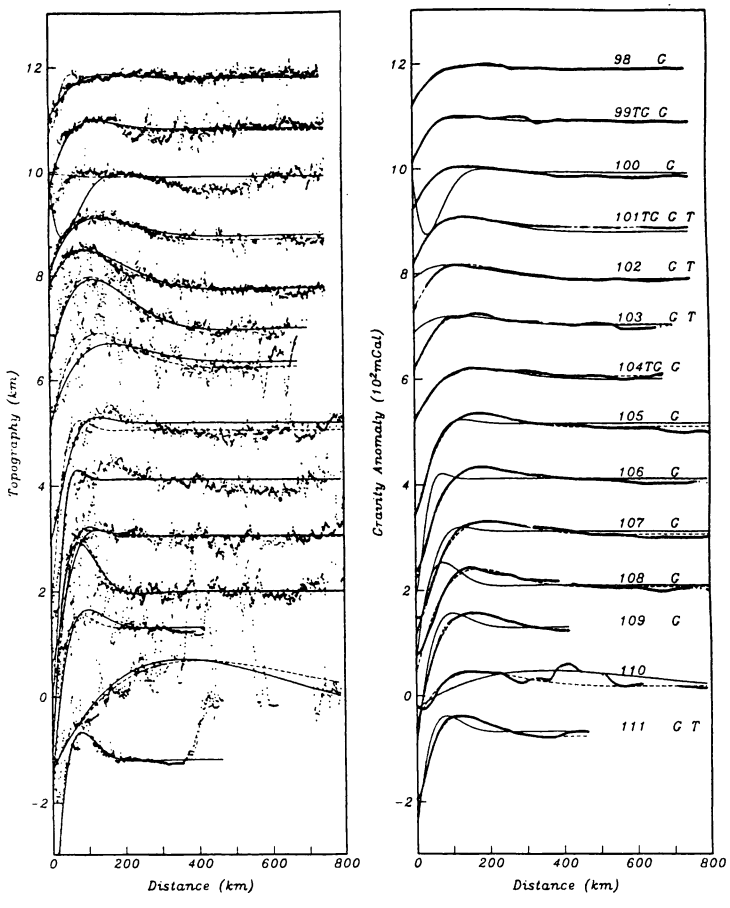

Figure 5. (continued)

highlights the limitations of trench flexural modeling. According to *Wessel* [1992], the underlying problem with h_m versus age data is that the estimated quantities have far more degrees of freedom than lithospheric age alone. At trenches, complications due to inelastic processes, inplane stress, unbending history and thermal stress history cannot be constrained adequately and are affected by unknown factors such as vertically integrated rheology, load size, local and regional stress history and thermal history.

Curvature-induced inelastic processes result in progressive failure in the plate and a variable flexural rigidity throughout a given profile. Though our profiles were adequately fit by a simple elastic model, several profiles exhibited fits with a systematic error. For example, in profile 68, the landward slope from the outer bulge is steeper than the model predicts, whereas the seaward slope is more gradual than the model predicts, implying that rigidity is diminished as the plate migrates across the outer rise. According to *Judge and McNutt* [1991], values of elastic thickness found by assuming constant rigidity along profiles can be considered weighted averages of the true elastic thickness along the length of the profile. Our flexural rigidity and effective elastic thickness data correspond closely to the values near the trench and outer rise due to our fitting-weighting scheme. Nevertheless, curvatures obtained by *Judge and McNutt* [1991] using variable rigidity were approximately 1.6 times the curvatures calculated assuming constant rigidity. Therefore our h_m values may underestimate the true mechanical thickness for high curvature profiles where inelastic processes result in variable rigidity.

Regional in-plane stress, both compressive [*Bodine and Watts*, 1979] at the Bonin Trench and Southern Marianas Trench and tensile [*Judge and McNutt*, 1991] at the Peru Trench and Chile Trench, has been invoked to explain flexure and seismicity observations. S. Mueller and R. J. Phillips (unpublished manuscript, 1992) fit elastic models to synthetic profiles with various inplane stress histories and were unable to recover the appropriate value of inplane stress. Moreover, the imposition of compressive stress before and after bending did not change the effective elastic thickness determined, though 5 km uncertainty was introduced. Conversely, regional tension tended to make lithosphere appear substantially weaker and thinner. Unfortunately, regional stress fields in the vicinity of trench flexure are still poorly constrained by intraplate focal mechanisms [*Wiens and Stein*, 1984; *Bergman and Solomon*, 1984; *Bergman*, 1986].

Wessel [1992], in an effort to explain the bimodal nature of h_m versus age data at seamounts and trenches, evaluated the combined effects of flexural bending stresses and thermal

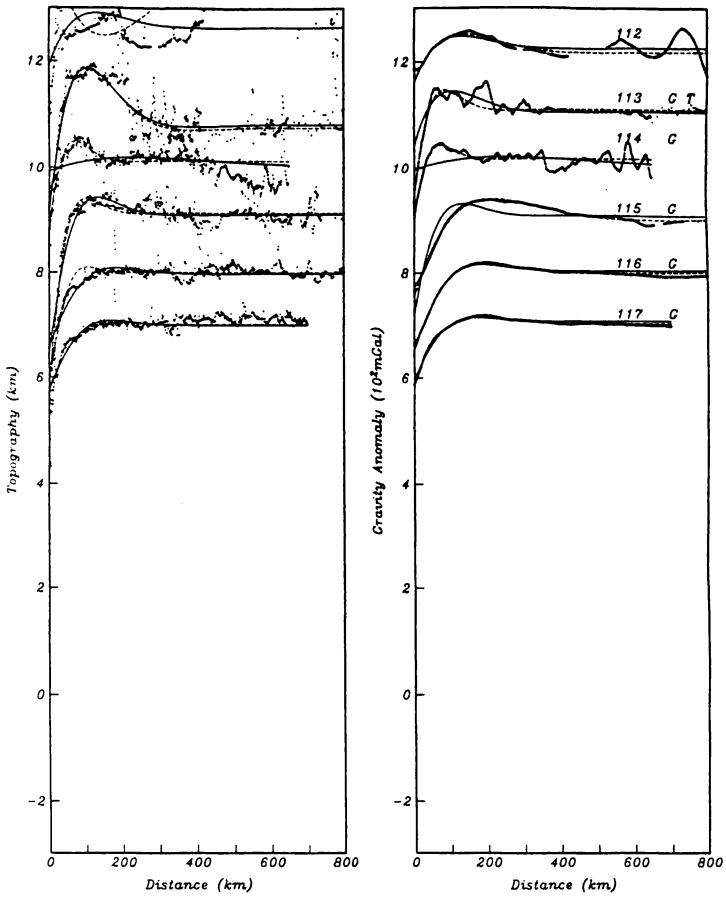

Figure 5. (continued)

bending stresses due to depth-dependent, temporally integrated cooling of the lithosphere. Constructive interference beneath seamounts drives the plate to premature failure, therefore giving the impression of a relatively weaker plate. Conversely, thermal stresses at trenches are largely relieved by the opposite flexural bending stresses and the plate appears to be stronger [*Wessel*, 1992]. The result of this stress superposition for 30 Ma lithosphere is a 5-20% overestimation of h_e at trenches and a 10-40% underestimation of h_e at seamounts for curvatures less than 4×10^{-7}. *Wessel* [1992, Figure 12b] provides bias estimates for trenches and seamounts over a range of ages and curvatures. Approximately 10 profiles in the present study suggest an overestimation bias which exceeds 10% (Figure 9). Notably, profiles 10 (Aleutians), 96, and 101 (Peru), which lie significantly above the general h_m trend at 30-50 m.y., are lowered by about 30%, back to the expected value. The corrected mechanical thicknesses demonstrate an approximate age$^{1/2}$ correlation, though substantial scatter still prohibit resolution of the best fitting lithospheric basal isotherm model.

Conclusions

A global survey of trench profiles, from depth soundings and satellite gravity grid data, demonstrates that the majority of subducting plate profiles contain an outer rise, in response to a bending moment applied by the subducted plate. These profiles can be quantitatively fit, after high-resolution age correction, using a simple elastic model with no required tilt. A modeling scheme which simultaneously fits gravity and topography is utilized to exclude models which poorly constrain the flexural parameter and flexural amplitude due to nonflexural deformation in topographic modeling and deep structure in gravity. In accordance with previous investigations, elastic thickness values exhibit a discrepancy between topographic and gravitational modeling values; gravitational elastic thicknesses exceed those obtained by topographic modeling. Parameter values obtained from a combined data set fitting scheme, are selected for goodness of fit, sensitivity of fit to the flexural parameter and approximate noncompensation. A primary attribute of the combined topography-gravity modeling scheme is that the best fitting models are restricted to those for which the flexural parameter and amplitude are consistent for both the topography and gravity data sets.

The value of the depth parameter at the first zero crossing was obtained from the modeling procedure, yielding depth determinations at the oldest possible location prior to subduction. Though we have not accounted for sediment loading, we find that between 80 and 100 Ma and 135-145 Ma

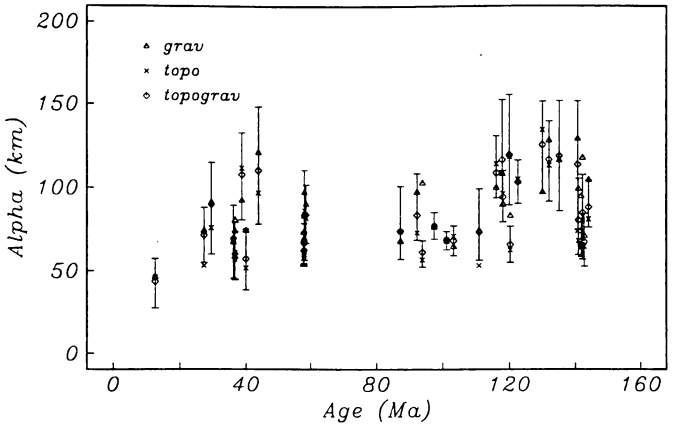

Figure 6. Flexural parameter (α) estimates for the topograv (λ = 0.4), grav ($\lambda = \infty$), and topo (λ = 0) values which correspond to the 37 "successfully fit" topograv models with respect to model ages at the first zero crossing from a two-dimensional interpolation of an age grid [*Roest et al.*, 1992]. Error bars correspond to the 10% misfit ranges for the topograv modeling scheme.

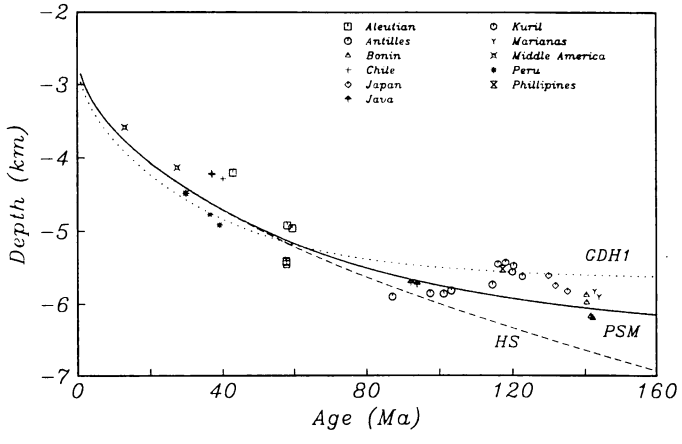

Figure 7. Best fit model depths at the first zero crossing with respect to model ages at the first zero crossing from a two-dimensional interpolation of an age grid [*Roest et al.*, 1992], with predicted depths according to the HS (dashed), PSM (solid), and GDH1 (dotted) thermal models. See key on figure for trench symbols.

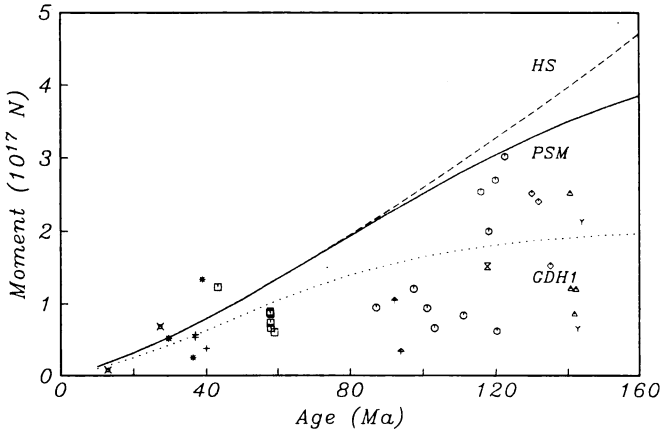

Figure 8. Bending moment values determined using the thin elastic plate model (equation (12)) with respect to model ages at the first zero crossing from a two-dimensional interpolation of an age grid [*Roest et al.*, 1992], with saturation moments predicted according to the HS (dashed), PSM (solid), and GDH1 (dotted) thermal models. Trench symbol assignment is identical to Figure 7.

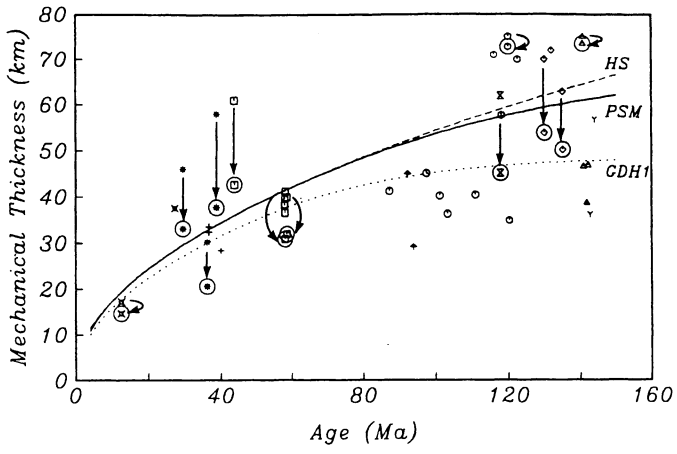

Figure 9. Mechanical thicknesses determined using the h_e to h_m conversion method proposed by *McNutt and Menard* [1982] with respect to model ages at the first zero crossing from a two-dimensional interpolation of an age grid [*Roest et al.*, 1992], with predicted model thicknesses according to the HS (dashed), PSM (solid), and GDH1 (dotted) thermal models with base depth corresponding to the 750° isotherm. Trench symbol assignment is identical to Figure 7. Circled points correspond to values corrected for thermal stress bias [*Wessel*, 1992].

the PSM model fits best, while between 110 and 130 Ma the GDH1 model fits best. A sediment correction would further establish the superior fit of the PSM over the GDH1 model to the depth parameter.

The moderate and high curvatures present at a majority of profiles imply that a substantial component of stress relief is occurring by inelastic processes so that the effective elastic thickness values substantially underestimate the true mechanical thickness. Bending moments calculated at the first zero crossing were compared with the saturation moment predicted by the half-space and plate cooling models of *Parsons and Sclater* [1977] and the GDH1 model of *Stein and Stein* [1992]. Since approximately one half of the observed moments at trenches older than 120 Ma exceeded the saturation moment, we conclude that the GDH1 lithosphere is too hot and thin to maintain the observed outer rises seaward of many subduction zones. Mechanical thickness estimates were obtained from the elastic thickness and curvature values but scatter in the data, due to bathymetric noise and poor constraint of complicating factors (inplane stress, unbending history, and remnant thermal stress), precludes discrimination between the half-space, plate, and GDH1 cooling models.

Acknowledgments. We thank the associate editor and the referees, David McAdoo and Herbert McQueen, for their careful and constructive reviews of the original manuscript. Walter Smith and Pal Wessel provided useful advice regarding the use of GMT and the significance of yield strength envelopes and thermal stresses, respectively. We thank Catherine Johnson and Andrew Goodwillie for important insights and suggestions regarding conceptual and technical matters. Daniel Levitt was supported by an NSF Graduate Fellowship. Additional support was provided by the NASA Venus Data Analysis Program NAGW-3503 and the NSF MG&G Program OCE-9217164.

References

Bergman, E. A., Intraplate earthquakes and the state of stress in oceanic lithosphere, *Tectonophysics, 132*, 1-35, 1986.

Bergman, E. A., and S. C. Solomon, Source mechanisms of earthquakes near mid-ocean ridges from body waveform inversion: Implications for the early evolution of oceanic lithosphere, *J. Geophys. Res., 89*, 11,415-11,441, 1984.

Bodine, J. H., and A. B. Watts, On lithospheric flexure seaward of the Bonin and Mariana trenches, *Earth Planet. Sci. Lett., 43*, 132-148, 1979.

Brace, W. F., and D. L. Kohlstedt, Limits on lithospheric stress imposed by laboratory experiments, *J. Geophys. Res., 85*, 6248-6252, 1980.

Caldwell, J. G., and D. L. Turcotte, Dependence of the thickness of the elastic oceanic lithosphere on age, *J. Geophys. Res., 84*, 7572-7576, 1979.

Caldwell, J. G., W. F. Haxby, D. E. Karig, and D. L. Turcotte, On the applicability of a universal elastic trench profile, *Earth Planet. Sci. Lett., 31*, 239-246, 1976.

Carey, E., and J. Dubois, Behavior of the oceanic lithosphere at subduction zones: Plastic yield strength from a finite-element method, *Tectonophysics, 74*, 99-110, 1981.

Carter, D. J. T., *Echo Sounding Correction Tables: Formerly Matthews' Tables*, 150 pp., Hydrographic Department, Ministry of Defense, Taunton, Somerset, England, 1980.

Cochran, J. R., Variations in subsidence rates along intermediate and fast spreading mid-ocean ridges, *Geophys. J. R. Astron. Soc., 87*, 421-459, 1986.

DeBremaecker, J. C., Is the oceanic lithosphere elastic or viscous?, *J. Geophys. Res., 82*, 2001-2004, 1977.

Goetze, C., and B. Evans, Stress and temperature in the bending lithosphere as constrained by experimental rock mechanics, *Geophys. J. R. Astron. Soc., 59*, 463-478, 1979.

Gunn, R., A quantitative evaluation of the influence of the lithosphere on the anomalies of gravity, *J. Franklin Inst., 236*, 373-396, 1943.

Hayes, D. E., Age-depth relationships and depth anomalies in the Southeast Indian Ocean and South Atlantic Ocean, *J. Geophys. Res., 93*, 2937-2954, 1988.

Jones, G. M., T. W. C. Hilde, G. F. Sharman, and D. C. Agnew, Fault patterns in outer trench walls and their tectonic significance, *J. Phys. Earth, 26*, S85-S101, 1978.

Judge, A.V., and M. K. McNutt, The relationship between plate curvature and elastic plate thickness: A study of the Peru-Chile trench, *J. Geophys. Res., 96*, 16,625-16640, 1991.

Kirby, S. H., Rheology of the lithosphere, *Rev. Geophys., 21*, 1458-1487, 1983.

Marty, J. C., and A. Cazenave, Regional variations in subsidence rate of oceanic plates: A global analysis, *Earth Planet. Sci. Lett., 94*, 301-315, 1989.

Mathworks, Matlab: High-performance numeric computation and visualization software, report, Natick, Mass., 1993.

McAdoo, D. C., and C. F. Martin, Seasat observations of lithospheric flexure seaward of trenches, *J. Geophys. Res., 89*, 3201-3210, 1984.

McAdoo, D. C., J. G. Caldwell, and D. L. Turcotte, On the elastic-perfectly plastic bending of the lithosphere under generalized loading with application to the Kuril Trench, *Geophys J. R. Astron. Soc., 54*, 11-26, 1978.

McAdoo, D. C., C. F. Martin, and S. Poulose, Seasat observations of flexure: Evidence for a strong lithosphere, *Tectonophysics, 116*, 209-222, 1985.

McKenzie, D. P., Some remarks on heat flow and gravity anomalies, *J. Geophys. Res., 72*, 6261-6273, 1967.

McNutt, M. K., Lithospheric flexure and thermal anomalies, *J. Geophys. Res., 89*, 11,180-11,194, 1984.

McNutt, M. K., and H. W. Menard, Constraints on yield strength in the oceanic lithosphere derived from observations of flexure, *Geophys. J. R. Astron. Soc., 71*, 363-394, 1982.

McQueen, H. W. S., and K. Lambeck, The accuracy of some lithospheric bending parameters, *Geophys. J., 96*, 401-413, 1989.

Molnar, P., and T. Atwater, Interarc spreading and cordilleran tectonics as alternates related to the age of subducted oceanic lithosphere, *Earth Planet. Sci. Lett., 41*, 330-340, 1978.

Nelder, J. A., and R. Mead, A simplex method for function minimization, *Comput. J., 7*, 308-313, 1965.

Neumann, G. A., D. W. Forsyth, and D. T. Sandwell, Comparison of marine gravity from shipboard and high-density satellite altimetry along the Mid-Atlantic Ridge, 30.5-35.5°S, *Geophys. Res. Lett., 20*, 1639-1642, 1993.

Parsons, B., and P. Molnar, The origin of outer topographic rises associated with trenches, *Geophys. J. R. Astron. Soc., 45*, 707-712, 1976.

Parsons, B., and J. G. Sclater, An analysis of the variation of oceanic floor bathymetry and heat flow with age, *J. Geophys. Res., 82*, 803-827, 1977.

Roest, W. R., R. D. Mueller, J.-Y. Royer, and L. M. Gahagan, A high resolution digital age map of the world's oceans, *Eos Trans. AGU, 73* (43), Fall Meeting suppl., 586, 1992.

Sandwell, D. T., Along-track deflection of the vertical from Seasat: GEBCO overlays, *NOAA Tech. Memo., NOS NGS-40*, 8 pp., 1984.

Sandwell, D. T., Antarctic marine gravity field from high-density satellite altimetry, *Geophys. J. Int., 109*, 437-448, 1992.

Sandwell, D. T., and M. B. Ruiz, Along-track gravity anomalies from Geosat and Seasat altimetry: GEBCO Overlays, *Mar. Geophys. Res., 14*, 165-227, 1992.

Sandwell, D. T., and W. H. F. Smith, global marine gravity from ERS-1, Geosat, and Seasat reveals new tectonic fabric, *Eos Trans. AGU, 73* (43), Fall Meeting suppl., 133, 1992.

Smith, W. H. F., On the accuracy of digital bathymetric data, *J. Geophys. Res., 98*, 9591-9603, 1993.

Stein, C. A., and S. Stein, A model for the global variation in oceanic depth and heat flow with lithospheric age, *Nature, 359*, 123-129, 1992.

Turcotte, D. L., Flexure, *Adv. Geophys., 21*, 51-86, 1979.

Turcotte, D. L., and E. R. Oxburgh, Finite amplitude convection cells and continental drift, *J. Fluid Mech., 28*, 29-42, 1967.

Turcotte, D. L., and G. Schubert, *Geodynamics: Applications of Continuum Physics to Geological Problems*, John Wiley, New York, 1982.

Turcotte, D. L., D. C. McAdoo, and J. G. Caldwell, An elastic-perfectly plastic analysis of the bending of the lithosphere at a trench, *Tectonophysics, 47*, 193-205, 1978.

Watts, A. B., An analysis of isostasy in the world's oceans, 1, Hawaiian-Emperor seamount chain, *J. Geophys. Res., 83*, 5989-6004, 1978.

Wessel, P., Thermal stress and the bimodal distribution of elastic thickness estimates of the oceanic lithosphere, *J. Geophys. Res., 97*, 14,177-14,193, 1992.

Wessel, P., and W. H. F. Smith, Free software helps map and display data, *Eos Trans. AGU, 72*, 441-446, 1991.

Wiens, D. A., and S. Stein, Intraplate seismicity and stresses in young oceanic lithosphere, *J. Geophys. Res., 89*, 11,442-11,464, 1984.

D. A. Levitt and D. T. Sandwell, Scripps Institution of Oceanography, 9500 Gilman Drive, La Jolla, CA 92093-0225.

(Received September 28, 1993; revised September 1, 1994; accepted September 13, 1994.)

This chapter, in full, is a reprint of the material as it appears in Journal of Geophysical Research, V. 100, 1995. The dissertation author is the primary investigator and author of this paper.

CHAPTER 3

MODAL DEPTH ANOMALIES FROM MULTIBEAM BATHYMETRY:

IS THERE A SOUTH PACIFIC SUPERSWELL?

ELSEVIER

Earth and Planetary Science Letters 139 (1996) 1–16

EPSL

Modal depth anomalies from multibeam bathymetry: Is there a South Pacific superswell?

Daniel A. Levitt, David T. Sandwell *

Scripps Institution of Oceanography, University of California at San Diego, Geological Research Division MC0215, 9500 Gilman Drive, La Jolla, CA 92093-0902, USA

Received 12 April 1995; accepted 8 December 1995

Abstract

A region west of the southern East Pacific Rise (SEPR), between the Marquesas and Austral Fracture Zones has previously been found to exhibit anomalous depth–age behavior, based on gridded bathymetry and single-beam soundings. Since gridded bathymetry has been shown to be unsuitable for some geophysical analysis and since the area is characterized by unusually robust volcanism, the magnitude and regional extent of depth anomalies over the young eastern flank of the so called 'South Pacific Superswell' are re-examined using a mode-seeking estimation procedure on data obtained from several recent multibeam surveys. The modal technique estimates a representative seafloor depth, based on the assumption that bathymetry from non-edifice and edifice-populated seafloor has a low and a high standard deviation, respectively. Flat seafloor depth values are concentrated in a few bins which correspond to the mode. This method estimates a representative seafloor value even on seafloor for which more than 90% of coverage is dominated by ridge and seamount clusters, where the mean and median estimates may be shallow by hundreds of meters. Where volcanism-related bias is moderate, the mode, mean and median estimates are close.

Depth–age results indicate that there is only a small anomaly (< 200 m) over 15–35 Ma Pacific Plate seafloor with little age-dependent shallowing, suggesting that the lithosphere east of the main hot-spot locations on the 'superswell' is normal. An important implication is that, in sparsely surveyed areas, depths from ETOPO-5 are significantly different from true depths even at large scales (~ 1000 km) and thus are unsuitable for investigations of anomalies associated with depth–age regressions. We find that seafloor slopes on conjugate profiles of the Pacific and Nazca Plates from 15 to 35 Ma are both slightly lower than normal, but are within the global range. Proximate to the SEPR, seafloor slopes are very low (218 m $Myr^{-1/2}$) on the Pacific Plate (0–22 Ma) and slightly high (~ 410 m $Myr^{-1/2}$) on the Nazca Plate (0–8 Ma); slopes for older Pacific seafloor (22–37 Ma) are near normal (399 m $Myr^{-1/2}$). Seafloor slopes are even lower north of the Marquesas Fracture Zone but are highly influenced by the Marquesas Swell. We find that the low subsidence rate on young Pacific seafloor cannot be explained by a local hot-spot or a small-scale convective model exclusively and a stretching/thickening model requires implausible crustal thickness variation (~ 30%).

Keywords: South Pacific; superswells; multichannel methods; bathymetry; hot spots

* E-mail: dsandwell@ucsd.edu

SSDI 0012-821X(95)00247-2

1. Introduction

A fundamental principle of the plate tectonics paradigm is that the depth of ocean floor is controlled by the thermal evolution of a boundary layer, the lithosphere, as it is transported from the mid-oceanic ridge [1]. Two primary types of models have evolved to describe the relation between lithospheric cooling and contraction and the observed monotonic decrease of heat flow and increase of basement depth with crustal age [2]. In the half space model [3,4], the lithosphere is the cold upper boundary layer of a cooling half space, so that depth and heat flow vary with an $age^{1/2}$ and $age^{-1/2}$, respectively. In the plate model [5,6] lithosphere is treated as a cooling plate with an isothermal lower boundary. Due to additional heat input to the base of the lithosphere by hot-spots [7] or by some type of small-scale convection [8] the depth and heat flow curves flatten out with age with a best-fitting asymptotic old-age plate thickness of 125 km and a basal temperature of 1350°C [9].

Over the past 20 years attention has focused on depth anomalies, those areas of the seafloor which have shown departure from the expected depth for a given age [10]. Several investigators have noted a correlation between broad, anomalously shallow regions, termed swells, and the location of prolific, hot-spot-related volcanism [11–16]. For the majority of mid-plate swells, the presence of positive geoid and gravity anomalies suggest that a large part of the swell topography is compensated by thermally rejuvenated lithosphere [15].

In a seminal paper, McNutt and Fischer [17] advanced the superswell hypothesis in order to reconcile a number of unique observations in the south-central Pacific which are inconsistent with a standard hot-spot rejuvenation model [17], including a 250–1000 m shallow depth anomaly covering the majority of French Polynesia, corresponding to a negative geoid anomaly [18]; elastic thicknesses beneath seamounts and islands typical of much younger lithosphere [19]; high spreading rates [20]; and a disproportionately large number of hot-spot volcanic chains.

The superswell is defined by a regional depth anomaly distribution [17]; based on bathymetric data acquired from the 5′ digital SYNBAPS bathymetry [21] averaged to 0.25° and corrected for the variations of sound speed in water, sediment loading and seafloor age, using the standard thermal-plate model [9]. The superswell hypothesis relies heavily on recognizing a depth anomaly which has a magnitude and spatial distribution inconsistent with the simple superposition of anomalies attributed to the individual hot-spots identified in the region [17,18]. Since the anomaly extends well eastward of the hot-spot tracks region, to young lithosphere west of the southern East Pacific Rise (SEPR), McNutt and Fischer [17] proposed that the asymptotic lithospheric thickness in this area is less than normal (75 km) and the asthenosphere is hotter than normal (1385°C). They also noted that the depth anomaly terminates at the Marquesas Fracture Zone (FZ). This abrupt termination indicated that the cause of the anomaly is related to the lithosphere or uppermost mantle, rather than thermal and/or chemical buoyancy from a deep mantle plume. They suggested that the anomaly was related to small-scale convective instabilities in the low-viscosity zone at the base of the lithosphere.

While the superswell model may effectively explain additional anomalous observations, such as low mantle seismic velocities and low elastic-plate thicknesses (note contrary elastic thickness observations [22,23]), the first-order conclusion is that there is a regional depth anomaly which is independent of the effects of overlapping hot-spots, thickened crust and sedimentary aprons. This hypothesis is critically dependent upon the quality of the bathymetric data acquired over the young seafloor just east of the hot-spot tracks (Fig. 1); first, because the observation of anomalously shallow depths in this area is largely responsible for the long-wavelength (presumably age-dependent) anomaly; and, second, because the anomaly attributed to the difference between a 125 km thick plate with a 1350°C basal isotherm and a 75 km thick plate with a 1385°C basal isotherm [17] would be very small in this region (less than 300 m for 40 Ma lithosphere). We show here that ETOPO-5 (which is equivalent to SYNBAPS in ocean areas) is inappropriate for estimating depth anomaly patterns at intermediate wavelengths (hundreds of kilometers) in this poorly surveyed region.

The depth–age relationship on the flanks of the SEPR adjacent to the superswell has been investigated using single beam acoustic data [24]. Depth

soundings from a suite of near-parallel tracks were stacked (arithmetic mean) after matching isochrons and removing sections of bathymetry that were obviously perturbed by seamounts and ridges. For young seafloor (0–5 Ma) between 9°S and 22°S, Cochran [24] finds a pronounced asymmetry in seafloor slope; the western flank has a seafloor slope of 200–225 m $Myr^{-1/2}$ and the eastern flank, 350–400 m $Myr^{-1/2}$ (since there are alternative processes to thermal subsidence which affect the final observed seafloor slope, 'subsidence rate' is strictly defined as the process of seafloor deepening with age, while 'seafloor slope' refers to the observed change in depth with age for adjacent seafloor sections). By an age of 5 Ma the west flank is 300 m shallower than the east flank. The youngest seafloor west of the SEPR is already characterized by unusual depth–age behavior even near the SEPR axis. Since the rise axis in that area is anomalously deep to start with (2625–2872 m), there is no anomalously shallow seafloor on the western flank. The main anomaly is the very high seafloor slope and deep seafloor on the eastern flank [24].

Proper assessment of the westward extension of the region of low seafloor slope is limited by the paucity of data and by an abundance of large seamounts. Seamounts on normal seafloor generally account for about 0.5% of the normal crustal volume [25] (i.e., 30 m of extra crustal thickness). However, on the west flank of the SEPR (6°S–23°S) and in the Tiki Basin (15°S–21°S) seamount population density is much greater than normal [26,27], especially near the SEPR between 15°S and 19°S on 0–6 Ma crust, where the volume of volcanoes and flows is up to 120 m of extra average crustal thickness [28]. On a pair of recent cruises (GLOR3B–04MV) we found that the unusually high seamount abundance also extends much further to the west-northwest, along the Pukapuka chain [29]. Major ridges along this chain consist of individual segments that are 40 km long, < 10 km wide and range in peak amplitude from 800 m to over 4000 m. Four of the seven tracks used by Cochran [24] west of 128°W, in the area where a 500 m shallowing is inferred, cross these major ridges, resulting in substantial shallowing bias.

In addition to the problems with the single-beam coverage in this area, gridded bathymetry, which is based largely on these few tracks, will also have the bias caused by the volcanic ridges as well as the many other problems associated with the ETOPO-5 dataset [30]. The purpose of this paper is to apply a mode estimation technique (histogram) to multibeam data (Fig. 1) in order to establish the correct seafloor depth between the SEPR and the Tuamotus plateau. These results are compared with similarly obtained, depth–age profiles on the conjugate section of the Nazca Plate and on the Pacific Plate north of the Marquesas FZ and are also compared with the global variation in seafloor slope [31]. Deviations from expected subsidence behavior are used to place reliable constraints upon the amplitude and regional extent of the superswell depth.

2. Data

2.1. Bathymetry

Multibeam data were culled from 8 survey legs (GLOR3BMV, GLOR04MV, WEST01MV, WEST04MV, ARIA02WT, RC2608, TUNE02WT and PPTU03WT). The first 7 comprise the majority of the swath coverage between the Marquesas and Austral FZ's (Fig. 1). GLOR3BMV and GLOR04MV bathymetry are from our recent survey of the Pukapuka Ridge System. Legs designated WT and RC use an older generation of SeaBeam, having 16 beams spanning a swath 2/3 times the ocean depth and legs designated MV use a newer SeaBeam2000 system, with 121 beams mapping a much wider swath of 3.4 times the ocean depth at ~ 100 m resolution for normal ocean depths. Travel times for pings are converted to bathymetry using a local sound velocity profile measured with expendable bathothermographs (XBT). Bathymetric data are cleaned and merged with continuous-time Global Positioning System satellite navigation and processed using MB-system software [32]. Since interference by pinger bursts during periods of dredging operation result in erroneous bathymetry, all records for which ship speed is less than 3 km/h were edited from the day files.

The speed-filtered ping record files were grouped into six independent datasets (Fig. 2) and gridded at 200 m cell size in order to even out the data density while preserving the characteristic high resolution of multibeam data; gaps were not filled with interpo-

lated values. The first E–W dataset consists mainly of GLOR3BMV–GLOR04MV cruise multibeam data; it is supplemented by RC2608 and TUNE02WT in the immediate vicinity of the cruise track (within approximately 70 km). The second E–W dataset consists of only the WEST01MV transit data and, thus, it does not follow any particular topographic features. The third and fifth E–W datasets consist of WEST04MV data, which samples both the west (third) and east (fifth; not shown) flanks of the SEPR, along a line of latitude 16°45′S. The fourth E–W dataset consists of the ARIA02WT cruise data; it is used to constrain seafloor depth just north of the Austral FZ. The sixth E–W dataset, PPTU03WT (Fig. 1), is used to constrain seafloor depth north of the Marquesas FZ, the reported boundary of the superswell [17]. All together, the first 4 datasets cover the eastern flank of the superswell and thus provide a regional view of the depth. The depth anomaly in this area, based on ETOPO-5 data, ranges from 250 m at 125°W to 400–600 m at 135°W (contours in fig. 2 from McNutt and Judge [18]). The last two datasets constrain seafloor depth on the nearby non-superswell conjugate Nazca Plate and north of the Marquesas FZ on the Pacific Plate.

2.2. Magnetics

Ages were determined along the multibeam bathymetry datasets using a suite of selected mag-

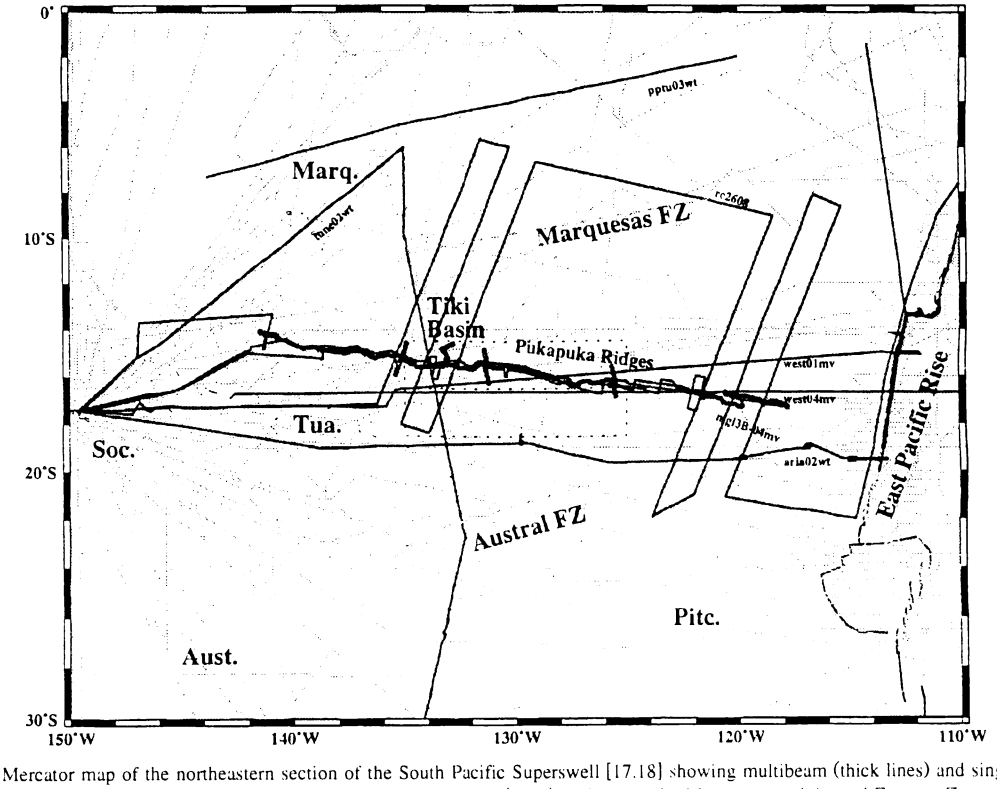

Fig. 1. Mercator map of the northeastern section of the South Pacific Superswell [17,18] showing multibeam (thick lines) and single beam (thin lines) surveys. Also shown are portions of the East Pacific Rise (solid) in the east, the Marquesas and Austral Fracture Zones, the Tiki Basin and the centers of major local hot-spot swells (Austral, Marquesas, Pitcairn, Society and Tuamotus). The dashed rectangles delineate boundaries of data used for a comparison of single-beam bathymetry and ETOPO-5 (see below). Note that, while there appears to be substantial single-beam coverage of seafloor bathymetry south of the Marquesas Fracture Zone on proposed 'Superswell' seafloor, much of the region is characterized by unusually pervasive volcanism, which may bias seafloor depth estimation (see below).

netic anomaly profiles in the region (except for datasets 5 and 6, see below). Magnetic profiles from legs amph1, aria2, c1306, cn011, gecsj, gecsk, ggl34, ggl92, kk717, kk723, v1905 and vlcn8 (not shown) were acquired from the Lamont–Doherty Earth Observatory on-line geophysical database [30] and legs glor3b, glor04 and west04 were acquired from the SIO–GDC. Magnetic anomaly picks (Fig. 2) along the multibeam tracks were mostly made from the individual surveys; in some portions of the survey ambiguous magnetic information was supplemented by interpolation between nearby magnetic profiles.

Anomaly picks were straightforward for datasets 1, 2, 3 and 4 (on the Pacific Plate south of the Marquesas FZ) over the majority of the track lengths. From the ridge crest to anomaly 5A (11.8 Ma in a revised timescale [33]) the isochrons correspond closely to previous anomaly picks [24,33,34]. Complicated seafloor spreading history [24,34,35] in the early–middle Miocene (12–20 Ma) obscures much of the anomaly pattern between anomaly 5A and anomaly 7 (~ 122°W–128°W). However, the magnetic anomaly pattern recorded from the recent glor3b, glor04 and west04 tracks confirms magnetic anomaly picks locally from 5A through 6AA. These picks result in a period of uncharacteristically slow spreading (~ 30 km/Ma) between anomalies 6AA and 7. Nevertheless, only moderate error (a few hundred thousand years, equivalent to a depth error on the order of a few tens of meters) is likely to be introduced by accepting these picks instead of assuming uniform moderate spreading (~ 60 km/Ma) over this interval. From anomaly 7 to 16, the magnetic signature is clear; isochron locations based on the magnetic data are clear and correspond closely to previous studies [29,36]. Therefore, ages are well constrained over the older section of the survey, where the proposed superswell-related depth anomaly is expected to be greatest.

Anomaly picks on the conjugate section of the

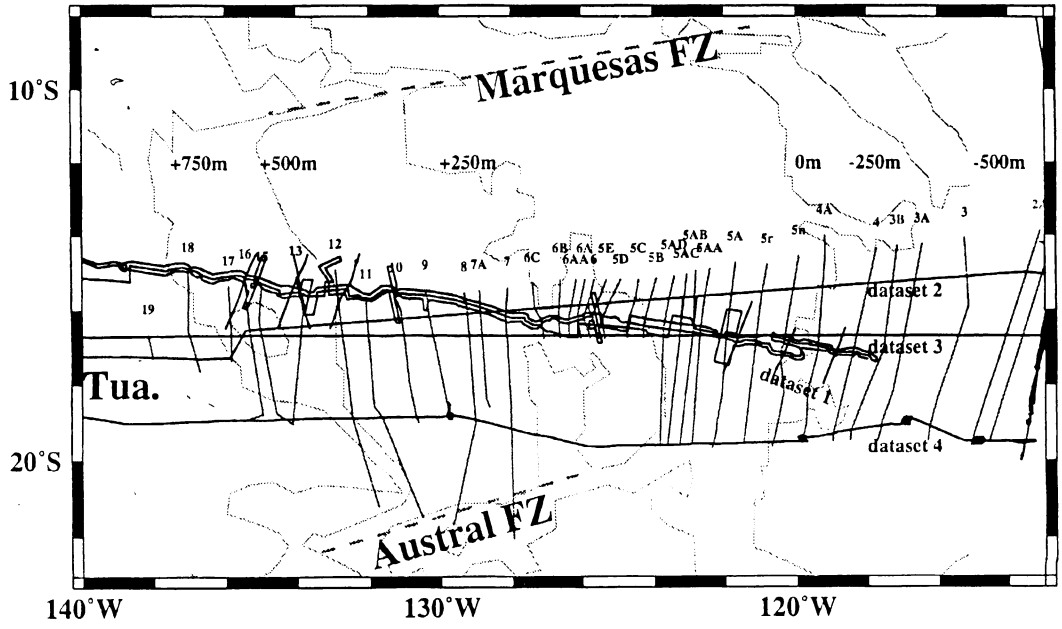

Fig. 2. Mercator map showing 5 E–W multibeam transect datasets on the west flank of the East Pacific Rise: 1 = the GLOR3B-04MV; 2 = WEST01MV; 3 = WEST04MV-west; 4 = ARIA02WT dataset (thick lines). Multibeam data from WEST04MV-east (dataset 5) and PPTU03WT are located east of the SEPR and north of the Marquesas FZ, respectively, and are not shown on the map. Contours correspond to depth anomalies assuming a 125 km thick lithospheric plate digitized directly from fig. 2 of McNutt and Judge [18]. Short dashed lines represent isochron locations based on anomaly picks from a suite of local magnetic profiles and age calibration is based on a revised magnetostratigraphic timescale [33].

Nazca Plate (for dataset 5) were obtained directly from [36] and Cande [pers. commun., 1995]. Although the magnetic signature is unclear from 91°W–100°W (near the Mendana FZ), and we suspect that the track crosses an undocumented fracture zone near 106°W, the interpolated age trend is nearly

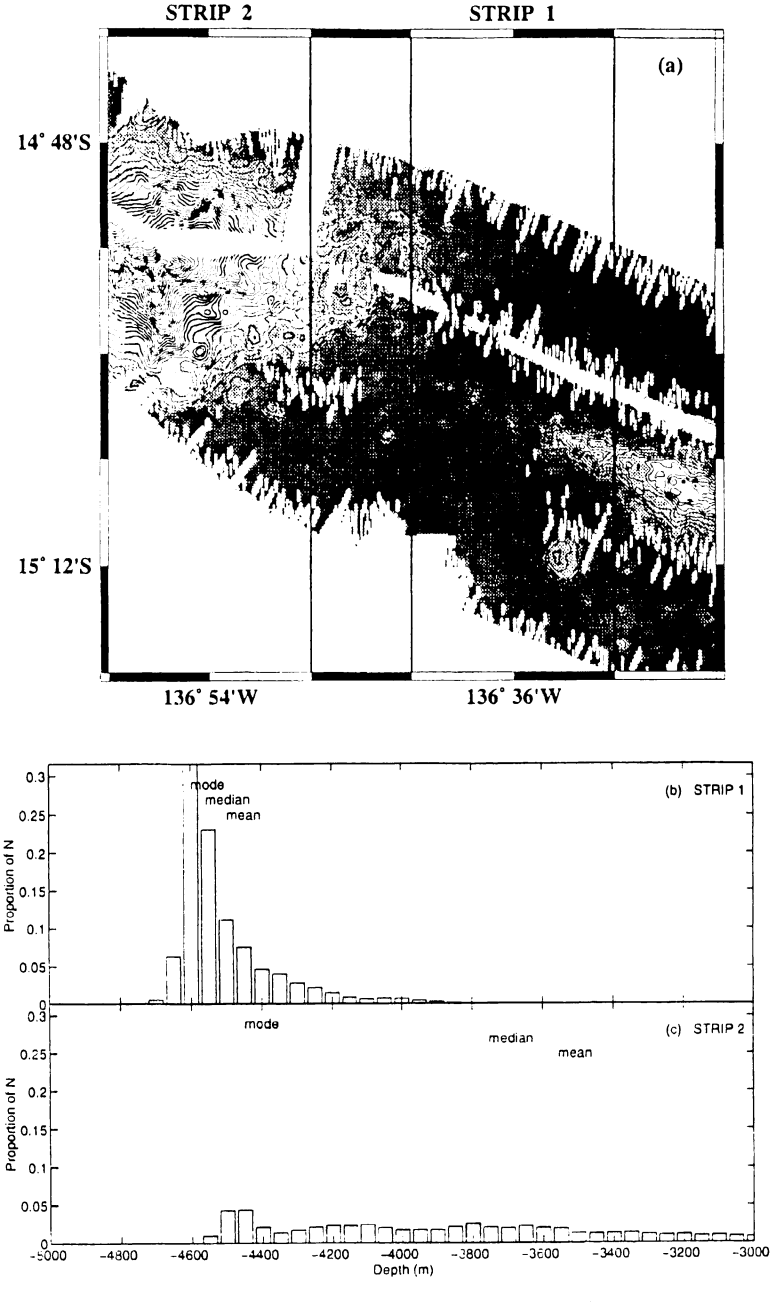

constant from the spreading axis at 118°W to 39 Ma at 79°W, near the Nazca Ridge. A comparison of a digital age database [37] and our aforementioned picks on conjugate sections of the Pacific and Nazca Plates south of 10°S reveals an approximate correspondence (within 2 Ma) over the profile length. Since little new magnetic information is available on the Pacific Plate north of the Marquesas FZ, age determination for dataset 6 (on the Pacific Plate north of the Marquesas FZ) was obtained directly from the digital age database [37].

Magnetic anomaly picks were correlated with a new magnetostratigraphic time scale [33]. The new time scale contains several significant modifications in the ages attributed to isochrons, mostly due to changes in calibration points. Most importantly, age estimates for the subdivisions of the Paleogene have changed considerably. Ages attributed to anomalies 9–19 may be 2–4 Myr younger than most previous time scales, making depths of 25–35 Ma seafloor appear approximately 50–70 m shallower. Once ages are established for control points corresponding to the anomaly picks, ages are estimated at other points along each dataset (except for dataset 6, as noted above) by cubic spline interpolation. Errors related to splining are small (a few ten thousand years) in comparison to the timescale variation, because the greatest separation of control points is about 3 Myr (except for dataset 5) and because spreading rate can be expected to remain reasonably constant in between.

3. Mode estimation

The standard parametric approach to evaluating distribution density assumes that the data are drawn from a known distribution, such as the normal distribution (Gaussian, with mean μ and variance σ^2). In this case, the mean is used to estimate the most likely value of the data. There are several complicating factors which affect the distribution of seafloor depth, causing it to be poorly fit by a Gaussian or even Poisson distribution function. Thus, the most likely seafloor depth is best estimated using a simple non-parametric approach: the histogram. Although other estimation techniques, such as the naive estimator and the kernel estimator [38], are, perhaps, more precise and mathematically rigorous, the histogram is employed here due to its shorter computation time and ease of interpretation.

We developed an automatic procedure for estimating unperturbed 'true' seafloor depth in areas containing numerous seamounts and ridges, based directly on the flatness of the unperturbed sections and the ruggedness of the disturbed sections, using a binning procedure. Seafloor depth data from the seamounts and ridges will have a low, broad histogram while the data from the flat surrounding seafloor will have a tall, narrow histogram. We assume that the tallest bin corresponds to the 'true' seafloor depth in a given area. The method estimates the 'true' seafloor depth in areas where less than 20% of the seafloor contains flat bottom values (see below). Estimation sensitivity should, in theory, increase with decreasing section area or bin width, although in practise it is limited by 'real' topographic noise.

3.1. Means, medians and modes

An example of the modal method from an area of rugged topography, is shown in Fig. 3a, a section of seafloor from dataset 1. The section contains an elongated ridge terminating at about 136°34′W and a tall seamount centered at 136°57′W. Fig. 3b and c show 50 m wide bin histograms of the bathymetry recovered from 0.2° wide north–south strips, cen-

Fig. 3. (a) Shaded contour map of SeaBeam2000 data acquired during survey legs GLOR3B-04MV (dataset 1; between 137°00′W and 136°12′W) and gridded with 200 m grid cell dimensions. Shading ranges from −4900 to −3500 m in depth. (b) Histogram of depths in strip 1 of data (between 136°42′W and 136°30′W) in 50 m bins. Note that the bin populations are normalized by the total number of data values and that the displayed bin range is from −5000 to −3000 m. The small difference between the mean, median and mode estimators suggests that the mean and median are adequate for nearly flat seafloor. (c) Histogram of depths in strip 2 of data (between 137°00′W and 136°48′W) in 50 m bins. The large difference between the mean, median and mode estimators suggests that the mean and median are biased estimators of seafloor depth over highly perturbed terrain.

tered at 136°36′W and 136°54′W, respectively. Strip 1 is representative of mostly flat seafloor, with perturbations due to the toe of the ridge to the east, a small seamount in the south and the downward slope of the large seamount in the west. The distribution of depths at this location (Fig. 3b) has a small standard deviation (155 m) and is only slightly skewed to shallow values, so that the mean (−4499 m), the median (−4559 m) and the mode (−4600 m) are fairly close. In this case the median is an adequate estimator of the 'true' seafloor depth, although it may be consistently biased to shallow values. Depths along strip 2, only 30 km to the west, have a completely different histogram, reflecting the presence of a large (3 km high) seamount (Fig. 3c). The histogram of depths shows a multimodal distribution which is extremely long-tailed. The standard deviation is large (820 m) because the seamount is tall and highly sloped. The seafloor depths estimated by the parametric mean (−3557 m) and median (−3754 m) are very different from that obtained by the non-parametric mode (−4450 m), which approximately corresponds to the intuitive expectation for the unperturbed seafloor depth and is also close to the value of the seafloor depth in strip 1. In this example, the 'true' seafloor depth was estimated even though flat seafloor (in the southeast corner of strip 2) covered less than 10% of the swath.

3.2. Bin resolution and dataset size

The automated selection of the modal bin depends on two adjustable parameters: the depth resolution used for the bins and the size of the area included in the histogram. Our goal is to estimate a representative depth for the seafloor which is suitable for depth–age regression, to retain intermediate wavelength depth–age variation. As shown in Fig. 3b, the modal estimation of seafloor depth is particularly effective when the seafloor is mostly flat, but seafloor generated at faster spreading ridges contains abyssal hills, which consist of elongate, ridge-parallel topography at 1–10 km spacing and ~100 m of relief. Abyssal hills are observed along the multibeam surveys with an amplitude of 50–200 m and a wavelength of one to tens of kilometers. To minimize errors associated with abyssal hill-related multimodes, the bin width in this area should be greater than or equal to the typical abyssal hill relief. Furthermore, variable sedimentary deposition, on the order of a few tens of meters, throughout the survey areas is likely to limit further depth estimation resolution. Based on trial and error, a 50 m bin is used, although some fine tuning of the result was obtained by calculating the mean of all data within 100 m of the modal bin.

A second related issue regarding modal depth estimation is the size of the area to include when constructing the histogram. For a given bin width, as the survey area becomes more populated with constructional features, it becomes increasingly likely that the bin which represents the seafloor depth will be mislocated. Once again, trial and error suggests that, for 0.2° wide datasets, 98% of the estimates corresponded to the intuitive expectation of the value (the remaining 2% estimate an anomalously tall bin from the tail), while that percentage decreased dramatically as window size is decreased. This dataset windowing size is optimal for dataset 1, which focused on the Pukapuka Ridges, as well the other datasets, which were obtained from 'average' seafloor, because of its relatively increased coverage (three swaths of wider SeaBeam2000). Intra-window subsidence should not substantially bias the depth estimation since, for an average spreading rate of 70 km Myr^{-1} and a subsidence rate of 350 m $Myr^{-1/2}$, the subsidence-related change in seafloor depth should only be of the order of tens of meters over the 5–36 Ma survey age range. However, estimates may reflect roughness attributed to abyssal hill relief at a wavelength approximately equal to the window size. While the short wavelength (tens of kilometers) roughness inherent in this windowing scheme will be useful for considering the respective amplitude of abyssal hill fabric and surficial volcanics as they affect the various seafloor depth estimators, it is not likely to bias the overall depth–age regression trends significantly.

4. Results

The seafloor depth estimates along dataset 1, in the vicinity of the Pukapuka Ridge System, illustrate the advantages of non-parametric techniques in de-

termining an unbiased seafloor depth value. Mode-estimated values for the 0.2° wide window are almost universally deeper than values estimated by the mean and median (Fig. 4). Over the interval from 117°W to 137°W, the average modal depth (−3922 m) is 81 m deeper than the median value and 165 m deeper than the mean. The sharp peaks observed in the mean and median estimators (Fig. 4) correspond to a large topographic feature within the window. Conversely, the ruggedness of the mode estimation is nearly uncorrelated, at short wavelength, with the mean and median variation and with the location of ridges and seamount clusters and is almost entirely attributed to abyssal hill relief. While the short-wavelength variation in the mode is generally less than 100 m, the mean frequently varies by several hundred meters, due to the great volume of perturbing volcanics. Areas in which the mode–mean difference is consistently large, from 117°W to 121°W, from 125°W to 127°W, from 129°W to 130°W, and from 134°W to 139°W, correspond directly to areas which are observed to contain the largest concentration of prominent volcanic features [29].

Since the mode corresponds to the unperturbed seafloor depth, the integrated volume of volcanic material can roughly be calculated by subtracting the volume below the mode, attributed to abyssal hill topography, from the volume above the mode. For dataset 1 the average columnar height is 150 m, roughly equivalent to about 2.5% of the volume of the crust. This large value is not surprising, since the primary goal of GLOR3B-04MV was to survey a set of continuous prominent ridges.

The other seafloor depth estimation datasets (2–5; not shown) do not purposely encounter high concentrations of volcanoes so that the mean, median and mode values are very close. The selected mode values for datasets 2 and 3 are very close to the dataset 1 values for nearby locations, confirming the improved depth estimation availed by the mode estimator over rugged terrain. Most importantly, these results suggest that, where there is sufficient swath coverage, the mode estimation technique can provide a more accurate (deeper) and reliable depth value than the mean and median in areas of robust volcanism, as in dataset 1, and an equally accurate and reliable depth value in areas of flat seafloor. The amount of extrusive volcanic material averaged over the length of these surveys is equivalent to a marginal fraction of crustal volume (< 0.5%). Accurate quantitative estimation of the small volume of the diffuse distribution of volcanics for these surveys is likely to be highly sensitive to the distribution of abyssal hill scarps relative to the dataset cutoff locations and the area of non-volcanics sampled. Thus, an automatic procedure is only possible by elimination of non-volcanic data points and finer-scale seafloor bottom determination [28].

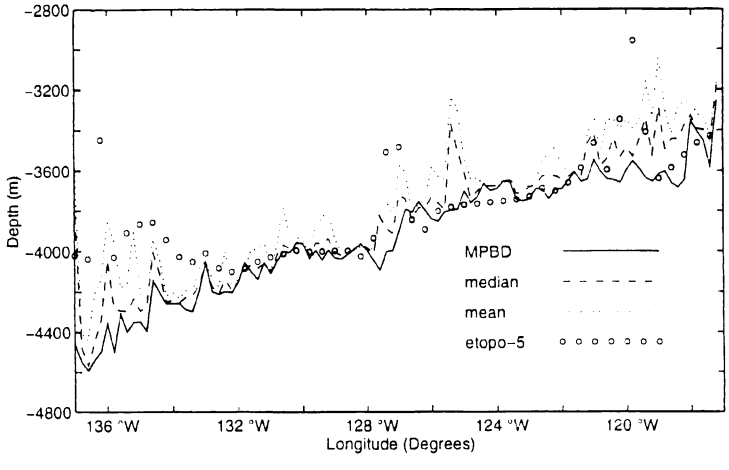

Fig. 4. Estimated depths (mode, median and mean) and ETOPO-5 depths for 0.2° wide (E–W) strips of the combined GLOR3B-04MV dataset (1) near the Pukapuka Ridges (see Fig. 1).

5. Discussion

5.1. Modal depth versus age

The modal depth estimates can be compared with the expected depth based on the standard plate cooling model [9] (PSM; Fig. 5a–f). Fig. 5a–d shows the variation of modal and the ETOPO-5 depths (both corrected for a representative, uniform 50 m thick sediment layer), with age on the EPR west flank south of the Marquesas FZ (datasets 1–4), in comparison with the PSM predicted depth. Seafloor proximate to the EPR axis (datasets 3 and 4) is deeper than the prediction of the standard model [9]. Although older seafloor (0–38 Ma) generally subsides monotonically nearly as fast as the rate predicted by the standard model; a shallowing depth anomaly gradually increases from 0 m, near 10 Ma, to over 200 m, near 22 Ma, in a region characterized by rough bathymetry and complexities in the magnetic anomaly pattern, which have been associated with the Miocene reorganization of the spreading center [24,34,35,39]. Importantly, the depth anomaly diminishes to zero just prior to rising sharply at the toe of the Tuamotus Plateau.

The GLOR3B–04MV survey (dataset 1) obtained multibeam bathymetry in close proximity to a set of volcanic ridges, which are confined to the trough of a set of gravity lineations [29]. The dataset 2 and 3 modal values corroborate the main depth–age regression features of dataset 1 (Fig. 5b and c); more than 95% of the synchronous estimates fall within 50 m bounds for the three datasets. Thus, the depth–age trends observed in the Pukapuka Ridge survey data are not the result of a deepening bias by a bathymetric trough or as a flexural response to the load of volcanic ridges. Dataset 4 modal values, ~ 200 km to the south, show a similar depth–age relationship.

Taken together, these depth–age profiles demonstrate that the depth anomaly proposed for the young section of the superswell region is of the order of 200 m or less. The improved depth estimation method of multibeam soundings and the shift in age attributed to the recently revised magnetostratigraphic calibration of Cande and Kent [33] are the most likely explanations for the failure of the present study to verify large depth anomalies (> 500 m) [17,18,24].

5.2. Gridded depth versus age

The existence of an age-dependent anomaly over the superswell [17] is based on the sediment-corrected, gridded bathymetry (McNutt and Fischer [17], fig. 3). Our depth–age results (Fig. 5a–c), approximately match the gridded bathymetry up to 30 Ma but at older ages (30–37 Ma) our depth estimates are progressively deeper, by 200–400 m, where we surveyed a sequence of large seamounts and guyots [29]. From 28 to 37 Ma the gridded bathymetry appears to reflect an affinity for the −4000 m contour (before 50 m sediment correction), suggesting that the overly shallow ETOPO-5 bathymetry is the result of splining sparse seamount-derived con-

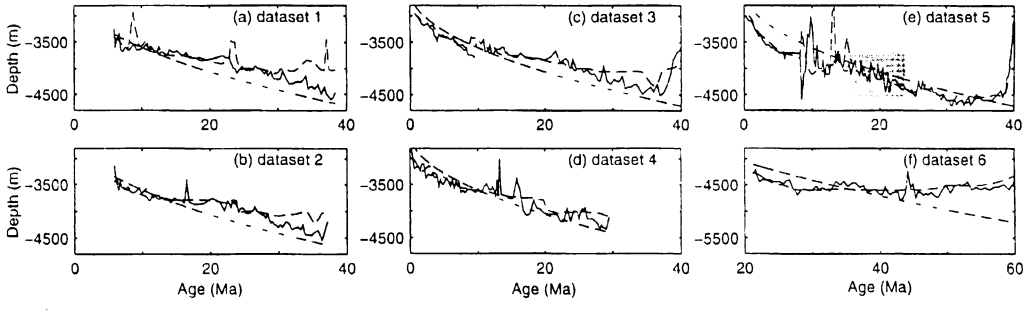

Fig. 5. Mode estimated (solid) and ETOPO-5 (short dash) depths for 0.2° wide (E–W) strips obtained from six datasets used in this study plotted as a function of age (see text), corresponding to datasets 1–6. Datasets 1–4 are on the Pacific Plate south of the Marquesas FZ, dataset 6 is north of the Marquesas and dataset 5 is on the conjugate section of the Nazca Plate. The plate-model depth is shown for comparison (long dash). The area where there are no clear magnetic anomaly picks is shaded in (e). Note the age range difference in (f).

tour maps, which are unrepresentative of the ambient seafloor depth.

The tendency for the various digital bathymetry databases to show bulges and excessive flatness, particularly at integral multiples of the 500 m contour interval, has been noted [30]. It has been attributed to the fact that ship soundings were not directly used in gridding — they were prepared by digitizing contours from GEBCO charts and by gridding the coordinates of these contours. Fig. 6 shows a comparison of ETOPO-5 (which includes SYNBAPS) with all ship soundings obtained from the SIO–GMT database [30] within two adjacent and parallel 2° wide E–W corridors from 125°W to 135°W (see Fig. 1). The gridded bathymetry and ship soundings show an increasingly shallow anomaly in the gridded database from 125°W to 130°W. However, for the western portion of the area (130°W–133°W), the gridded data are increasingly shallow, by up to 300 m, in comparison to sounding data. The smooth, age-related anomaly observed over this young section of the proposed superswell (> 500 m) is mostly the product of flatness in a gridded bathymetry database which does not adequately represent the seafloor depth. Whatever anomaly exists (~ 250 m), tapers off to near zero just prior to encroaching upon the thickened crust and sedimentary aprons of the Tuamotus plateau [40].

5.3. Anomalous subsidence and the 'superswell'

A depth anomaly of the order of 100 m is within the global range of variation of seafloor slope [31]. Furthermore, the depth anomaly attributed to the spreading segment on the Pacific Plate between the Austral and the Marquesas FZs is similar in magnitude to those observed on the Pacific Plate north of the Marquesas FZ (Fig. 5f) and on the conjugate section on the Nazca Plate (Fig. 5e), so that the depth anomaly is not bounded by tectonic elements such as fracture zones and spreading axes. The depth–age trend on the west flank of the SEPR is similar to the conjugate section on the east flank of the SEPR. In particular, from 13 to 35 Ma, the Nazca Plate appears to subside roughly at the same rate as the corresponding 'superswell' section on the Pacific Plate but is deeper by approximately 250 m. Note that observations of the general trend of depth with age on the east flank of the SEPR are not susceptible to possible inaccurate age assignment from 100°W to 92°W, since the expected error based on the offset across the Mendana FZ [37] (~ 1 Myr)

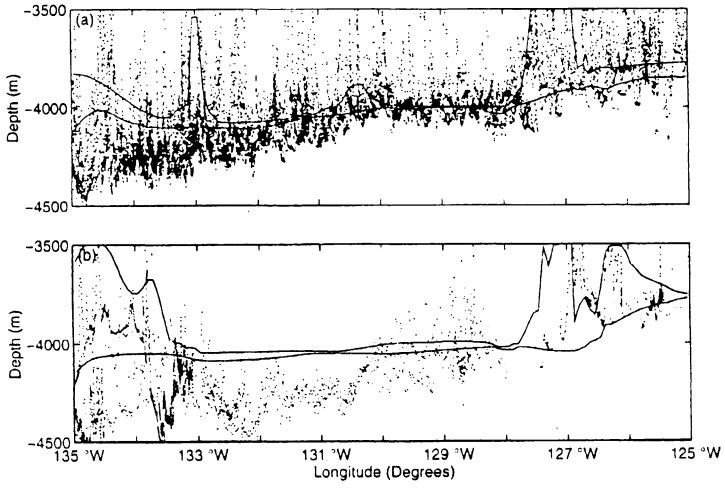

Fig. 6. Original single-beam ship sounding depths (points) in comparison with the upper and lower boundary (solid lines) for all ETOPO-5 gridded depths for two adjacent, parallel, E–W strips from 125°W to 135°W (shown in Fig. 1). (a) 14.5°S–16.5°S. (b) 16.5°S–18.5°S. ETOPO-5 adequately represents seafloor depths from 125°W to 130°W but further west the gridded bathymetry underestimates depth by several hundred meters.

is equivalent to an error of 50 m in relation to age. The large drop in the depth anomaly across the Marquesas FZ suggested that the Marquesas FZ presents a natural boundary between anomalously thin and hot superswell lithosphere, to the south, and normal lithosphere, to the north [17,18]. However, the depth estimates in the present study fail to reproduce this comparative constant shallowing offset for the southern segment. While the northern estimates (Fig. 5f) from 125°W to 136°W (29–52 Ma) show a depth anomaly that increases from −200 m to 600 m (extremely low seafloor slopes), the geographically corresponding southern estimates (16–37 Ma) show a near-constant shallow anomaly of approximately 100 m. For the period 29–37 Ma, the difference in depth is approximately 100–250 m, less than the present offset across fracture zones at the EPR axis.

Most importantly, the new depth estimates fail to establish an anomalous, age-related, long wavelength trend in the shallowing of the data, since the seafloor of 13–37 Ma is very nearly as deep as the plate-model prediction. On the contrary, similar to Cochran's results [24], the anomalous ridge flank subsidence extends throughout the entire region *younger* than the middle Miocene ridge reorientation (~ 24 Ma). Interestingly, with the exception of the youngest section, where the seafloor slope is unusually high (over 400 m $Myr^{-1/2}$), a similar pattern is developed on the east flank of the SEPR (with a 300 m deepening offset; see Fig. 5e), although details of the depth–age correlation on the Nazca Plate are limited by coarse magnetic anomaly identification and the possible presence of an uncharted fracture zone at 106°W. The greatest difference in subsidence behavior is *not* in the superswell but is evident in the *younger* section on the west flank of the SEPR, in the area associated with the development of gravity lineations and with the recent production of pervasive, unusually robust volcanics.

6. Models

The west flank of the EPR has recently been the focus of intense research due to observations of abundant volcanism, lineations in the altimetric gravity field and an age-dependent, shallowing depth anomaly. While ~~the~~ our study fails to confirm the long-wavelength 'superswell' depth anomaly, it is

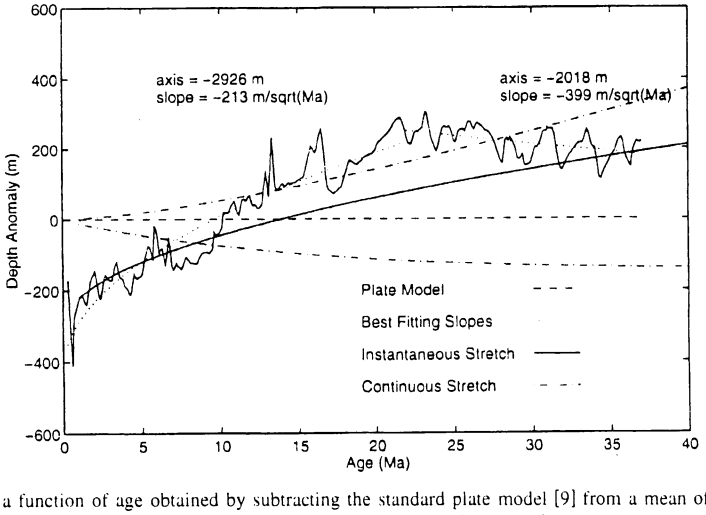

Fig. 7. Depth anomaly as a function of age obtained by subtracting the standard plate model [9] from a mean of modal estimates derived from datasets 1–4 on the west flank of the SEPR, south of the Marquesas FZ (solid line). The horizontal line (dashed) represents no anomaly with respect to the plate model. The best fitting seafloor slope curves are shown for two subintervals (dotted line: see text). An instantaneous stretching episode of 30% ($\beta = 1.3$), affecting 0–37 Ma crust, nearly fits the estimated depth curve. Continuous stretching (upper dot-dashed line) over the same interval with a moderate strain rate ($\epsilon = 3.1 \times 10^{-16}\ s^{-1}$, resulting in 1% Myr^{-1} stretching; lower dot-dashed line) barely fits the data, even when the isostatic effect is removed due to continuous crust replacement.

clear that both flanks of the SEPR have undergone periods of anomalous subsidence, although the magnitude of the corresponding depth anomalies appears to be minor (Fig. 7). The ridge axis is anomalously deep by about 200 m but by 20 Ma the seafloor is anomalously shallow by about 200 m; at older ages the depth anomaly decays to zero. One can also interpret this depth anomaly in terms of anomalous seafloor slope. Between 0 and 22 Ma the slope is anomalously low, 218 m $Myr^{-1/2}$, while between 22 and 37 Ma the slope is anomalously high, 399 m $Myr^{-1/2}$ (Fig. 7). Next, we investigate several possible mechanisms for the depth anomaly on the west flank of the EPR. The models considered are: mantle plume; small scale convection; stretching (instantaneous and continuous); and, finally, variations in crustal thickness (on-ridge and off-ridge). When discussing each model we will also consider constraints from the other geophysical anomalies in the area, such as gravity rolls and low elastic thickness.

6.1. Mantle plume

Mantle plumes have traditionally explained a range of observations associated with midplate swells, such as age-progressive linear seamount chains (hot-spot) and a depth anomaly which can exceed 2 km in amplitude and have a wavelength of 1000–2000 km [13,14]. The depth anomaly distribution on 7–37 Ma Pacific Plate seafloor resembles, in planform, a subtle midplate swell (~ 300 m tall). However, the closest hot-spots, Marquesas and Pitcairn, are too distant to be associated with this plume. The recently charted Pukapuka chain lies in the center of this depth anomaly but the age progression of dredged samples along the Pukapuka chain [29] is not consistent with published absolute plate motion poles attributed to the mini-hot-spot model [41] and the youngest volcanoes are in an areas of zero depth anomaly. While the volcanic expression of a mantle plume is apparently lacking in the area, perhaps a broad, weak plume with a moderate temperature anomaly and dynamic support is maintaining the swell [42], or perhaps flow from more distant plumes is channeled toward the ridge beneath the thinner lithospheric segment south of the Marquesas FZ [43]; this would also provide thermal buoyancy for the swell.

6.2. Small-scale convection

Small-scale convection in low-viscosity asthenosphere [8] has been proposed to explain lineations in the gravity field aligned roughly parallel to the recent absolute plate motion direction [44] on the west flank of the SEPR and the anomalously low seafloor slope there [17,45]. The original model includes the thermal interaction of the lithospheric thermal lid with a convective, variable low-viscosity boundary layer below, which supplies advective heat [45]. Convection begins at a model age younger than 5 Ma, effectively thinning the thermal lithosphere; causing a progressive shallowing of the seafloor (~ 150 m from 10 to 20 Ma) with respect to the standard depth–age model. While the heat delivery of small-scale convection may be sufficient to explain the growing depth anomaly, it does not explain the reduction in the depth anomaly on older seafloor in an area where the gravity rolls are strong. Moreover, more than 90% of the volcanic volume attributed to the Pukapuka Ridges is confined to a trough of the lineations, even though the convective pattern predicts a downgoing flow there. Nevertheless, it is difficult to falsify a small-scale convection model because it is dependent on a variety of poorly constrained parameters [46].

6.3. Lithospheric stretching

Lithospheric stretching has been proposed to explain the formation of the Pukapuka Ridges as well as the formation of the gravity lineations by boudinage [29]. Stretching has two effects on seafloor depth anomaly: crustal stretching/thinning increases with depth while lithospheric stretching/thinning decreases with depth, causing a swell. Stretching could occur as a single event or continuously with time. For instantaneous stretching of a cooling half-space, the depth $\Delta d(t)$ anomaly is given by:

$$\Delta d(t) = -\left(1 - \frac{1}{\beta}\right)\left[z_c \frac{(\rho_c - \rho_m)}{(\rho_m - \rho_w)} - \frac{2\alpha\rho_m T_m (\kappa t/\pi)^{1/2}}{(\rho_m - \rho_w)}\right] \quad (1)$$

where: t is the age of the lithosphere; β is the

stretching coefficient [6]; z_c (6000 m) is the unstretched crustal thickness; ρ_c (2800 kg m^{-3}) is the crustal density; ρ_m (3300 kg m^{-3}) is the mantle density; ρ_w (1000 kg m^{-3}) is the seawater density; α (3×10^{-5} °K^{-1}) is the volume coefficient of thermal expansion; κ (9.75×10^{-7} m^2 s^{-1}) is the thermal diffusivity; and T_m (1300°K) is the asthenospheric temperature. Instantaneous stretching with $\beta = 1.3$ (Fig. 7, solid curve) approximately matches the depth anomaly on both young and old lithosphere but underestimates the anomaly in the 10–30 Ma age range. A larger amount of stretching may provide a better fit to the data, but such a large deformation of the lithosphere would be apparent in the spacings of the fracture zones [47]. If the instantaneous extension is accompanied by crustal replacement consisting of extension-generated melt [48] even greater extension may be required.

It is unlikely that stretching of the Pacific plate would occur instantaneously. The other end-member model is a lithosphere that is extending at a constant strain rate ($\epsilon = 3.1 \times 10^{-16}$ s^{-1}, resulting in 1% Myr^{-1} stretching). In this case the depth anomaly at a seafloor age [49], t, is:

$$\Delta d(t) = -\epsilon t z_c \frac{(\rho_m - \rho_c)}{(\rho_m - \rho_w)} + \frac{2\alpha\rho_m T_m}{(\rho_m - \rho_w)} \times \left\{ \left(\frac{\kappa}{\pi} \right)^{1/2} \left[\left(\frac{1 - e^{-2\epsilon t}}{2\epsilon} \right)^{1/2} - 1 \right] \right\} \quad (2)$$

Continuous stretching results in a deepening of the lithosphere with respect to the standard model, since the integrated crustal isostatic response (first term) to thinning exceeds the shallowing thermal response (second term). Thus, this model does not adequately fit the depth anomaly data (Fig. 7; lower dot-dashed curve). A modification of this model is to replace crust continuously by intrusive and extrusive volcanism, so it maintains a constant thickness, and the first term in Eq. (2) is zero. In this case, the seafloor shallows with age but provides a poor fit to the data, especially at the spreading ridge (Fig. 7; upper dot-dashed curve). Instantaneous stretching requires much less total strain than continuous stretching to produce the same depth anomaly because, during the interval of continuous stretching, the thermal perturbation has time to decay. Most importantly, in all cases, a great amount of stretching is required to yield significant variations in depth anomaly and seafloor slope.

6.4. Crustal thickness

Finally, we consider that the depth anomaly is caused by variations in crustal thickness. This model predicts that the crust over the highest point on the swell (200 at 20 Ma) is 2.2 km thicker than the crust at the spreading ridge axis (−200 m at 2 Ma). First, consider on-ridge variations in crustal production with time. An increase of 50°C in an adiabatically decompressing mantle temperature at the rise axis is expected to result in increased partial melt volume with a 5 km crustal thickness increase [48], so this mechanism is possible. However, we believe it is unlikely to account for the entire 2.2 km of crustal thickness variation, because such large variations are not observed at high spreading rate ridges [50]. Moreover, the mechanism predicts a symmetrical depth anomaly across the ridge, which is not observed (Fig. 6e). The other possibility is that crustal generation at the ridge axis has remained normal for the past 35 Ma and the depth anomaly is caused by off-axis crustal production, although we do not find a positive correlation between the depth anomaly and the volume of volcanic material corresponding to the Pukapuka Ridges.

7. Conclusions

We assessed the magnitude and regional distribution of the depth anomaly on the youngest, eastern section of the proposed 'superswell', away from the influence of recognized nearby hot-spots and the thickened crust of the Tuamotus plateau, where it was expected to grow to over 500 m. Seafloor depths were estimated using the mode of datasets provided by 6 multibeam surveys (4 on the west flank of the EPR south of the Marquesas FZ), because the area is characterized by robust volcanism which biases the parametric mean and median estimators. This method accurately estimates seafloor depth even where the majority of seafloor is covered by large constructive

features. We found that, throughout our survey, the mode was sensitive to seafloor variation while the mean and median were sensitive to the volcanism. Our results suggest that, where there is sufficient swath coverage, the mode estimation technique can provide a more accurate and reliable depth value than the mean and median in areas of robust volcanism and an equally accurate and reliable depth value in areas of flat seafloor.

The depth anomaly, referenced to the plate model [9] was less than 200 m, independent of proximity to a volcanic feature or a gravity lineation trough. The age-related flattening in the original gridded bathymetry (SYNBAPS) was caused by erroneous splining of contour maps, which were regionally unrepresentative of the seafloor depth. The depth anomaly distribution did not show a long-wavelength, age-dependent component, since the anomaly decreases to near-zero for old ages, and the depth anomaly was not bounded by tectonic elements such as the SEPR spreading axis or the Marquesas FZ. The anomalous region of seafloor slope appears to be *younger* than the mid-Miocene spreading reorientation (~ 24 Ma), where the average seafloor slope is 218 m $Myr^{-1/2}$, while older seafloor is subsiding at a near-normal rate (399 m $Myr^{-1/2}$). After 10 Ma, a similar pattern is developed on a conjugate section of the Nazca Plate, but 250 m deeper.

The small magnitude of the depth anomaly on the west flank of the SEPR suggests the presence of a weak, subcrustal hot-spot, although none have been identified locally and the Pukapuka Ridges appear to have a non-hot-spot origin. A simple small-scale convection model does not provide sufficient advective heat to the lithosphere to fit the observed shallowing, unless a possible additional thermal perturbation is considered. Variation in crustal thickness, both at the rise axis and, subsequently, due to instantaneous/continuous stretching could account for anomalous seafloor slopes, although a great amount of stretching (~ 30%) is required and normal faulting was not observed in the area. Other models, involving subcrustal intrusive thickening, dynamic support or 'fingering' from a hot-spot in an asthenospheric channel, are still poorly understood. Proper testing of models requiring crustal thickness variation should be accomplished by seismic determination of the Moho depth in the region.

Acknowledgements

Multibeam and magnetic data for three cruises — ARIA02WT, PPTU03WT and TUNE02WT — were available through the Scripps Institution of Oceanography Geological Data Center (SIO–GDC). RC2608 and WEST01MV data were provided generously by Barry Parsons and by Tetsuro Urabe, respectively. WEST04MV data was obtained with funding from the National Science Foundation with the help of David Epp. The authors benefitted from insightful discussions with Andrew Goodwillie, Catherine Johnson, Steve Cande, Jason Phipps-Morgan and Mara Yale, as well as constructive reviews by Norman Sleep, Dan McKenzie and Miriam Kastner. This research was supported by the National Science Foundation, Marine Geology and Geophysics Program (OCE90-19712). *[MK]*

References

[1] D.L. Turcotte and E.R. Oxburgh, Finite amplitude convective cells and continental drift, J. Fluid Mech. 28, 29–42, 1967.
[2] J.G. Sclater, R.N. Anderson and M.L. Bell, Elevation of ridges and evolution of the central eastern Pacific, J. Geophys. Res. 76, 7888–7915, 1971.
[3] R.L. Parker and D.W. Oldenburg, Thermal model of ocean ridges, Nature 242, 137–139, 1973.
[4] E.E. Davis and C.R.B. Lister, Fundamentals of ridge crest topography, Earth Planet. Sci. Lett. 21, 405–413, 1974.
[5] M.G. Langseth, X. LePichon and M. Ewing, Crustal structure of the mid-ocean ridges, 5, Heat flow through the Atlantic Ocean floor and convection currents, J. Geophys. Res. 71, 5321–5355, 1966.
[6] D. McKenzie, Some remarks on the development of sedimentary basins, Earth Planet. Sci. Lett. 40, 25–32, 1978.
[7] R.L. Heestand and S.T. Crough, the effect of hot spots on the oceanic age–depth relations, J. Geophys. Res. 86, 6107–6114, 1981.
[8] F.M. Richter and B. Parsons, On the interaction of two scales of convection in the mantle, J. Geophys. Res. 80, 2579–2541, 1975.
[9] B. Parsons and J.G. Sclater, An analysis of ocean floor bathymetry and heat flow with age, J. Geophys. Res. 82, 803–827, 1977.
[10] H.W. Menard, Depth anomalies and the bobbing motion of drifting islands, J. Geophys. Res. 78, 5128–5137, 1973.
[11] R.S. Detrick, R.P. von Herzen, S.T. Crough, D. Epp, and U. Fehn, Heat flow on the Hawaii Swell and lithospheric reheating, Nature 292, 142–143, 1981.
[12] J. Morgan, Plate motions and deep mantle convection, Mem. Geol. Soc. Am. 132, 7–22, 1972.

[13] R.S. Detrick and S.T. Crough, Island subsidence, hotspots, and lithospheric thinning, J. Geophys. Res. 83, 1236–1244, 1978.
[14] S.T. Crough, Thermal origin for mid-plate hot-spot swells, Geophys. J. R. Astron. Soc. 55, 451–459, 1978.
[15] S.T. Crough and R.D. Jarrard, the Marquesas-line swell, J. Geophys. Res. 86, 11763–11771, 1981.
[16] J. Mammerickx, Depth anomalies in the Pacific: Active, fossil, and precursor, Earth Planet. Sci. Lett. 53, 147–157, 1981.
[17] M.K. McNutt and K.M. Fischer, The South Pacific Superswell, in: Seamounts, Islands and Atolls, Am. Geophys. Union, Geophys. Monogr. 43, 25–34, 1987.
[18] M.K. McNutt and A.V. Judge, The Superswell and mantle dynamics beneath the South Pacific, Science 248, 969–975, 1990.
[19] S. Calmant and A. Cazenave, Anomalous elastic thickness of the oceanic lithosphere in the south-central Pacific, Nature 328, 236–238, 1987.
[20] C. DeMets, G.R. Gordon, D.F. Argus and S. Stein, Current plate motions, Geophys. J. Int. 101, 425–578, 1990.
[21] R. Van Wykhouse, SYNBAPS, Tech. Rep. TR-233. Natl. Oceanogr. Off., Washington, DC, 1973.
[22] A.M. Goodwillie and A.B. Watts, An altimetric and bathymetric study of elastic thickness in the central Pacific Ocean, Earth Planet. Sci. Lett. 118, 311–326, 1993.
[23] P.E. Filmer, M.K. McNutt and C.J. Wolfe, Elastic thickness of the lithosphere in the Marquesas and Society Islands, J. Geophys. Res. 98, 19565–19577, 1993.
[24] J.R. Cochran, Variations in subsidence rates along intermediate and fast spreading mid-ocean ridges, Geophys. J. R. Astron. Soc. 87, 421–454, 1986.
[25] D.K. Smith and T.H. Jordan, Seamounts statistics in the Pacific Ocean, J. Geophys. Res. 93, 2899–2918, 1988.
[26] G.A. Abers, B. Parsons and J.K. Weissel, Seamount abundances and distributions in the southeast Pacific, Earth Planet. Sci. Lett. 87, 137–151, 1988.
[27] K.G. Bemis and D.K. Smith, Production of small volcanoes in the Superswell region of the South Pacific, Earth Planet. Sci. Lett. 118, 251–262, 1993.
[28] Y. Shen, D. Forsyth, D.S. Scheirer, and K.C. Macdonald, Two forms of volcanism: Implications for mantle flow and off-axis crustal production on the west flank of the southern East Pacific Rise, J. Geophys. Res. 98, 17,875–17,889. 1993.
[29] D.T. Sandwell, E.L. Winterer, J. Mammerickx, R.A. Duncan, M.A. Lynch, D.A. Levitt and C.L. Johnson, Evidence for diffuse extension of the Pacific Plate from Pukapuka Ridges and Crossgrain gravity lineations, J. Geophys. Res. 100, 15,087–15,099, 1995.
[30] W.H.F. Smith, On the accuracy of digital bathymetric data, J. Geophys. Res. 98, 9591–9603, 1993.
[31] J.C. Marty and A. Cazenave, Regional variations in subsidence rate of oceanic plates; a global analysis, Earth Planet. Sci. Lett. 94, 301–315, 1989.
[32] D.N. Chayes and D.W. Caress, Processing and display of multibeam echosounder data on the R/V Maurice Ewing, EOS Trans. Am. Geophys. Union 74, 562, 1993.
[33] S.C. Cande and D.V. Kent, A new geomagnetic polarity time scale for the Late Cretaceous and Cenozoic, J. Geophys. Res. 97, 13917–13951, 1992.
[34] D. Handschumacher, Post-Eocene plate tectonics of the eastern Pacific, Am. Geophys. Union, Geophys. Monogr. 19, 177–202, 1976.
[35] E.M. Herron, Sea-floor spreading and the Cenozoic history of the East-central Pacific, Geol. Soc. Am. Bull. 83, 1671–1691, 1972.
[36] S.C. Cande, Nazca–South America plate interactions since 50 mybp, in: Peru–Chile trench offshore Peru, Atlas 9, D.M. Hussong, S.P. Dang, L.D. Kulm, R.W. Couch and T.W.C. Hilde, eds., Ocean Margin Drilling Program, Regional Atlas Series, Marine Science International, Woods Hole, MA, Sheet 14, 1986.
[37] R.D. Muller, W.R. Roest, J.-Y. Royer, L.M. Gahagan and J.G. Sclater, A digital age map of the ocean floor, SIO Ref. Ser. 93-30, 1993.
[38] B.W. Silverman, Density Estimation for Statistics and Data Analysis, 175 pp., Chapman and Hall, London, 1986.
[39] J. Mammerickx, R.N. Anderson, H.W. Menard and S.M. Smith, Morphology and tectonic evolution of the East-central Pacific Geol. Soc. Am. Bull. 86, 111–117, 1975.
[40] J. Talandier and E.A. Okal, Crustal structure in the Society and Tuamotu Islands, French Polynesia, Geophys. J. R. Astron. Soc. 88, 499–528, 1987.
[41] L. Fletiout and C. Moriceau, Short-wavelength geoid, bathymetry and the convective pattern beneath the Pacific Ocean, Geophys. J. Int. 110, 6–28, 1992.
[42] N.M. Ribe and U.R. Christensen, Three-dimensional modeling of plume–lithosphere interaction, J. Geophys. Res. 99, 669–682, 1994.
[43] W.J. Morgan, Rodriguez, Darwin, Amsterdam,..., a second type of hotspot island, J. Geophys. Res. 83, 5355–5360, 1978.
[44] W.F. Haxby and J.K. Weissel, Evidence for small-scale mantle convection from Seasat altimetric data, J. Geophys. Res. 91, 3507–3520, 1986.
[45] W.R. Buck and E.M. Parmentier, Convection beneath young oceanic lithosphere: Implications for thermal structure and gravity, J. Geophys. Res. 91, 1961–9174, 1986.
[46] E.M. Robinson and B. Parsons, Effect of a shallow low-viscosity zone on small-scale instabilities under the cooling oceanic plates, J. Geophys. Res. 93, 3469–3479, 1988.
[47] A.M. Goodwillie and B. Parsons, Placing bounds on lithospheric deformation in the central Pacific Ocean, Earth Planet. Sci. Lett. 111, 123–129. 1992.
[48] D. McKenzie and M.J. Bickle, The volume and composition of melt generated by extension of the lithosphere, J. Petrol. 29, 3, 625–679, 1988.
[49] A. Agnon and V. Lyakhovsky, Oceanic topography and heatflow: indications for a silent discharge of cold rock into a convecting earth, Geophys. Res. Lett. 22, 1273–1276, 1995.
[50] Y.J. Chen, Oceanic crustal thickness versus spreading rate, Geophys. Res. Lett. 19, 753–756, 1992.

This chapter, in full, is a reprint of the material as it appears in Earth and Planetary Science Letters, V. 139, 1996. The dissertation author is the primary investigator and author of this paper.

CHAPTER 4

PUKAPUKA RIDGES:

INTERACTION BETWEEN MELTING ANOMALIES

AND LITHOSPHERIC ZONES OF WEAKNESS

ABSTRACT

Three models have been proposed to account for the presence of small volcanic chains in association with short wavelength lineations in the altimeter gravity field on the west flank of the South East Pacific Rise: mini-hotspots, small-scale convection and lithospheric extension. Two primary predictions of the two mantle convection models are tested. First, does the orientation of the Pukapuka system, a chain of elongate volcanoes, follow the prediction of the *fixed* hotspot hypothesis? Second, are volcanoes in the region associated with the crests of altimeter gravity anomaly lineations?

Multibeam bathymetry is fit to a three-parameter model. The Pukapuka ridges can be tightly fit to a small circle (mean absolute misfit = 0.16 ^{o} ~ 20 km) and the pole corresponding to the best-fit parameter set is distinct from standard Pacific absolute rotation poles (0-18 Ma). Therefore the ridges are inconsistent with one or several small fixed hotspots arranged end-to-end. These results suggest an additional model, asthenospheric channeling to the spreading axis.

Volcanic centers serve as markers for places which have satisfied the condition of adequate melt supply of sufficient hydraulic head to penetrate lithosphere. In order to compare the location of volcanoes and the longer wavelength gravity lineations, the satellite-gravity signal (small-scale bumps) attributed to volcanoes must be isolated from the residual field. An analytical mode estimates the background value and a nearby-volcano search scheme identifies altimeter gravity anomaly grid cells attributed to a constructive edifice. Multibeam bathymetry and corresponding altimeter gravity at the Pukapuka ridges are closely correlated, suggesting that satellite altimeter gravity may be used for locating and quantifying volcanic edifices larger than 75 km^3 in unsurveyed regions of the world seafloor. In the Pukapuka region over 90% of large volcanoes (<18 mgal peaks) are concentrated in gravity lineations troughs. The results are not due to flexural response to the loads themselves. Also, there are nearly no large volcanoes north of the Marquesas Fracture Zone where altimeter gravity anomaly lineations are strong, indicating that sublithospheric melt pools exist independently of the lineations-generating process.

The seafloor near the Pukapuka ridges is characterized by many propagating rifts and small volcanoes. The majority of hotspot-attributed chains in the southcentral Pacific fail to exhibit long-lived monotonic age variation consistent with the hotspot model; instead they appear to be intermittent and easily deflected along lines of weakness due to older chains and fracture zones. Possibly the young southcentral Pacific sub-lithosphere is populated by many small melting anomaly pools which only erupt in weak lithospheric zones, such as tension-induced boudin troughs.

1. INTRODUCTION

Volcanism on the ocean floor has been studied in detail in two independent provinces, intra-plate and at tectonic spreading centers. The paradigms of plate tectonics (*Wilson*, 1963) and hotspots (*Morgan*, 1972a,b) have been used cooperatively to model volcanic and tectonic processes in the ocean basins; in the first, the surface of the earth is composed of rigid lithospheric plates which move in response to stress generated and relieved at the margins; in the second, volcanic chains record the motion of these plates over hotspots, deep, melting anomalies. The majority of volcanic production by volume is in the form of mid-ocean ridge basalts produced by decompression-melting of passively upwelling upper mantle (asthenosphere) at the plate separation margin (*McKenzie and Bickle*, 1988). Volcanism attributed to hotspots is volumetrically minor in comparison, but this model has been rigorously tested because its predictions are explicit and accessible.

The concept of hotspots must be distinguished by two distinct hypotheses. The *kinematic* hotspot describes the motion of the plate over a source of melt in the mantle (*Wilson*, 1963), presumably a plume, resulting in a linear, volcanic sequence with monotonically increasing ages and with a geochemically unique signature attributed to a deep-mantle source. In the *fixed* hotspot hypothesis these melting anomalies are fixed relative to one another (*Dietz and Holden*, 1970) and define the absolute motion reference frame (*Morgan*, 1972a,b). These particular constraints have made the *fixed* hotspot model easily testable; it can be verified for a given volcanic chain if it can be shown to have an absolute pole of rotation consistent with established absolute poles based on other volcanic sequences.

Another generation of models explains linear volcanic chains as the surficial expression of horizontal upper-mantle convective rolls (*Haxby and Weissel*, 1986; *Buck and Parmentier*, 1986; *Bonatti and Harrison*, 1976; *Bonatti et al.*, 1977). Such models predict lineations in the gravity field oriented along the absolute motion direction as well as non-monotonic age progressions. Still, the central assertion common to both the hotspot and small-scale convection models is that volcanism is attributed to the

upward flux of hot, potentially melt-generating mantle, not passively melting due to stretching. Therefore volcanic constructive features should trace the location of warm upwelling upper mantle; associated geophysical observations should be positive bathymetric and gravity anomalies along the volcanic lines. Alternative models, in which melt is either generated by stretching, diverted to lines of weakness (*Epp*, 1984), or is only capable of complete penetration when lithosphere is unusually thin all predict volcanism to be associated with weak lithosphere.

With the advent of a high-resolution global satellite-altimeter gravity anomaly dataset (*Sandwell and Smith*, 1995), the spatial distribution of volcanic features will be asserting an increasing diagnostic role in distinguishing among potential models for volcano formation principally because it is readily accessible and universal. Volcanic centers mark places which have satisfied the condition of an adequate supply of heat or magma capable of producing melt of sufficient hydraulic head and latent heat to penetrate lithosphere of a given age (*Vogt*, 1974). Thus, regions which are characterized by the absence of volcanism adjacent to volcanically robust areas may denote a dramatic decrease of melt availability and/or lithospheric penetrability. The altimeter gravity anomaly database has dramatically increased in resolution (~5 km at low-latitudes; 1/4 λ) due to recent inclusion of altimeter passes for the ERS-1 and declassified Geosat orbiters. Fine-scale resolution now allows for the precise location (within a few km) of medium-sized individual volcanic features (see below) as well as rough estimates of amplitudes and widths.

The purpose of this study is to test the primary predictions of the hotspot and small-scale convection models with respect to the locations of volcanic features on the young Pacific plate south of the Marquesas Fracture Zone (MFZ). Section 2 describes available data and previous work. In section 3, multibeam bathymetry will be used to determine whether the Pukapuka ridges follow the Pacific absolute pole of rotation (PAPR) for the last 0-18 Ma as is predicted by both the hotspot and small-scale convection models. I will show that the *fixed* hotspot and small-scale convection models are inadequate. Instead the Pukapuka ridges (and possibly other nearby chains) are demonstrated to lie remarkably along a small circle with a different orientation. In section 4, I will show that altimeter gravity "bumps" corresponding to volcanic features are located in the troughs of gravity lineations. A review of the complex tectonic and

volcanic nature of this portion of the Pacific Plate is presented in section 5, indicating that robust volcanism south of the Marquesas Fracture Zone is associated with many propagating rifts and that sublithospheric melt anomalies exist independently of the gravity lineations-generating process. Alternative models for the formation of volcanic chains in the southcentral Pacific are explored in section 6.

2. BACKGROUND

A recent multibeam survey (Gloria legs 3B-4) based on an older generation of Geosat/ERM altimetry revealed a set of prominent volcanic ridges which extend from the East Pacific Rise (EPR) for about 2600 km WNW to Pukapuka Island, a member of the Tuamotus (*Sandwell et. al.*, 1995). This triple-swath coverage, together with two additional multibeam transects (Westward legs 1, 4), comprise the vast majority of swath imaging of seafloor between the EPR and the Tuamotus. The Pukapuka system consists of 50 ridge segments, arranged both end-to-end and en echelon; it lies within a band 3000 km long and approximately 75 km wide. Major ridges consist of individual segments that are 40 km long, <10 km wide (though western edifices are nearly equant) with peak amplitudes from 800 m to over 4000 m; clusters of seamounts ranging in height from hundreds of meters to the limits of resolution are strewn throughout the survey area. These ridges do not show a clear hotspot-related age progression (*Sandwell et al.*, 1995).

The region of young seafloor west of the south EPR (SEPR) (figure 4.1) has been the focus of intense study due to a number of unique observations which include: a disputed (*Levitt and Sandwell*, 1996) 250-1000 m shallow depth anomaly covering the majority of French Polynesia and corresponding to a negative geoid anomaly (*McNutt and Judge*, 1990), elastic thicknesses beneath seamounts and islands typical of younger lithosphere (*McNutt and Menard*, 1978; *Calmant and Cazenave*, 1987; *Goodwillie and Watts*, 1993; *Filmer et al.*, 1993; *Goodwillie*, 1996), low seismic surface wave velocities (*Nishimura and Forsyth*, 1985), high spreading rates (*Minster and Jordan*, 1978; *DeMets et al.*, 1990) and a disproportionately large number of hotspot volcanic chains with unusually enriched and highly variable trace element and isotopic signatures (*Hart*, 1984; *Staudigel et al.*, 1991).

The discovery of short wavelength lineations in the altimeter gravity field with an amplitude of tens of mgal (figure 4.1) on the west flank of the SEPR aligned roughly parallel to the recent absolute-plate-motion direction (*Haxby and Weissel*, 1986) and with an anomalous low subsidence rate, prompted three principle hypotheses. The first proposed small-scale convection in low-viscosity asthenosphere (*Buck and Parmentier*, 1986; *McNutt and Fischer*, 1987), the second proposed that such lineations are the signature of numerous hotspots (*Fleitout and Moriceau*, 1992) and the third proposed that the lineations and volcanoes result from lithospheric stretching and boudinage (*Winterer and Sandwell*, 1987; *Sandwell et al.*, 1995).

Buck and Parmentier [1986] found that for an asthenosphere with a temperature- and pressure-dependent viscosity structure, small-scale convective cells can develop for young ages which grossly resemble the wavelength (150-250 km) and amplitude (8-20 x 10^{-5} m s^{-2}) of the altimeter gravity lineations, though the mechanism requires sublithospheric viscosities on the order of 10^{18} Pa, and freezing-in at young ages (<10 Ma). However, though the small-scale convection model predicts volcanism to occur over gravity and topography highs, where temperatures are higher, more than 95% of the volcanic volume attributed to the Pukapuka volcanic system is confined within a trough of the lineations (*Sandwell et al.*, 1995; figure 4.1). Also, it has been suggested that it is difficult to reconcile the orientation of lineations on seafloor older than 30 Ma with accepted absolute poles of rotation if the lineations are frozen at young ages (*Moriceau and Fleitout*, 1989).

The ages of dredge samples from the Pukapuka ridges (however sparse) provide the strongest evidence against a simple mini-hotspot model (*Fleitout and Moriceau*, 1992), requiring upwards of two semi-coaxial hotspots (*Sandwell et al.*, 1995). Allowing for a nearly arbitrary uncertainty on the order of 100 km in the location of the 0-18 Ma Pacific absolute pole of rotation (PAPR) does not improve matters significantly, as the projected location of the hotspot at 8.5 Ma is still more than 1000 km from the 8.5 Ma sample at Wahoo Guyot. The PAPR also does not explain the predominant east-west orientation of many altimeter gravity field lineations and volcanic ridge chains (as observed in the altimeter gravity field).

According to *Sandwell et al.* [1995] and *Winterer and Sandwell* [1987] lithospheric stretching-extension is least inconsistent with observations for the Pukapuka and Crossgrain ridges. The altimeter gravity lineations are the signature of lithospheric boudinage developing in response to extension of a non-linear strong layer above a weak asthenosphere and melt; the ridges reflect linear cracks/faults in the upper brittle crust, concentrated in thinner boudin troughs, which allow for the escape of melt from an independent partial melt reservoir. The surveyed sequence of Pukapuka ridges has previously been assigned to a single gravity trough (*Sandwell et al.*, 1995) suggesting, together with their highly elongated morphology, lithospheric stretching. The fine-scale resolution of the recent dataset reveals that the relation of the ridges to a single lineations trough is unclear between 123 ^{o}W and 128 ^{o}W (figure 4.1) and that the entire section of 0-40 Ma Pacific Plate seafloor south of the MFZ is characterized by abundant volcanism on a similar order as the Pukapuka ridges. Though the stretching model explains the wavelength of lineations and orientation of ridges, two potential problems are insufficient fracture zone separation (*Goodwillie and Parsons*, 1992) and a lack of extensional faults in the Pukapuka survey area (chapter 5).

It is clear that seafloor in the southcentral Pacific is characterized by pervasive volcanism, in excess of the 0.5% of crustal volume attributed to other Pacific provinces (*Jordan et. al.*, 1983; *Smith and Jordan*, 1987; *Smith and Jordan*, 1988; *Smith*, 1988; *Abers et al.*, 1988; *Bemis and Smith*, 1993; *Shen et al.*, 1993). Recent evidence from several swath bathymetry studies indicates that there is an unusually high concentration of seamounts and ridges in specific locations near the spreading axis (*Shen et al.*, 1993) and in bands extending west from the EPR axis. On the young flank of the EPR *Shen et al.* [1993] observe voluminous volcanism in the form of flows and seamounts accounting for up to 2% of the crustal volume. Thirty significant seamount chains are observed between 15 ^{o}S and 19 ^{o}S on 0-6 Ma crust comprising one of the densest populations of small volcanic structures in the world ocean. The abundance of seamounts in the Rano Rahi Field (especially between 17 ^{o}S and 19 ^{o}S) is 3-4 times that of comparable seamounts in a well-surveyed area near the north EPR.

There is evidence of increased volcanism on the Pacific Plate on this segment of the SEPR at the axis, which is the longest intra-transform span and where spreading is within 1% of the highest current

rates (*Demets et al.*, 1990). Elevation in Sr^{87}/Sr^{86} and He^{4}/He^{3} centered at 17.5 ^{o}S, suggesting off-axis plume input (*Mahoney et al.*, 1994), is associated with asymmetric spreading and subsidence (*Cochran*, 1986) and with fast axial propagation (*Cormier and Macdonald*, 1994); minor plate reorganizations may be common; though the magnetic anomaly sequence is seemingly continuous from the axis through anomaly 19 (*Levitt and Sandwell*, 1996), bathymetry and altimetry exhibit at least 2 propagating rifts (running NW at 127.8 ^{o}W, 16.8 ^{o}S and north at 133.5 ^{o}W, 15.5 ^{o}S; figure 4.1), and the abyssal hill fabric here and to the south (*Searle et al.*, 1995) manifests a complicated transition from ENE-WSW to WNW-ESE spreading unlike the simple tectonic history described by *Lonsdale* [1989].

3. SMALL CIRCLE FIT TEST

3.1 Bathymetry Data Processing

All Pukapuka survey multibeam data (Glor3bmv, Glor04mv, Rc2608, Tune02wt, West01mv and West04mv) are gridded using Mbsystem software (*Chayes and Caress*, 1993), with a 500 m grid-cell size where erroneous dredge-time data are edited with a 3 km/hour ship-speed minimum.

The goal of the bathymetry fitting experiment is to determine the best-fit small circle to a series of volcanoes represented in a multibeam bathymetry dataset. Bathymetric variation in the survey area can be attributed to long-wavelength subsidence with time and to short wavelength variation due to abyssal hill seafloor fabric in addition to constructive volcanism (*Levitt and Sandwell*, 1996). Since only the volcanic height is of interest, a method (figure 4.2) is devised to edit "non-volcanic" grid cells from the dataset (figure 4.3a) and translate bathymetry from presumed volcanic points to height above surrounding seafloor. The method consists of two steps: determine a grid corresponding to normal seafloor depth (figure 4.3b) then retain original grid cells proximate to volcanic peaks as height above seafloor (figure 4.3c).

First, normal seafloor depths (step 2; figure 4.3b) are estimated using the bin-modal method of *Levitt and Sandwell* [1995] where the bin width (50 m) and moving window width (12.5 km east-west, 50

km north-south) are chosen to reflect sensitivity to abyssal-hill seafloor depth variation (spacing of 10's of km and amplitude ~150 m). Second, similar to *Shen et al.* [1993], a small square window (3.5 km) is passed over the datasets. If the maximum difference between original and filtered (normal) seafloor grid cells is less than 250 m then the central cell is eliminated. Thus only grid cells proximate to a volcanic peak higher than 250 meter are retained. Finally, heights are determined for the remaining grid cells by subtracting the corresponding original and normal seafloor grid cells (figure 4.3c). A coarser grid (2 km spacing) is then input to the fitting algorithm for faster computation.

3.2 Bathymetry Small Circle Fitting

Approximately 15000 longitude-colatitude-height triplets are modeled by fitting them to a small circle. A curved line (i.e. a circle of unknown radius and origin) can be characterized by 3 parameters. Thus the misfit formula minimizes the difference between observed data and predicted values, in order to obtain a best-fitting set for 3 model parameters: the longitude, ξ_m, and colatitude, γ_m, of the best-fitting pole in the geographic coordinate system, and the angular distance between the pole and the curved line, θ_m (figure 4.4). A standard linear least-squares approach is not used as this is a non-linear parameter estimation problem and there may be local minima that do not correspond to the global minimum. The minimization algorithm uses the downhill simplex method (*Nelder and Mead*, 1965) implemented in Matlab (*Mathworks*, 1993) similar to *Levitt and Sandwell* [1995].

The penalty function is the minimum of the sum of the absolute difference in colatitude between the observation and the small circle in the fitting pole reference frame weighted by the height of the point above nearby seafloor:

$$\psi = \frac{\sum_{i=1}^{N} |\theta_i - \theta_m| \, z_i}{\sum_{i=1}^{N} z_i}, \qquad (1)$$

where N is the number of data points, z_i is the height of the observation, and θ_m and θ_i are the colatitude of the current model and the colatitude of the observation relative to the current model pole, respectively; θ_i is calculated by the coordinate transformation:

$$\theta_i = \cos^{-1}\{[\cos\ \mu_i\ \cos\ \gamma_m] + [\sin\ \mu_i\ \sin\ \gamma_m\ \cos(\lambda_i - \xi_m)]\}, \quad (2)$$

where μ_i and λ_i are the colatitude and longitude of the observations in the geographic reference frame. The L_1 norm misfit parameter, ψ, is the mean error, in degrees, between the observations and the best-fitting small circle. The L_1 norm is used rather than the L_2 norm so as to diminish the weight of outliers.

3.3 Bathymetry Fitting Results

Standard best-fit pole determination for the rotation of a plate over the hotspot reference frame is based both on the location and age of volcanic members of the hotspot chain (*Gripp and Gordon*, 1990; *Fleitout and Moriceau*, 1992). The present test of small circle fit — whether the Pukapuka chain is restricted to a particular curved line — lacks the additional age constraint. Therefor, the significance of the proposed fit to a 3-parameter model should be considered with skepticism. The results below justify great confidence.

The best-fit parameter set for the model is: ξ_m = -73.7 ^{o} and γ_m = 8.5 ^{o}, for the northern hemisphere pole, and θ_m = 101.0 ^{o} for the small circle colatitude about this pole (figures 4.4, 4.5). The best-fit pole is located near the geographic pole and the best-fit small circle lies south of its equator (a great-circle; angular distance, θ_m, is 90 ^{o}). With one notable exception, minimization runs for varying initial parameter sets resulted in the same best-fit parameter set choice within precision limits (or the equivalent southern hemisphere location of the pole); if the initial parameter set was close (within 500 km) to the "correct" value then a nearby pole, a local minimum, would be selected.

One of the remarkable characteristics of the Pukapuka chain is that it represents essentially continuous volcanism in a narrow 75 km-wide band for over 2600 km. This extreme linearity, shown here

to closely follow a small circle (figures 4.5, 4.6), is reflected in the small misfit for the optimal parameter set (mean absolute error = 0.16 ^{o}) and the relative insensitivity to the location of individual edifices and grid cell dimension. A histogram of the absolute misfit (figure 4.6b) shows that more than 80% of the data are located within 0.3 ^{o} of the optimal small circle, on the order of the cross-track widths of the volcanoes themselves. A primary concern in interpretation of this close fit is that seagoing reconnaissance is limited to be proximate to features in the survey plan. However, surveying of volcanoes attributed to the Pukapuka chain was constrained mainly by the location of anomalous highs in the satellite altimetry dataset and preliminary single-beam acoustic transects, not by transit practicalities. Furthermore, volcanic volume falls rapidly with distance even within the main survey line, as very little volcanic volume is observed in eight excursions (*Sandwell et al.*, 1995). Finally, the altimeter gravity dataset shows no unsurveyed anomalies within 100 km of the optimal small circle (see below). Therefor it is not surprising that the location of the best-fitting pole did not vary significantly with increased grid-cell dimension (i.e. reduced data-set size) until 50 km, when only 154 values were input to the minimization scheme. The large equant volcanoes in the west fall to the north of the optimal small circle, taking on a northwesterly trend if only for 200 km; still, results did not vary with the elimination of all data west of 138 ^{o}W. Thus the location of this best-fit pole of rotation is not sensitive, in a gross sense, to the input grid-cell dimension, to the initial simplex parameter set, or to a few individual edifices.

A measure of the pole location confidence is provided by the increase in mean absolute error with distance from the best-fit pole (figure 4.5). The error ellipses are highly elongated orthogonal to the Pukapuka ridge azimuth; along this line error is easily accommodated by an adjustment in the small circle colatitude about the pole; poles located off of the bisector (such as the 0-18 Ma PAPR) have larger error because their resultant small circles cross the ridges at an angle. Interestingly, the pole corresponding to a great circle fit (i.e. an equator about a pole) is not significantly larger in error than the best-fit small circle pole. The choice of the definitive error-ellipse about the pole is somewhat arbitrary but commonly-accepted PAPR's (e.g. *Morgan*, 1972a,b; *Clague and Jarrard*, 1973; *Duncan*, 1981; *Minster et al.*, 1974; *Minster and Jordan*, 1978; *Duncan and Clague*, 1985; *Lonsdale*, 1988; *Fleitout and Moriceau*, 1992) are

clearly rejected (figure 4.5). Based on this test, it appears either that a proposed Pukapuka hotspot follows a different pole from the standard absolute Pacific-hotspot poles (i.e. hotspots are not fixed with reference to the Pacific Plate), that the standard pole locations are significantly incorrect, or that the Pukapuka volcanic system melting anomaly cannot be attributed to mini-hotspots. A test rejecting the fixed hotspot hypothesis is not necessarily a rejection of the hotspot hypothesis in general, as motion has been reported between major, well-established hotspots across plate boundaries (*Molnar and Stock*, 1987). Nevertheless, because Pukapuka dredge samples do not exhibit monotonic age progressions (*Sandwell et al.*, 1995) or OIB geochemical signatures (*MacDougall et al.*, 1994) the classic hotspot hypothesis affords minor testable predictive value for this volcanic system.

Finally, the best-fitting parameters should not be taken literally — volcanic volume above seafloor is the best available proxy for the magma source below, but clearly substantial volumes may be frozen in the lithosphere during ascent in addition to a large proportion of surficial volcanic flow which is observed to accompany seamounts nearby (*Shen et al.*, 1993). Nevertheless, the overall conclusion regarding a remarkable fit to a pole distinct from the PAPR is likely to be insensitive to such misrepresentation. Most importantly, the overall orientation of the Pukapuka ridges is inconsistent with any end-to-end arrangement of fixed hotspots (based on standard 0-18 Ma Pacific absolute poles of rotation) regardless of age progression, unless all such poles are grossly incorrect.

4. VOLCANO TOPOGRAPHY-GRAVITY AND LINEATIONS TEST

The present section rigorously tests whether volcanoes in the region, mapped in the altimeter gravity field, are preferably located in the crests or troughs of gravity lineations. First, a method is developed to isolate the gravity signal attributed to volcanoes from the residual, "background" field. Second, the relation between volcanic volume and gravity signal is assessed with respect to the well-surveyed Pukapuka volcanoes in order to examine the validity of using gravity as a proxy for volcanic construction. Finally, the mean gravity signal for a given basal depth is estimated in order to test whether

gravity features interpreted to be volcanic edifices are preferentially concentrated in troughs or crests of altimeter gravity undulations.

The first goal of the altimeter gravity processing is to separate the signal attributed to volcanoes from the background field. A straightforward method is developed (figure 4.7) which locates and estimates the volcano-related gravity signal without bias. The second goal is to calculate another grid which represents the volcanoless base values, replacing grid cells from volcanoes with the estimated local background value. Bias due to long-wavelength gravity trend is removed prior to data analysis. Depression of the base altimeter gravity field due to the flexural response of lithosphere to edifice loading is more difficult to estimate and remove; the relative importance of this potential bias source is discussed.

4.1 Altimeter Gravity Processing

Altimeter gravity anomaly data is acquired following the method of *Sandwell and Smith* [1995] and *Sandwell and Smith* [1996]. A portion of the global grid extending over an area slightly larger than the intended study area is detrended from a planar surface (step 2; figure 4.8) using the GMT public-domain software package (*Wessel and Smith*, 1991) in order to diminish trend-related inaccuracy in subsequent processing. Detrended data processing (steps 3-5) is designed to identify and resolve between the two following types of features: first, volcanic edifices, which are positive, of a wavelength shorter than ~50 km and of high spatial gradient; second, smooth gravity lineations with a wavelength greater than ~100 km.

The detrended altimeter gravity grid is subtracted from a modal lowpass filtered grid (step 3) where only points with a proximate (within 20 km) gravity peak value (12 mgal above the local mode) are retained (step 4). However, the lowpass filtering method for altimeter gravity differs from that implemented for bathymetry above because the very high frequency bathymetry component ($\lambda < 1$ km) is damped in corresponding altimeter gravity; thus, in contrast to the bathymetry dataset, there are no sharp boundaries in the distribution of values (*Levitt and Sandwell*, 1996). Therefor, rather than picking a modal bin, the analytical mode (figure 4.8b) is calculated for a 0.75^{o} square window with the GMT application

grdfilter (step 3; *Wessel and Smith*, 1991). Values of 20 km and 12 mgal are chosen for the search window reflecting the minimum radius and gravity amplitude of retained constructive features. These parameter choices, based on a comparison of survey bathymetry and altimeter gravity maps, are conservative; as the cutoff is reduced below 12 mgal extraneous non-volcano features are progressively retained within the Pukapuka survey area. The "volcano-only" grid shows that there are nearly no unsurveyed large ridges near the Pukapuka system (step 5; figure 4.8c) confirming results in section 3.

The "volcano-only" grid is subtracted from the detrended grid (step 5). It is important to note that, for most of the volcanoes, the subtraction results in seamless transition between the subtracted volcano base and nearby gravity values; this reflects the robust estimation of volcano-mass-related gravity signal. For large volcanoes the post-volcano-subtraction base values are slightly positively biased. A thin gravity trough is observable surrounding the largest subtracted edifices (e.g. ridges centered at 116 ^{O}W, 13.7 ^{O}S; 130 ^{O}W, 21 ^{O}S, 119 ^{O}W, 16 ^{O}S; 124.5 ^{O}W, 18.2 ^{O}S) because a mode was utilized in the volcano-signal estimation scheme rather than the minimum value, which would have corresponded instead to the deepest part of the local flexural trough (figure 4.9). Therefore, this grid is expected to represent the gravity field without volcanoes, which are essentially replaced with the local-background-representing modal value; flexural signatures attributed to the lithospheric response to loading is retained near the ridge, but to a much lesser extent directly at edifice locations.

The section of the altimeter gravity grid assessed in the analysis (133 ^{O}W-114 ^{O}W, 22.5 ^{O}S-11 ^{O}S) is high-pass frequency filtered (ramp, total pass below 700 km, total cut above 900 km wavelength) in order to minimize any regional trend (step 6; figure 4.8d). A two column dataset is input to the analysis in section 4.3 consisting of base value and "volcano" amplitude value pairs for each grid cell in the study area.

4.2 Pukapuka Topography versus Altimeter Gravity Signal

The "volcano-only" grid is used along with the multibeam-bathymetry signature of the Pukapuka volcanic system to determine the minimum edifice height and volume that can be detected in the altimeter-

derived gravity. Identical sections of the volcano-only gravity and topography grids were extracted corresponding to the location of ridge segments, seamounts and atolls (volcanic features). For each feature, three relevant parameters are calculated from topography and altimeter gravity; topography parameters are the maximum height, mean height and total volume; altimeter gravity parameters are maximum and mean gravity and the mean anomaly times the number of grid cells (here termed altimeter gravity "volume").

Essentially, the mode-base and edifice-search scheme is a highly effective, simple and automatic method of recovering the gravitational signal attributed to constructive features in a satellite altimeter gravity anomaly grid. Figure 4.10a-c shows the relation between corresponding gravity and bathymetry parameters. Out of 94 edifices selected from the bathymetry, 73 were also selected in the gravity. The gravity signal identification threshold is about 1 km peak topographic height (approximately equivalent to 300 m mean height or 75 km^3 volume). Above the threshold a nearly linear relation is observed and the values are highly correlated. Still, the gravity field at sea surface is the resultant of several superposed factors including bottom topography and subsurface density variations. Because topography is compensated and partially supported by variably thick lithosphere the gravitational signal amplitude attributed to a particular topographic feature is a function of lithospheric thickness (and therefor age) at feature emplacement time (*Watts et al.*, 1980). Furthermore gravity measurements based on seasurface altimetry is the upward continued signal from the seafloor below. For example, the gravity/bathymetry ratio is somewhat higher than the average value for the largest structures (figure 4.10) probably because they are closer to the sea surface. Therefor the topography-gravity relation is not expected to be linear.

Nevertheless, it is now possible to semi-automatically identify and grossly-quantify the majority of large volcanoes in the ocean basins and to redefine constraints on the processes which control their emplacement and development (*Craig and Sandwell*, 1988; *Smith*, 1990). More accurate altimeter-gravity-based topography parameter estimates could be obtained if the seafloor depth is known. These results are obtained on young seafloor for edifices which are nearly compensated (*Goodwillie*, 1996); on more competent lithosphere, more of the gravity signal should be recoverable. Conversely, sedimentary obstruction might be an important factor on older seafloor. Most importantly, the close relation between

topography and gravity suggests that it is appropriate to assume in the following analysis that the above-local-base, high-frequency, positive features are a proxy for volcanic production, though other processes may be responsible for positive features in unsurveyed areas.

4.3 Volcanoes-lineations Analysis

The principal prediction of the moving point source (hotspot) and convective line (small-scale convection) hypotheses is a correlation of volcanism with topographic/gravitational bulges; stretching models and models involving interactions with zones of weakness predict volcanics in gravity troughs. A cursory examination of the altimeter gravity anomaly field on young (0-40 Ma) Pacific seafloor just south of the MFZ shows that the majority of small volcanic chains are associated with altimeter gravity troughs (figure 4.1). The goal of the analysis is to quantitatively assess preferential location of volcanic edifices in undulation troughs or crests, low and high base values, respectively. The test involves the variation of mean volcanic gravity signal with respect to the base gravity values (here termed base values). Figure 4.11a is the total sum of volcano-derived gravity signal in mgal corresponding to points within a particular 1-mgal-wide base value interval. Figure 4.11b is a histogram of gravity base values. For example, of the total number of base values (196650), ~2000 base values are between -10 and -9 mgal. The total sum of volcano-only gravity values corresponding to base values in this interval is ~4000 mgal. Figure 4.11c is the mean volcanic gravity for all 1-mgal-wide base value intervals (figure 4.11a data divided by figure 4.11b data). In the example, over the -10 to -9 mgal base range the mean volcanic signal amplitude is 1.8 mgal.

The distribution of base values is smooth, gaussian, non-skewed and centered at 0 mgal (figure 4.11b). In comparison, the volcanics-at-base-interval signal is rough and skewed to negative values (figure 4.11a). While the majority of volcanism is still associated with the center of the base value distribution, clearly volcanism is preferentially located in the negative tail; over 2/3 of the volcanic signal is present in the lower half of the base distribution (figure 4.11c). Interestingly, if the minimum volcano retention height is increased from 12 to 18 mgal (step 4), the disparity is even greater (figure 4.11d-f); over 90% of

the volcanic gravity signal is located in the lower half of the base value distribution (figure 4.11d). This demonstrates that while the general volcanic population is preferentially located in regions of low base values (such as altimeter gravity troughs), this is principally due to large volcanoes which are nearly all located in lows, while small volcanoes are distributed almost evenly with respect to the base. These results are fairly insensitive to the 800 km high-pass filter (results without filtering are not shown), first because the long wavelength variation within the study area (a few mgal) is much less than the crest-trough peak difference (~20 mgal) and second because there are no substantial regional trends in volcanic productivity.

Because the flexural depression of lithosphere in response to constructive emplacement is generally a function of load mass and lithosphere strength (and age) at the time of loading (*Watts et al.*, 1980), a primary concern is that base gravity values at edifice locations are negatively biased due to flexural compensation, erroneously indicating volcano concentration in lineation troughs. With the exception of the Pukapuka system, large volcanic structures in the region are unsurveyed; of these, only six have reliable age dates. Thus proper age-modeled unloading correction is not possible for the vast majority of volcanoes.

A simple compensation study (not shown) of 1500-3000 m cones located 4000 m below the sea surface indicates that flexural troughs should be less than 10 mgal for thin (3 km) elastic plates. As well, a Pukapuka flexural study (*Goodwillie*, 1996) showed that structures are compensated by anomalously very thin lithosphere so that flexural troughs are localized near and beneath the edifices. Therefore, flexural troughs in the region may be 5-10 mgal. Mode filtering, the processing step which essentially determines the base value, estimates a mode over an area (75^{o} square ~ 6500 km^2) which is on the order of the flexural trough. Still, the mode corresponds to the regional value which is significantly higher than the minimum of the flexural trough (compare basal values in figure 4.9d from volcano locations and nearby basal values). In the example area shown (figure 4.9d), the mode base value estimated beneath the ridge at 128.6 ^{o}W, 121.3 ^{o}S is higher than the base value 100 km to the east, where the flexural response is negligible as there are no volcanic loads. Also, in the case of the 18-mgal volcano dataset the required flexural bias would have to be high (7 mgal) in order to account for the results. Most importantly, these results are consistent

with a visual assessment of the altimeter gravity anomaly field in the region (compare figure 4.8c and 4.8d) which clearly shows that the majority of volcanoes are associated with long altimeter gravity troughs which extend past the features.

5. SOUTHCENTRAL PACIFIC ALTIMETER GRAVITY ANOMALY FIELD — COMPLEX TECTONICS AND ABUNDANT VOLCANISM

5.1 Volcanism

The southcentral Pacific altimeter gravity anomaly field (figure 4.1) exhibits a wide range of well studied volcanic and tectonic features including: volcanic chains and ridges, fracture zones and plateaus. *McNutt and Fischer* [1987] and *McNutt and Judge* [1990] advanced the superswell hypothesis noting the dramatic increase in the number of large, hotspot-attributed volcanic chains south of the MFZ on seafloor older than the Pukapuka ridges. The spatial distribution of such chains is not uniform. Clearly volcanic chains are focused near each other, even for chains attributed to different periods in time. This results in an overall pattern of patches of interlaced volcanic chains separated by nearly volcanoless regions.

Though smoothly undulating gravity lineations are evident throughout the region (though obscured by multiply overprinting volcanic chains; figure 4.1) a great variation in fine-scale roughness, attributed to volcanic features, is observed in subregions of the map. In particular, for 0-40 Ma seafloor, roughness is drastically greater south of the MFZ than to the north. In addition to the near absence of spreading semi-parallel lineations (i.e. propagating rifts), a volcano-search performed on the section of seafloor north of the MFZ (not shown) reveals no volcanic features which are nearly ubiquitous between the MFZ and the Foundation Seamounts.

The sharp distinction between seafloor sections directly north and south of the MFZ has been described by *Bemis and Smith* [1993], noting a threefold increase in seamount density to the south, and has been previously attributed to the Superswell. Sediment thicknesses north and south of the MFZ are 100-

300 m and 50 m respectively. *Bird and Pockalny* [1994] find that seafloor roughness is diminished by 50% with an increase in sediment thickness of 50 m to 300 m for abyssal hill fabric with a root-mean-square roughness which is generally less than 300 m. Therefor, the present observations of regional differences in volcanic edifice density are not a function of sediment obscuration, because the altimeter gravity database is insensitive to features smaller than several hundred meters, the range of typical sediment thickness and abyssal hill scarp heights in both regions.

5.2 Propagating Rifts and Asymmetric Spreading

Tectonic history is clearly complex on this section of the EPR in accord with observations for perturbed transition from ENE-WSW to WNW-ESE along the central portion of the Pitcairn-Crough-Easter Microplate section further south (*Searle et al.*, 1995). Spreading has been asymmetric for the last few million years (faster to east). In addition to all constructive features greater than 75 km^3, the high-resolution dataset reveals tectonic detail which has been studied only recently in the altimeter gravity anomaly field. Perhaps the most intriguing observation at the finest scale of resolution, is the ubiquity of very narrow linear gravity troughs, interpreted as propagating rifts (figures 4.1, 4.8a; *Hey et al.*, 1980; *Sandwell and Phipps Morgan*, 1994). Nearly straight segments extend through a range of inclinations to the paleo-spreading axis-parallel directions. Propagators range in signature from clear troughs to feint lineation patterns. In the multibeam surveys they appear as rather pronounced abyssal fabric, with orientations angled to the local abyssal pattern. All together, the section of young Pacific Plate south of the MFZ is dramatically different from seafloor to the north and on the conjugate section of the Nazca Plate (not shown); tectonic history is complex and volcanism is pervasive.

6. DISCUSSION

6.1 Volcanic Chains and Altimeter Gravity Lineations in the Southcentral Pacific

The relation of altimeter gravity lineations to volcanism and tectonism remains unclear (figure 4.1). First, there is no obvious correlation between smooth undulating lineations and the location and orientation of fracture zones. Locally, the overall azimuth of the Pukapuka ridges is ~N95 ^{o}W while the nearby lineations azimuth is ~N105 ^{o}W. While volcanic features in the young section are preferentially located in altimeter gravity lineation troughs the majority of troughs still lack volcanism. Second, there are lineations north and south of the MFZ. However, these areas may be characterized by completely different thermal and rheological properties; in addition to the proximity of many hotspot chains, the concentration of volcanoes larger than 75 km^3 south of the MFZ and seafloor spreading irregularities clearly argue in favor of augmented volcanic and complex tectonic activity there. Elsewhere in the southcentral Pacific there is little correspondence between the location and azimuth of volcanic chains and nearby lineations (aside from the flexural trough generated by the volcanic load itself). This indicates that sublithospheric melt sources exist independently of the process which produces altimeter gravity lineations.

6.2 Volcanic Chains in the Southcentral Pacific — Evidence of Transient Melt Anomalies and Channeling

The number of confirmed hotspots and their relative fixity is a subject of much controversy; only two hotspot sequences have been used to establish the PAPR over the past 60 Ma, Hawaii-Emperor and Louisville (*Lonsdale*, 1988), but up to 20 additional volcanic chains have monotonically increasing age sequences in variable agreement with the prediction. Still, the number of volcanic features in the Pacific (*Smith and Jordan*, 1988; *Craig and Sandwell*, 1988) exceeds the number which may be attributed to "known" hotspots by at least an order of magnitude. Also, a number of theoretical and empirical problems with the strict hotspot model have arisen (*Okal and Batiza*, 1987). For example, it is difficult to reconcile

the fixed plume hypothesis with a mantle which is convecting on various scales and with mantle-lithosphere coupling. Furthermore, plume dynamic models and laboratory simulations suggest that hotspot plumes spread upon impinging on the base of the lithosphere (*Campbell et al.*, 1989; *Sleep*, 1990; *Ribe and Christensen*, 1994).

The classic *fixed* hotspot hypothesis, in which several deep-mantle melting anomalies were fixed relative to each other, has been tested rather extensively. In particular, samples ages along chains have been compared with monotonic age progressions predicted by accepted hotspots elsewhere. Nearly all volcanic chains in the southcentral Pacific have failed to exhibit monotonic age trends, including the Cook-Australs, the Tuamotus, the Line Islands and the Oeno-Crough volcanic line. The Cook-Austral chain cannot be reasonably fit by a single fixed hotspot (*Turner and Jarrard*, 1982); instead, the majority of features belonging to the chain can be geometrically fit by three semi-parallel small point-source tracks corresponding to the 0-18 Ma PARP, with small circle colatitudes of 106.7 ^{o}, 109.3 ^{o} and 109.6 ^{o}. The Tuamotus Plateau, composed of reef-covered atolls, has been attributed to two hotspots (*Okal and Cazenave*, 1985; *Ito et al.*, 1995). Though seismic, paleontologic and radiometric evidence suggest that the northwest section formed 47-55 Ma (*Schlanger et al.*, 1984), the small-scale alignment directions are more east-west. Plateau compensation studies indicate low elastic thicknesses. *Ito et al.* [1995] consider the plateau structure to be highly influenced by proximity to the Farallon-Pacific spreading center and a lithosphere transfer zone west of a southward propagating segment. Essentially 2-3 hotspots interact with the nearby-rise axis by channeling, generating linear volcanic ridges atop less competent scarred lithosphere. The altimeter gravity field reveals many crisscrossing pinnacle alignments. The Tuamotus plateau may thus be composed of several small and possibly highly transient hotspots which are sensitive to lithospheric structural heterogeneity. Non-monotonic age progression of Line Islands Cretaceous to Oligocene edifices defy a simple single-hotspot model (*Henderson and Gordon*, 1982; *Duncan*, 1983; *Schlanger et al.*, 1984; *Epp*, 1984). The superposition of ESE striking lineations of overly young volcanoes on the overall SSE trend has suggested that either an older hotspot thinned and weakened the lithosphere such that it was more penetrable for subsequent small hotspots with a more east-west azimuth or that the

latter trend is related to channeling to a nearby spreading ridge (*Epp*, 1984). Finally, the Oeno-Crough volcanic line (figure 4.1, ~25 ^{O}S) surveyed in detail by *Searle et al.* [1995] and associated with complex age progressions, follows a near east-west azimuth corresponding to the best-fit pole for the Pukapuka ridges, not the 0-18 Ma PAPR of *Fleitout and Moriceau* [1992].

Over the past 15 years, investigations of volcanic groups has focused on processes which alter the expected orientations and age relations of a reported hotspot track, principally due to lithospheric lines of weakness and to the interaction of plume sources and the mid-ocean-rise melt reservoir. *Epp* [1984] investigated observed and hypothetical potential causes of perturbation and the consequent volcanic trace geometries. *Morgan* [1978] proposed that magma may flow along a pipeline from a hotspot located near a spreading axis to the axis itself, thus generating a "second type" of hotspot chain (in association with the Galapagos, Reunion and other hotspots) with an azimuth that is the vector sum of plate-hotspot and plate-plate motion. *Sager and Pringle* [1987] proposed a tectonic model which explains the age progression and ridge orientations of the Musician Seamounts and which requires two necessary ingredients, a nearby hotspot and a spreading boundary reorganizing with long interlocking fingers such that magma is localized along lines of weakness within a salient segment of the ancient Farallon Plate between Pacific sections. The concept of hot-lines, originally proposed for Easter-Salas y Gomez (*Bonatti and Harrison*, 1976; *Bonatti et al.*, 1977), has also been invoked to explain the confused age relations in the Oeno-Crough volcanic line (*Searle et al.*, 1995), with a complex interaction between convective roles, plume sources and lithospheric tension on a section of the Pacific Plate overlying the Superswell.

Recently, additional impetus for plume-rise interaction has come from mounting indirect evidence (seismic, geoid and geochemical) for a mantle asthenosphere which facilitates the communication process (*Phipps Morgan et al.*, 1995). Along-isochron variation of residual Mantle Bouger Anomalies (ΔMBA) and residual bathymetry (ΔRB) with distance between a spreading axis and a hotspot exhibit a hotspot influence on nearby spreading systems upto a distance of ~500 km (*Ito and Lin*, 1995). Along-axis gradients in the strength of the hotspot-marking Ocean Island Basalt (OIB) geochemical signature indicates a supply of hotspot material to the rise-axis Mid Ocean Ridge Basalt (MORB) reservoir (*Schilling*, 1991). Hotspot

influence may extend to disturbing thermal regimes beneath spreading centers; plume excess temperatures weaken the lithosphere and the rise axis relocates toward the hotspot by asymmetric spreading and discrete ridge jumps (*Small*, 1995).

Taken together, it is increasingly apparent that an alternative to the hotspot model is required, especially in the southcentral Pacific. The present results suggest that many transient point-source melting anomalies beneath the lithosphere are responsible for linear volcanic chains; additional hypotheses (see below), perturbations to a trace along lines of weakness attributed to previous hotspot traces and tectonic deformation may be required to explain details of the spatial-age distribution. Ad hoc perturbations should be tested carefully subsequently, but it is clear that most of the volcanoes in the southcentral Pacific exhibit monotonic age progressions over only short distances which can be reasonably attributed to intermittent, short-lived sources of melt.

6.3 A New Model

Observations of the Pukapuka ridges and other volcanic chains in relation to the altimeter gravity anomaly field are inconsistent with standard hotspot (*Morgan*, 1972a,b) and small-scale convection (*Buck and Parmentier*, 1986) models. These volcanic chains are logically attributed to a less-robust reservoir than deep-mantle plumes. For example, the Pukapuka dredge samples exhibit normal and enriched MORB geochemical signatures, not OIB (*MacDougall et al.* 1994). Such traces are sensitive to the location of lines of weakness in the lithosphere attributed to several different processes: older volcanic traces, fracture zones and zones of deformation. Robust volcanism in this region, both attributed to hotspots and not suggest that melt is abundantly available beneath the lithosphere and that the young lithosphere is in general quite penetrable.

The Pukapuka melt source is not clear at the present time; possibly melt is channeled in the astenosphere (*Phipps Morgan et al.*, 1995), supplied by hotspot plumes to the west from old thick lithosphere up and towards thinner lithosphere at the EPR spreading axis (*Ribe and Christensen*, 1994).

This may account for the close linearity of the Pukapuka system and axial Sr^{87}/Sr^{86} and He^{4}/He^{3} elevation centered at 17.5 ^{o}S, which are attributed to off-axis plume input (*Mahoney et al.*, 1994). A few small sublithospheric melting anomalies (mini-hotspots) may reside beneath the young Pacific Plate moving nearly opposite to the relative spreading direction and producing end-to-end ridges; one such mini-hotspot may have migrated close to the EPR axis, producing a high concentration of seamounts on 0-6 Ma seafloor (*Shen et al.*, 1993), where absence of ridge formation may coincide with the cessation of tensional stress (see below). The Musicians Seamounts may present a Cretaceous analog, where hotspot-spreading axis interaction may have occurred in response to tectonic reorganization, except that there, the easternmost chain of seamounts record the absolute motion of the Pacific Plate oblique to the spreading direction (*Pringle*, 1993) and elongate ridges extend en echelon to the axis on young seafloor which has undergone a recent spreading reorganization (*Sager and Pringle*, 1987). Alternatively, the complicated tectonic history characterized by propagating-rift scarred seafloor, asymmetric spreading and ultrafast axial discontinuity migration (*Cormier and Macdonald*, 1994) may indicate melt extraction from a rise-axis source. With this hypothesis, a melt-rich decompressing layer may refreeze into the mantle or pool and then erupt off-axis (*Sparks and Parmentier*, 1994).

The concentration of volcanism in altimeter gravity lineations troughs, inferred to be sites of thinner, weaker lithosphere (*Sandwell et al.*, 1995), and their individual elongation orientation (see chapter 5) are consistent with lithospheric tension. Ordinary lithosphere may be resistant to penetration even at young ages. However, Pukapuka ridge flexural modeling suggests that lithosphere is overly thin and weak (*Goodwillie*, 1996). Though normal faulting has not been observed and melt is not likely to be generated by extension, it may be possible that lithospheric tension has persisted from the time of the Pacific-Nazca spreading reorganization at 24 Ma to 6 Ma. In this case lithosphere is weaker and more susceptible to penetration. If boudins develop lithospheric strength in tension may be nearly zero in the troughs so that a buoyant melt crack may easily propagate to the seafloor where volcanic construction is observed.

7. CONCLUSIONS

1) Volcanism attributed to the Pukapuka ridge system is closely focused in a narrow band. Volcanic edifices line-up tightly about a small circle best-fit with a rotation pole that is distinct from standard 0-18 Ma Pacific absolute poles of rotation. These results are insensitive to processing and multibeam surveying has recovered nearly all volcanism in the system. Therefor, in addition to age progression constraints, they are inconsistent with a single or even several coaligned hotspots. Instead, they suggest that an alternative mechanism is required, perhaps asthenospheric channeling.

2) A method was developed to isolate the gravity anomaly signal attributed to constructive features (presumably volcanoes) from the satellite altimeter gravity anomaly field. A comparison of Pukapuka bathymetry and altimeter gravity showed close correlation for corresponding diagnostic parameters (such as maximum height, mean height and volume). Satellite altimeter gravity may be used for locating and quantifying volcanic edifices larger than 75 km^3 in unsurveyed regions of the world ocean.

3) Altimeter gravity signal attributed to volcanism is focused in the troughs of gravity lineations. These results are not produced by flexural depression due to volcano loading. Mechanisms which attribute volcanism to upward flux of hot, potentially melt-generating, mantle (hotspots and small-scale convection) predict volcanism in gravity lineation crests. If lineation troughs correspond to lithospheric zones of tension and weakness, then they may be more easily penetrated by sub-lithospheric pools of melt.

4) The section of Pacific seafloor south of the MFZ is characterized by much greater volcanism than the northern section, though altimeter gravity anomaly lineations exist in both. Also, many nearly north-south lineaments, interpreted as propagating rifts, are present only south of the MFZ in association with asymmetric spreading. The two lithospheric seafloor sections bordered by the MFZ differ and melting anomalies south of the MFZ exist independently of the process responsible for altimetric gravity lineations.

5) There is minimal evidence for small-scale convection in the southcentral Pacific. Also, many volcanic chains in the region are inconsistent with the hotspot model, with non-monotonic age progressions and orientation oblique to the *fixed* hotspot prediction. This has suggested small melt anomaly interaction

with lithospheric zones of weakness and sublithospheric channeling. Perhaps the abundance of small volcanoes on the young flank of the superfast segment of the SEPR can be attributed to the interaction of many small melting anomalies and zones of easy penetration within young lithosphere, caused by the reorientation of spreading directions and the initiation of extension and boudinage.

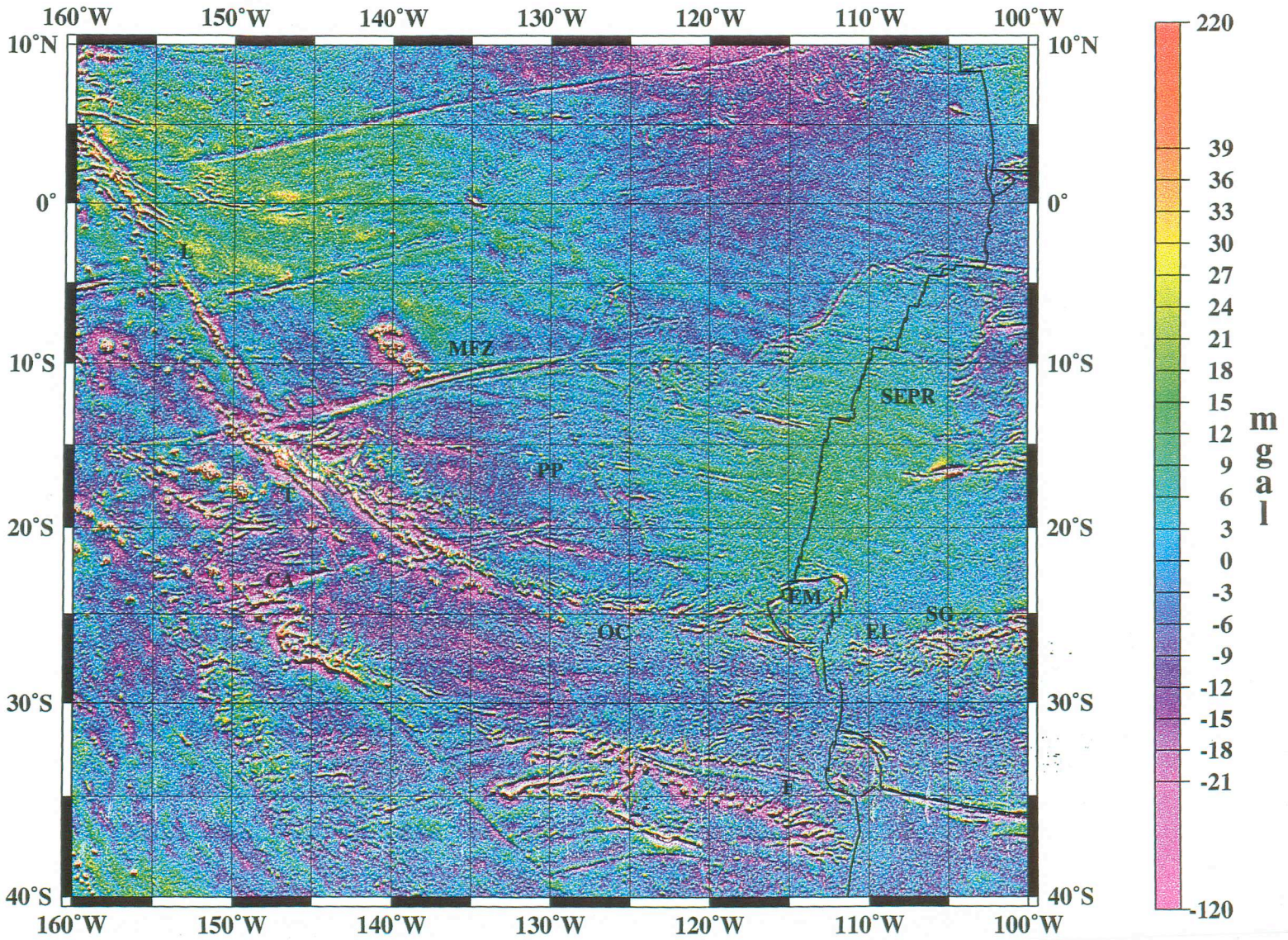
160°W
150°W
140°W
130°W
120°W
110°W
100°W
10°N
0°
10°S
20°S
30°S
40°S
MFZ
SEPR
PP
OC
EM
EI
SG
mgal
220
39
36
33
30
27
24
21
18
15
12
9
6
3
0
-3
-6
-9
-12
-15
-18
-21
-120

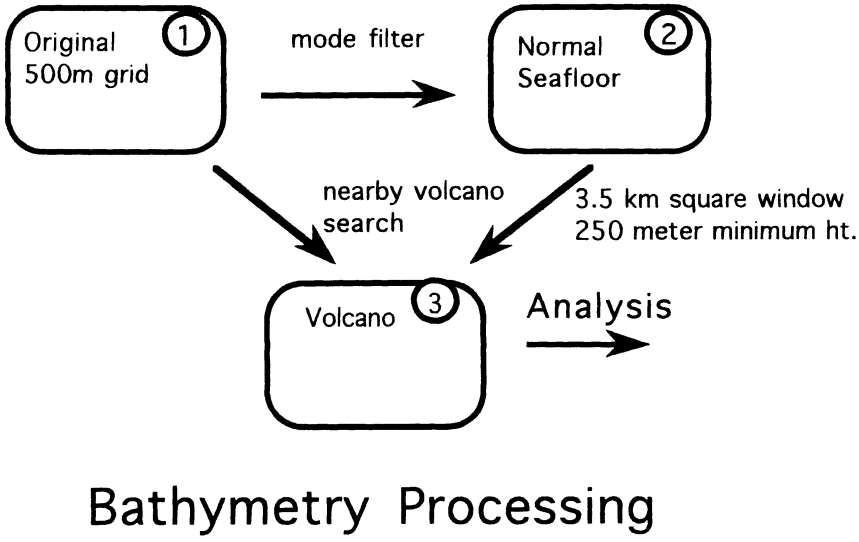

Figure 4.2 A flow chart of processing of multibeam bathymetric data from Glor3bmv, Glor04mv, West01mv, West04mv, Rc2608 and Tune02wt, corresponding to the Pukapuka ridges. Normal (modal) seafloor data are acquired using a tallest-bin Matlab searching algorithm similar to *Levitt and Sandwell* [1996]. Volcano data are retained and calculated using the proximate peak Matlab (250 m height minimum) algorithm described in the text. These data are input to the small circle fitting algorithm.

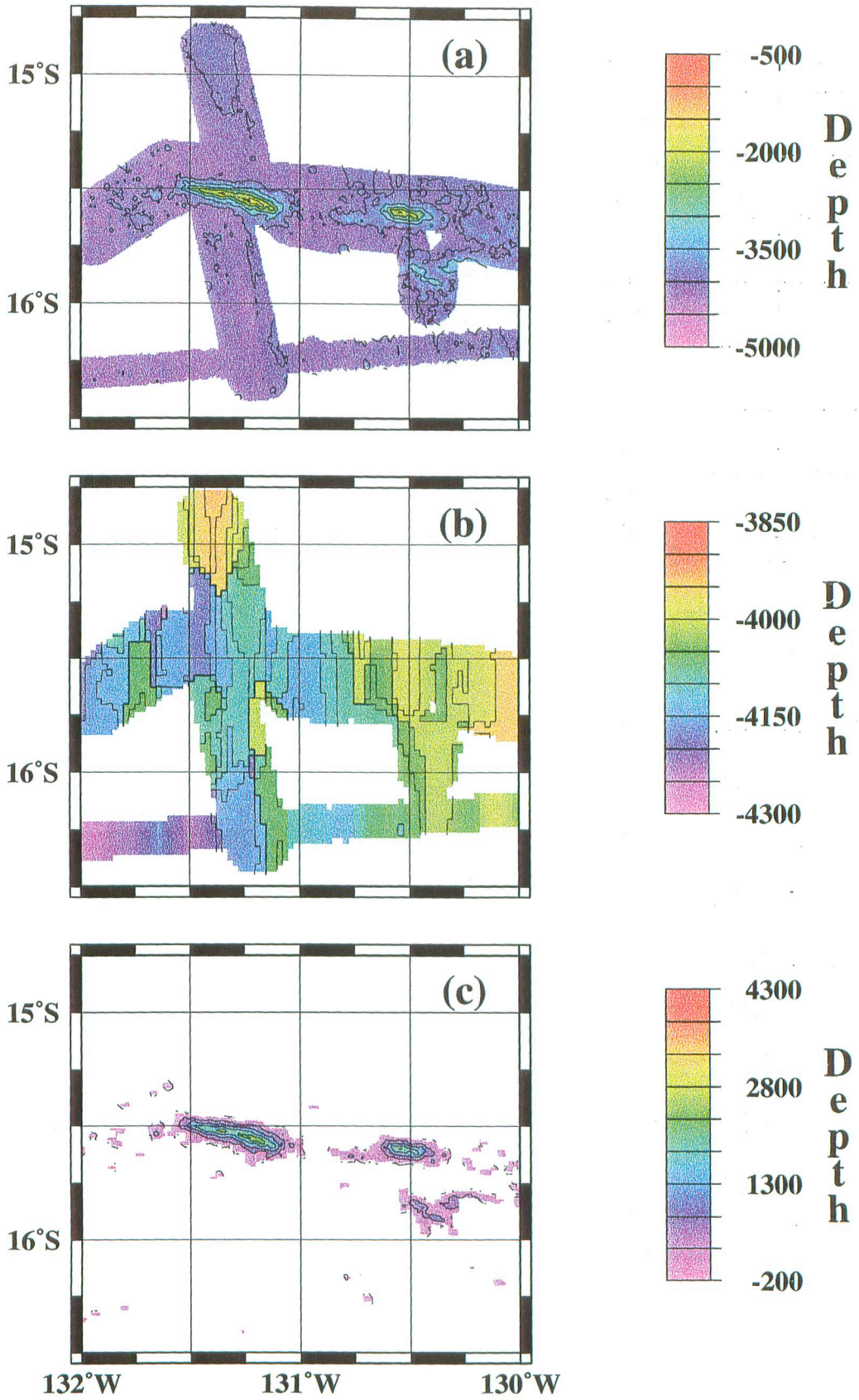
(a)
15°S
16°S
-500
-2000
-3500
-5000
Depth
(b)
15°S
16°S
-3850
-4000
-4150
-4300
Depth
(c)
15°S
16°S
4300
2800
1300
-200
Depth
132°W
131°W
130°W

Figure 4.4 Model parameters for the small circle fitting. Points near P are the actual locations of data. The best-fit pole is shown at C.

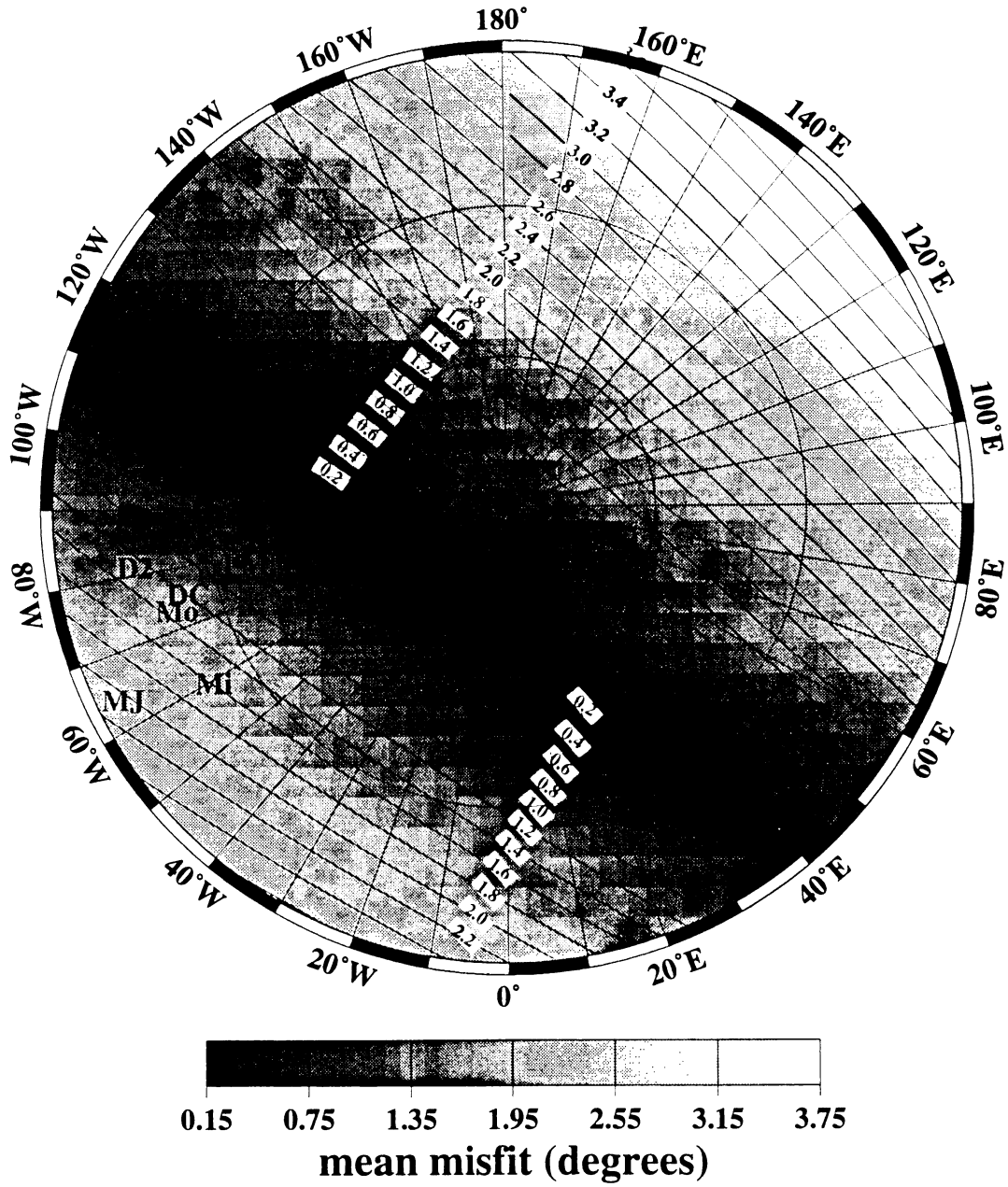

Figure 4.5 Grey-scale contour map of mean misfit in degrees (viewed about the north pole). The best-fit pole is shown with a circle. For comparison, the Pacific absolute rotation poles of *Clague and Jarrard* [1973] (0-43 Ma) is CJ, of *Duncan* [1981] (0-36 Ma) is D1, of *Duncan* [1981] (0-21 Ma) is D2, of *Duncan and Clague* [1985] (0-43 Ma) is DC, of *Fleitout and Moriceau* [1992] (0-18 Ma) is FM, of *Lonsdale* [1988] is L, of *Minster et al.* [1974] is Mi, of *Minster and Jordan* [1978] (10-0 Ma) is MJ and of *Morgan* [1972a,b] (0-40 Ma) is Mo.

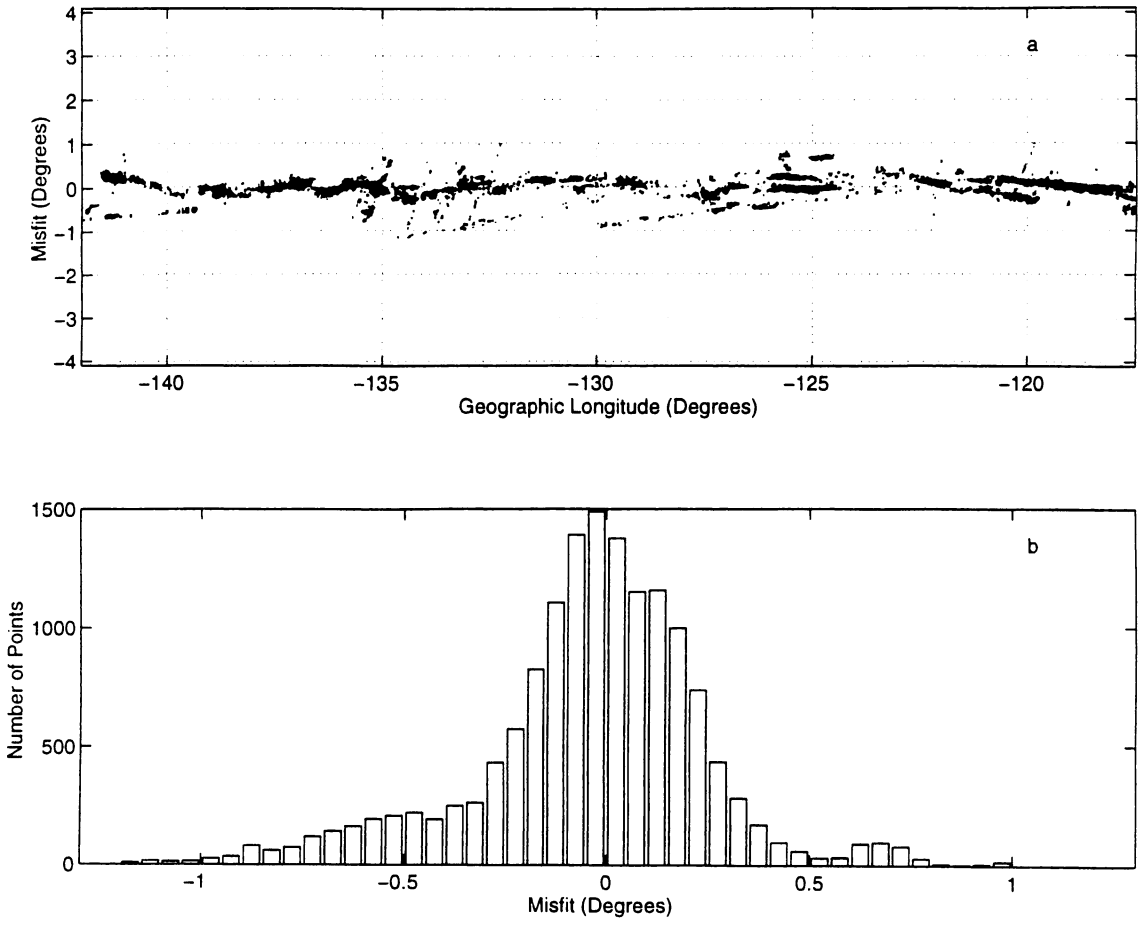

Figure 4.6

a) Misfit of points as a function of geographic longitude.

b) Histogram of misfit. The vast majority of points are within 0.3 ^{o} (~30 km) of the best-fitting small circle.

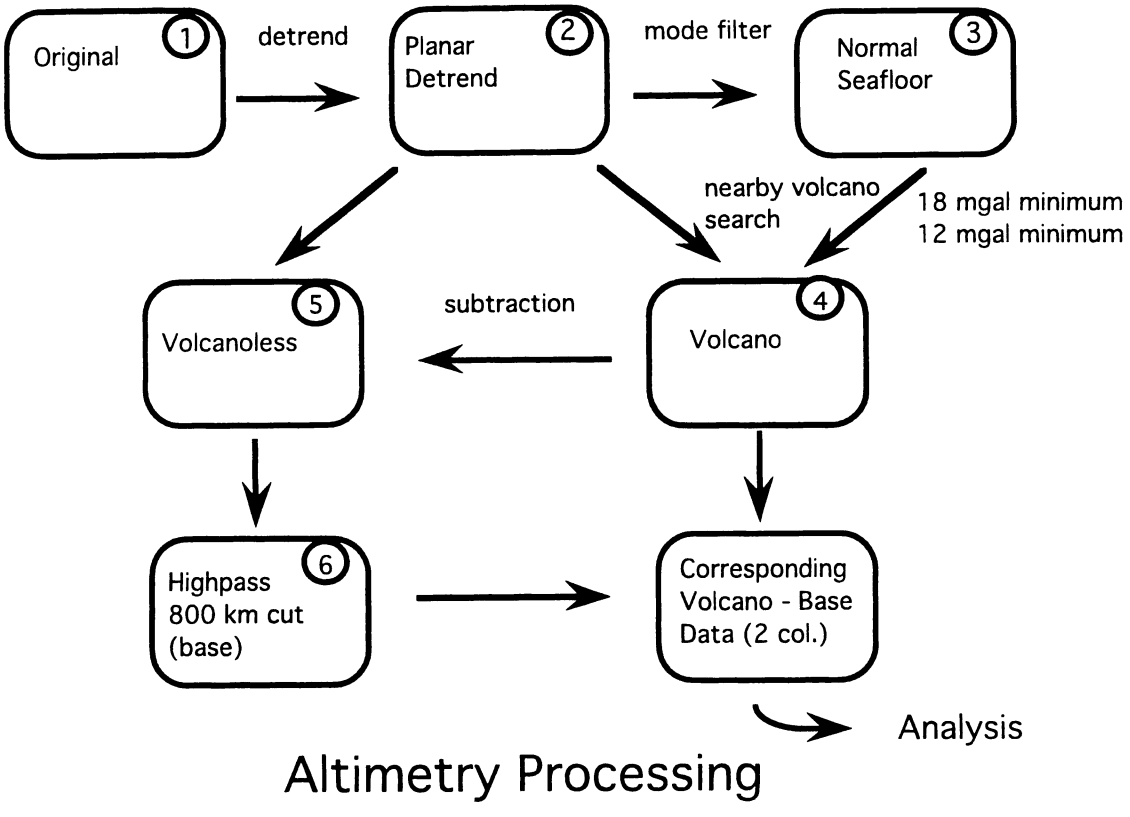

Figure 4.7 A flow chart of altimeter gravity anomaly data processing (shown in figure 4.8) west of the South East Pacific Rise and south of the Marquesas Fracture Zone. Two alternative sets of data are output with 12 and 18 mgal cutoff minimums. Each dataset consists of two columns, the volcano and base gravity value for every point in the study area.

(a)

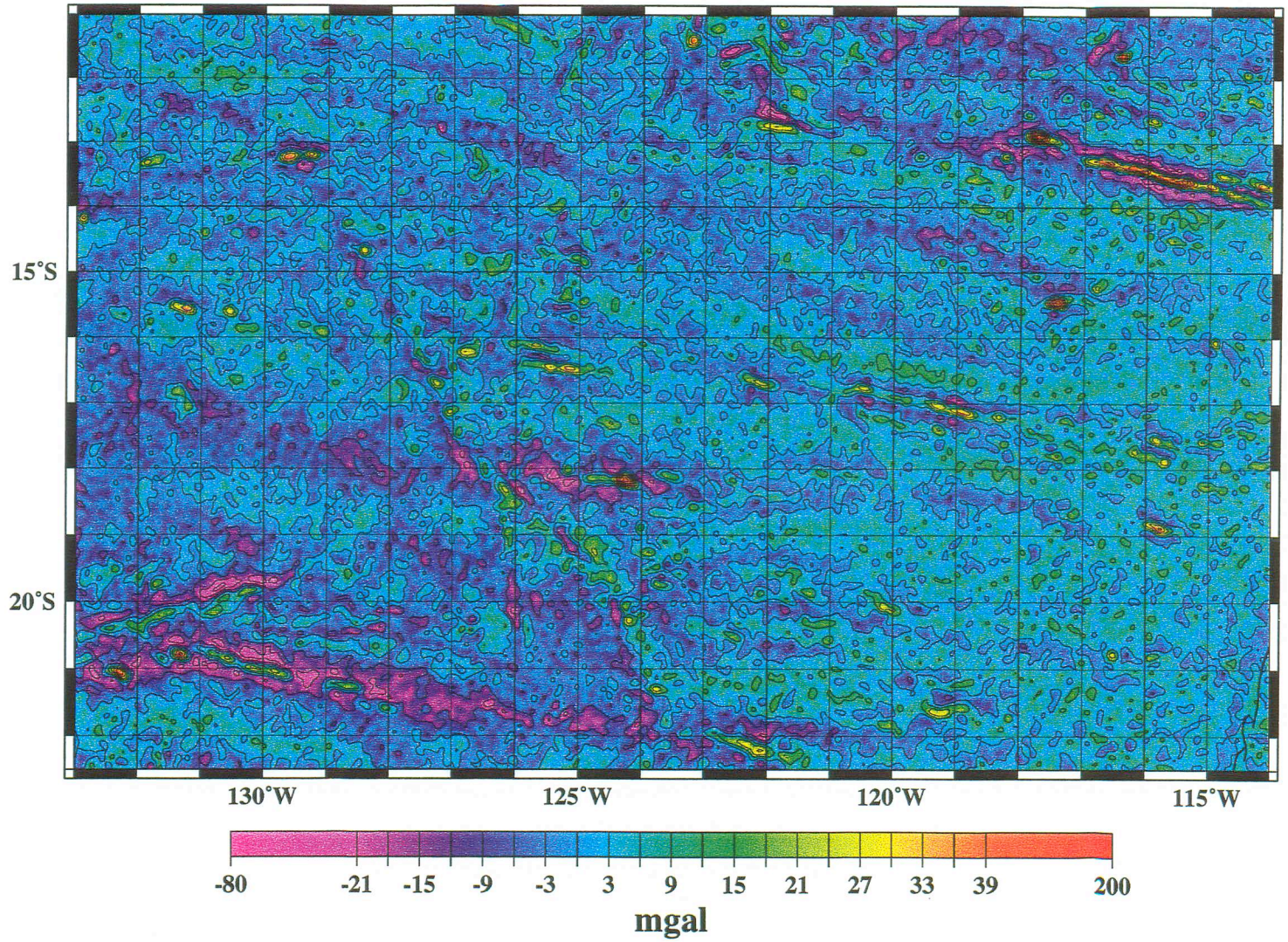

(b)

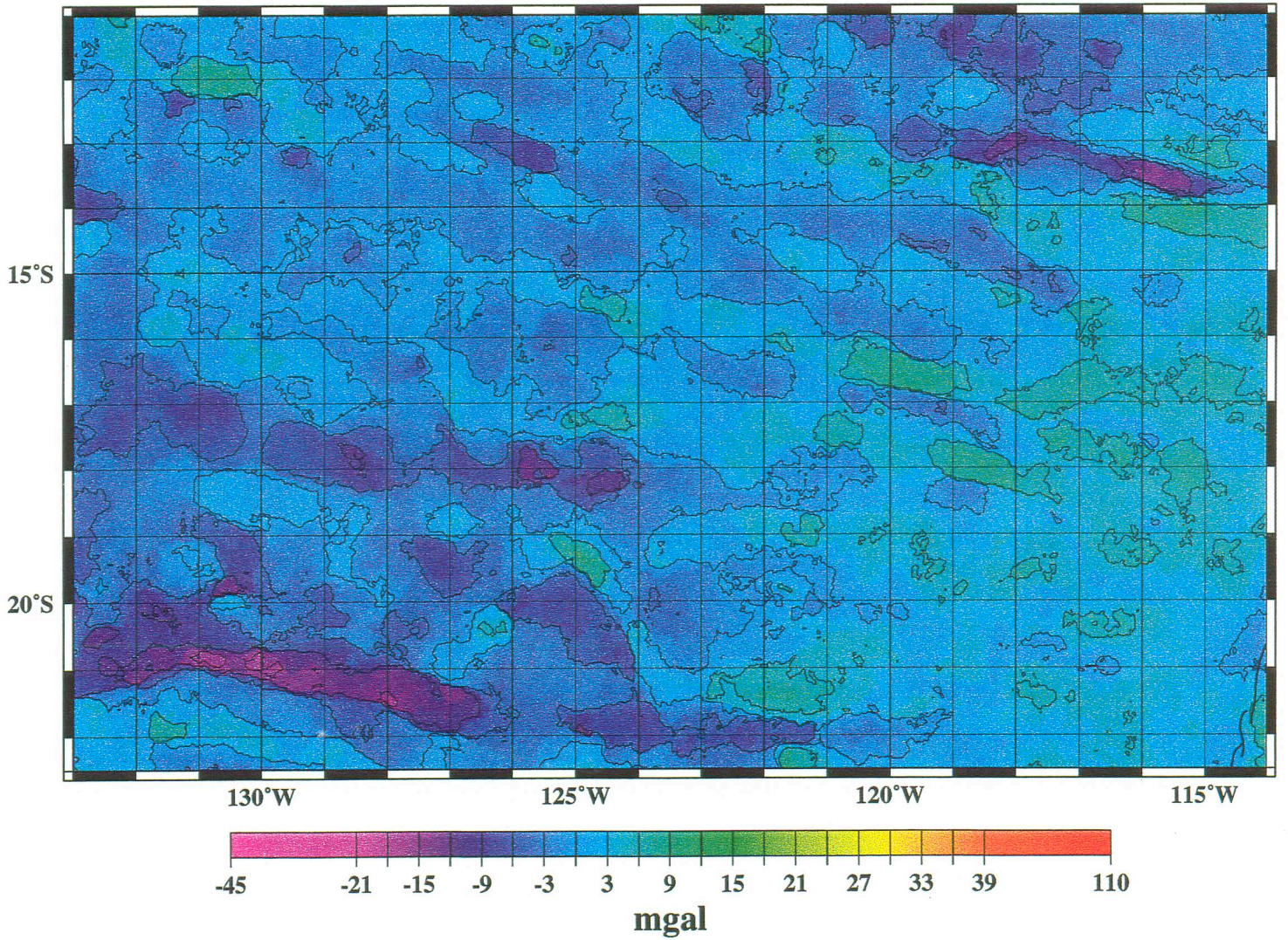

(c)

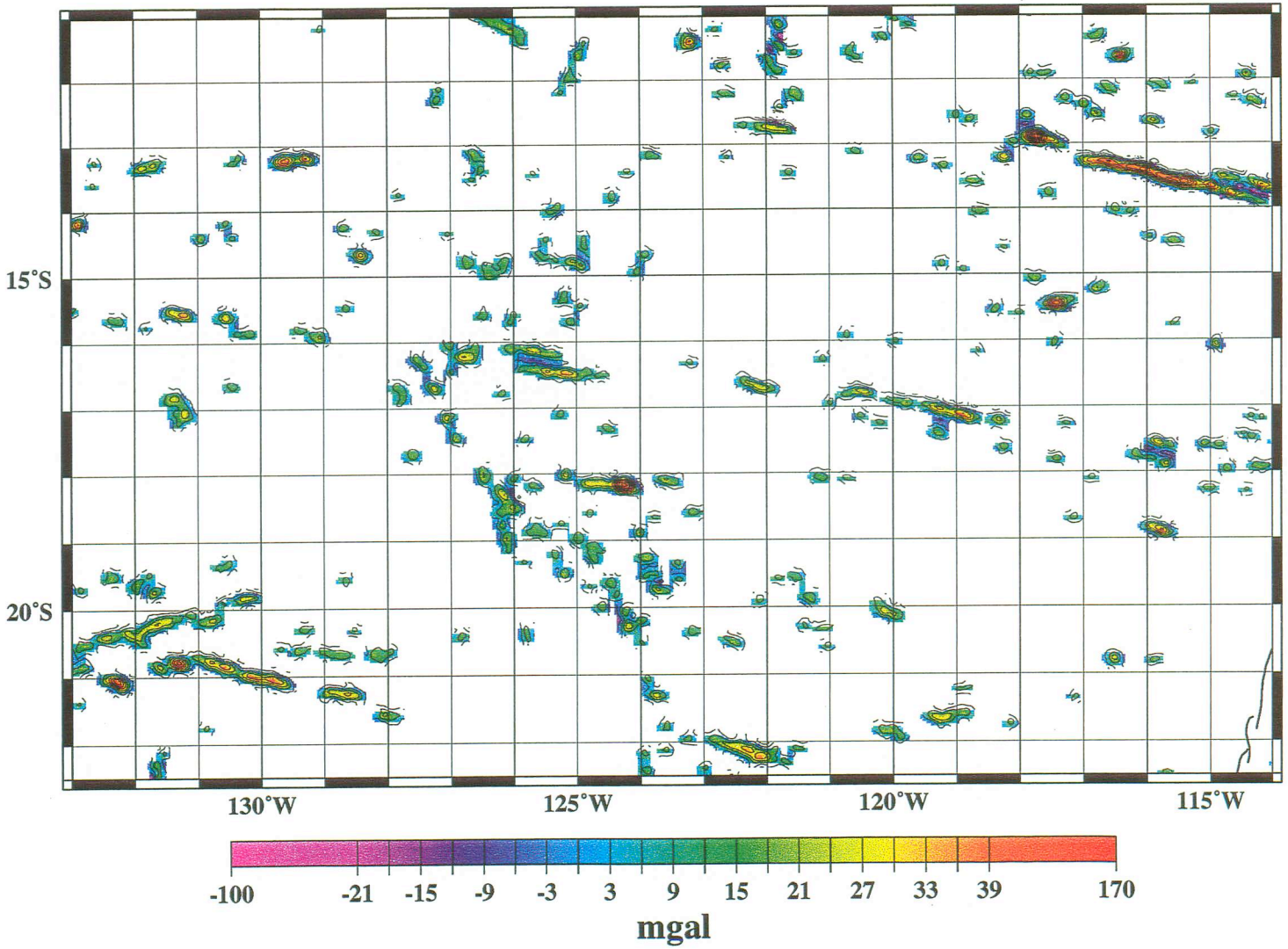
15°S
20°S
130°W
125°W
120°W
115°W
-100
-21
-15
-9
-3
3
9
15
21
27
33
39
170
mgal

(d)

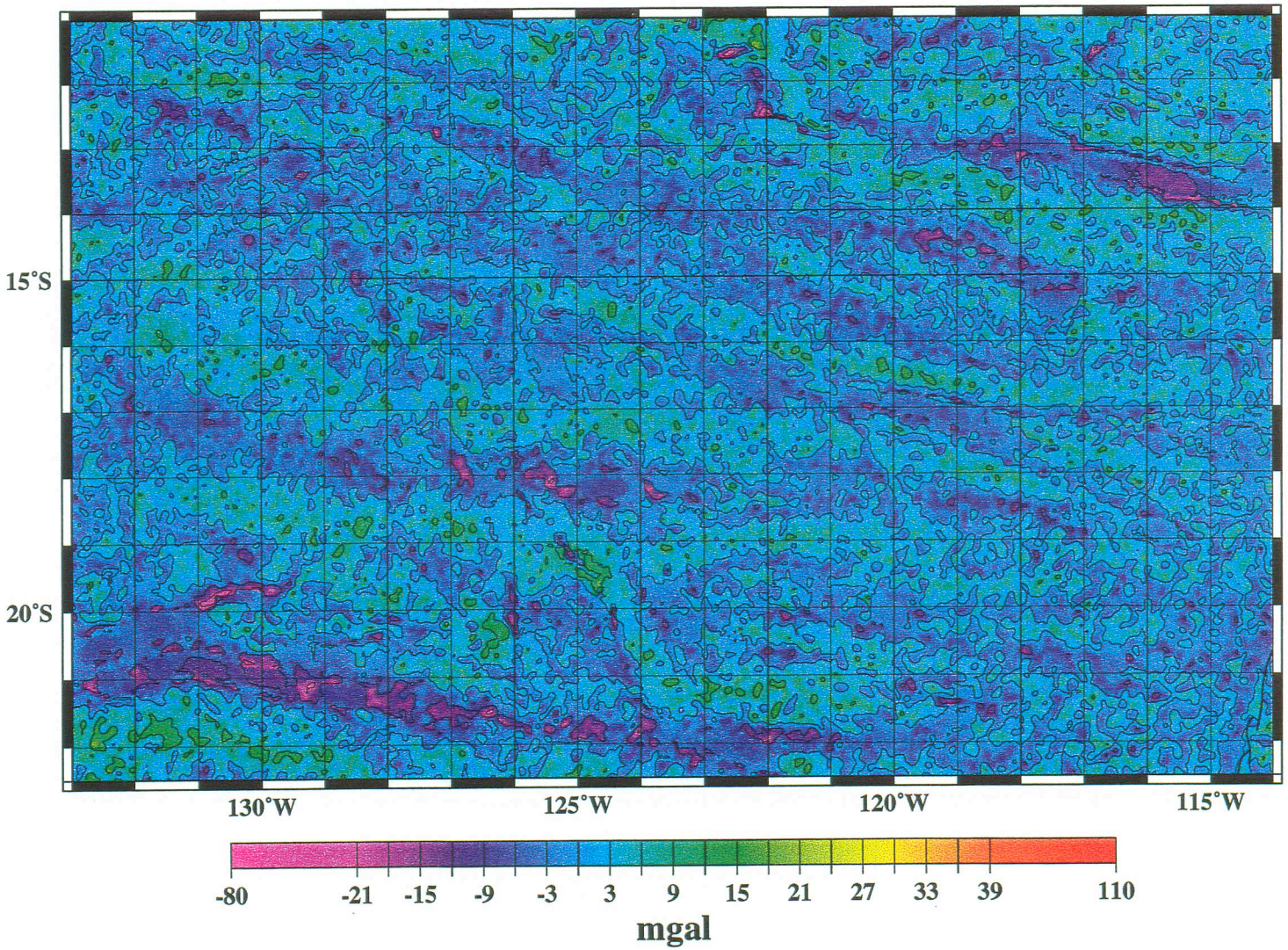

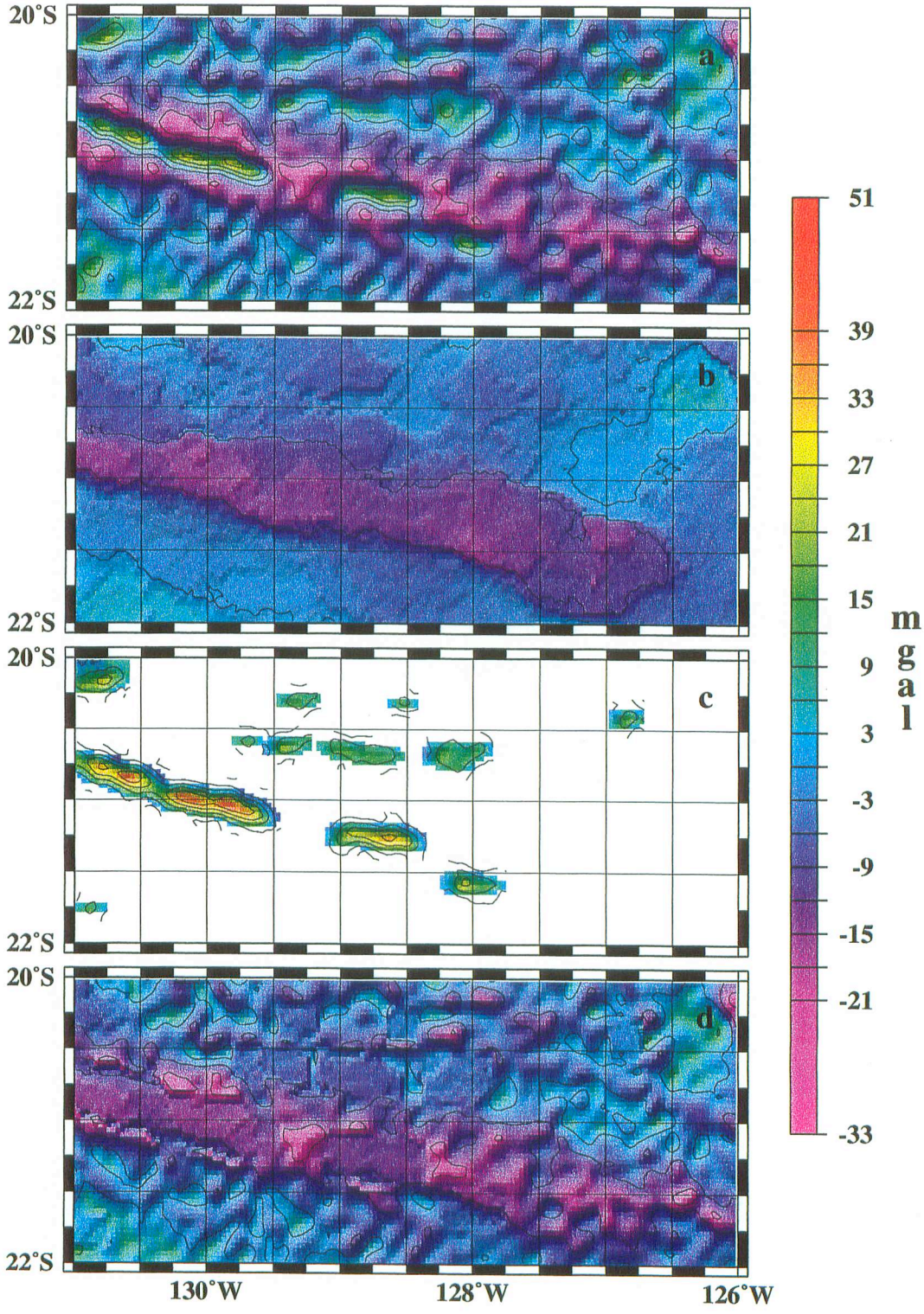
20°S
22°S
a
b
c
d
130°W
128°W
126°W
51
39
33
27
21
15
9
3
-3
-9
-15
-21
-33
mgal

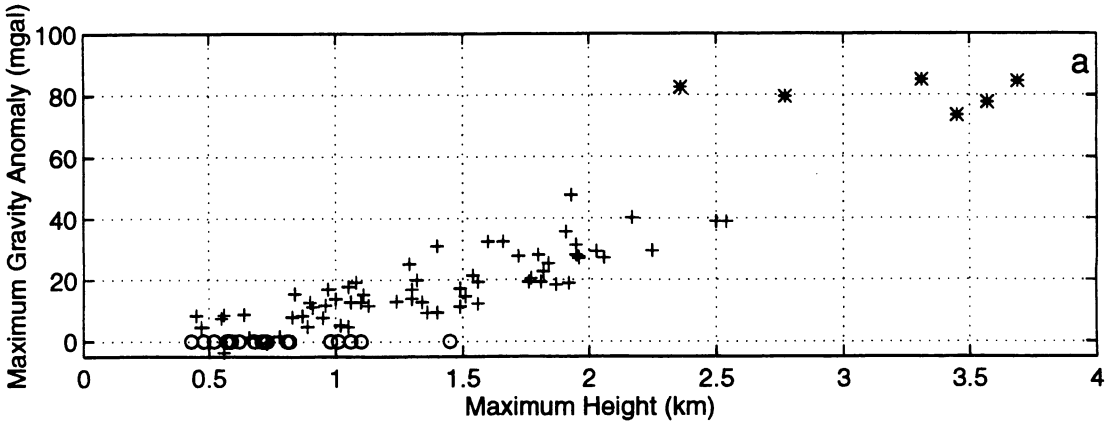
Maximum Gravity Anomaly (mgal)
100
80
60
40
20
0
0
0.5
1
1.5
2
2.5
3
3.5
4
Maximum Height (km)
a

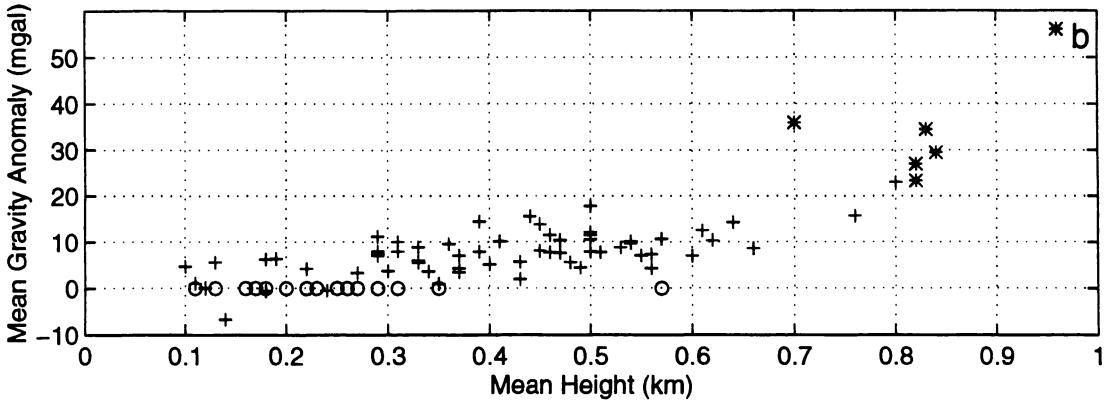
Mean Gravity Anomaly (mgal)
50
40
30
20
10
0
−10
0
0.1
0.2
0.3
0.4
0.5
0.6
0.7
0.8
0.9
1
Mean Height (km)
b

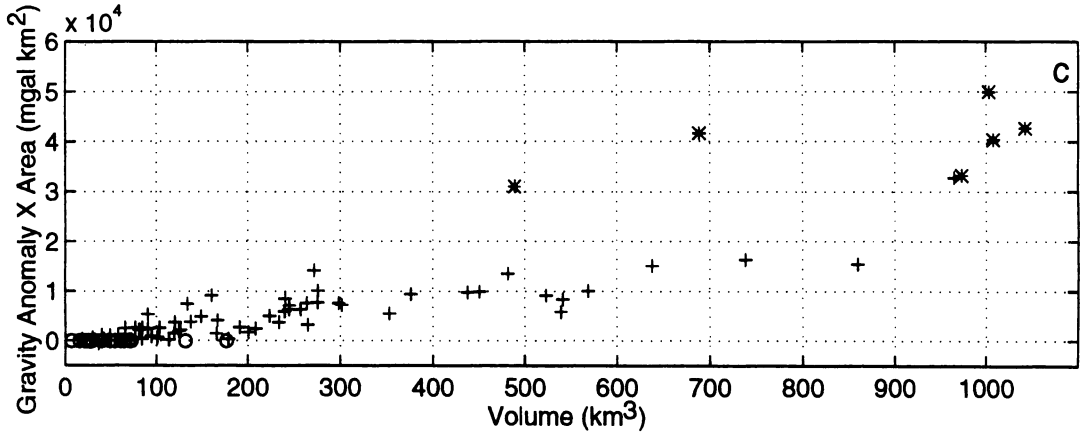
x 10^4
Gravity Anomaly X Area (mgal km^2)
6
5
4
3
2
1
0
0
100
200
300
400
500
600
700
800
900
1000
Volume (km^3)
c

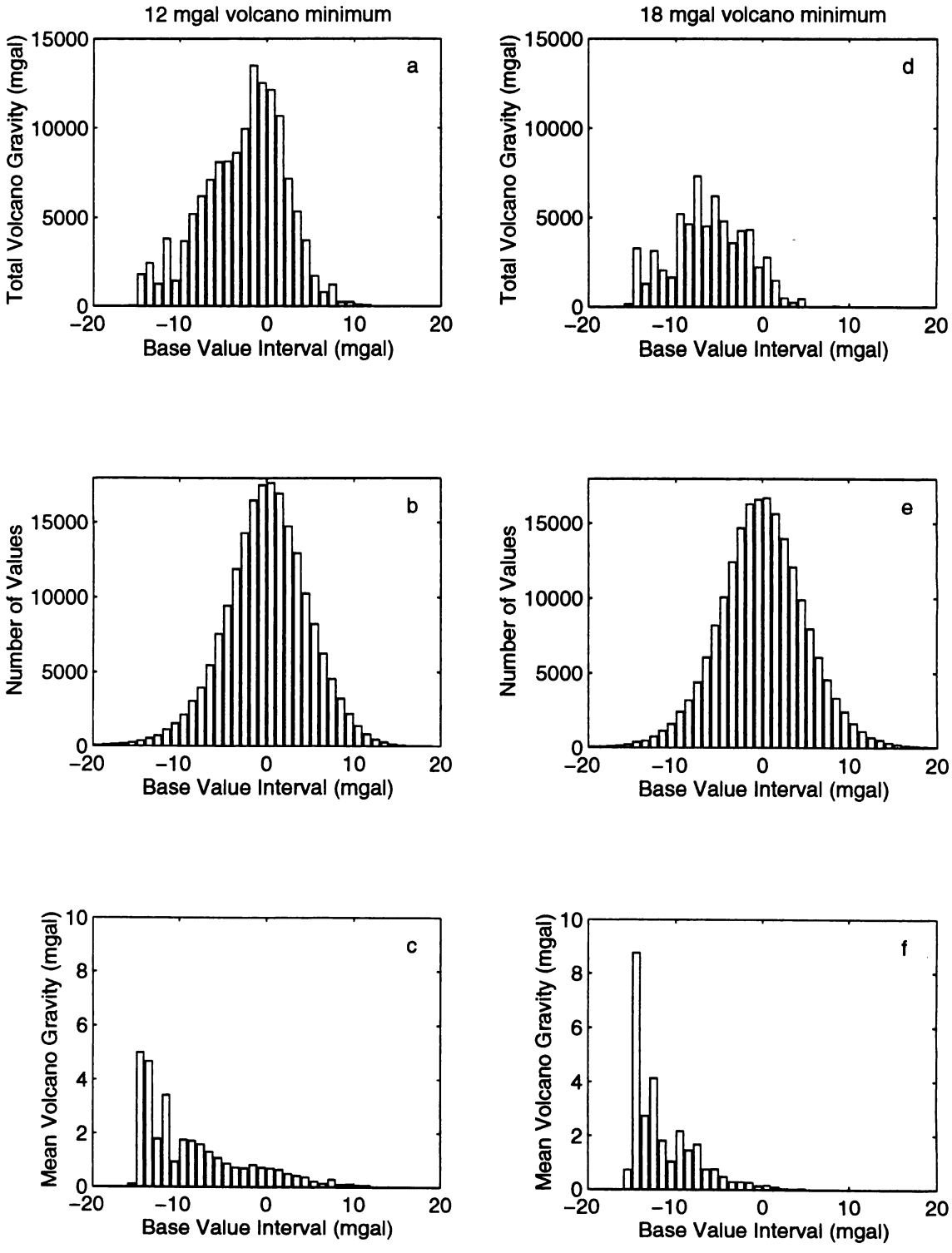
12 mgal volcano minimum
18 mgal volcano minimum
Total Volcano Gravity (mgal)
Number of Values
Mean Volcano Gravity (mgal)
Base Value Interval (mgal)
a
b
c
d
e
f
15000
10000
5000
0
10
8
6
4
2
−20
−10
0
10
20

9. REFERENCES

Abers, G. F., Parsons, B., and J. K. Weissel, Seamount abundances and distributions in the Southeast Pacific, *Earth and Planet. Sci. Lett.*, 87, 1-2, 137-151, 1988.

Bemis, K. G., and D. K. Smith, Production of small volcanoes in the superswell region of the South Pacific, *Earth and Planet. Sci. Lett.*, 118, 1-4, 251-262, 1993.

Bird, R. T., and R. A. Pockalny, Late Cretaceous and Cenozoic seafloor and oceanic basement roughness; spreading rate, crustal age and sediment thickness corrections, *Earth and Planet. Sci. Lett.*, 123, 1-4, 239-254, 1994.

Bonatti, E., and C. G. A. Harrison, Hot lines in the Earth's mantle, *Nature*, 263, 5576, 402-404, 1976.

Bonatti, E., Harrison, C. G. A., Fisher, D. E., Honnorez, J., Schilling, J., Stipp, J. J., and M. Zentilli, Easter volcanic chain (Southeast Pacific); a mantle hot line, *J. Geophys. Res.*, 82, 17, 2457-2478, 1977.

Buck, W. R., and E. M. Parmentier, Convection beneath young oceanic lithosphere; implications for thermal structure and gravity, *Earth and Planet. Sci. Lett.*, 91, 2, 1961-1974, 1986.

Calmant, S., and A. Cazenave, Anomalous elastic thickness of the oceanic lithosphere in the south-central Pacific, *Nature*, 328, 6127, 236-238, 1987.

Campbell, I. H., Griffiths, R. W., and R. I. Hill, Melting in an Arcaean mantle; heads it's basalts, tails it's komatiites, *Nature*, 339, 6227, 697-699, 1989.

Chayes, D. N., and D. W. Caress, Processing and display of multibeam echosounder data on the R/V Maurice Ewing, *EOS Trans. Amer. Geophys. Union*, 74, 562, 1993.

Clague, D. A., and R. D. Jarrard, Tertiary Pacific plate motion deduced from the Hawaiian-Emperor seamount chain, *Geol. Soc. Amer. Bull.*, 86, 991-998, 1973.

Cochran, J. R., Variations in subsidence rates along intermediate and fast spreading mid-ocean ridges, *Geophys. Jour. of the Royal Astr. Soc.*, 87, 2, 421-459, 1986.

Cormier, M.-H., and K. C. Macdonald, East Pacific Rise 18 degrees - 19 degrees S; asymmetric spreading and ridge reorientation by ultrafast migration axial discontinuities, *J. Geophys. Res.*, 99, 1, 543-564, 1994.

Craig, C. H., and D. T. Sandwell, Global distribution of seamounts from Seasat profiles, *J. Geophys. Res.*, 93, 9, 10408-10420, 1988.

DeMets, C., Gordon, R. G., Argus, D. F., and S. Stein, Current plate motions, *Geophys. Jour. Int.*, 101, 2, 425-478, 1990.

Dietz, R. S., and J. C. Holden, Reconstruction of Pangaea, breakup and dispersion of continents, Permian to present, *Jour. Geophys. Res.*, 75, 4939-4956, 1970.

Duncan, R. A., Hotspots in the southern oceans; an absolute frame of reference for motion of the Gondwana continents, *Tectonophysics*, 74, 29-42, 1981.

Duncan, R. A., Overprinted volcanism in the Line Islands and Pacific Plate motion since 100 m.y., *EOS Trans. Amer. Geophys. Union*, 64, 45, 843, 1983.

Duncan, R. A., and D. A. Clague, Pacific Plate motion recorded by linear volcanic chains, in: The Pacific Ocean, Vol. 7a, 89-121, 1985.

Epp, D., Possible perturbations to hotspot traces and implications for the origin and structure of the Line Islands, *Jour. Geophys. Res.*, 89, 13, 11273-11286, 1984.

Filmer, P. E., McNutt, M. K., and C. J. Wolfe, Elastic thickness of the lithosphere in the Marquesas and Society Islands, *Jour. Geophys. Res.*, 98, 11, 19565-19577, 1993.

Fleitout, L., and C. Moriceau, Short-wavelength geoid, bathymetry and the convective pattern beneath the Pacific Ocean, *Geophys. Jour. Int.*, 110, 1, 6-28, 1992.

Goodwillie, A. M., Short-wavelength gravity lineations and unusual flexure results at the Puka Puka volcanic ridge system, *Earth and Planet. Sci. Lett.*, 136, 3-4, 297-314, 1996.

Goodwillie, A. M., and B. Parsons, Placing bounds on lithospheric deformation in the central Pacific Ocean, *Earth and Planet. Sci. Lett.*, 111, 1, 123-139, 1992.

Goodwillie, A. M., and A. B. Watts, An altimetric and bathymetric study of elastic thickness in the central Pacific Ocean, *Earth and Planet. Sci. Lett.*, 118, 1-4, 311-326, 1993.

Gripp, A. E., and R. G. Gordon, Current plate velocities relative to the hotspots incorporating the NUVEL-1 global plate motion model, *Geophys. Res. Lett.*, 17, 8, 1109-1112, 1990.

Hart, S. R., A large-scale isotope anomaly in the Southern Hemisphere mantle, *Nature*, 309, 5971, 753-757, 1984.

Haxby, W. F., and J. K. Weissel, Evidence for small-scale convection from Seasat altimeter data, *Jour. Geophys. Res.*, 91, 3, 3507-3520, 1986.

Henderson, L, J., and R. G. Gordon, Fixed hotspots and recurrent volcanism along the Line Islands Chain, *Geol. Soc. Amer. -Abst. with Prog.*, 14, 7, 513, 1982.

Hey, R., Duenebier, F. K., and W. J. Morgan, Propagating rifts on midocean ridges, *Jour. Geophys. Res.*, 85, 87, 3647-3658, 1980.

Ito, G., McNutt, M., and R. L. Gibson, Crustal structure of the Tuamotu Plateau, 15 degrees S, and implications for its origin, *Jour. Geophys. Res.*, 100, 5, 8097-8114, 1995.

Ito, G., and J. Lin, Oceanic spreading center-hotspot interactions; constraints from along-isochron bathymetric and gravity anomalies, *Geology*, 23, 7, 657-660, 1995.

Jordan, T. H., Menard, H. W., and D. K. Smith, Density and size distribution of seamounts in the eastern Pacific inferred from wide-beam sounding data, *Jour. Geophys. Res.*, 88, 12, 10508-10518, 1983.

Levitt, D. A., and D. T. Sandwell, Lithospheric bending at subduction zones based on depth soundings and satellite gravity, *Jour. Geophys. Res.*, 100, 1, 379-400, 1995.

Levitt, D. A., and D. T. Sandwell, Modal depth anomalies from multibeam bathymetry; is there a south Pacific Superswell?, *Earth. Planet. Sci. Lett.*, 139, 1-2, 1-16, 1996.

Lonsdale, P. F., Geography and history of the Louisville hotspot chain in the southwest Pacific, *Jour. Geophys. Res.*, 93, 4, 3078-3104, 1988.

Lonsdale, P. F., Segmentation of the Pacific-Nazca spreading center, 1 degrees N - 20 degrees S, *Jour. Geophs. Res.*, 94, 9, 12197-12225, 1989.

MacDougall, J. D., Winterer, E. L., Sandwell, D. T., Lynch, M. A., Duncan, R. A., and J. H. Natland, Tholeiitic and alkalic volcanism along extensional ridges on the western flank of the superfast East Pacific Rise, *EOS Trans. Amer. Geophys. Union*, 75, 44, 582, 1994.

Mahoney, J. J., Sinton, J. M., Kurz, M. D., MacDougall, J. D., Spencer, K. J., and G. W. Lugmair, Isotope and trace elements characteristics of a super-fast spreading ridge; East Pacific Rise, 13-23 degrees S, *Earth. Planet. Sci. Lett.*, 121, 1-2, 173-193, 1994.

Mathworks, Matlab: High-performance numeric computation and visualization software, report, Natick, Mass., 1993.

McKenzie, D., and M. J. Bickle, The volume and composition of melt generated by extension of the lithosphere, *Jour. of Pet.*, 29, 3, 625-679, 1988.

McNutt, M., and K. M. Fischer, The South Pacific Superswell, in: Seamounts, Islands and Atolls, *Amer. Geophys. Union. Geophys. Monogr.*, *43*, 25-34, 1987.

McNutt, M. K., and A. V. Judge, The Superswell and mantle dynamics beneath the South Pacific, *Science*, 248, 4958, 969-975, 1990.

McNutt, M., and H. W. Menard, Lithospheric flexure and uplifted atolls, *Jour. Geophys. Res.*, 83, B3, 1206-1212, 1978.

Minster, J. B., Jordan, T. H., Molnar, P., and E. Haines, Numerical modeling of instantaneous plate tectonics, *Geophys. J. Roy. Astr. Soc.*, 36, 541-576, 1974.

Minster, J. B., and T. H. Jordan, Present-day plate motions, *Jour. Geophys. Res.*, 83, B11, 5331-5354, 1978.

Molnar, P., and J. Stock, Relative motions of hotspots in the Pacific, Atlantic, and Indian Oceans since late Cretaceous time, *Nature*, 327, 587-561, 1987.

Morgan, J. W., Deep mantle convection plumes and plate motions, *Am. Assoc. Pet. Geol. Bull.*, 56, 2, 203-213, 1972a.

Morgan, J. W., Plate motions and deep mantle convection, Studies in Earth and Space Sciences, *Geol. Soc. Amer. Mem.*, 132, 7-22, 1972b.

Morgan, W. J., Rodriguez, Darwin, Amsterdam, . . . , a second type of hotspot island, *Jour. Geophys. Res.*, 83, 5355-5360, 1978.

Moriceau, C., and L. Fleitout, A directional analysis of the small wavelength geoid in the Pacific Ocean, *Geophys. Res. Lett.*, 16, 3, 251-254, 1989.

Nelder, J. A., and R. Mead, A simplex method for function minimization, *Comput. J.*, 7, 308-313, 1965.

Nishimura, C. E., and D. W. Forsyth, Anomalous Love-wave phase velocities in the Pacific; sequential pure-path and spherical harmonic inversion, *Geophys. Jour. of the Royal Astr. Soc.*, 81, 2, 389-407, 1985.

Okal, E. A., and R. Batiza, Hotspots; the first 25 years, in: Seamounts, Islands and Atolls, *Amer. Geophys. Union, Geophys. Monogr. 43*, 1-11, 1987.

Okal, E. A., and A. Cazenave, A model for the plate tectonic evolution of the east-central Pacific based on SEASAT investigation, *Earth Planet. Sci. Lett.*, 72, 1, 99-116, 1985.

Phipps Morgan, J., Morgan, W. J., Zhang, Y.-S., and W. H. F. Smith, Observational hints for a plume-fed, suboceanic asthenosphere and its role in mantle convection, *Jour. Geophys. Res.*, 100, 7, 12753-12767, 1995.

Pringle, M. S., Age progressive volcanism in the Musicians Seamounts; a test of the hot spot hypothesis for the Late Cretaceous Pacific, in: The Mesozoic Pacific; geology, tectonics and volcanism, *Amer. Geophys. Union, Geophys. Monogr. 77*, 187-215, 1993.

Ribe, N. M., and U. R. Christensen, Three-dimensional modeling of plume-lithosphere interaction, *Jour. Geophy. Res.*, 99, 1, 669-682, 1994.

Sager, W. W., and M. S. Pringle, Paleomagnetic constraints on the origin and evolution of the Musicians and South Hawaiian seamounts, Central Pacific Ocean, in: Seamounts, Islands and Atolls, *Amer. Geophys. Union ,Geophys. Monogr.* 43, 133-162, 1987.

Sandwell, D. T., Winterer, E. L., Mammerickx, J., Duncan, R. A., Lynch, M. A., Levitt, D. A., and C. L. Johnson, Evidence for diffuse extension of the Pacific plate from Pukapuka ridges and cross-grain gravity lineations, *Jour. Geophys. Res.*, 100, B8, 15087-15099, 1995.

Sandwell, D. T., and J. Phipps Morgan, Systematics of ridge propagation south of 30 degrees S, *Earth and Planet. Sci. Lett.*, 121, 1-2, 245-258, 1994.

Sandwell, D. T., and W. H. F. Smith, Marine Gravity from Satellite Altimetry (poster), the Geological Data Center, Scripps Inst. of Oceanography, La Jolla, Ca. 92093, (digital file, version 7.2) anonymous ftp to baltica.ucsd.edu, 1995.

Sandwell, D. T., and W. H. F. Smith, Marine gravity anomaly from Geosat and ERS-1 altimetry, submitted to *Jour. Geophys. Res.*, 1996.

Schilling, J.-G., Fluxes and excess temperatures of mantle plumes inferred from their interaction with migrating mid-ocean ridges, *Nature*, 352, 6334, 397-403, 1991.

Schlanger, S. O., Garcia, M. O., Keating, B. H., Naughton, J. J., Sager, W. W., Haggerty, J. A., Philpotts, J. A., and R. A. Duncan, Geology and geochronology of the Line Islands, *Jour. Geophys. Res.*, 89, 13, 11261-11272, 1984.

Searle, R. C., Francheteau, J., and B. Cornaglia, New observations on mid-plate volcanism and the tectonic history of the Pacific Plate, Tahiti to Easter Microplate, *Earth Planet. Sci. Lett.*, 131, 3-4, 395-421, 1995.

Shen, Y., Forsyth, D. W., Scheirer, D. S. and K. C. Macdonald, Two forms of volcanism; implications for mantle flow and off-axis crustal production on the west flank of the southern East Pacific Rise, *Jour. Geophys. Res.*, 98, 10, 17875-17889, 1993.

Sleep, N. H., Hotspots and mantle plumes; some phenomenology, *Jour. Geophys. Res.*, 95, 5, 6715-6736, 1990.

Small, C., Observations of ridge-hotspot interactions in the Southern Ocean, *Jour. Geophys. Res.*, 100, B9, 17931-17946, 1995.

Smith, D. K., Shape analysis of Pacific seamounts, *Earth Planet. Sci. Lett.*, 90, 4, 457-466, 1988.

Smith, D. K., The size distribution of Pacific seamounts, *Geophys. Res. Lett.*, 14, 11, 1119-1122, 1987.

Smith, D. K., and T. H. Jordan, Seamount statistics in the Pacific Ocean, *Jour. Geophys. Res.*, 93, 4, 2899-2918, 1988.

Smith, W. H. F., Marine Geophysical studies of seamounts in the Pacific Ocean basin, Doctoral thesis, Columbia University, New York, NY, 1990.

Sparks, D. W., and E. M. Parmentier, The generation and migration of partial melt beneath oceanic spreading centers, in: Magmatic Systems, International Geophysics Series, 57, 55-76, 1994.

Staudigel, H., Park, K. H., Pringle, M. S., Rubenstone, J. L., Smith, W. H. F., and A. Zindler, The longevity of the South Pacific isotopic and thermal anomaly, *Earth Planet. Sci. Lett.*, 102, 1, 24-44, 1991.

Turner, D. L., and R. D. Jarrard, K-Ar dating of the Cook-Austral island chain; a test of the hot-spot hypothesis, *Jour. Volc. Geotherm. Res.*, 12, 3-4, 187-220, 1982.

Vogt, P. R., Volcano spacing, fractures and thickness of the lithosphere, *Earth Planet. Sci. Lett.*, 21, 235-252, 1974.

Watts, A. B., J. H. Bodine, and N. M. Ribe, Observations of flexure and the geological evolution of the Pacific ocean basin, *Nature*, 283, 532-537, 1980.

Wessel, P., and W. H. F. Smith, Free software helps map and display data, *EOS Trans. Amer. Geophys. Union*, 72, 41, 441, 1991.

Wilson, J. T., Continental Drift, *Scient. Amer.*, 208, 86-100, 1963.

Winterer, E. L., and D. T. Sandwell, Evidence from en-echelon cross-grain ridges for tensional cracks in the Pacific Plate, *Nature*, 329, 6139, 534-537, 1987.

CHAPTER 5

PUKAPUKA PRISMATIC RIDGES:

A FLANK RIFT-ZONE MODEL AND LITHOSPHERIC TENSION

ABSTRACT

The Pukapuka volcanic system consists of a 2500-km-long series of long volcanic features on young Pacific seafloor south of the Marquesas Fracture Zone. The most remarkable members of the system are large, linear, volcanic structures with high axial ratios, rift-like summit vents, and parallel flank contours, resembling elongated prisms. Though morphology has suggested a fracture-mechanics origin due to north-south directed tension, it is clear that normal fault scarps expected to accompany diffuse extension are absent from multibeam bathymetry and imagery. Alternative mechanisms by which linear volcanism may occur are explored.

Pukapuka volcanic features are roughly classified in a gradational sequence, where form is distinctly a function of size. As height increases, east-west oriented summit vents, flank rift zones, and a narrow, linear, crestal ridge develop. While a near east-west segment azimuth is maintained for all size ranges, horizontal gradient and linearity increase with size. Features of similar form congregate within subregions. This indicates that the majority of features are formed by a similar process with a variation in governing parameters, such as lithospheric thickness, deviatoric stress and magma-supply rate. Also, relation to abyssal hill scarp location indicates that seafloor structure affects the thermal and stress regimes of rising magma-filled conduits.

The Pukapuka prismatic ridges resemble Hawaiian flank-rift-zone ridges morphologically and morphometrically, suggesting that their internal conduit structure, eruptive and mass-wasting modes are similar. Nonetheless, a source of regional stress other than summit-directed stress and edifice proximity (operating in Hawaii) is required; otherwise a 3-armed rift geometry is expected. The preferred orientation of volcanic segments normal to the least-compressive-stress direction predicted by *Sandwell et al.* [1995] in the region suggests that a tectonic stress controls azimuth. North-south directed tension affects stress regimes during ascent and within growing edifices. Pukapuka morphologic trends may be explained by variable coalescence between buoyancy-driven, fluid-filled cracks and the formation of a preferred magma

path which increases with increased magma supply or decreased deviatoric stress. Finally, it is noted that a lack of normal faulting topographic evidence is not inconsistent with tension and extension in magmatically robust regions.

1. INTRODUCTION

Submarine volcanism is the principal information source regarding processes of melt production and migration through oceanic lithosphere. While many studies have focused on large, hotspot-attributed island and guyot chains, only with the advent of high-resolution mapping systems has attention progressed to more numerous, small volcanic features on the ocean floor called seamounts (*Menard and Ladd*, 1963). Seamounts have been adequately approximated as flat-topped cones or domes (*Smith*, 1988), particularly for young, near-spreading-axis edifices (*Scheirer and Macdonald*, 1995). However, *Vogt and Smoot* [1984] observed a gradational development of summit protuberances which lengthen with increasing volcano height. These linear volcanic extensions, termed flank rift zones (FRZ's), grow because less work is required to pump magma laterally than to a tall summit. While some of the first surveyed submarine volcanoes, Davidson, San Juan and Westfall Seamounts (*Shepard and Emery*, 1941; *Menard*, 1959; *Lonsdale*, 1991) are elongated, the vast majority of oceanic volcanoes exhibit radial symmetry.

Recently a morphologically and structurally distinct class of feature, the linear ridge group, has been defined prompted by the discovery of the Crossgrain (*Winterer and Sandwell*, 1987; *Lynch*, 1993; *Searle et al.*, 1995) and Pukapuka volcanic systems (*Sandwell et al.*, 1995). Of these the Pukapuka system is younger and has been surveyed in greater detail. The system (figure 5.1) consists of a series of discrete volcanic structures which are about 40 km long, <10 km wide and which vary in amplitude (800-4000 m) and regularity of form (*Winterer et al.*, 1993). The most remarkable members of the Pukapuka volcanic system are large (>1500 m high) linear volcanic structures with high axial ratios, rift-like summit vents and parallel flank contours, resembling elongated prisms (here termed large prismatic ridge segments).

Based on these morphologic data, as well as association with an altimetric gravity-lineation trough and a dredge-sample age-progression inconsistent with the hotspot model *Sandwell et al.* [1995] proposed that Pukapuka volcanoes are produced by lithospheric stretching. This model suffers from two serious problems. First, extension has not been required from plate reconstructions and *Goodwillie and Parsons* [1992] observe less than 100 km of fracture zone separation, much less than the strain required in this

model. Second, multibeam bathymetry in the vicinity of the ridges in sediment-blanketed abyssal terrain fails to show evidence of extensional faulting parallel to the ridges. Therefore, a fracture mechanics model for the Pukapuka and Crossgrain Ridges, by which ridges grow by propagation from a small edifice nucleus (*Lynch*, 1993) may be insufficient.

The morphologic resemblance of large prismatic members of the Pukapuka system (figure 5.1) to large volcanic rifts extending from Hawaiian volcanoes suggests that the morphology of these ridges may be controlled by the same factors including processes occurring during melt ascent in the lithosphere and within the growing edifice. Also, a systematic variation of form with size suggested to *Winterer et al.* [1993] an evolutionary sequence.

The purpose of the present analysis is to examine processes which control the formation of large prismatic Pukapuka ridge segments. Data processing, measurement methods and definitions are presented in section 2. In section 3, multibeam bathymetry and sidescan images are used to document morphologic volcano gradation and the absence of normal faulting. In section 4, specific morphometric parameters (dimensions, gradient and azimuth) are used to explore the gradational form of volcanic features. *Lynch* [1993] qualitatively examined the relation of the Crossgrain ridges to proposed linear volcanic analogs. In similar fashion, section 5 presents a quantitative comparison between the prismatic Pukapuka ridges, Puna Ridge and Loihi Seamount. In section 6, results from mechanical modeling and numerical simulation experiments on surficial dike-propagation and lithospheric melt-ascent are discussed as they relate to the Pukapuka volcanic system. A hypothetical prismatic ridge generation model will be proposed which does not require extensional cracking as the primary source of melt, but instead results from the vertical propagation of buoyancy or pressure-driven fluid-filled melt from beneath the crust in a tensional environment.

2. METHOD AND DEFINITIONS

2.1 Data

The primary sources of information regarding the Pukapuka system are multibeam bathymetry (SeaBeam2000) and imagery (Sidescan), ship gravity, magnetics and 3.5 kHz seismics. The ridges are sparsely sampled — only 6 dateable samples have been obtained from in excess of 30 major ridge segments with only one ridge successfully sampled more than once. Moreover, no fine-scale ground-truthing is available via drilling, deep-tow sidescan, and submersible photography; thus, only gross structural and volcanic features can be discerned.

SeaBeam2000 multibeam bathymetry and imagery were collected at sea aboard R/V Melville from December, 1992, through February, 1993 (Gloria legs 3b and 4). These data constitute a focused survey of the Pukapuka ridges and are supplemented by older multibeam bathymetry surveys and more recent transects (Westward 1 and 4). The processing of multibeam bathymetry is described in detail in chapter 4. Two grid types are produced, original bathymetry and topography, with 100 m and 500 m grid-cell size, respectively. Bathymetry grids consist of all values measured from the sea surface; these are used to make color-contour maps of ridge segments and their vicinity which can be used for volcanic and structural interpretation. Topography grids consist of height above normal nearby seafloor where all non-edifice grids are eliminated following the method developed in chapter 4; these are used to measure vital parameters of ridge segments discussed in sections 4 and 5.

SeaBeam2000 sidescan images are primarily used to locate highly sloped reflectors and acoustically bright, flat terrain. Image data collected at sea are digitized with 16-bit amplitude resolution (0-65535) for 1000 samples across a swath (*Chayes and Caress*, 1993). Mbsystem processing merges amplitude data with satellite navigation. These data are plotted directly where acoustically reflective and non-reflective regions are shaded dark and light, respectively. Though detailed water-velocity correction is not attempted, distortion is minimal. However, acoustic noise prohibits identification of fine-scale features.

2.2 Segment Classification

Pukapuka volcanic features are distributed neither uniformly nor randomly along the entire system (figure 5.1). Similar to *Vogt and Smoot* [1984], the distribution is subdivided here in the form of a hierarchy consisting of (1) the system itself, (2) ridge group, (3) a seamount cluster or ridge segment, and (4) an individual small edifice. The chosen principal unit of measurement is the seamount cluster or ridge segment reflecting a genetic interpretation that they both represent a discrete volcanic event or sublithospheric melt pool. These are labeled by longitude (figure 5.1).

In theory, a segment consists of an individual elongate edifice following a distinct azimuth where height monotonically decreases nearly continuously from the summit; therefor, sharp changes in along-axis slope or direction may be interpreted as segment boundaries. In practice the definition of segment terminus is semi-arbitrary and greatly dependent on both practical considerations and genetic assumptions; as overlap increases the distinction between adjacent coalescing rift zones is particularly difficult based on morphology alone. Some ridge segment complexes exhibit a clear boundary (e.g. 118.2-119.1, 119.2-120.1-120.2, 122.1-122.2, 125.1-125.2, 125.3-125.4, 131.1-131.2), but others do not (e.g. 129.1-129.2-129.3). Indeed boundary distinction within the small/irregular size groups is almost entirely arbitrary (e.g. 119.3-120.3-120.4, 126.1, 130.4-130.5, 134.2). At the small size range it is occasionally difficult to discern volcanic features altogether. For purposes of measurement, segments are here distinguished based on a saddle height which is less than 2/3 of the summit and/or a change in azimuth greater than 10^{o}.

2.3 Morphometric Measurement

A topographic grid is extracted for each segment with bounds in table 5.1. Length and width values are measured directly, though these values are somewhat sensitive to boundary definitions. Maximum height, mean height and volume are calculated above the automatically chosen modal basal contour as in chapter 4. Representative cross- and along-axis profiles are obtained for large prismatic

ridges only. Characteristic slopes are obtained from a stack of parallel cross-sections extracted from the topographic grid; along-axis profiles are taken along the crest.

Rather than estimating a segment's characteristic mean slope and azimuth by eye an automatic quantitative method is implemented based on the gradient at every topographic grid cell. The characteristic slope and azimuth are defined here as the mean horizontal gradient and the zero-slope direction for all cells in the topographic grid, respectively. The gradient of a topographic grid is calculated in two orthogonal directions, in this case, east-west and north-south, using the grdgradient program in the GMT software package (*Wessel and Smith*, 1991). The maximum 2-dimensional gradient of a given cell is calculated as the vector sum of the north-south and east-west components. The mean of these values is the characteristic gradient for a given ridge segment.

Since the ratio of the two orthogonal gradient components is the tangent of the angle of the maximum-slope vector, the arc-tangent of the ratio of the two components is perpendicular to the zero-slope azimuth. This azimuth is calculated for all grid cells in a region. Azimuthal distributions cannot be evaluated with standard linear statistical methods because directions wrap around with no origin. Also, the distribution of maximum directions is bimodal for the vast majority of ridges because a narrow ridge with a persistent crestal azimuth has two preferred and opposite maximum sloping directions. The statistical estimation method employed here assumes that the slope distribution is universally bimodal and that these modes are antipodal. Following the method of *Batschelet* [1981] the modes are superposed by doubling the angle and subtracting 2π radians from azimuths exceeding 2π (mod-2π). The resultant distribution of values for a single feature is usually unimodal and approximately gaussian. A circular standard deviation (not shown) is calculated following *Batschelet* [1981].

3. PUKAPUKA SYSTEM MORPHOLOGY

3.1 Normal Extensional Faulting

Unlike larger volcanic ridges (e.g. Louisville; *Lonsdale*, 1988) which are essentially chains of discrete volcanoes connected at basal levels, parallel flank base-to-crest contours characteristic of elongate prismatic ridge segments (see below) in the Pukapuka system require an episode of volcanism over the entire edifice. One problematic mechanism for the production of an elongate ridge over time with a single source is the standard stretching-extension model which states that primary normal faults in the upper-brittle crust present a conduit for rising magma (*Sandwell et al.* 1995). Pressure-release melting does not provide melt, requiring a reservoir of partial melt beneath the lithosphere (*Sandwell et al.* 1995) so that magma should be present prior to cracking (*Lynch*, 1993). Long ridge segments are expected to correspond to elongated cracks in the lithosphere which exist independently of volcanism. Still, diffuse stretching is less than 160 km (*Goodwillie and Parsons*, 1992) and there is no evident normal faulting in the survey area.

Figure 5.2 is a multibeam bathymetry map and sidescan image of seafloor immediately south of the 131.1-131.2 ridge complex. High-resolution sidescan is particularly effective for distinguishing features smaller than multibeam accuracy can allow. The data are acquired along two parallel nearly north-south tracks centered on dark (reflective), center-beam lines. The image basically shows two types of features: irregular lineations which semi-parallel the track direction and patchy/circular features. The former are abyssal hill reflectors produced at the East Pacific Rise (EPR) axis along the paleo-spreading-center azimuth. The latter are seamounts with associated reflective seafloor. Most often, solitary seamounts in the region are flat-topped or conical, and riftless even for large edifices (133.8). Many seamounts are aligned on major abyssal hill scarps.

Abyssal hill reflectors correspond very closely in most places to the location of sharp scarps in the bathymetry where offset is usually on the order of 100-200 m. However, in the western portion faint,

though clearly discernible, lineations exist with less than 100 m offset. This section of seafloor was chosen because faults are most visible when they semi-parallel the ship track. For the majority of the Pukapuka survey the ship progressed in a nearly east-west direction which would parallel expected normal extensional faults. A careful review of sidescan for the entire survey (not shown) fails to reveal evidence for such faulting. Bright slope reflection and surface volcanism does extend past ridge segment ends. Nevertheless, though this and sediment coverage (30-100 m) may partly obscure normal faults it is not reasonable that faults are everywhere too small to be "seen". This suggests that an alternate mechanism which does not require primary normal faulting should be explored.

3.2 The Pukapuka Gradational Sequence

This section presents a geologic and morphologic review of several Pukapuka ridges. Numerous volcanic features have been surveyed in the Pukapuka system. Detailed descriptions of the overall Pukapuka system and individual classes (in an evolutionary context) have already been presented by *Winterer* [1993]. Since a comprehensive description of every individual edifice is unnecessary and since discrete volcanic features appear to be broadly distributed in a few morphologic classes, only one example of each class is provided. A gradation of form with size may be interpreted such that each stage of increased volume represents a successive arrested stage in development; conversely, each stage may represent the end result of a common process which differs in some critical parameter such as magmatic flux, differential stress, or lithospheric thickness (section 6). In the latter case, a given prismatic ridge need not progress through smaller classes.

Definitions and descriptions of structural and volcanic units pertaining to the linear ridge class have been comprehensively detailed by *Lynch* [1993] with respect to the Crossgrain Ridges. While the Crossgrain Ridges are older than 40 Ma, are buried beneath hundreds of meters of sediment (*Winterer and Sandwell*, 1987; *Lynch*, 1993), and are only partially surveyed, most of the Pukapuka ridges east of 135 ^{o}W are young (< 10 Ma), are covered by only a thin veneer of sediments (< 150 m; *Sandwell et al.*, 1995), and

are nearly completely surveyed. Therefor, for the Pukapuka system, it is possible to discern smaller volcanic features representing modest magmatic volumes as well as finer base detail (abyssal hills and debris).

3.2.1 Seamount Cluster and Flows

The smallest ridge class is represented by a loose cluster of round volcanoes (*Winterer*, 1993; *Lynch*, 1993) following the same azimuth as more robust ridges (~WNW-ESE; figure 5.3). Several short seamount chains are present along a N115 ^{o}E azimuth. While the sidescan image is somewhat obscure, ship-facing seamount side-slopes appear as clear, arcuate reflectors, while the tops are commonly non-reflective. The sidescan image shows all of the volcanoes identified in the bathymetry and additional ones which are smaller than bathymetry can resolve. Thus seamounts in the image are densely packed linearly, nearly overlapping. Heights are on the order of a few hundred meters and side-slopes are fairly moderate; most seamounts grade into a basal, low-slope platform elevated ~100 meters above the local seafloor depth. Reflective patches are associated with a pair of seamounts to the north. Many studies of seamount volcanism near spreading axes have correlated reflective seafloor with recent volcanism or debris flow deposits (*Barone and Ryan*, 1990; *Shen et al.*, 1993). A Gloria leg 4 core obtained in a reflective region contained no fresh lava. Reflective flat patches must remain enigmatic, as it seems premature to attribute all such relations to recent volcanism. If they are recent flows then the age progression within the system is complex.

Abyssal hill fabric is recognizable in a few locations despite the orthogonal ship track direction. Abyssal hill faults appear to exert control on the location of seamounts (121 ^{o}32 'W) and their elongation. Elsewhere, larger ridge segments often extend "legs" of seamounts at their bases along the local abyssal hill direction (133.1; *Winterer*, 1993). The largest seamounts are irregular in shape with preferential directions along the abyssal hill and overall chain azimuth. Dark (reflective) patches in direct association with

seamounts truncate along two prominent scarps evident in the bathymetry; such bright-dark relations in association with seamounts and bounded by abyssal fault scarps are typical throughout the system.

3.2.2 Small Irregular Ridge Segment

Two adjacent small, irregular ridge segments (132.3, 132.4) are shown in figure 5.4. Ridges of this category typically appear in this region in sets and exhibit a remarkable consistency in form (see also 130.4, 130.5, 133.3, 133.4, 133.7). Whereas edifices belonging to the seamount chain class extend bases nearly to the local seafloor, maintaining integrity of shape, edifices within a small, irregular ridge segment maintain closed contours only for the upper half; instead, they reside atop an irregular platform a few hundred meters above the seafloor. While edifice flank slopes are fairly high (up to 20 ^{o}), the platform-to-seafloor gradation is moderate (~5 ^{o}). The sidescan image is reflective and mottled throughout so that no trace of abyssal hill fabric is evident (compare with figures 5.2 and 5.3). This suggests that flows and debris extend far away from the edifices themselves on nearly flat seafloor. The abyssal hill faulting direction still exerts control on volcanic structure as elongate north-south extensions and central edifice alignment are superposed on the overall segment direction. At this stage structural control related to the overall segment azimuth is limited as summit volcanoes have not developed discernible rifts, are poorly aligned and are not consistently elongated along the segment azimuth.

3.2.3 Irregular Lineated Ridge Segment

The degree to which volcanism is focused linearly increases with ridge segment size. A set of irregular, lineated segments (129.1-129.2-129.3), connected end-to-end, is shown in figure 5.5. Irregular lineated segments are distinguished by initiation of near-summit, lineated volcanic features which clearly connect between volcanic edifices; these are interpreted as rifts. Summit vents, in one or more rows (*Winterer*, 1993; *Lynch*, 1993), are commonly elongated along the overall ridge azimuth. Flank contours

are often parallel and persistent along the entire segment even at upper levels suggesting that volcanism has occurred over the entire feature. Such flows appear as arcuate reflectors (especially for ship-facing slopes) radiating from a summit at upper levels or as steplike cuspate chains at mid-level. Most likely flows emanating from a linear crestal region seek the steepest grade resulting in parallel contours with time.

Near the base, satellite volcanoes and associated highly reflective seafloor extend both NNW and SSE from the western segment along a distinct abyssal hill azimuth. A chain of small equant seamounts 5 km to the south of the ridge segment follows the overall ridge azimuth (N105 ^{O}E). Tonguelike basal features are fans composed of debris flows and slumps; usually they are directly below amphitheaters and are volumetrically minor. Contours generally remain even and fairly steep almost to the base.

3.2.4 Large Prismatic Ridge Segment

The most distinctive members of the Pukapuka volcanic system are regular-shaped, large, elongate ridge segments with parallel base-to-crest contours, appearing singly (figure 5.6) or connected end-to-end. In general they resemble long prisms with a central high point (130.3; *Winterer*, 1993; *Lynch*, 1993) or even crest (125.1) that tapers towards the edges. Segments typically have relatively uniform cross-sectional slopes generally exceeding 20 ^{O} and steepening upward to about 30 ^{O} near the summit (*Winterer*, 1993). Summit edifices and calderas are absent. Though contours are universally very linear at all levels, some local flank contour linearity variation and over-steepening corresponds closely to upslope summit vents. Also, a stepped pattern is occasionally developed (119.2; *Winterer*, 1993) though treads do not maintain the same height along segment.

The along-segment asymmetry of this particular segment is noteworthy, reflecting interaction with crustal structure. The segment consists of a 14 km long plateau, capped with three elongate vents between a steeply dipping section to the west and a more moderate, stepped section to the east. While the eastern section tapers stepwise to distal portions, the western section truncates abruptly against a lineament oriented approximately NNW-SSE; an abyssal hill scarp is observable with the same trend to the north of

the western terminus and curving to the north. Other nearby abyssal hill scarps (not shown) have the same trend. Segment truncation against abyssal hill scarps or their projection appears universal (figure 5.1); single-segment endpoints (e.g. 126.1, 126.2, 127.6) and multi-segment intra-ridge boundaries (e.g. 122.1-122.2, 125.1-125.2, 125.3-125.4, 129.1-129.2-129.3, 131.1-131.2) correspond to large-offset abyssal hill scarps. This observation contrasts with the observation of small seamount preferential alignment along abyssal scarps, possibly reflecting the near-surface interaction of rising magma with a stress field disturbed by abyssal hill discontinuity and with seawater cooling (*Batiza and Vanko*, 1983). As for irregular, lineated ridges, tonguelike basal features extend below amphitheaters, but are volumetrically minor. Also, large overall segment volume is accompanied by decreased nearby volcanism as satellite volcanoes are rare.

3.2.5 Large Equant Edifices

Large, equant edifices (guyots and islands; figure 5.7) appear west of ~135 ^{o}W, in marked contrast to elongate features described above. Generally, they closely resemble older Pacific guyots well described by *Vogt and Smoot* [1984]. In particular, each edifice can be distinguished by an upper region of steep slopes and star-shaped radial protuberances (flank rift zones) and a lower region of more gentle slopes. Wahoo Guyot contains more than 5 rifts extending from the summit and upper flanks; a few exhibit terminal bifurcation. Rift orientation is clearly asymmetric, preferring a near east-west azimuth along the overall edifice and summit elongation direction. Deeper regions are covered by a moderate amount of debris (compare with 141.1-141.2, Napuka Island) organized in aprons issuing from intra-flank-rift amphitheaters. In the western Pacific such basal debris is a mixture of volcaniclastic and shallow water bioclastic and pelagic debris transported from upper levels by slumps and debris flows (*Menard*, 1956; *Vogt and Smoot*, 1984); a dredge of Wahoo Guyot recovered a zooxanthellate coral and phosphorite-containing planktonic formanifers from upper levels (*Winterer*, 1993). A few small satellite volcanoes are observed at lower levels.

4. PUKAPUKA MORPHOMETRY

4.1 Azimuth Persistence

The Pukapuka system is distinguished by the remarkable east-west elongation of large, prismatic ridges. Segments of all size ranges exhibit a persistent elongation azimuth (figure 5.8a). The mean azimuth of all ridges is N107 ^{o}E, though the dispersion is high for small segments. Dispersion is reduced as poorly constrained azimuth values (number of points <600; high standard deviation) are edited out; the mean value of well-constrained azimuths is N103 ^{o}E and nearly all values lie between N85 ^{o}E and N115 ^{o}E (figure 5.8b). The noteworthy exceptions are the westernmost ridge segments on the Tuamotus Plateau and a group of segments exhibiting a wide range of azimuthal orientations near 127 ^{o}W longitude which are associated with a prominent propagator (figure 5.8c). Otherwise, there is little variation of azimuth with longitude along the system. Importantly, even small ridge segments and seamount groups are elongated along an azimuth consistent with larger segments (though their dispersion is greater; figure 5.8d), indicating that a single process controls the azimuth of nearly all volcanic features regardless of size and location.

The mean orientation of segments is very close to the recent Nazca-Pacific relative spreading direction (N103 ^{o}E) and the Pacific-hotspot absolute motion direction (N102 ^{o}E) of NUVEL-1 and HS-NUVEL-1 models in this region (*DeMets et al.*, 1990; *Gripp and Gordon*, 1990). However, all samples obtained from the Pukapuka ridges (except the western islands) are younger than the spreading reorganization at 24 Ma. Therefor, while the overall system direction is N95 ^{o}E (chapter 4), the orientation of individual segments is nearly identical to the relative spreading and absolute motion directions during volcano formation time. A similar set of seamount chains and ridges east of the Pukapuka system and near the EPR axis (the Rano Rahi Field) exhibits a similar mean orientation (*Scheirer and Macdonald*, unpublished manuscript, 1995). If the ridges and seamount chains of both systems are not produced by a

small moving sublithospheric point-source then another mechanism is required to produce persistent orientation along the plate motion direction.

4.2 Linearity, Gradient and Form Variation with Height

Even a cursory examination of the system (figure 5.1) reveals that ridge segment linearity and surficial gradient increase with size; while seamount groups and small, irregular segments are widely dispersed and irregular, the crests of large, prismatic segments are highly linear and side-slopes are steeper. This is reflected in an increased standard deviation of grid-cell azimuths for individual segments with decreased height (not shown). As shown qualitatively in section 3.2, the Pukapuka system exhibits a regular form variation with size (figure 5.9a); while class assignment in section 3.2 is slightly arbitrary for small segments, clearly members of a given class constitute a particular size range. Thus, the acquisition of extended rift zones and parallel flank contours from base to crest (large, prismatic class) corresponds to a 1.5-2.5 km height range, radial symmetry characteristic of equant, western guyots (large, equant class) requires a 2.5 km minimum height and seamount chains and irregularly shaped ridge segments (small, irregular classes) are generally lower than 1.5 km.

The mean surficial gradient is the mean of all grid-cell slopes for a given segment. This value is naturally less than cross-sectional slopes taken from prismatic segment centers (see section 5.1). Ridge segment gradient increases nearly linearly with height from a minimum of 0.1 (5.7 ^{o}) for the seamount chain 123.2 up to 0.24 (13.5 ^{o}) for large prismatic segments 131.1 and 131.2 (figure 5.9b). Small volcanic fields and small, irregular ridge segments do not develop the steeply-sloped rift-zone morphology of large, prismatic ridge segments. If such rift zones represent lateral magma injection (*Ryan et al.*, 1981) then steeply dipping, intruded blade-like sheets are expected to sustain a steeper surficial gradient (see below). The large (>3 km), western, equant guyots have lower mean gradients reflecting the low angle of repose characteristic of volcaniclastic and shallow water bioclastic debris transported from shallower levels to deeper, low-slope aprons (*Vogt and Smoot*, 1984).

Considered together these results suggest that Pukapuka volcanics are produced by a process which yields a characteristic elongation in a direction persistent for all size ranges and throughout the survey. According to *Sandwell et al.* [1995] the component of slab-pull force parallel to absolute plate motion is exactly balanced by the integrated asthenospheric drag stress on the base of the plate, while the perpendicular, slab-pull force is transmitted between trenches. Thus near the spreading axis the maximum tensile stress (nearly north-south) is perpendicular to the absolute motion direction (nearly east-west). Therefore ridge segment orientation along the recent absolute spreading direction is consistent with the diffuse-extension model (*Sandwell et al.*, 1995) prediction near the paleo-spreading-axis. The form of features is a function of size. As height increases, ridge segments develop elongated rifts and increase surficial gradient and linearity. Thus conduit structure progresses from semi-parallel single fields to a single crestal rift. Interestingly, Pukapuka volcanic forms are not distributed randomly; instead similarly-formed segments congregate with some overlap (e.g. prismatic, 118 ^{o}W-122.5 ^{o}W; prismatic, 125 ^{o}W-127 ^{o}W; seamount group-small, irregular, 132.5 ^{o}W-135 ^{o}W; equant edifice, 135 ^{o}W-142 ^{o}W). A particular distinction is required for large, equant edifices in the west formed on older lithosphere (*Sandwell et al.*, 1995); these may be ascribed to a different process altogether.

5. PUKAPUKA PRISMATIC RIDGES AND HAWAIIAN FLANK RIFTS

It is clear that the growth of long rift zones and linear crests in the Pukapuka system is limited to large, prismatic segments. The development of flank rift eruptive centers is expected to be a natural consequence of size because increased summit height increases magma column basal pressure such that it is relatively easier to pump magma laterally into flank rift zones (*Vogt and Smoot*, 1984). Hawaiian volcanoes are noted for extending long, volcanic submarine rift zones as much as 100 km from their summits. Each of the 14 volcanic centers that constitute the Hawaiian chain from Kauai to Hawaii has two or more identifiable rift zones (*Fiske and Jackson*, 1972) which grow by lateral injection of thin, steeply-dipping, blade-like dikes. An injection event is generally observed by a down-rift eruption along fissures

oriented parallel to the regional rift zone trend and are accompanied by down-rift earthquake swarm migration and summit deflation. The morphologic resemblance of Pukapuka prismatic ridge segments to Hawaiian rift zones suggests that they are similarly formed.

5.1 Morphologic Similarity — Cross-section

Ridge cross-sections are a function of constructive and destructive processes. Puna Ridge is a 70 km long, northeast-trending volcanic rift, the submarine extension of the subaerial East Rift Zone of Kilauea volcano. Surface ship studies (*Malahoff and McCoy*, 1967; *Moore and Fiske*, 1969) and submersible investigations (*Fornari et al.*, 1978; *Lonsdale*, 1989) have shown that Puna Ridge consists of purely constructional volcanic terrain on its crest and upper flanks. While the crestal region appears fresh, flank regions are increasingly weathered and covered with sediment down slope (*Fornari et al.*, 1978; *Lonsdale*, 1989). Mass wasting events produce fault-blocks at upper levels and redeposition at lower levels. Because Puna Ridge is young relative to other Hawaiian rifts, it exhibits the dominance of volcanic/intrusive constructive processes rather than slumping events and carbonate reef terrace development (*Fornari*, 1987). Pukapuka prismatic ridges also exhibit a dominance of construction over mass wasting processes, as noted before.

The transverse profile of Hawaiian rift-zone ridges is controlled at the crest by the width of the dike intrusion zone and on the flanks by the mobility of erupted lavas at young ages and susceptibility to slumping at older ages (*Fornari et al.*, 1978; *Lonsdale*, 1989). Puna Ridge and most prismatic Pukapuka ridges are very similar in cross-section (figure 5.10a). Almost the entire length of Puna Ridge contains a 11-km-wide dike complex (*Malahoff and McCoy*, 1967) and most of the ridge crest has a flattened axial area 2-3 km wide (*Lonsdale*, 1989). The low mobility of Puna pillow lavas accounts for narrow ridges imposed on the crestal flattening. Similarly, prismatic Pukapuka ridge segments are characterized by a narrow summit platform a few kilometers wide capped by elongate vents. Puna Ridge flanks dip nearly smoothly with an average slope of 8-12 ^{o}, with intermittent, small, arcuate, outward-facing scarps that are

interpreted as slope failure scars (*Lonsdale*, 1989); also talus ramps photographed on steep slopes are attributed to superficial mass wasting. Pukapuka prismatic segments are as even in slope but universally steeper, with 19-27 ^{o} slopes over central portions. *Fornari* [1987] attributes asymmetric over-steepening to lack of buttressing by surrounding edifices. A survey of asymmetric slopes of Pukapuka ridges fails to confirm such a relation (table 5.1; figure 5.10a). Perhaps like Loihi Seamount's western block (*Fornari*, 1987) Pukapuka segments are underlain by a dike complex that is more resistant to weathering as dredging near ridge crests was mostly unsuccessful (*Winterer*, 1993).

5.2 Morphologic Similarity — Along-section

A dike propagates if its stress-intensity factor is greater than a critical value, K_C, the fracture toughness of the rock (*Rubin and Pollard*, 1987). For a dike to propagate laterally with a stable height, the stress intensity factor, K, must exceed K_C at the down rift edge and must be less than K_C at top and bottom. Essentially, this means that vertical dike trapping requires the driving pressure within the dike to be larger in the center than at the top and bottom. The factors influencing stress intensity are far more complex than the simple porous volcano, hydraulic potential models of *Lacey et al.*[1981] and *Angevine et al.* [1984] and include both factors pertaining to dike geometry and to the driving pressure (the difference between the magma pressure and the remote stress) acting on the dike plane (*Rubin and Pollard*, 1987). Dike internal pressure factors include reservoir magma pressure, density and vesiculation which affect the vertical driving forces, and viscous head loss which reduces lateral driving with distance. Remote stress factors include edifice density stratification, ridge gravity loading (*Fiske and Jackson*, 1972), previous intrusions, thermal memory, faulting (*Dietrich*, 1988) and plate tectonic forces. The final along-axis plunge angle of a given rift is a function of variation in all these in addition to the time-integrated effects of subsidence. Therefore, while the along-axis profiles of Hawaiian rifts are generally smooth, axial submarine plunge angle prediction (away from coralline platforms) is not straightforward.

In general the slope angles of Hawaiian volcanoes decrease with length, ranging from 10 ^{o} for the young, small Loihi seamount (*Fornari et al.*, 1988) to 3 ^{o} for Puna Rift (*Lonsdale*, 1989); ruggedness is related to eruptive activity recency. They exhibit a rounded nose profile, with increasing plunge angle at distal portions, rather than tapering smoothly (*Lonsdale*, 1989). The along-axis profiles of prismatic Pukapuka ridge segments (figure 5.10b) are less smooth and more variable but in general plunge angles are similar. The along-axis profiles of Pukapuka prismatic ridges can be distinguished by three domains, a jagged crestal portion, a moderately dipping flank rift and a rounded nose with increased dip. Bumps along the crestal portion correspond to circular and elongate vents and share a common plateau depth. As well, flank rift plunge angles decrease with length from 11 ^{o} (130.3, 131.1 and 131.2) to 2.7 ^{o} (122.2).

6. DISCUSSION

6.1 Pukapuka Ridges — A Hawaiian Rift Model?

Dikes naturally propagate normal to the least principal stress direction (*Anderson*, 1972) and continued injection extends a dike down-rift along the long axis. In general, the location, orientation and persistence of dike injection within the flank rift of a shield volcano, such as Hawaii, is constrained by the location and height of the summit caldera, by a driving pressure that requires lateral extension and by local stress directions. In Hawaii, these sources of stress are usually attributed to the topographic response to gravitational force. *Fiske and Jackson* [1972] demonstrated with fluids injected into the axes of prismatic gelatin molds that gravitational sag within an elongate ridge focuses fluid propagation along the axis; as well, neighboring edifices generate a tensional stress field which controls the trend of radial dikes or rift zones. In this manner, the Puna Ridge is fixed by the buttressing of Mauna Loa's East Rift while the north-south orientation of Loihi is dictated by the position of Kilauea's East and Southwest rift zones. Therefore, the elongate shape of closely-packed, ridge-like edifices is expected to maintain local stress field

persistence and dike emplacement direction. *Wyss* [1980] alternatively contends that the orientation of a new rift is along the greatest compressive stress direction which radiates from older edifices.

Clearly, the morphologic and morphometric similarity of Hawaiian flank rifts and the large prismatic Pukapuka ridge segments suggests that their internal conduit structure and eruptive and mass-wasting modes are similar. However, two main problems remain. First, while Hawaiian-type rifts (such as the Puna Ridge) laterally project from a cylindrical summit caldera, there is no equivalent summit region for Pukapuka prismatic ridge segments. Instead, the entire crestal region is elongate and very narrow. Similarly, Loihi seamount has been dominated by constructional volcanism from early ages (*Fornari et al.*, 1988); if it had been dominated by summit eruption then it would have acquired a circular form with rifts as radial appendages. Long-term magmatic and volcanic activity along rift zones results in pronounced elongation. Nevertheless, Loihi still has a small summit region. The prismatic Pukapuka segments exhibit no equivalent central, circular conduit; instead the jagged narrow crestal plateaus (>50 km for segment 125.1) are likely underlain by an elongate complex of rising dikes. Individual shallow crestal regions (~3 for segment 125.1) may correspond to coaligned robust sources.

Second, models involving rift gravitational sag and control by other edifices (*Fiske and Jackson*, 1972; *Wyss*, 1980) cannot apply to produce the Pukapuka prismatic ridges because most ridge segments exist in isolation or end-to-end (figure 5.1). Essentially, bilateral rift symmetry is inconsistent with a hydrofracture model in absence of a regional stress, because a third arm is expected to develop in an isotropic stress distribution. Therefor, alternative mechanisms must be considered which maintain persistent azimuth for all ridge segments and which produce elongated primary eruptive centers. Two principal factors, regional tectonic stress and reservoir elongation are considered below.

6.2 Tectonic Regional Stress — Seafloor and Ascent Processes

The preferred orientation of Pukapuka volcanic segments normal to the least compressional stress direction predicted by the stretching model (*Sandwell et al.*, 1995) suggests that a tectonic regional stress

controls azimuth. *Nakamura* [1977] defined tectonic stress regimes (extensional versus contractional) and principal stress directions based on the orientation of dike fissures. Fissures are vertical in cross-section and directed horizontally along the plane defined by the greatest and intermediate principal stress directions. The orientation of principal local stresses governing a given volcano can be mapped out based on the strike of its dike and rift systems, central conduit elongation and parallel flank contour development (*Nakamura*, 1977; *Nakamura et al.*, 1977); a linear edifice alignment and common rift zone direction for a field of volcanoes are ascribed to a tectonic stress that governs the whole area. If this model is extended to the Pukapuka region then the persistent orientation of fissures and eruptive events along the rift-dominated ridges is determined by a regional tectonic stress pattern consistent with *Sandwell et al.* [1995]'s prediction of nearly north-south directed tension.

An additional cause of edifice elongation and orientation may relate to processes occurring during melt ascent from magmagenic regions in the upper mantle to crustal magma chambers and to the surface. Over the past 15 years a number of numerical and mechanical models have demonstrated that fracture propagation is the primary mechanism by which positively buoyant magmas are transported through the lithosphere (*Maaloe*, 1987; *Lister*, 1990; *Spence and Turcotte*, 1990; *Takada*, 1990; *Lister and Kerr*, 1991; *Heimpel and Olson*, 1994). According to such models, when a crack is sufficiently large and the fluid sufficiently buoyant, the leading edge stress intensity exceeds the fracture toughness of the surrounding country rock and the fracture propagates upward. As for rift-zone dikes, rising cracks are oriented along the plane defined by the maximum and intermediate compressive directions and are shaped like inverted tear drops in cross section.

Recently, *Takada* [1994a-c] has examined the role of buoyancy-driven and pressurized-crack interaction in the accumulation of magma during ascent. On the basis of viscous fluid-gelatin tank experiments and numerical stress analysis *Takada* [1994a] tested the coalescence of cracks with variable crack separation and relative height. Systematically, crack coalescence and preferential direction are a function of supply rate, principal stress orientation and deviatoric stress (the difference in principal stress magnitude). First, vertical propagation requires that the minimum compressive component is horizontal; a

maximum component in the vertical plane may lead to normal faulting. Second, if the orthogonal horizontal stress components are sufficiently unequal, then a parallel crack system normal to the least compressive stress is expected; if they are equal, then a radial crack system is expected. Third, with a decreasing difference between the vertical and minimum horizontal components and/or an increasing magma production/supply rate, magma is increasingly focused in space along an azimuth normal to the least compressive stress; a preferred linear magma path is formed which maintains the continuity of eruptive sites with time (*Takada*, 1994b).

The deviatoric stress-buoyant rising crack interaction mechanism in conjunction with the tectonic stress orientation predicted by *Sandwell et al.* [1995] agree with several observations of the Pukapuka volcanic system. *Sandwell et al.* [1995] predicts a lithostatic vertical stress (maximum), tension oriented nearly north-south (minimum), and gradually increasing east-west tension (intermediate) with distance from the spreading axis. Therefor east-west cracks are predicted near the axis and radial cracks are predicted on older, distant seafloor where the horizontal components are closer. This is consistent with the progression from elongate rifts to equant guyots and islands from young to old seafloor (at formation time). An additional contribution to an isotropic reservoir distribution may be longer ascent paths for large, equant guyots. Alternatively, this variation could be related to formation of older, equant volcanoes before tension initiation. The Pukapuka ridge segments exhibit a distinct variation of form with height, as extended linear rift zones develop only for segments taller than 1500 m. Subregions of the system are characterized by similar features. If the height of ridge segments is indicative of magma production or supply rate, then perhaps the progression to prismatic ridges represents greater coalescence and accumulation of magma-filled cracks during ascent, where the convergent magma path corresponds to the central crestal location. In this case a subregion of similarly formed segments corresponds to coeval events with the same deviatoric stress, lithospheric thickness and magma supply rate parameters.

The planar distribution of sublithospheric magma is likely an important factor as seamount clusters are elongate along the same direction as larger features even in absence of crack-mechanics related topography. An elongate magma lens beneath the East Pacific Rise axis supplies magma in one or more

coaligned centers to buoyantly-rising and laterally-spreading dikes yielding a sheeted dike complex above. Perhaps the uniform elongation and orientation of most Pukapuka system volcanoes is attributed to elongate or coaligned partial melt reservoirs (*Gurnis*, 1986; *Scheirer and Macdonald*, unpublished manuscript, 1995) where central-rift-dominated volcanism results from an augmented, coalescing supply and a preferred crustal magma path. The mechanisms described above may act cooperatively; for example, Hawaiian-model lateral flank dike propagation away from an edifice magma chamber is expected to follow the rise of buoyancy-driven, fluid-filled cracks through lithosphere characterized by varying degrees of deviatoric stress.

6.3 Magma Overpressure and Fault Suppression

The absence of normal faulting evidence within the Pukapuka system has been a principal criticism of the diffuse extension (*Sandwell et al.*, 1995) and volcano-fault-nucleation (*Lynch*, 1993) models. A careful review of multibeam bathymetry and sidescan imagery confirms the absence of surficial features consistent with faulting. Nevertheless, extension need not necessarily be attended by a great deal of normal faulting if magmatism is pervasive. For example, extension at the East Pacific Rise, East African Rift and Snake River Plane is accommodated by increased magmatism (*Parsons and Thompson*, 1991). Tabular basaltic intrusions acting against and increasing the magnitude of the minimum compression direction (reducing deviatoric stress) act to suppress normal faulting and the accompanying topographic relief and seismicity (*Parsons and Thompson*, 1991). Robust volcanism evidenced by pervasive Pukapuka volcanoes and regional altimetry gravity anomaly bumps attributed to volcanoes south of the Marquesas Fracture Zone (chapter 4) indicates that abundant melt sources may exist beneath the lithosphere. Possibly, numerous dikes are emplaced in addition to a large number of extrusive events that comprise observed surficial features. Thus, it may be possible that a small amount of regional, north-south directed extension is relieved by east-west oriented vertical dike emplacement.

7. CONCLUSIONS

1) Though the morphology of Pukapuka ridges is consistent with north-south extension, the lack of normal faulting evidence excludes a dry-fracture mechanics model.

2) Pukapuka segment morphologic form is a function of size. With increased height, east-west oriented summit vents, flank rift zones and a narrow linear crestal ridge are developed. Azimuth is persistent for all size ranges while linearity and horizontal gradient increase with size. Features of similar form congregate regionally. Thus features are formed by a similar process with a variation in governing parameters such as lithospheric thickness, deviatoric stress and magma supply.

3) Small seamounts are preferentially located on abyssal hill scarps, whereas small, irregular ridges are perturbed along abyssal hill directions and large, prismatic ridge segments truncate abruptly.

4) Pukapuka prismatic ridge segments resemble in form large, submarine, Hawaiian flank rift ridges, suggesting that their internal structure and eruptive and mass-wasting modes are similar.

5) An additional source of regional stress is required. The preferred orientation of volcanic segments normal to the least compressive stress direction predicted by *Sandwell et al.* [1995] in the region suggests that tectonic stress controls azimuth. North-south directed tension affects stress regimes during ascent and within growing edifices.

6) Pukapuka morphologic trends may be explained by variable coalescence between buoyancy-driven, fluid-filled cracks and the formation of a preferred magma path which increases with increased magma supply or decreased deviatoric stress.

7) Though normal faults are not observed in the model, north-south directed tensional stress may have occurred during volcano formation as normal faulting may be suppressed in this region due to the abundance of available magma.

Figure 5.1 Color-scale contiguous multibeam bathymetry map sections of the Pukapuka volcanic system (Gloria legs 3b and 4, Westward legs 1 and 4, RC2608, Tune02wt). The contour interval is 200 meters. Ridge segments and seamount clusters are labeled by longitude.

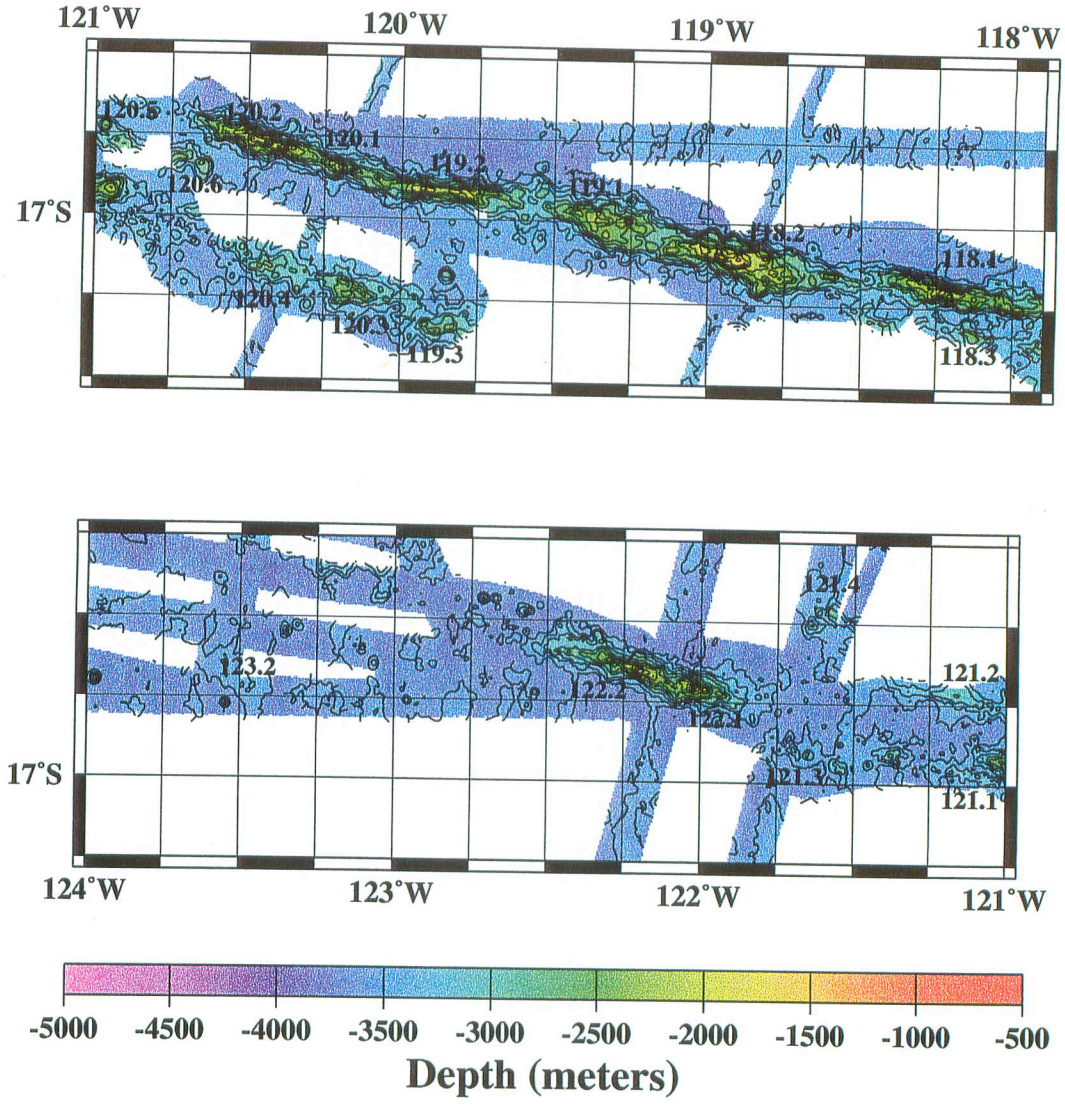
121°W
120°W
119°W
118°W
17°S
120.5
120.2
120.1
119.2
119.1
120.6
118.2
118.1
120.4
120.3
119.3
118.3
124°W
123°W
122°W
121°W
17°S
123.2
122.2
122.1
121.4
121.2
121.3
121.1
-5000
-4500
-4000
-3500
-3000
-2500
-2000
-1500
-1000
-500
Depth (meters)

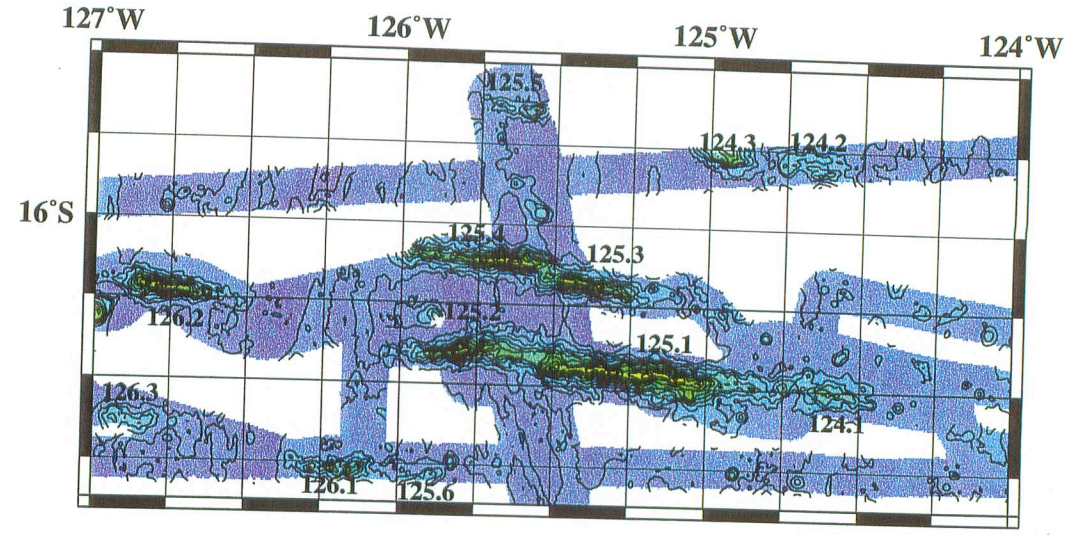
127°W
126°W
125°W
124°W
16°S
125.5
124.3
124.2
125.4
125.3
126.2
125.2
125.1
126.3
124.1
126.1
125.6

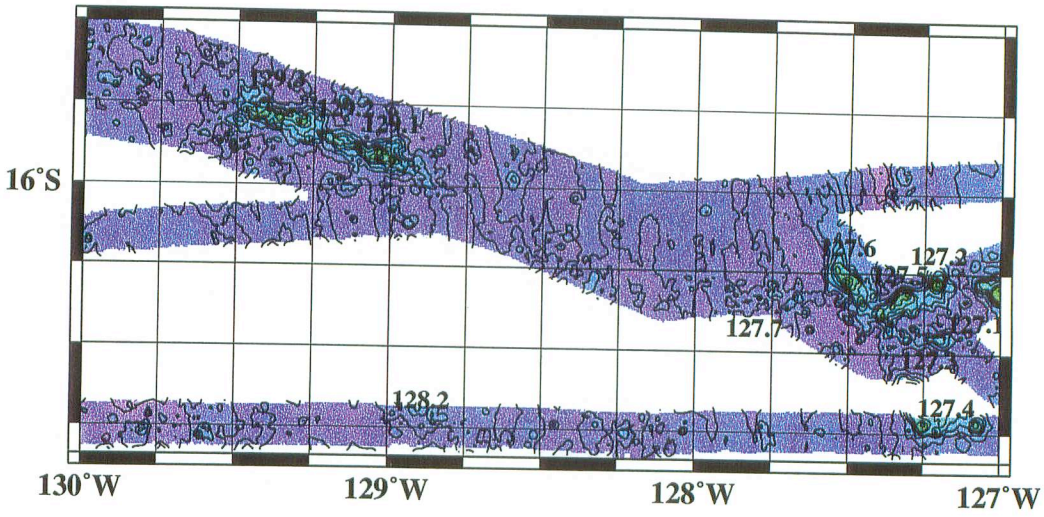
16°S
127.6
127.3
127.7
128.2
127.4
130°W
129°W
128°W
127°W

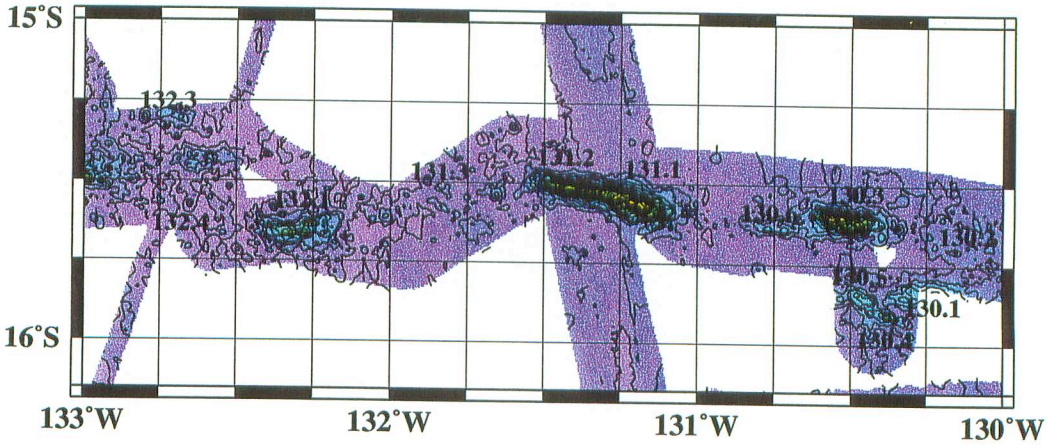
15°S
132.3
131.3
131.2
131.1
132.4
130.2
130.1
16°S
133°W
132°W
131°W
130°W

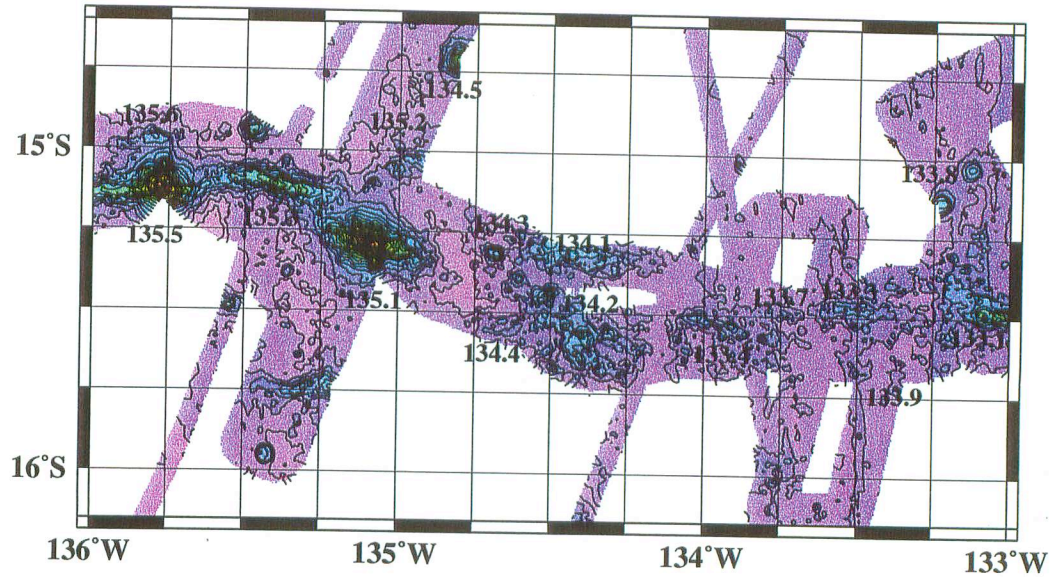
15°S
16°S
136°W
135°W
134°W
133°W
134.5
135.2
133.8
135.5
134.3
134.1
135.1
134.2
134.4
133.9

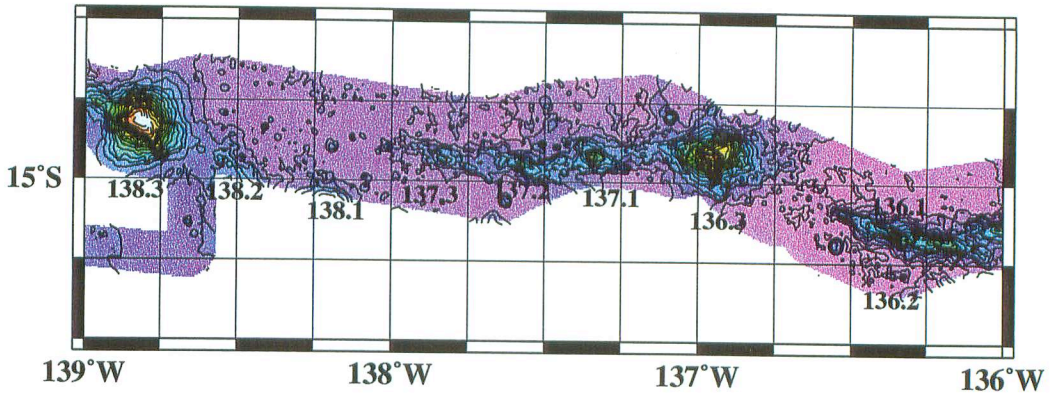
15°S
139°W
138°W
137°W
136°W
138.3
138.2
138.1
137.3
137.1
136.3
136.1
136.2

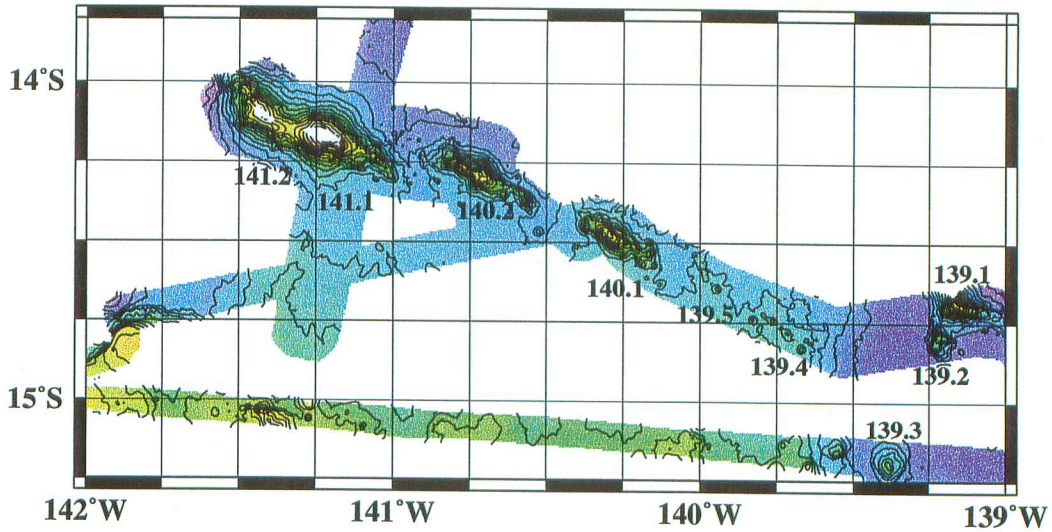
14°S
15°S
142°W
141°W
140°W
139°W
141.2
141.1
140.2
140.1
139.5
139.1
139.4
139.2
139.3

Abyssal Hills

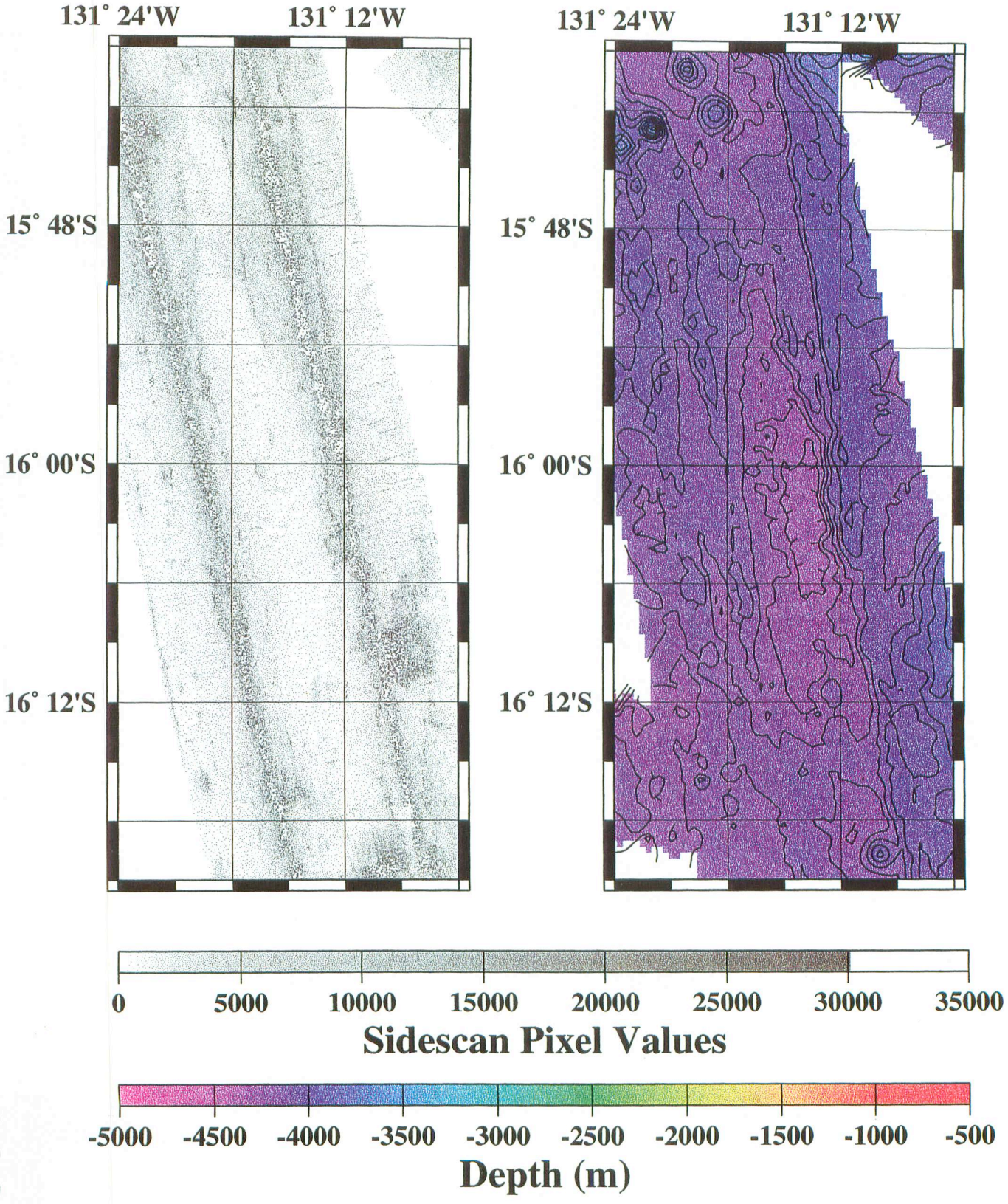

Seamount Cluster (and Volcanic Flows?)

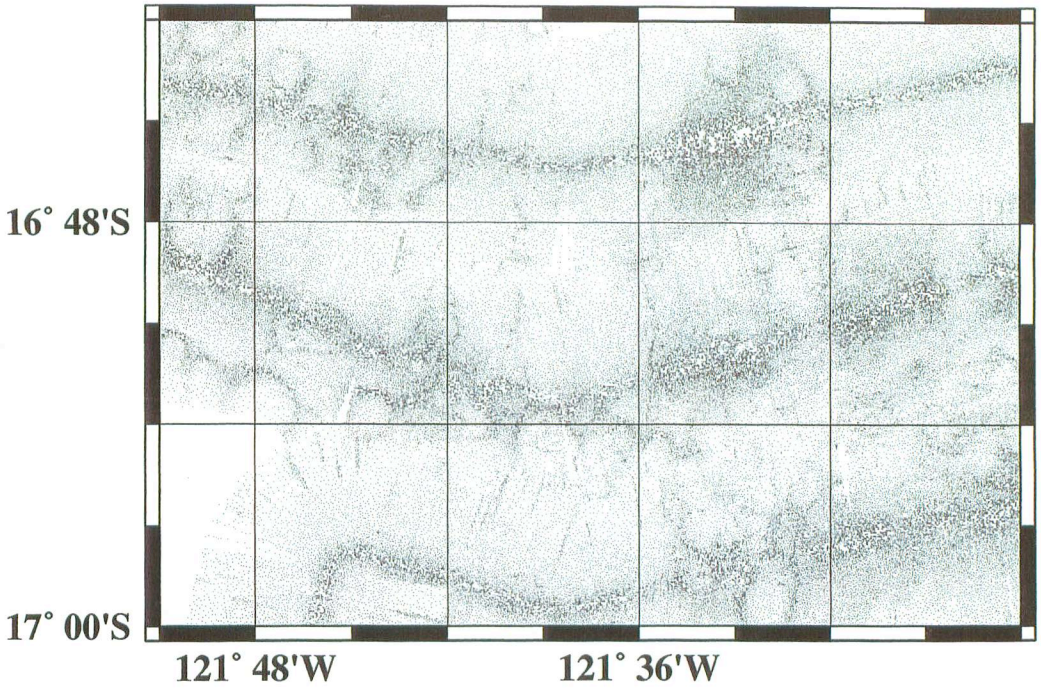

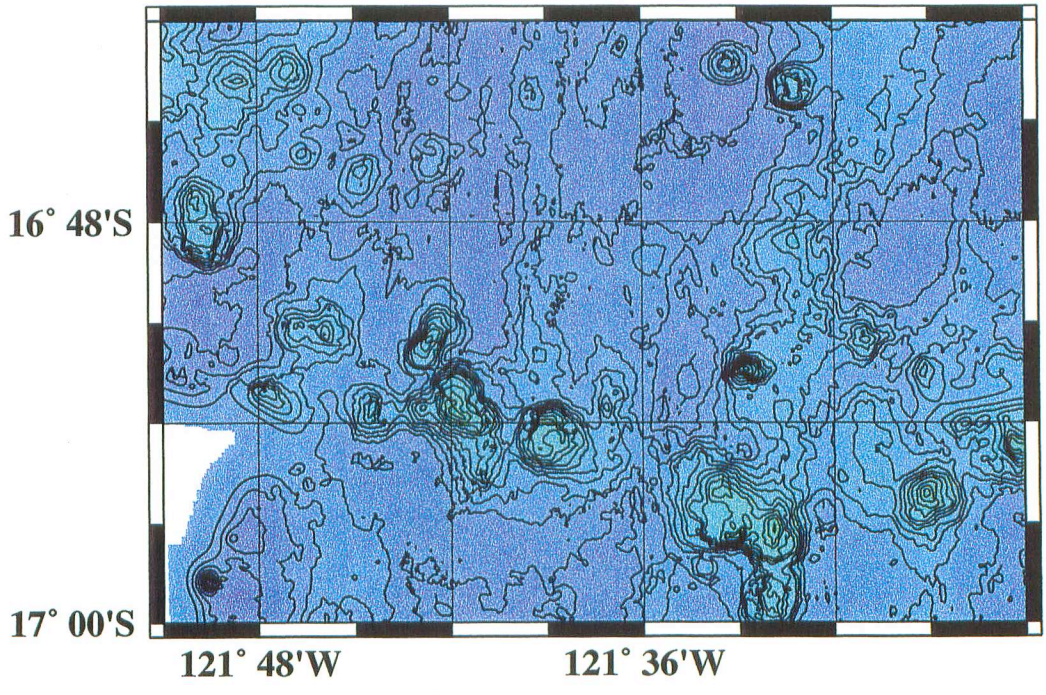

Small Irregular Ridge Segments

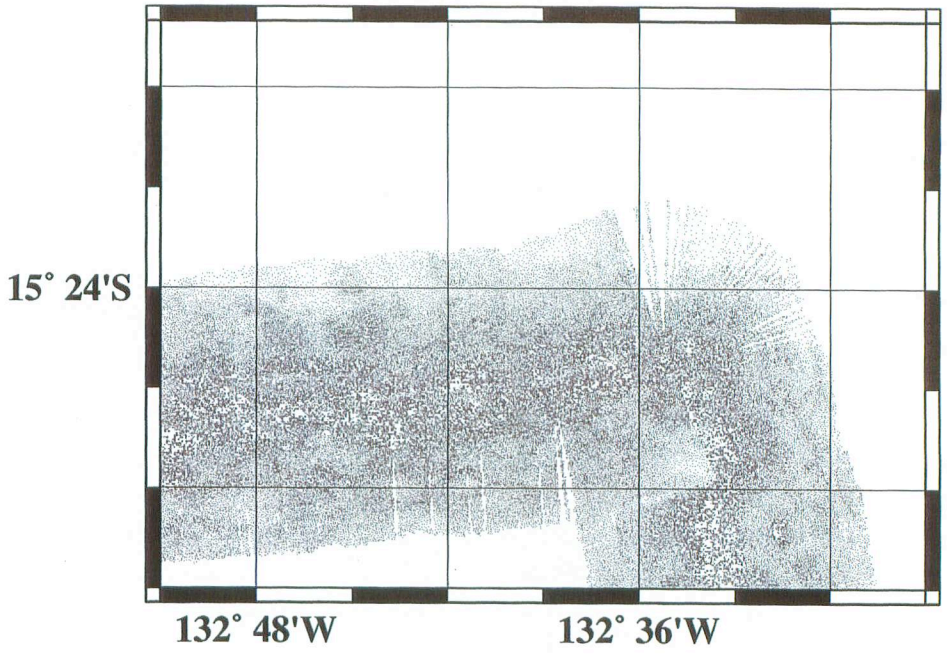

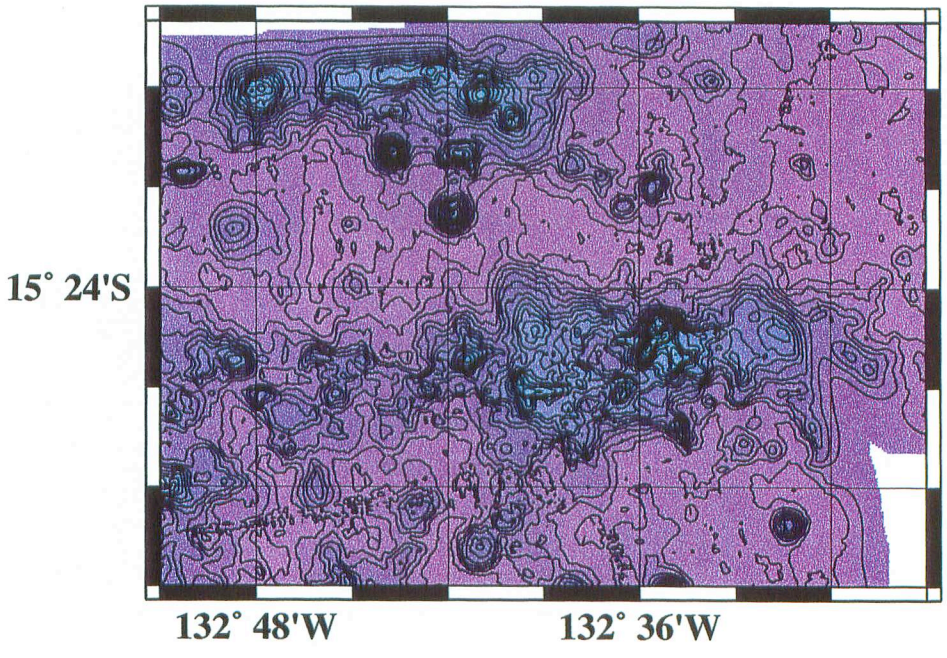

Irregular Lineated Ridge Segment Chain

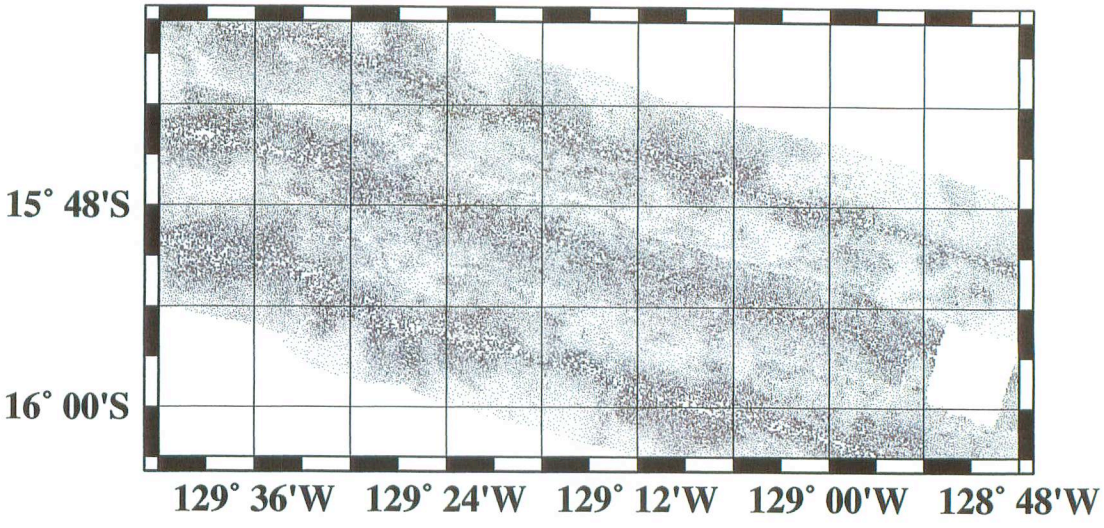

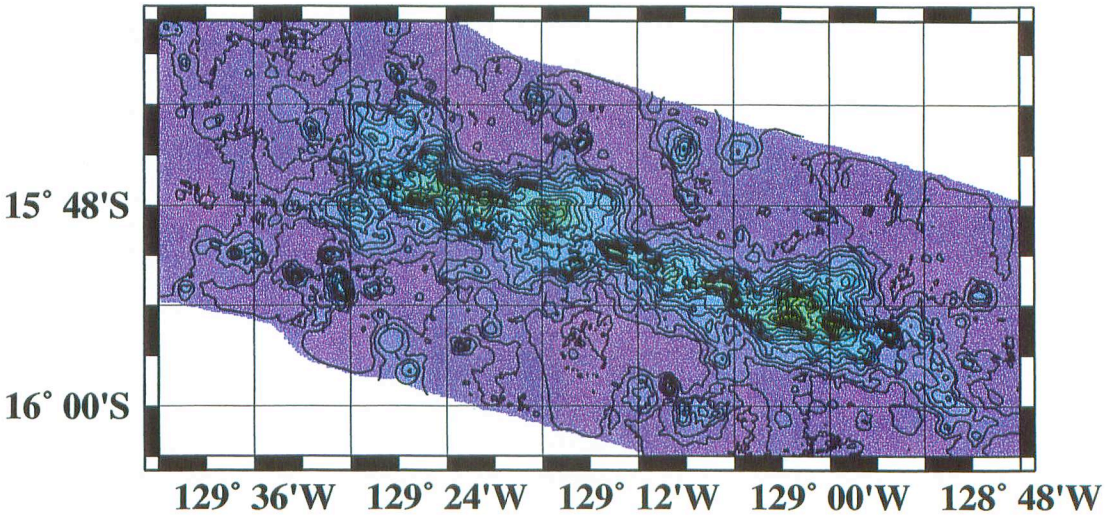

Large Prismatic Ridge Segment

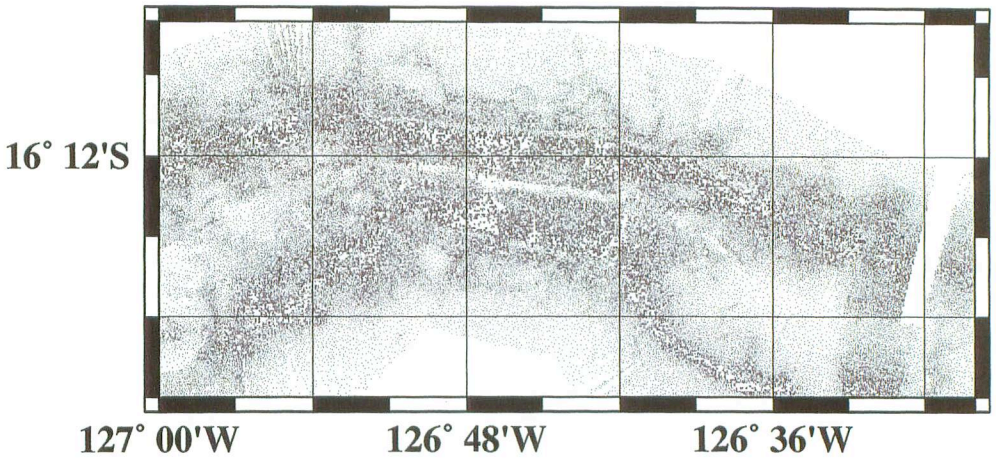

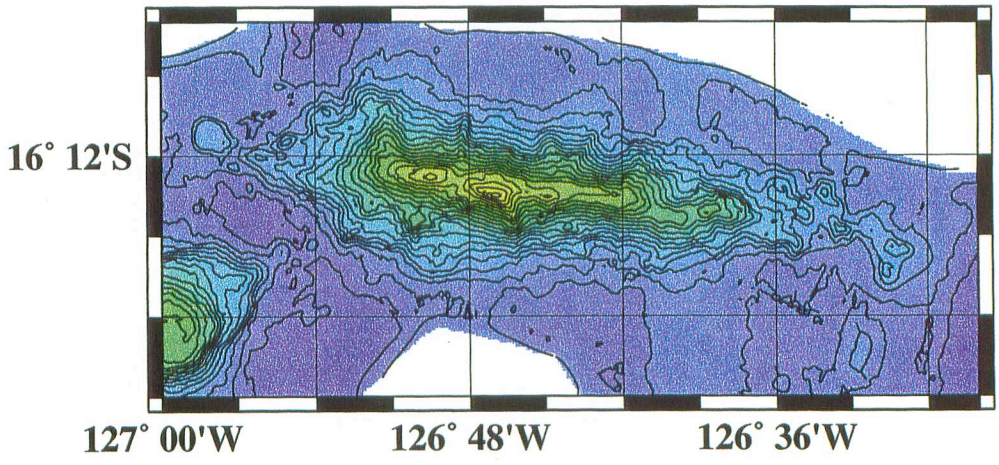

Large Nearly-equant Volcano

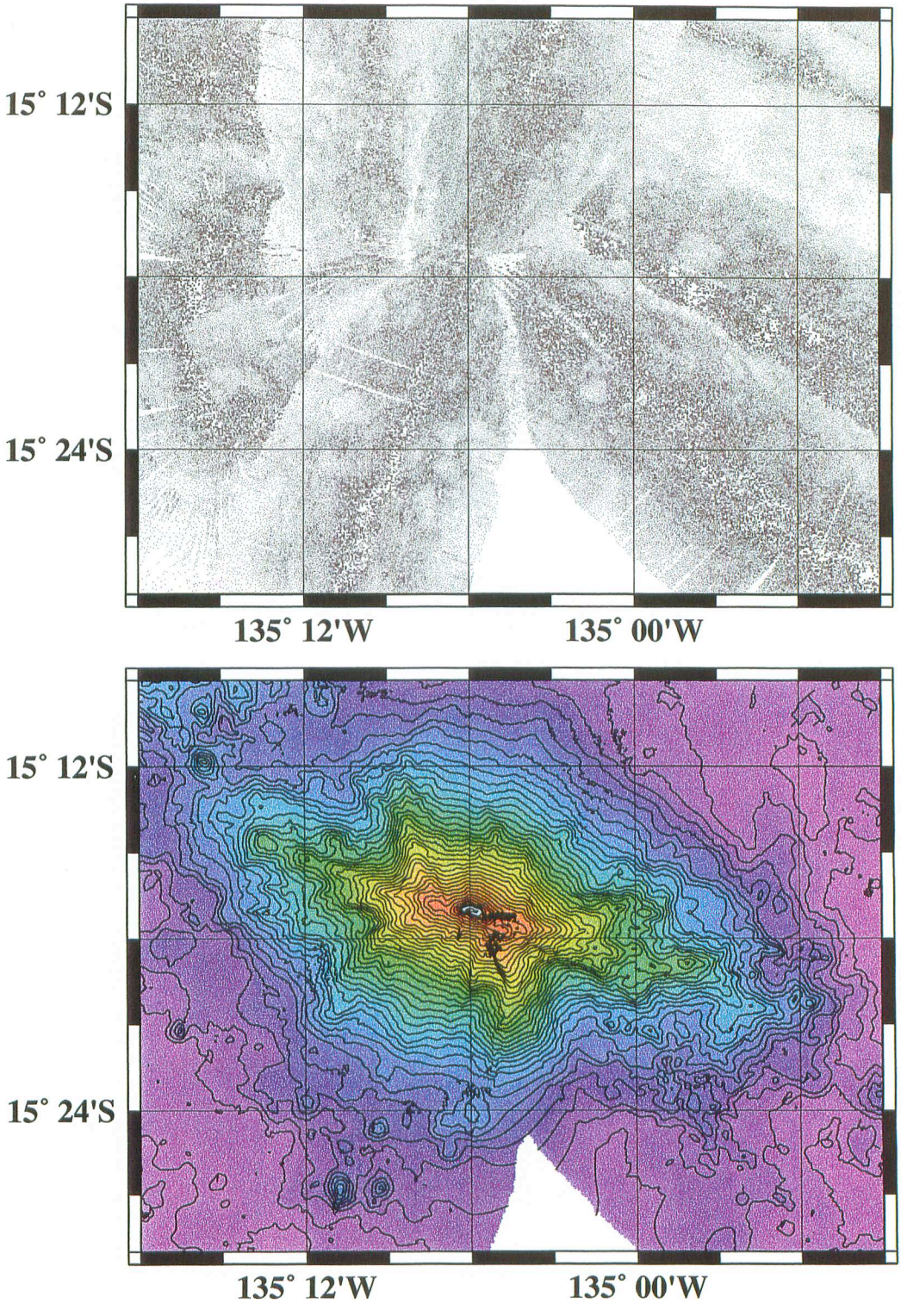

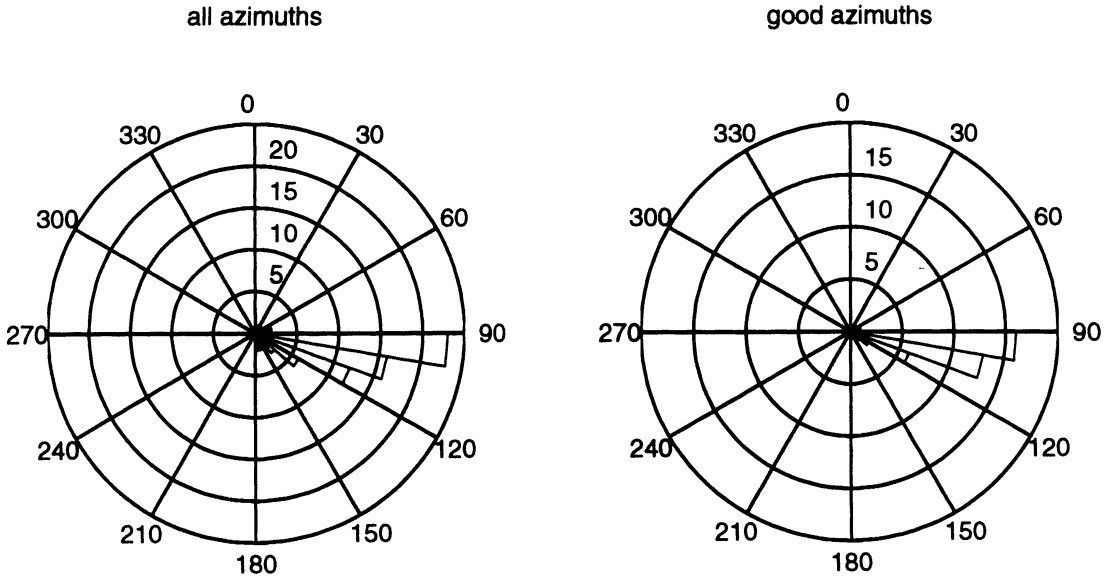
all azimuths
good azimuths
0
30
60
90
120
150
180
210
240
270
300
330
20
15
10
5
15
10
5

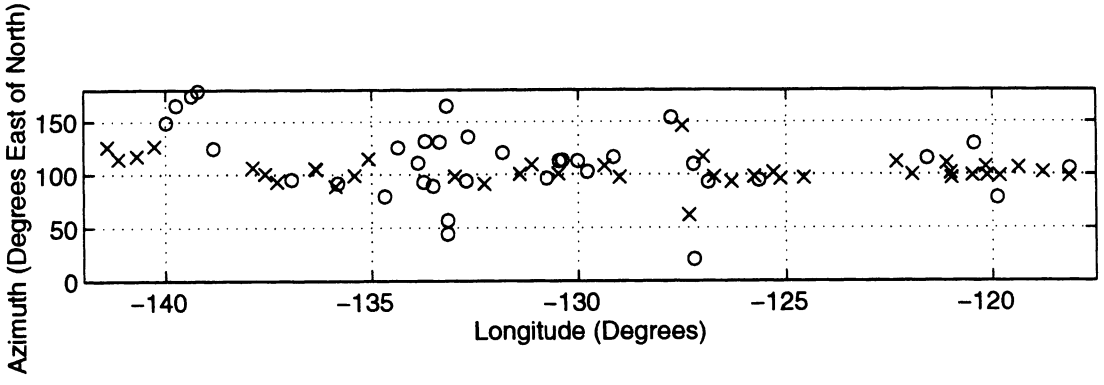
Azimuth (Degrees East of North)
150
100
50
0
−140
−135
−130
−125
−120
Longitude (Degrees)

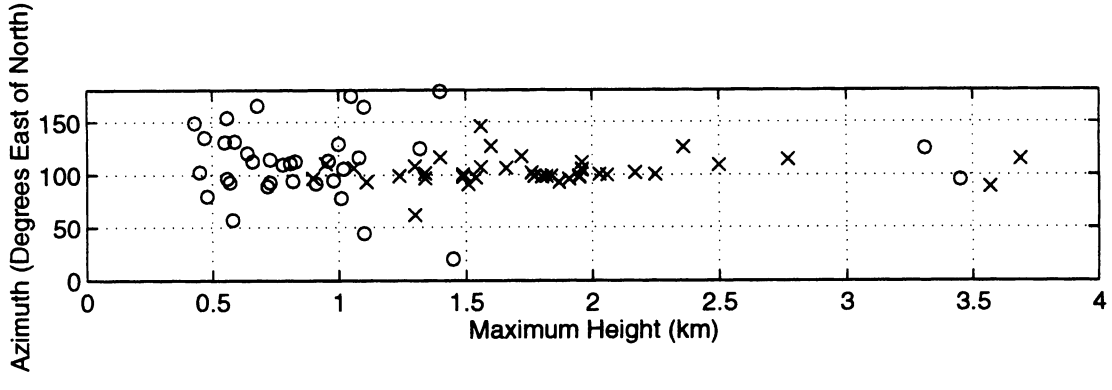
Azimuth (Degrees East of North)
150
100
50
0
0
0.5
1
1.5
2
2.5
3
3.5
4
Maximum Height (km)

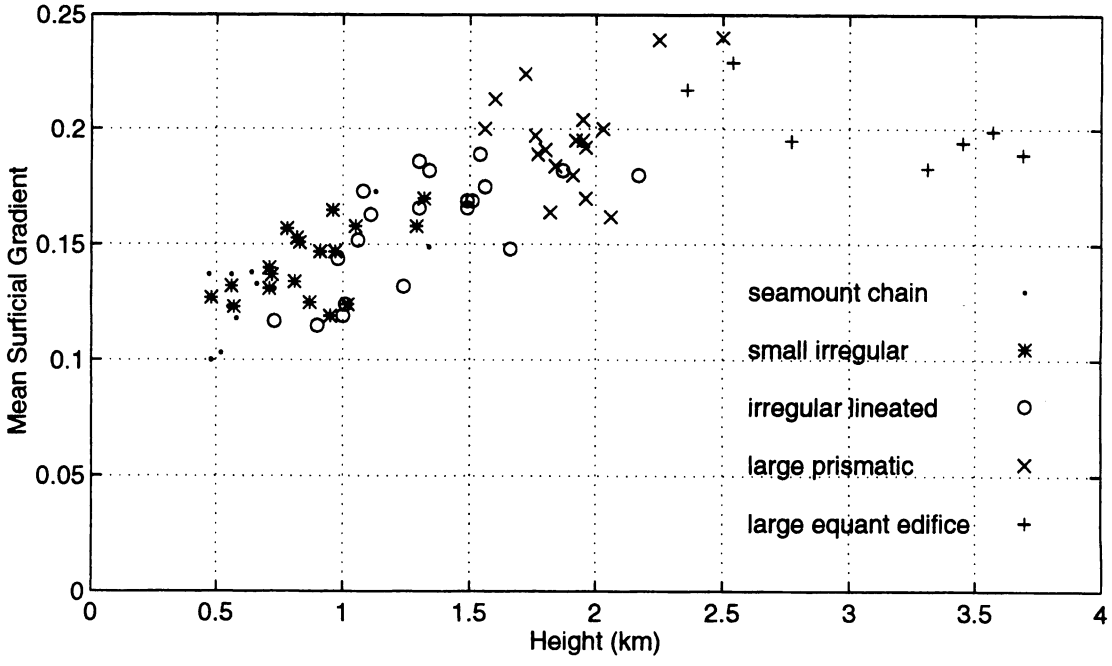
Mean Surficial Gradient
Height (km)
seamount chain
small irregular
irregular lineated
large prismatic
large equant edifice
0.25
0.2
0.15
0.1
0.05
0
0
0.5
1
1.5
2
2.5
3
3.5
4

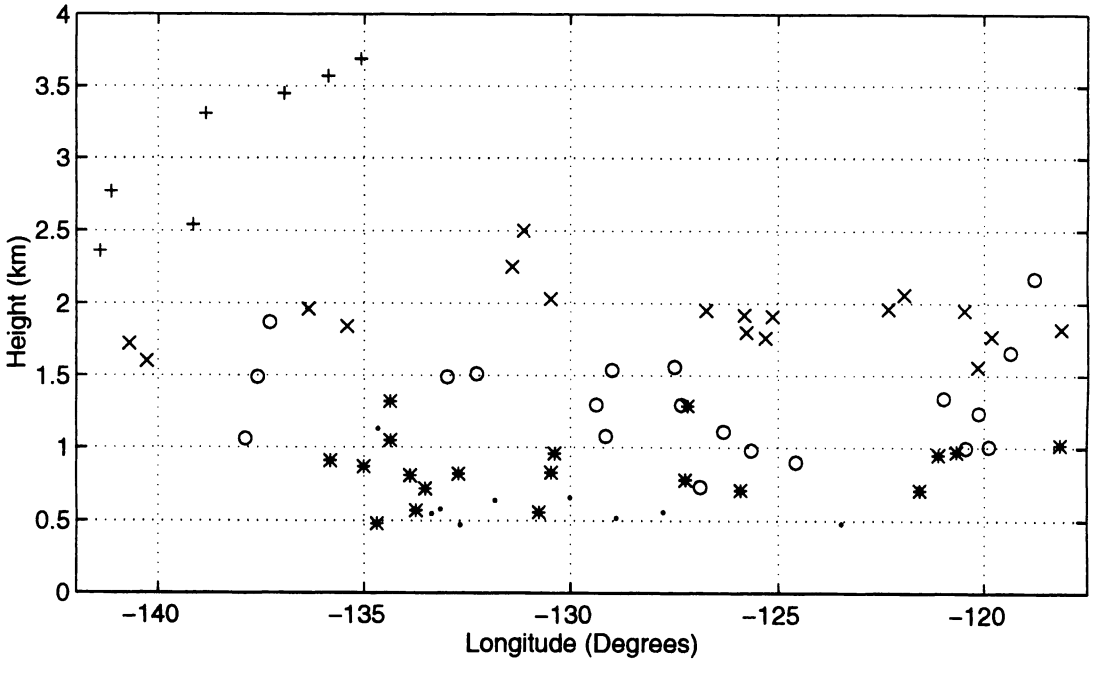
Height (km)
Longitude (Degrees)
4
3.5
3
2.5
2
1.5
1
0.5
0
−140
−135
−130
−125
−120

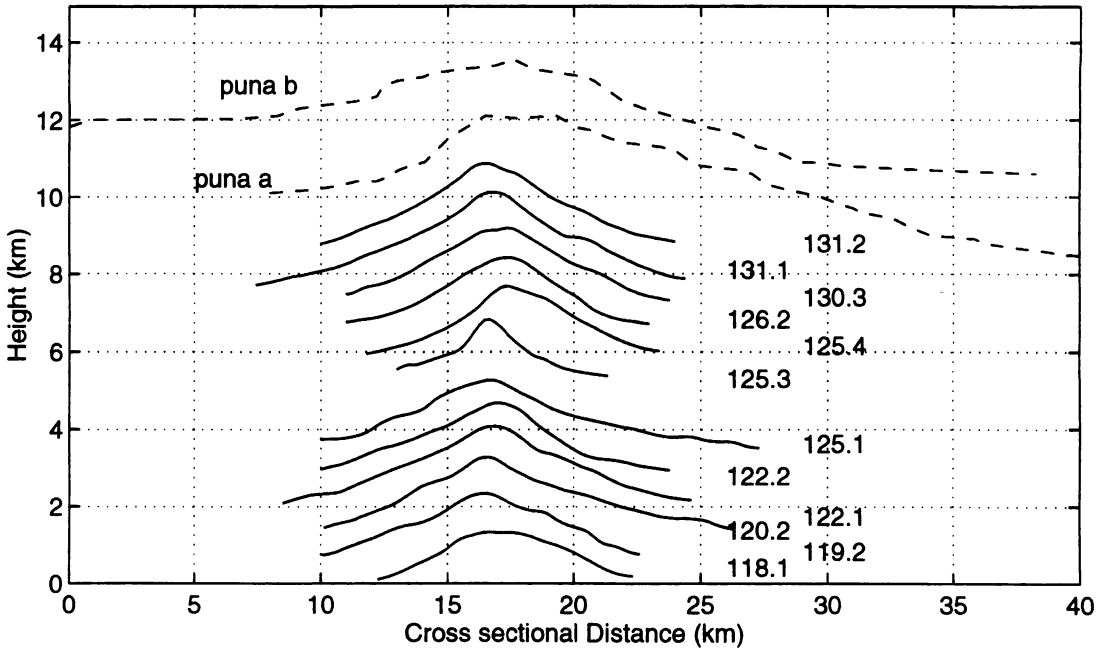
puna b
puna a
131.2
131.1
130.3
126.2
125.4
125.3
125.1
122.2
122.1
120.2
119.2
118.1
Height (km)
Cross sectional Distance (km)

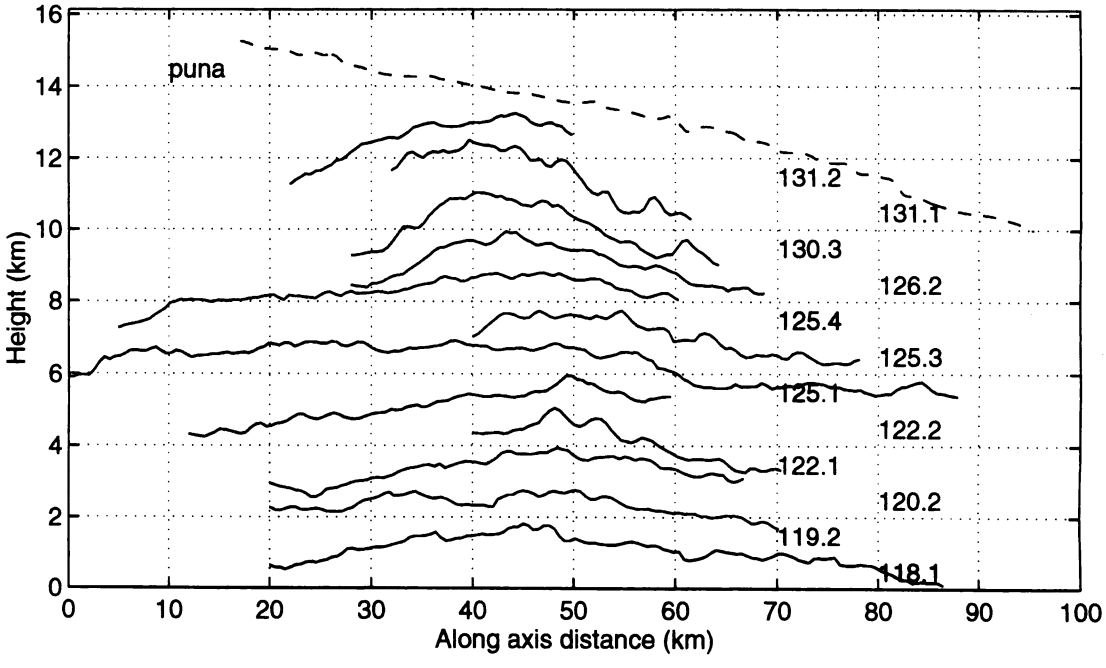
puna
131.2
131.1
130.3
126.2
125.4
125.3
125.1
122.2
122.1
120.2
119.2
118.1
Height (km)
Along axis distance (km)

Table 5.1

Segment	Longitude		Latitude		Type	Length	Width	Azimuth	Maximum	Mean Height	Volume Height	Cross	Gradient Gradient	
	West	East	South	North										
						km	km	N°E		km	km	km^3	(n,s)	
118.1	-118.47	-117.82	-17.28	-17.10	lpr	60.5	9.5	97		1.82	0.53	539	0.22,0.19	0.16
118.2	-119.09	-118.47	-17.26	-16.98	ilr	43.5	15.5	102		2.17	0.66	860	------	0.18
118.3	-118.23	-118.05	-17.38	-17.27	sir	17.0	8.0+	(106)		1.02	0.37	84	------	0.12
119.1	-119.58	-119.16	-17.13	-16.85	ilr	39.0	16.5	106		1.66	0.56	569	------	0.15
119.2	-120.07	-119.58	-17.02	-16.83	lpr	47.0	11.0	99		1.77	0.60	541	0.26,0.27	0.19
119.3	-120.03	-119.73	-17.40	-17.23	ilr	20.0	9.0	(78)		1.01	0.35	177	------	0.12
120.1	-120.26	-120.07	-16.93	-16.78	lpr	19.0	10.0	107		1.56	0.56	166	------	0.20
120.2	-120.72	-120.26	-16.89	-16.67	lpr	45.0	14.0	99		1.95	0.55	523	0.29,0.21	0.20
120.3	-120.29	-119.97	-17.33	-17.13	ilr	30.0	11.0	99		1.24	0.43	265	------	0.13
120.4	-120.60	-120.29	-17.25	-17.07	ilr	21.5	9.5	(129)		1.00	0.37	191	------	0.12
120.5	-121.12	-120.87	-16.97	-16.83	ilr	22.5	9.5	97		1.34	0.40	125	------	0.18
120.6	-120.75	-120.60	-16.91	-16.77	sir	13.5+	7.5	------		0.97	0.36	85	------	0.15
121.1	-121.25	-120.78	-17.13	-16.85	sc	39.5	5.5	101		1.34	0.27	208	------	0.15
121.2	-121.40	-120.83	-16.82	-16.67	sir	56.0	8.0	111		0.95	0.30	179	------	0.12
121.3	-121.82	-121.37	-17.02	-16.83	sc	37.5	5.0	(115)		0.73	0.18	66	------	0.13
121.4	-121.68	-121.48	-16.54	-16.40	sir	14.0+	6.0+	------		0.71	0.26	54	------	0.13
122.1	-122.10	-121.80	-16.80	-16.60	lpr	25.5	13.5	98		2.06	0.54	302	0.20,0.19	0.16
122.2	-122.57	-122.10	-16.77	-16.50	lpr	47.5	12.0	112		1.96	0.51	438	0.21,0.22#	0.17
123.2	-123.57	-123.38	-16.80	-16.62	sc	30.0+	4.0+	------		0.48	0.16	23	------	0.10
124.1	-124.71	-124.43	-16.57	-16.42	ilr	24.5	9.5	97		0.90	0.33	138	------	0.12
125.1	-125.57	-124.71	-16.60	-16.32	lpr	83.5	16.0	96		1.91	0.57	965	0.27,0.22	0.18
125.2	-126.07	-125.57	-16.47	-16.32	lpr	47.0	10.5	------		1.92	0.50	353	------	0.20
125.3	-125.49	-125.12	-16.27	-16.10	lpr	35.0	9.0	102		1.76	0.50	257	0.35,0.29#	0.20
125.4	-126.03	-125.49	-16.23	-16.03	lpr	48.5	12.5	98		1.80	0.57	481	0.21,0.21#	0.19
125.5	-125.78	-125.52	-15.77	-15.58	ilr	22.0	4.5	(95)		0.98	0.23	65	------	0.14
125.6	-126.02	-125.79	-16.83	-16.71	sir	21.0+	5.0+	------		0.71	0.22	40	------	0.14
126.1	-126.56	-126.08	-16.82	-16.71	ilr	24.5	6.0	93		1.11	0.31	103	------	0.16
126.2	-126.93	-126.53	-16.29	-16.14	lpr	33.5	9.0	98		1.95	0.50	272	0.25,0.24	0.20
126.3	-126.98	-126.77	-16.70	-16.58	ilr	19.0	6.0	(93)		0.73	0.29	72	------	0.12
127.1	-127.09	-126.91	-16.37	-16.23	s	14.0	9.5	117		1.40	0.43	101	------	0.21
127.2	-127.25	-127.16	-16.34	-16.23	s	7.0	7.5	(20)		1.45	0.57	72	------	0.19

Table 5.1 (continued)

Segment	Longitude West	Longitude East	Latitude South	Latitude North	Type	Length	Width	Azimuth Maximum	Mean Height	Volume Height	Cross	Gradient Gradient	
						km	km	N°E	km	km	km^3	(n,s)	
127.3	-127.33	-127.13	-16.50	-16.41	sir	19.0	5.5	(110)	0.78	0.24	43	------	0.16
127.4	-127.33	-127.03	-16.79	-16.68	sir	26.5+	7.0+	------	1.29	0.46	149	------	0.16
127.5	-127.42	-127.25	-16.40	-16.28	ilr	16.0	7.0	62	1.30	0.48	120	------	0.19
127.6	-127.58	-127.42	-16.40	-16.13	ilr	18.5	9.0	146	1.56	0.46	167	------	0.18
127.7	-127.91	-127.63	-16.44	-16.27	sc	29.0	7.0	(154)	0.56	0.14	37	------	0.14
128.2	-129.00	-128.78	-16.77	-16.68	sc	19.5	6.0+	------	0.52	0.20	27	------	0.10
129.1	-129.08	-128.92	-15.98	-15.83	ilr	14.5	12.0	97	1.54	0.45	120	------	0.19
129.2	-129.22	-129.08	-15.93	-15.80	ilr	14.5	8.0	(116)	1.08	0.41	81	------	0.17
129.3	-129.53	-129.22	-15.88	-15.67	ilr	24.0	7.0	108	1.30	0.37	240	------	0.17
130.1	-130.40	-130.06	-15.90	-15.77	?	28.5+	7.0+	------	0.84	0.31	91	------	0.14
130.2	-130.27	-129.77	-15.75	-15.55	sc	44.5	4.5	(113)	0.66	0.12	47	------	0.13
130.3	-130.67	-130.30	-15.69	-15.53	lpr	26.5	10.5	101	2.03	0.50	264	0.30,0.28#	0.20
130.4	-130.47	-130.31	-15.94	-15.88	sir	12.0	5.0	(113)	0.96	0.29	40	------	0.17
130.5	-130.54	-130.40	-15.88	-15.80	sir	11.0	4.5	(113)	0.83	0.33	42	------	0.15
130.6	-130.87	-130.67	-15.67	-15.58	sir	14.5	4.0	(97)	0.56	0.19	30	------	0.13
131.1	-131.29	-131.00	-15.63	-15.47	lpr	22.0	13.5	109	2.50	0.76	376	0.29,0.33#	0.24
131.2	-131.57	-131.29	-15.60	-15.43	lpr	28.0	12.5	100	2.25	0.64	298	0.29,0.24#	0.24
131.3	-132.12	-131.57	-15.73	-15.30	sc	------	------	(121)	0.64	0.12	50	------	0.14
132.1	-132.45	-132.13	-15.75	-15.57	ilr	26.5	10.5	91	1.51	0.39	245	------	0.17
132.3	-132.82	-132.63	-15.38	-15.27	sir	18.0	5.5	(94)	0.82	0.27	49	------	0.15
132.4	-132.90	-132.47	-15.73	-15.53	sc	33.0	------	(135)	0.47	0.11	23	------	0.14
133.1	-133.17	-132.83	-15.53	-15.42	ilr	23.5	8.5	98	1.49	0.47	223	------	0.17
133.3	-133.63	-133.43	-15.55	-15.43	sir	18.5	6.0	(89)	0.72	0.25	61	------	0.14
133.4	-134.12	-133.67	-15.67	-15.45	sir	34.0	5.0	(111)	0.81	0.18	132	------	0.14
133.5	-133.32	-133.02	-16.48	-16.32	sc	------	------	(57)	0.58	0.11	16	------	0.12
133.7	-133.84	-133.67	-15.52	-15.45	sir	17.5	4.0	(93)	0.57	0.16	20	------	0.12
133.8	-133.27	-133.08	-15.18	-14.98	s	------	------	(44)	1.10	0.31	69	------	0.14
133.9	-133.57	-133.18	-15.73	-15.55	sc	31.0	3.5	(131)	0.55	0.13	32	------	0.12
134.1	-134.58	-134.15	-15.39	-15.24	sir	35.5	8.5+	------	1.05	0.29	134	------	0.16
134.2	-134.58	-134.17	-15.73	-15.40	sir	35.0	15.5	(125)	1.32	0.29	276	------	0.17
134.3	-134.75	-134.58	-15.45	-15.25	sc	11.0+	5.5	------	1.13	0.18	49	------	0.17

Table 5.1 (continued)

Segment	Longitude		Latitude		Type	Length	Width	Azimuth	Maximum	Mean	Volume	Cross	Gradient	
	West	East	South	North						Height	Height		Gradient	
							km	km	N°E	km	km	km^3	(n,s)	
134.4	-134.75	-134.63	-15.60	-15.49	sir	9.0	5.0	(80)	0.48	0.17	22	------	0.13	
134.5	-134.89	-134.77	-14.78	-14.63	s	10.0+	10.5+	------	1.81	0.50	78	------	0.19	
135.1	-135.29	-134.87	-15.43	-15.16	lee	43.5	25.5	115	3.69	0.84	1007	------	0.19	
135.2	-135.12	-134.90	-15.13	-14.98	sir	19.5+	7.0	------	0.87	0.34	95	------	0.13	
135.3	-135.62	-135.27	-15.20	-15.03	lpr	33.5	9.5	99	1.84	0.61	451	------	0.18	
135.5	-136.13	-135.62	-15.25	-14.99	lee	51.0	25.0	99	3.57	0.82	1042	------	0.20	
135.6	-135.93	-135.70	-15.00	-14.92	sir	20.0	6.0	(91)	0.91	0.33	58	------	0.15	
136.1	-136.65	-136.03	-15.26	-15.03	lpr	56.5	14.5	105	1.96	0.54	638	------	0.19	
136.2	-136.58	-136.15	-15.36	-15.16	sc	41.0	7.0	106	1.96	0.45	275	------	0.19	
136.3	-137.13	-136.73	-15.07	-14.77	lee	35.0	25.5	(95)	3.45	0.82	973	------	0.19	
137.1	-137.43	-137.13	-14.97	-14.87	ilr	28.0*	9.5*	93	1.87	0.62	234	------	0.18	
137.2	-137.72	-137.43	-15.03	-14.87	ilr	17.0*	7.5*	101	1.49	0.40	200	------	0.17	
137.3	-138.03	-137.72	-14.98	-14.86	ilr	22.5*	8.0*	107	1.06	0.29	91	------	0.15	
138.1	-138.30	-138.06	-15.07	-14.93	?	------	------	------	1.06	0.27	64	------	0.13	
138.2	-138.62	-138.40	-15.07	-14.87	?	21.5+*	6.5+*	------	0.89	0.35	114	------	0.11	
138.3	-139.03	-138.64	-15.00	-14.67	lee	41.5*	32.5*	(125)	3.31	0.83	1003	------	0.18	
139.1	-139.25	-139.03	-14.76	-14.62	lee	24.0+*	15.5+*	------	2.54	0.80	241	------	0.23	
139.2	-139.27	-139.16	-14.87	-14.75	?	10.0*	9.0*	(179)	1.40	0.44	66	------	0.21	
139.3	-139.43	-139.30	-15.26	-15.11	s	11.5*	14.5*	(174)	1.05	0.37	72	------	0.14	
139.4	-139.84	-139.64	-14.85	-14.72	?	22.0*	6.5*	(165)	0.68	0.18	29	------	0.14	
139.5	-140.06	-139.91	-14.67	-14.52	?	17.5*	5.5*	(149)	0.43	0.11	7	------	0.14	
140.1	-140.42	-140.13	-14.58	-14.40	lpr	30.0*	9.5	127	1.60	0.39	161	------	0.21	
140.2	-140.87	-140.53	-14.42	-14.18	lpr	35.5*	13.5*	118	1.72	0.46	245	------	0.22	
141.1	-141.33	-140.98	-14.32	-14.03	lee	39.0*	24.5*	115	2.77	0.70	688	------	0.20	
141.2	-141.52	-141.33	-14.22	-13.98	lee	24.5*	16.0*	126	2.36	0.96	489	------	0.22	

9. REFERENCES

Anderson, E. M., The dynamics of faulting, Hafner Pub. Co., New York, NY, 1972.

Angevine, C. L., Turcotte, D. L., and J. R. Ockendon, Geometrical form of aseismic ridges, volcanoes and seamounts, *Jour. Geophys. Res.*, 89, 13, 11287-11292, 1984.

Barone, A. M., and W. B. F. Ryan, Single plume model for asynchronous formation of the Lamont Seamounts and adjacent East Pacific Rise terrains, *Jour. Geophys. Res.*, 95, 7, 10801-10827, 1990.

Batiza, R., and D. Vanko, Volcanic development of small oceanic central volcanoes on the flanks of the East Pacific Rise inferred from narrow-beam echo-sounder surveys, *Mar. Geol.*, 54, 53-90, 1983.

Batschelet, E., *Circular statistics in biology*, Academic Press, New York, NY, 1981.

Chayes, D. N., and D. W. Caress, Processing and display of multibeam echosounder data on the R/V Maurice Ewing, *EOS Trans. Amer. Geophys. Union*, 74, 43, 562, 1993.

Clague, D. A., Hon, K. A., Anderson, J. L., Chadwick, W. W. Jr., and C. G. Fox, Bathymetry of Puna Ridge, Kilauea Volcano, Hawaii, in *Miscellaneous Field Studies Map*, MF-2237, *U. S. Geol. Survey*, 1994.

DeMets, C., Gordon, R. G., Argus, D. F., and S. Stein, Current plate motions, *Geophys. Jour. Int.*, 101, 2, 425-478, 1990.

Dietrich, J. H., Growth and persistence of Hawaiian volcanic rift zones, *Jour. Geophys. Res.*, 93, 5, 4258-4270, 1988.

Fiske, R. S., and E. D. Jackson, Orientation and growth of Hawaiian volcanic rifts; the effect of regional structure and gravitational stresses, *Proc. Roy. Soc. London Ser. A*, 329, 299-326, 1972.

Fornari, D. J., Malahoff, A., and B. C. Heezen, Volcanic structure of the crest of the Puna Ridge, Hawaii; geophysical implications of submarine volcanic terrain, *Geol. Soc. Amer., Bull.*, 89, 4, 605-616, 1978.

Fornari, D. J., The geomorphic and structural development of Hawaiian submarine rift zones, *U.S. Geol. Prof. Paper*, 1350, 125-132, 1987.

Fornari, D., Garcia, M. O., Tyce, R. C., and D. G. Gallo, Morphology and structure of Loihi Seamount based on Seabeam sonar mapping, *Jour. Geophys. Res.*, 93, 12, 15227-15238, 1988.

Goodwillie, A. M., and B. Parsons, Placing bounds on lithospheric deformation in the central Pacific Ocean, *Earth and Planet. Sci. Lett.*, 111, 1, 123-139, 1992.

Gripp, A. E., and R. G. Gordon, Current plate velocities relative to the hotspots incorporating the NUVEL-1 global plate motion model, *Geophys. Res. Lett.*, 17, 8, 1109-1112, 1990.

Heimpel, M., and P. Olson, Buoyancy-driven fracture and magma transport through the lithosphere; models and experiments, in: *Magmatic Systems*, Academic Press, San Diego, CA., 1994.

Lacey, A., Ockendon, J. R., and D. L. Turcotte, On the geometrical form of volcanoes, *Earth Planet. Sci. Lett.*, 54, 1, 139-143, 1981.

Lister, J. R., Buoyancy-driven fluid fracture; the effects of material toughness and of low-viscosity precursors, 210, 263-280, 1990.

Lister, J. R., and R. C. Kerr, Fluid-mechanical models of crack propagation and their application to magma transport in dykes, *Jour. Geophys. Res.*, 96, 10049-10077, 1991.

Lonsdale, P., F., Geography and history of the Louisville hotspot chain in the Southwest Pacific, *Jour. Geophys. Res.*, 93, 4, 3078-3104, 1988.

Lonsdale, P. F., A Geomorphological reconnaissance of the submarine part of the East Rift Zone of Kilauea Volcano, Hawaii, *Bull. Volc.*, 51, 123-144, 1989.

Lonsdale, P. F., Structural patterns of the Pacific floor offshore of Peninsular California, *AAPG Memoir*, 47, 7, 87-125, 1991.

Lynch, M. A., The crossgrain ridges; linear ridge groups; new evidence for intraplate tension, Doctoral thesis, University of California San Diego, Scripps Institution of Oceanography, La Jolla, CA, 1993.

Maaloe, S., The generation and shape of feeder dykes from mantle sources, *Contrib. Mineral. Petrol.*, 96-47-55, 1987.

Malahoff, A., and F. McCoy, The geologic structure of Puna submarine ridge, Hawaii, *Jour. Geophys. Res.*, 72, 2, 541-548, 1967.

Menard, H. W., Minor lineations in the Pacific Basin, *Geol. Soc. Amer. Bull.*, 70, 1491-1496, 1941.

Menard, H. W., Archipelagic aprons, *Am. Assoc. Petrol. Geol. Bull.*, 40, 913-918, 1983.

Menard, H. W., and H. S. Ladd, Islands, seamounts, guyots and atolls in: *The Sea*, vol. 3, pp. 365-385, Wiley-Interscience, New York, 1983.

Moore, J. G., and R. S. Fiske, Volcanic substructure inferred from dredge samples and ocean-bottom photographs, Hawaii, *Geol. Soc. Amer., Bull.*, 80, 7, 1191-1201, 1969.

Nakamura, K., Volcanoes as possible indicators of tectonic stress orientation; principle and proposal, *Jour. Volcan. Geotherm. Res.*, 2, 1, 1-16, 1977.

Nakamura, K., Jacob, K. H., and J. N. Davies, Volcanoes as possible indicators of tectonic stress orientation; Aleutians and Alaska, *Pure Appl. Geophys.*, 115, 1-2, 87-112, 1977.

Parsons, T., and G. A. Thompson, The role of magma overpressure in suppressing earthquakes and topography; worldwide example, *Science*, 253, 5026, 1399-1402, 1991.

Rubin, A. M., and D. D. Pollard, Origins of blade-like dikes in volcanic rift zones, *U. S. Geol. Survey Prof. Paper*, 1350, 1449-1470, 1987.

Ryan, M. P., R. Y. Koyanagi, and R. S. Fiske, Modeling the three-dimensional structure of magma transport systems; application to Kilauea volcano, Hawaii, *Jour. Geophys. Res.*, 86, 7111-7129, 1981.

Sandwell, D. T., Winterer, E. L., Mammerickx, J., Duncan, R. A., Lynch, M. A., Levitt, D. A., and C. L. Johnson, Evidence for diffuse extension of the Pacific plate from Pukapuka ridges and cross-grain gravity lineations, *Jour. Geophys. Res.*, 100, B8, 15087-15099, 1995.

Scheirer, D. S., and K. C. Macdonald, Near-axis seamounts on the flanks of the East Pacific Rise, 8 degrees N to 17 degrees N, *Jour. Geophys. Res.*, 100, 2, 2239-2259, 1995.

Searle, R. C., Francheteau, J., and B. Cornaglia, New observations on mid-plate volcanism and the tectonic history of the Pacific Plate, Tahiti to Easter Microplate, *Earth Planet. Sci. Lett.*, 131, 3-4, 395-421, 1995.

Shen, Y., Forsyth, D. W., Scheirer, D. S., and K. C. Macdonald, Two forms of volcanism; implications for mantle flow and off-axis crustal production on the west flank of the southern East Pacific Rise, *Jour. Geophys. Res.*, 98, 10, 17875-17889, 1993.

Shepard, G. A., and K. O. Emery, Submarine topography of part of the deep-sea floor off the California Coast, *Geol. Soc. Amer. Sp. Paper*, 31, 1941.

Smith, D. K., Shape analysis of Pacific seamounts, *Earth Planet. Sci. Lett.*, 90, 4, 457-466, 1988.

Spence, D. A., and D. L. Turcotte, Buoyancy-driven magma fracture; a mechanism for ascent through the lithosphere and the emplacement of diamonds, *Jour. Geophy. Res.*, 95, 5133-5139, 1990.

Takada, A., Experimental study on propagation of liquid-filled crack in gelatin; shape and velocity in hydrostatic stress conditions, *Jour. Geophys. Res.*, 95, 8471-8481, 1990.

Takada, A., Accumulation of magma in space and time by crack interaction, in: *Magmatic Systems*, Academic Press, San Diego, CA., 1994a.

Takada, A., The influence of regional stress and magmatic input on styles of monogenetic and polygenetic volcanism, *Jour. Geophys. Res.*, 99, 7, 13563-13573, 1994b.

Takada, A., Development of a subvolcanic structure by the interaction of liquid-filled cracks, *Jour. Volcan. Geotherm. Res.*, 61, 3-4, 207-224, 1994c.

Vogt, P. R., and N. C. Smoot, The Geisha Guyots; multibeam bathymetry and morphometric interpretation, *Jour. Geophys. Res.*, 89, 13, 11085-11107, 1984.

Wessel, P., and W. H. F. Smith, Free software helps map and display data, *EOS Trans. Amer. Geophys. Union*, 72, 41, 441, 1991.

Winterer, E. L., Gloria leg 4 R/V Melville shipboard cruise report, 1993.

Winterer, E. L., Johnson, C., Levitt, D., Lynch, M. A., Mammerickx, J., Sandwell, D., Small, C., and M. Simons, Morphology of Pukapuka volcanic ridge system, Southeast Pacific, *EOS Trans. Amer. Geophys. Union*, 74, 16, 285, 1993.

Winterer, E. L., and D. T. Sandwell, Evidence from en-echelon cross-grain ridges for tensional cracks in the Pacific Plate, *Nature*, 329, 6139, 534-537, 1987.

Wyss, M., Hawaiian rift and recent Icelandic volcanism; expressions of plume generated radial stress fields, *Jour. Geophys.*, 47, 1-3, 19-22, 1980.